Deep Brain Stimulation Electrode Localization and Orientation Detection Using Magnetic Field Measurements

Dissertation

for the degree of Doctor of Engineering
(Dr.-Ing.)

Submitted to the Faculty of Engineering of
Christian-Albrechts-Universität zu Kiel

by

Mevlüt Yalaz

Kiel 2022

1st Referee: Prof. Dr.-Ing. Michael Höft
2nd Referee: Prof. Dr. Dr. h.c. Günther Deuschl
3rd Referee: Prof. Dr. rer. nat. habil. Ursula van Rienen

Date of oral examination: July 5th, 2022

Preface

This doctoral thesis was developed within the framework of the Collaborative Research Center 1261 *"Magnetoelectric Sensors: From Composite Materials to Biomagnetic Diagnostics"* at the Chair of Microwave Engineering of the Department of Electrical and Information Engineering of the Christian-Albrechts-Universität zu Kiel (CAU) and the Department of Neurology of the University Medical Center Schleswig-Holstein (UKSH) in Kiel.

I would like to thank my doctoral supervisor Prof. Dr.-Ing. Michael Höft and my second supervisor Prof. Dr. Dr. h.c. Günther Deuschl for their versatile support of my doctorate as well as the other reviewers and members of the examination committee Prof. Dr. rer. nat. habil. Ursula van Rienen, Prof. Dr. Martina Gerken and Prof. Dr. Robert Rieger.

In particular, I am very grateful to Prof. Cameron C. McIntyre and Dr. Sohail Noor for the excellent supervision during my stay abroad at the Neuromodulation Center of Case Western Reserve University in Cleveland (Ohio, USA). Furthermore, my special thanks go to Prof. Dr. Alfons Schnitzler and Prof. Dr. Markus Butz from the University Hospital Düsseldorf (UKD) for their tireless efforts during very long measurement days. Likewise, a big thank you goes out to Dr. Nicholas Maling and Dr. rer. nat León. M. Juárez-Paz from Boston Scientific Corporation for their many advice and discussions from an industrial point of view. The results achieved through these collaborations have contributed significantly to the success of this work.

I would also like to thank Prof. Dr.-Ing. Gerhard Schmidt, Prof. Dr.-Ing. Muthuraman Muthuraman, Prof. Dr. med. Ann-Kristin Helmers, Dr.-Ing. Alexander Teplyuk, Dr.-Ing. Philipp Durdeaut, Dr.-Ing. Jens Reermann, Dr. Jos S. Becktepe, Florian Stern, Henrik Wolframm, Chad Bartlett as well as Melanie Bork and all other members of the Chair of Microwave Engineering and the Department of Neurology for fruitful advices and frequent discussions.

In the context of the Collaborative Research Center 1261, I have especially benefited from the scientific collaboration and the many stimulating discussions. Therefore, I would like to especially thank my colleagues Prof. Dr.-Ing. Eckhard Quandt, Dr. rer. nat Dirk Meyners, Dr.-Ing. Eric Elzenheimer, Dr.-Ing. Patrick Hayes, Viktor Schell, and Mesut-Ömür Özden.

Last but not least, I would like to thank my mother, father, brother and sister for their motivational and mental support.

The biggest thanks comes at the end. The fact that my lovely wife Tuğba has always supported me, motivated me, and helped me through long lean periods despite her own professional commitments, I dedicate this work to her with heartfelt thanks. My darling.

Abstract

Deep brain stimulation (DBS) is a neurosurgical procedure for treating a wide range of patients with movement and neurological disorders such as Parkinson's disease, dystonia, epilepsy, obsessive-compulsive disorder, and essential tremor. To date, more than 200,000 patients have been treated with DBS worldwide. During surgery, small electrodes are implanted in specific target areas of the brain depending on the symptoms to be treated. These electrodes are connected via extension wires to a battery-powered neurostimulator that is placed under the skin in the upper chest. The neurostimulator sends continuous electrical pulses to the electrodes, thereby regulating abnormal brain activity. Proper adjustment of stimulation parameters is essential for successful DBS treatment and patient satisfaction. Current stimulation programming paradigms are based on trial-and-error principles and require a high level of experience on the part of the clinician. The significant number of possible combinations of stimulation parameters is further increased by novel electrode designs with the technology of directional stimulation, which makes the setting of individual parameters a time-consuming and exhausting undertaking. To facilitate and guide stimulation programming, knowledge of the precise position and orientation of the electrode within the anatomical structures of the brain is required. Therefore, the existence of a clinically reliable method to detect the localization and orientation of conventional and directional DBS electrodes is fundamental, not only to facilitate stimulation programming but also to verify the position of implanted electrodes, to evaluate the therapeutic and adverse effects of DBS, and to gain valuable insights into understanding DBS mechanisms. Currently, no generally accepted protocols have been established for electrode localization and orientation detection. Current approaches are based mainly on postoperative computed tomography scans that expose patients to ionizing radiation, and this process hinders further research and the conduct of long-term clinical studies of open DBS-related questions. Against this background, this dissertation presents a clinically promising method for localization and orientation detection of directional DBS electrodes that overcomes the fundamental drawbacks of current postoperative imaging techniques without exposing the patient to any radiation. The approach of this method is based on measurements of stimulation-induced magnetic fields and is, therefore, completely harmless to the patient. The basic idea is to exploit the spatial distribution of the high number of stimulation contacts of the electrode. Various contacts are activated against each other to generate a defined stimulation current with a known direction of current flow. The elec-

tric current, in turn, induces a known magnetic field. The distribution of the magnetic field can be measured around the head and, with precise electromagnetic models and detection algorithms, can be used to derive electrode position and orientation. Magnetic field measurements with bipolar omnidirectional and directional electrode configurations were used for electrode localization and electrode orientation detection, respectively. Using the clinically applied state-of-the-art magnetoencephalography (MEG) system and a head-torso phantom with realistic dimensions, localization accuracy of approximately 2 mm and orientation detection accuracy of approximately 4° were achieved. These accuracies were limited mainly by the spatial resolution of the MEG system. Although clinicians state that these detection accuracies are acceptable when considering the benefits of a radiation-free approach, the accuracy can be further increased by improving the spatial resolution of existing MEG systems or by using emerging flexible measurement systems. Should even higher detection accuracy be achieved in clinical applications, the proposed method for magnetic detection of electrode position and orientation will undoubtedly represent a major advance in neurology and will become the postoperative modality of choice to enable the full potential of patient-specific programming of directional DBS systems.

Kurzzusammenfassung

Die Tiefe Hirnstimulation (engl.: deep brain stimulation, DBS) ist ein neurochirurgisches Verfahren zur Behandlung eines breiten Spektrums von Patienten mit Bewegungs- und neurologischen Störungen wie der Parkinson-Krankheit, Dystonie, Epilepsie, Zwangsstörungen und essentiellem Tremor. Bis heute wurden weltweit mehr als 200.000 Patienten mit DBS behandelt. Während des Eingriffs werden je nach den zu behandelnden Symptomen kleine Elektroden in bestimmte Zielbereiche des Gehirns implantiert. Diese Elektroden sind über Verlängerungskabel mit einem batteriebetriebenen Neurostimulator verbunden, der unter der Haut im oberen Brustbereich platziert wird. Der Neurostimulator sendet kontinuierlich elektrische Impulse an die Elektroden und reguliert so die abnorme Hirnaktivität. Die korrekte Einstellung der Stimulationsparameter ist für eine erfolgreiche DBS-Behandlung und die Zufriedenheit der Patienten von entscheidender Bedeutung. Die derzeitigen Paradigmen der Stimulationsprogrammierung beruhen auf dem Prinzip von Trial-and-Error und erfordern ein hohes Maß an Erfahrung auf Seiten des Arztes. Die beträchtliche Anzahl möglicher Kombinationen von Stimulationsparametern wird durch neuartige Elektrodendesigns mit der Technologie der gerichteten Stimulation weiter erhöht, was die Einstellung der individuellen Parameter zu einer sehr zeitaufwändigen und anstrengenden Angelegenheit macht. Um die Stimulationsprogrammierung zu erleichtern und zu steuern, ist die Kenntnis der genauen Position und Orientierung der Elektrode innerhalb der anatomischen Strukturen im Gehirn erforderlich. Daher ist die Existenz einer klinisch zuverlässigen Methode zur Erkennung der Lokalisierung und Orientierungs konventioneller und gerichteter DBS-Elektroden von grundlegender Bedeutung, nicht nur zur Eleichterung der Stimulationsprogrammierung, sondern auch zur Überprüfung der Position der implantierten Elektroden, zur Bewertung der therapeutischen und unerwünschten Wirkungen der DBS und zur Gewinnung wertvoller Erkenntnisse über die Mechanismen der DBS. Derzeit gibt es keine allgemein anerkannten Protokolle für die Lokalisierung und Orientierungsbestimmung von Elektroden. Derzeitige Ansätze basieren hauptsächlich auf postoperativen Computertomographien, bei denen die Patienten ionisierender Strahlung ausgesetzt werden, was die weitere Forschung und die Durchführung klinischer Langzeitstudien zu offenen Fragen im Zusammenhang mit der DBS erschwert. Vor diesem Hintergrund wird in dieser Dissertation eine klinisch vielversprechende Methode zur Lokalisierung und Orientierungserkennung von direktionalen DBS-Elektroden vorgestellt, die die grundlegenden

Nachteile der derzeitigen postoperativen Bildgebungsverfahren überwindet, ohne den Patienten jeglicher Strahlung auszusetzen. Der Ansatz dieser Methode basiert auf der Messung von stimulationsinduzierten Magnetfeldern und ist daher für den Patienten völlig ungefährlich. Die Grundidee besteht darin, die räumliche Verteilung der hohen Anzahl von Stimulationskontakten der Elektrode auszunutzen. Verschiedene Kontakte werden gegeneinander aktiviert, um einen definierten Stimulationsstrom mit bekannter Stromflussrichtung zu erzeugen. Der elektrische Strom induziert wiederrum ein bekanntes Magnetfeld. Die Verteilung des Magnetfelds kann um den Kopf herum gemessen und mit präzisen elektromagnetischen Modellen und Detektionsalgorithmen zur Ableitung der Elektrodenposition und -orientierung verwendet werden. Magnetfeldmessungen mit bipolaren omnidirektionalen bzw. direktionalen Elektrodenkonfigurationen wurden zur Elektrodenlokalisierung bzw. zur Detektion der Elektrodenorientierung verwendet. Unter Verwendung des klinisch eingesetzten state-of-the-art Magnetoenzephalographie (MEG)-Systems und eines Kopf-Torso-Phantoms mit realistischen Abmessungen wurde eine Lokalisierungsgenauigkeit von etwa 2 mm und eine Orientierungserkennungsgenauigkeit von etwa 4° erreicht. Diese Genauigkeiten wurden hauptsächlich durch die räumliche Auflösung des MEG-Systems begrenzt. Obwohl Kliniker diese Werte in Anbetracht der Vorteile eines strahlungsfreien Ansatzes für akzeptabel halten, kann die Genauigkeit durch die Verbesserung der räumlichen Auflösung bestehender MEG-Systeme oder durch den Einsatz neuer flexibler Messsysteme weiter erhöht werden. Sollte in klinischen Anwendungen eine noch höhere Detektionsgenauigkeit erreicht werden, wird die vorgeschlagene Methode zur magnetischen Erkennung der Elektrodenposition und -orientierung zweifellos einen großen Fortschritt in der Neurologie darstellen und zur postoperativen Modalität der Wahl werden, um das volle Potenzial der patientenspezifischen Programmierung von direktionalen DBS-System zu ermöglichen.

Declaration

I hereby declare that I have written this dissertation entitled

Deep Brain Stimulation Electrode Localization and Orientation Detection Using Magnetic Field Measurements

independently and without improper external assistance and that I have identified all quotations of other authors. Furthermore, this thesis has not been, partially or completely, submitted to any other university or institute in the context of an examination procedure. Parts of the content of the work have already been published in my scientific publications and is stated accordingly. I declare that the following work has been written in compliance with the rules of good scientific practice established by the German Research Foundation.

Place, Date Mevlüt Yalaz

Table of Contents

Chapter 1

Introduction

1.1 Motivation and Goal of the Work

Deep brain stimulation (DBS) is a neurosurgical procedure for the treatment of a variety of movement and neurological disorders such as Parkinson's disease, essential tremor, dystonia, epilepsy, and obsessive-compulsive disorder; it is also being studied for use with many other conditions [Deu11; Kra19]. It is estimated that, to date, more than 200,000 patients have been treated with DBS worldwide, and that number continues to increase each year [Ved21]. The major factor driving the popularity of DBS is the rapidly aging population, with older people being at a high risk for neurological diseases. According to the World Population Ageing 2019 report, there were more than 700 million people aged 65 years or older worldwide in 2019. This number is expected to double to 1.5 billion by 2050. During surgery, a DBS electrode is implanted through a small opening in the skull into a specific and carefully selected brain region depending on the symptoms to be treated. The electrode is connected by a long extension wire to a battery-powered neurostimulator that is usually implanted under the skin in the upper chest (see Figure 1.1), and the neurostimulator delivers continuous electrical pulses to the electrode according to the patient's needs. It is notable to observe the behavior of Parkinsonian patients who have undergone DBS surgery when the neurostimulator is switched off. The symptoms, mainly the tremor, return immediately, and the full extent of the disability becomes visible. DBS can control not only the patients' tremors but also other symptoms such as rigor or dystonia. Although the immediate effect when the pulse is switched on and off is not visible, the symptoms are equally well-treated. This on/off mechanism of DBS indicates that the mentioned diseases are not curable and that the symptoms can only be suppressed.

A number of factors contribute to positive clinical outcomes in DBS treatment, including careful patient selection, precise implantation of the electrode in the specific target area, and effective programming of DBS neurostimulators. However, after the electrode has been implanted into the brain, the only aspect that can be modified to improve the

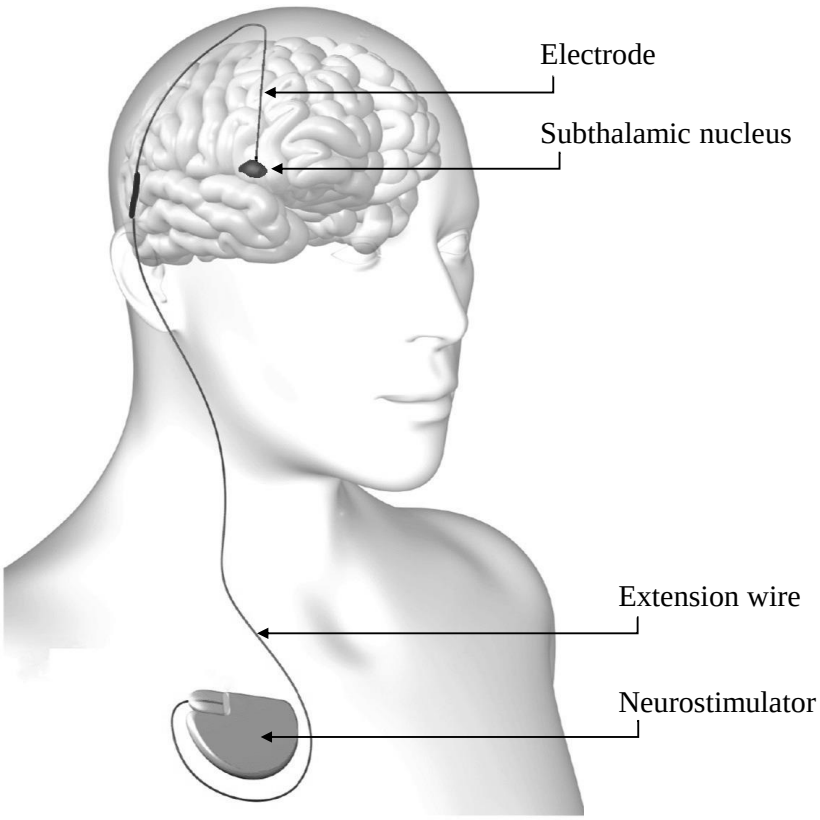

Figure 1.1: Typical deep brain stimulation (DBS) setup. The electrode is placed in the subthalamic nucleus (STN) and is connected via an extension wire to a battery-powered neurostimulator. Adapted from [Sha14].

clinical result is the programming of the neurostimulator. Programming becomes particularly important when the DBS electrode does not hit its target exactly, as stimulation that spreads away from the intended target area can cause a variety of adverse effects such as dysarthria, facial contractions, ocular deviations, and even mood and cognitive changes [Zar20]. However, the stimulation programming is an exhausting, time-consuming practice and is based on the trial-and-error principle, requiring a significant amount of experience on the part of the clinician [Pic16; And18]. This is largely due to the fact that a significant number of possible combinations of individual stimulation parameters exist. Since 2015, directional DBS electrode designs have become available with contacts that are divided into three segments along the circumference of the electrode (unlike conventional electrodes with cylindrical contacts) that allow the stimulation field to be moved in a desired direction [Ste19; Kra21]. These types of electrodes increase the complexity of stimulation programming, so improvements in programming algorithms, including a switch from trial-and-error to automated programming, are important to maximize the benefits of the new electrode designs. However, postoperative stimulation programming will require determining the exact position and rotational orientation of the electrode in relation to its anatomical environment. The availability of a clinically reliable method for electrode localization and electrode orientation detection is essential not only to facilitate

stimulation programming but also to verify the implanted electrode position; to help solve open neuronal issues for optimal DBS treatment, for example, to better understand the neurobiological mechanisms of DBS; to help identify even more precise and novel targets in the brain for various diseases; and to evaluate the benefits and side effects of DBS. The main open challenges in the field of DBS that can be addressed by precise electrode localization and orientation detection are discussed in more detail in the first section of the next chapter.

Current approaches for electrode localization are based on the fusion of preoperative and postoperative neuroimaging data, usually postoperative computed tomography (CT), which contains electrode-induced artifact patterns, with preoperative magnetic resonance imaging (MRI), which reveals a detailed visualization of the target structures [Lee10a; Pae11]. This technique introduces an error factor associated with the quality of registration of the two imaging modalities, such that poor registration contributes to significant error in electrode position detection [Gee16; Xia17]. Additionally, significant discrepancies between electrode locations estimated by postoperative CT and MRI as well as differences in localization results between different widely used software programs have been reported [Eng18; Bur21]. Moreover, the CT process exposes patients to ionizing radiation, whereas the MRI process cannot always be performed for safety reasons [Bou20]. Furthermore, reimaging and, in case of CT, reradiation of the patient are required to determine whether the electrode has moved in its implanted position over time. Similar to electrode localization, no established means for reviewing the electrode orientation have been described that sufficiently allow an accurate determination. Current methods include anteroposterior and lateral X-rays, standard CT, flat-panel CT, and rotational fluoroscopy [Sit17; Rei17; Hel18; Hun19; Egg21]. Techniques using X-rays and CT rely on high-quality images because specific artifact patterns generated by various elements of the directional electrode must be detected [Hel18]. However, the underlying artifact has 180° symmetry, which limits orientation detection to two possible solutions, and neither imaging technique is currently capable of resolving this ambiguity without further measurements. Rotational fluoroscopy seems to be a promising alternative [Rei17], but all existing methods for orientation detection expose patients to ionizing radiation, which may be detrimental to their health. Additionally, electrode migration, electrode torsion, any trauma or surgical intervention, and the natural course of neurodegenerative diseases may cause undesired electrode displacement and rotation, requiring the patient to be re-exposed to radiation or X-ray imaging [Mor17; Gor21]. This would hinder further research into whether and to what extent directional electrodes move and continue to rotate after implantation, and, therefore, long-term clinical studies may be quite difficult to conduct. A more detailed description of the challenges and limitations in both electrode localization and electrode orientation detection is provided in the next chapter.

Against this background, it is obvious that there is a need for a clinically reliable methodology for precise, effective, and radiation-free detection of electrode position and

orientation after the electrode has been implanted. This dissertation presents an alternative and clinically promising approach for determining electrode position and orientation based on measurements of the magnetic field generated by stimulating electrical pulses of DBS; this process, then, overcomes the fundamental drawbacks of current postoperative imaging techniques. The main advantage is that patients are not exposed to any radiation, which could make the proposed method a promising alternative to currently existing methods. The feasibility and potential of magnetic field recordings for such issues have not been investigated previously, so the method developed within the framework of this dissertation is the first of its kind. In contrast to this work, the focus of current DBS research in magnetic field measurements is on developing appropriate artifact rejection methods to eliminate the interference in the magnetic fields caused by DBS [Kan20]. However, the DBS pulses in the magnetic field measurements, commonly referred to as artifacts, are essential to the method presented in this dissertation because the source of the artifact allows conclusions to be drawn about the position and orientation of the electrode. The feasibility of DBS electrode localization based on scalp electroencephalography (EEG) has been investigated, but localization errors of more than 10 mm have been reported [Iac19], so this method may not be clinically applicable in its current version.

The main objective of the present work is to develop a simple, realistic, and patient-friendly measurement method for radiation-free determination of the position and orientation of a directional DBS electrode using magnetic field measurements that can be used in clinical practice. This includes investigating the magnetic properties of DBS pulses, identifying a possible solution for electrode position detection using magnetic field measurements, finding a possible approach for electrode orientation detection using magnetic field measurements, and investigating achievable accuracies and possible limitations of magnetic detection of electrode position and orientation. The investigations were all based on experiments on phantoms constructed specifically for this work and were conducted systematically. The first magnetic field recordings were performed on a simplified phantom with a measurement system constructed in-house in the magnetically shielded chamber at the Faculty of Engineering of Kiel University. Further measurements were performed with the clinically used state-of-the-art magnetoencephalography (MEG) system at the University Hospital Düsseldorf (ger.: Universitätsklinikum Düsseldorf, UKD), first on a simplified phantom and then on a realistically shaped head-torso phantom.

The present dissertation was developed within the framework of the Collaborative Research Center 1261, which was funded by the German Research Foundation (ger.: Deutsche Forschungsgemeinschaft, DFG). In an interdisciplinary collaboration among the departments of physics, materials science, electrical engineering, and medicine, various types of magnetic field sensors as well as their potential use in biomagnetic applications were researched. As the DBS project demonstrated promising progress in research and the clinical relevance became more and more evident, Boston Scientific Corporation (Marlbor-

ough, MA, USA), a manufacturer of DBS devices and surgical planning and programming software, indicated interest and participated in this project.

1.2 Outline

This dissertation is divided into four chapters, three of which follow this introductory chapter. Chapter 2 presents the fundamental theory used to understand this thesis and to further describe the method for magnetic detection of electrode position and orientation presented in this dissertation. It refers mainly to the four aspects mentioned in the title of this thesis: (1) DBS, (2) electrode localization, (3) electrode orientation detection, and (4) magnetic field measurements. First, in Section 2.1, the main challenges and open issues in the field of DBS are summarized, which can generally be addressed and solved by precise electrode localization and electrode orientation detection methods. Then, in Section 2.2, the current state of the art in electrode localization is outlined, followed by the description of the state of the art in electrode orientation detection in Section 2.3. In both sections, the advantages and disadvantages of currently existing methods are described in detail, and the advantages of the alternative method proposed in this dissertation are clarified. At the end of the chapter (Section 2.4), magnetic field measurements and magnetic field modeling, which represent the main components of the presented method, are discussed. Chapter 3 describes the main part of this dissertation and contains six journal publications, which were written according to a systematic workflow and are arranged chronologically by publication date. After each of the six publications, the key findings and scientific implications are summarized. Figure 1.2 provides an overview of the publications included in this dissertation and illustrates which publication is assigned to which of the three research areas (magnetic field measurements, electrode localization, electrode orientation detection). Finally, Chapter 4 summarizes this dissertation and presents a detailed outlook on further research related to this thesis.

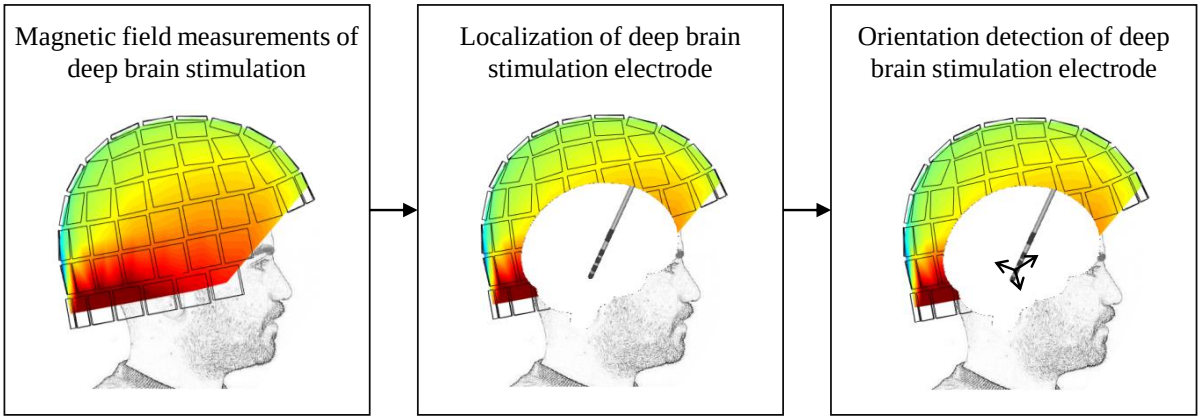

Section 3.1: M. Yalaz et al., "The Magnetic Properties of Electrical Pulses Delivered by Deep-Brain Stimulation Systems," in IEEE Transactions on Instrumentation and Measurement, July 2020.

Section 3.2: M. Yalaz et al., "Dipole Fit Localization of the Deep Brain Stimulation Electrode Using 3D Magnetic Field Measurements," in IEEE Sensors Journal, August 2020.

Section 3.3: M. Yalaz et al., "DBS Electrode Localization and Rotational Orientation Detection using SQUID-based Magnetoencephalography," in Journal of Neural Engineering, March 2021.

Section 3.4: M. Yalaz et al., "Investigation of Magnetoelectric Sensor Requirements for Deep Brain Stimulation Electrode Localization and Rotational Orientation Detection," in Sensors, April 2021.

Section 3.5: M. Yalaz et al., "Determining the Rotational Orientation of Directional Deep Brain Stimulation Electrodes using Magnetoencephalography," in Journal of Neural Engineering, October 2021.

Section 3.6: M. Yalaz et al., "MaDoPO: Magnetic Detection of Positions and Orientations of Segmented Deep Brain Stimulation Electrodes: A Radiation-free Method based on Magnetoencephalography," in Brain Sciences, January 2022.

Figure 1.2: Overview of publications included in Sections 3.1–3.6 of this dissertation (bottom box), indicating which publication is assigned to which of the three research areas illustrated above.

Chapter 2

Fundamentals

This chapter provides the essential fundamentals related to DBS and magnetic fields for the understanding of the present dissertation. The first section summarizes the main open challenges in DBS and explains why electrode localization and electrode orientation detection are generally needed to overcome them. The next two sections present the state of the art in DBS electrode localization and in electrode orientation detection, which are based on neuroimaging data. In contrast, the advantages of an alternative and radiation-free method developed as part of this dissertation are highlighted. Finally, the fundamentals of a magnetic field are discussed, as magnetic field measurements and magnetic field modeling form the core matter of this dissertation.

2.1 Challenges in Deep Brain Stimulation

DBS provides effective and safe relief from the impairing symptoms of movement disorders. The therapy enables people who suffer from these disorders and the associated symptoms to have better control over their movements, giving them greater freedom in their work and leisure time. Since the first description of the success of high-frequency stimulation to suppress tremors 35 years ago [Ben87], DBS has become an established therapy for various movement disorders [Deu11; Kra19]. Today, approximately 200,000 patients worldwide have been treated with DBS [Ved21]. In Germany, an estimated 700 DBS surgeries are currently performed annually on patients with movement disorders, and DBS has proved to be the most important therapeutic innovation of the past decade in the treatment of idiopathic Parkinson's syndrome [Loz19]. The major factor driving the popularity of DBS is the rapidly aging population and the accompanying high risk and prevalence of neurological diseases among older adults. According to the World Population Ageing 2019 report, there were approximately 703 million people aged 65 years or older worldwide in 2019, and this number is expected to double to 1.5 billion by 2050. Moreover, by 2050, one in six people in the world will be older than 65, compared to one in eleven in 2019. Other major factors behind the increasing demand for DBS are the availability of technologically

advanced devices and the minimally invasive procedures involved. Today, three major companies — Medtronic plc, Boston Scientific Corporation, and Abbott Laboratories (St. Jude Medical) — provide implantable DBS systems. The total market value of global DBS devices was USD 1.0 billion in 2019 and is projected to reach USD 2.8 billion by 2026 (according to Grand View Research, Inc.). Consequently, all such advancements in DBS technology will continue to lead to the growth in the popularity of this treatment in the future. As promising as DBS may be, several major challenges stand in the way of its further development and widespread application. An in-depth discussion of the complexity of these problems is beyond the scope of this chapter, but they are worth mentioning briefly as potential obstacles that can be solved by the developed method within the framework of this dissertation.

Despite extensive basic science and human studies, the exact neurobiological mechanisms of the actions of DBS are not yet fully understood. Basically, DBS is the application of electric fields to stimulate neuronal elements, especially axons around the electrode, resulting in the opening and closing of voltage-gated sodium channels, the generation of action potentials, and the control of neurotransmitter release. However, it is still unclear whether this is completely an inhibitory or excitatory mechanism or whether the effects are predominantly local or can be seen throughout a network. There are four possible mechanistic theories [Loz19; Lee19], (1) direct inhibition of neuronal activity [Ben00; Jen09; Ham17], (2) direct excitation of neuronal activity [Has03; McI04a; Mor11], (3) information interruption [Gri04; Agn13; Nam15], and (4) synaptic filtering [Erw00; Ros14]. The precise localization of the electrode within the brain structures after DBS implantation provides important data to confirm the relationship between the electrode and the target. This helps to explain intended or unexpected effects.

The exact identification of the target area in the brain is still not well-defined. The deep brain structures commonly used as target areas to reduce the motor symptoms of Parkinson's disease are the subthalamic nucleus (STN) for tremor and rigidity, the nucleus ventrointermedius (Vim) of the thalamus for tremor alone, and the globus pallidus internus (GPi) for rigidity, dyskinesia, or dystonia [Ewe18; Har19]. Depending on the motor symptoms to be treated, other structures such as the zona incerta or a thalamic subnucleus may also be stimulated [Hem10; Hol18; Pyc18; Lee19; Cag19]. Other target areas for DBS are currently the subject of intense research, so it is expected that more types of neurological disorders will become treatable with DBS. Examples of recent target areas include the pedunculopontine nucleus for Parkinsonian phenomena such as gait and balance disorders [Goe19; Lei19], the internal capsule for obsessive-compulsive disorders [Wid19; Den20], and Brodmann area 25 for depression [Cro19; Bro20]. Thus, it is expected that future clinical applications of DBS will include stimulation not only at the already identified targets, but also at a variety of brain structures and nuclei. Accurate localization of the electrode after DBS implantation is crucial in finding new targets for DBS.

Modern DBS programming consists largely of manual trial-and-error methods in which

clinicians test settings based on patient responses; this process is referred to as monopolar review. Manual programming represents a significant time burden for the clinician, while the patient may be exposed to discomfort. Additionally, this process is unlikely to result in optimized parameter settings. In the first year after surgery, it takes about 18 to 32 hours of clinical programming for the simplest electrode designs with four equally spaced contacts [Hun05]. To adapt and adjust the stimulation parameters, a patient makes between four and 17 visits to the programming center in the first year [Ond05]. There are more than 25,000 possible combinations of programming parameters such as pulse width, frequency, and amplitude, and 65 combinations of contact selection for the simplest four-contact electrode [Kun04]. The mathematical number of possible configurations for an electrode is exponential in the number of electrode contacts, so that more complex electrode designs make manual programming almost impossible, as the number of possible parameter combinations increases by many orders of magnitude [And18]. Therefore, there is a need for sophisticated strategies to precisely and effectively adjust stimulation parameters and electrode configurations once the electrodes are implanted. Some academic and commercial software solutions use concepts to model the spatial dimension of stimulation for a given set of stimulation parameters. They allow visualization of the anatomical context along with the predicted volume of tissue activated (VTA) and the functional mapping of thresholds for clinical efficacy and side effects. However, such software solutions require the knowledge of the precise electrode location in relation to the anatomical brain structures beforehand.

Conventional electrodes have four or eight cylindrical contacts and variable distances that extend over a vertical distance of 7.5 to 15.5 mm from the electrode tip (see Figure 2.1a–2.1c). The cylindrical contacts always generate a radial current flow in the horizontal plane of the electrode, and accurate positioning of the electrode in the x and y directions is critical to avoid adverse effects from current propagation outside the target area. Since the anatomical shape of most target areas — such as the STN, the Vim, and the GPi — is not spherical or uniform, there are practical limitations on how to achieve complete coverage of the intended target area by a single electrode with cylindrical contacts [Hor17a; Neu17]. In recent years, several new electrode designs have been proposed that allow for the shaping of the electric field perpendicular to the electrode. Industry experts and clinicians hoped that directional DBS would reduce the risk of stimulation-induced adverse effects and optimize the clinical benefit of DBS by allowing better-customized stimulation to individual patients and to better compensate for suboptimal DBS electrode placements. Prototypes ranged from electrodes with up to 40 small circular contacts of 0.66 mm, evenly distributed over the last 7.5 mm of the electrode (see Figure 2.1f), to simpler models that divided the conventional ring contacts into three segments extending over 90° or approximately 120° (see Figure 2.1d–2.1e) [Ste19]. In 2015, the Vercise Cartesia™ directional electrode from Boston Scientific Corporation received the Conformite Europeenne mark of approval for marketing in Europe. Clinical studies

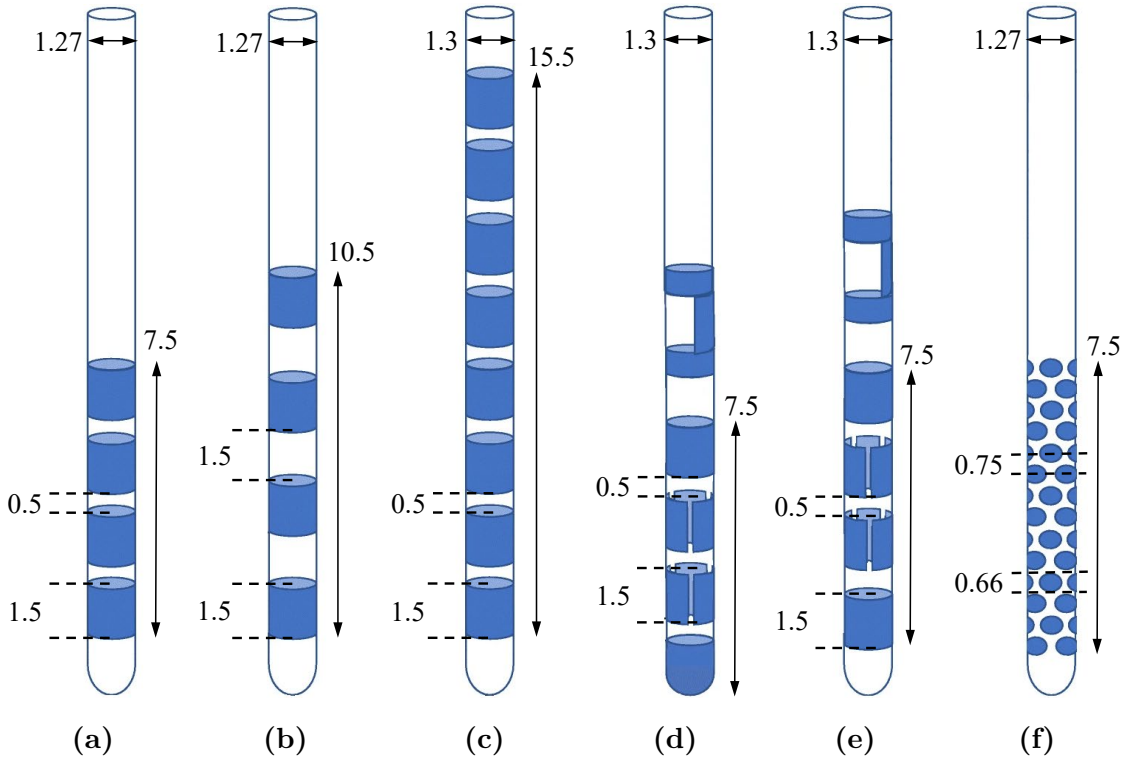

Figure 2.1: Overview of various electrode designs (all units in mm): (a)–(c) features the design of the most common DBS electrodes with four or eight cylindrical contacts and variable interspacings; (d)–(e) features the design of two currently available directional DBS electrodes with eight contacts; two middle electrode levels are segmented into three contacts each spanning 90° of the circumference, and both have a marker on top that allows the orientation of the electrode to be detected by imaging; and (f) features a 40-contact electrode design used only in studies. Adapted from [Ste19].

with these implanted types of electrodes emphasized the innovative technology [Ste16; Dem17; Reb18]. However, with the increasing number of electrode contacts and the more complex geometry of the electrodes, the already tedious programming process becomes a significant and costly challenge for the clinician to test through any combination of monopolar stimulation settings. For segmented DBS electrodes, especially those with higher-density contact arrays, the selection of stimulation parameters, therefore, requires new and automatic approaches. For these types of electrodes, both the position of the electrode and its rotational orientation with respect to the anatomical brain structures are of interest to tailor the current distribution and stimulation volume to the intended target volume.

2.2 State of the Art in Electrode Localization

Postoperative localization of DBS electrodes is essential to verify the implanted electrode position and to avoid the need for additional corrective surgery, to evaluate the therapeutic

and adverse effects of DBS, to provide valuable knowledge for understanding the DBS mechanism, to facilitate stimulation programming without the expense of a manual trial-and-error procedure, and to find the optimal stimulation setting for a patient-specific DBS treatment.

To date, no generally accepted protocol for electrode localization has been established. Current approaches are based on fusion of preoperative and postoperative neuroimaging data, most commonly fusion of preoperative MRI with postoperative CT [Shi07; Gor09; Lee10a; Pae11]. Preoperative MR imaging of the brain is generally performed in clinics to select patients who are candidates for DBS intervention. Postoperative MR imaging is generally avoided, and postoperative CT is preferred. This is due to the fact that, in MR imaging of patients with implanted DBS systems, there is a risk of electrode heating as a result of the electrical current induced by radio-frequency electromagnetic waves [Rez04; Rez05; Bou20]. A few cases of accidents related to MR imaging in patients with implanted neurostimulation systems have been published [Spi03; Hen05; Zri11]. Other safety issues associated with the performance of an MRI examination include magnetic field interactions with the DBS device, which may result in migration of the device; tissue damage due to induction of electrical currents; and functional disruption with the operating aspects of the device [Gup11; Bou20]. However, CT provides less tissue contrast needed to identify deep brain structures and, therefore, needs to be coregistered with the preoperative MRI that depicts a more detailed visualization of the target structures. This approach is considered to be acceptable for identifying the anatomical position of DBS electrodes [Shi10; Tha11; Bar15; Gee16; Xia17], with average localization errors ranging from 0.17 mm up to approximately 2 mm. The accuracies in localization are dependent mainly on the quality of the registration of two imaging modalities, so poor registration would contribute to a significant error in determining the final electrode position. It is reported that, on average, 1.2 mm difference in the coordinates of the deepest electrode contact was observed when calculated on four different commercially available coregistration devices [Eng18]. Other studies have presented comparable results [Sch09; Lee10b; Bur21]. Therefore, the determination of the electrode position remains a matter of assumption in a range of 1–2 mm.

The accuracy of both MRI and CT in localizing electrodes remains controversial [Sal16; Van21], and the use of registration software as well as the choice of various scanning modalities affect the observed location of the DBS electrode. The area around the electrodes is always corrupted in postoperative images because the platinum-iridium alloy used in the electrodes causes artifacts. Figure 2.2 depicts the result of MRI and CT fusion at four levels: at the level of the STN (Figure 2.2a), 3.5 mm above the STN (Figure 2.2b), 13.5 mm above the STN (Figure 2.2c), and 23.5 mm above the STN (Figure 2.2d). The irregular contour of the electrode artifacts from proximal to distal leads to the shape of the artifact on the images being different at each level (marked red spheres). Since the artifacts produced on MR and CT images are usually larger than the actual electrodes, it is not a simple

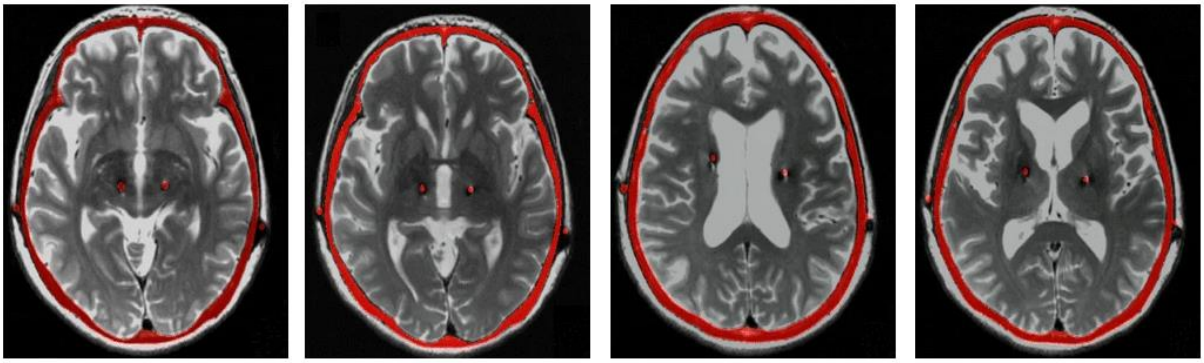

(a) **(b)** **(c)** **(d)**

Figure 2.2: Visualization of electrodes in the fused image of CT and MRI of the brain at four different slice levels in axial view, with (a) the lowest level at the height of the STN, (b) the level 3.5 mm above the STN, (c) the level 13.5 mm above the STN, and (d) the highest level 23.5 mm above the STN. The electrode artifacts from CT are seen as irregular round shapes and are marked as red spheres in the images. Adapted from [Lee10a].

matter to determine the appropriate electrode placement. For example, the diameter of a Medtronic electrode is 1.27 mm, but the size of the electrode artifacts typically measures 3.6 mm on MRI and 3.3 mm on CT [Hem09]. Several academic software solutions have been presented to facilitate the localization of DBS electrodes: DBSmapping [DaS15], PyDBS [DAl15], DBSproc [Lau16], and Lead-DBS [Hor15]. The MATLAB-based Lead-DBS is the most established toolbox for electrode localizations [Hus18]. While these toolboxes provide automatic localization, they require manual refinement steps afterwards. Thus, the final position of the electrode is determined by the user's experience. It is also worth noting that poor imaging complicates electrode reconstruction even for the experienced user.

Furthermore, it should be noted that the position of the electrodes is not a static phenomenon, as it may change over time due to brain shifts, electrode torsion, and electrode migration [Kim10; Van10; Mor17; Gor21]. Any trauma, surgical intervention, and the natural course of neurodegenerative diseases may further alter the position of the electrode in the brain. Therefore, this could explain the possible diminishing effect of DBS with long-term use. To determine the position of the electrode, a single scan immediately after surgery may be insufficient, and time-delayed postoperative scans may also be required. Although a few clinical studies have demonstrated no clinically relevant change after the first postoperative day [Nie20], it is still of significant importance to determine whether and how much DBS electrodes move. Long-term clinical studies with repeated CT measurements are not possible because CT scans are associated with high radiation doses. Furthermore, the risks associated with MR imaging have led to strict regulations that limit this technology's clinical and scientific utility.

The method presented in this thesis is intended to provide an alternative for determining electrode position that overcomes the fundamental drawbacks of current postoperative imaging techniques. This method employs measurements of the magnetic field induced by DBS electrical pulses around the head to derive the location of the electrode through the use of appropriate localization approaches and reconstruction algorithms. The risks associated with MR imaging and the radiation associated with CT imaging are avoided, allowing this method to be performed as often as desired at continuous intervals without hesitation. This would allow the conduct of long-term clinical studies with repeated measurements and would open up further research opportunities. To date, the potential of magnetic field recordings for electrode localization has been investigated only within the framework of this dissertation. Industry representatives and clinicians have indicated tremendous interest in this radiation-free approach, which would make this method a postoperative modality of choice if it can achieve clinically reliable accuracies. The feasibility of DBS electrode localization based on a scalp electroencephalogram (EEG) has been investigated in a single study, but an average error of approximately 13 mm was reported [Iac19], making its application in clinical practice infeasible.

2.3 State of the Art in Electrode Orientation Detection

As stated earlier, directional electrodes have become the new standard in DBS. Their ability to deliver the stimulation field not only along the electrode axis but also perpendicular to the electrode may help to control side effects and to improve the therapeutic window [Ste16; Dem17; Reb18; Koe19; Kra21]. This window is defined as the gap between the minimum stimulation current required to produce adverse effects and the current required to produce a beneficial effect. However, it is not clear whether the long-term clinical outcome is also better with directional stimulation than with conventional omnidirectional stimulation. Furthermore, directional DBS electrodes significantly increase the number of possible combinations of programming stimulation parameters from which an optimal subset must be selected for patient-specific DBS treatment. This selection procedure can be guided by probabilistic sweet spots within the STN [Dem19a; Pet19a; Ngu19] or by individual neuroimaging [Pet20]. To use the full potential of directional stimulation technology, the precise location and orientation of the electrode in relation to the surrounding brain anatomy must be determined. The challenges of electrode localization with currently existing approaches have already been described in the previous section. Similarly, there are presently no established means to verify electrode orientation. Current methods for determining electrode orientation include stereotactic X-ray [Sit17], rotational X-ray [Egg21], standard CT [Hel18], flat-panel CT [Hun19], and rotational fluoroscopy [Rei17]. Techniques using X-rays and CT scans rely on high-quality imaging following particular

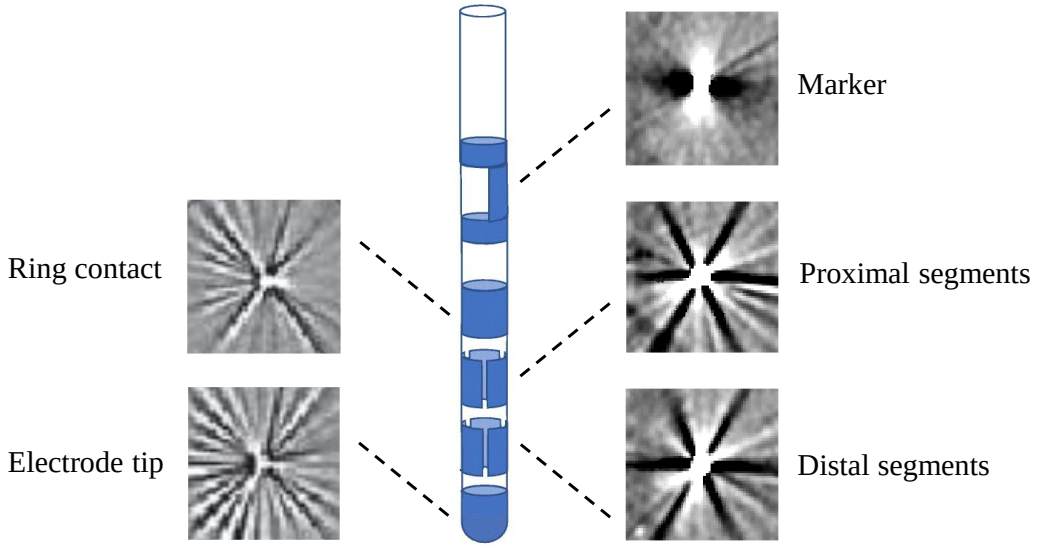

Figure 2.3: Illustration of the Boston Scientific Vercise Cartesia™ directional electrode and its characteristic artifact patterns at different levels in standard clinical CT resolution. The CT slice at the marker level exhibits strong 180° symmetry (two-streak artifact), the CT slice at the segmented electrode level presents a six-streak artifact pattern, and the CT slice at the ring contact and electrode tip level indicates an irregular pattern. Adapted from [Hel18] and [Kur20].

scanning recommendations, since specific artifact patterns generated by various elements of the directional electrode must be analyzed [Hel18]. Figure 2.3 illustrates the Boston Scientific Vercise Cartesia™ directional electrode and its characteristic artifact patterns at different levels of the electrode with standard clinical CT resolution. The CT slice at the marker level exhibits a two-streak artifact pattern, the CT slice at both middle levels of the segmented electrode exhibits a six-streak artifact pattern, and the CT slice at the level of the ring contact and the electrode tip exhibits an irregular pattern. However, on the one hand, orientation detection approaches rely on manual intervention by the user, and, on the other hand, the underlying artifact of the electrode at the marker level exhibits a strong 180° symmetry, which limits orientation detection to two possible solutions. Neither imaging method is currently capable of resolving this ambiguity without further measurements. Existing software tools, such as the academic DiODe algorithm integrated within the open-source toolbox Lead-DBS [Hel18] and the commercial Elements Lead Localization software package (Brainlab AG, Munich, Germany), rely on the intended orientation and assume that a deviation of more than ±90° is highly unlikely. When such a deviation occurs in clinical practice, it can lead to errors in the analysis of stimulation effects and to incorrect choices of stimulation parameters. Solutions to the ambiguity of artifact symmetry have been proposed recently, but additional X-ray imaging is needed to solve 100% of cases [Kur20; Dem21a].

The accuracy achieved in detecting electrode orientation depends on the imaging modality used and on the location of the electrode relative to the CT axis when the 180° am-

biguity is properly resolved. X-ray images provide only a rough estimate of electrode orientation as a function of the angle between the orientation marker of the electrode and the image plane. With rotational fluoroscopy, the rotation of the electrode could be determined with an average accuracy of less than 3° when the electrode is oriented parallel to the CT scanner axis [Rei17]. However, this setting is not realistic in clinical practice. With physiologically plausible orientations of the electrodes relative to the scanner axis, the mean accuracy is described as less than 10°. Results using postoperative CT imaging indicated that the orientation of segmented electrodes in directional DBS electrodes could be reliably determined with very high accuracy and precision. The mean detection accuracy was less than 2° [Hel18]. These results were stable at angles between the position of the electrode relative to the CT axis of up to 60°, which is a significant improvement over previously published methods and represents a clinically relevant situation. Except for the approach using standard postoperative CT imaging, remaining methods have the disadvantages of exposing the patient to additional radiation as well as additional costs and time.

Furthermore, it has been demonstrated that precise placement of a directional electrode in the desired direction by the neurosurgeon is difficult due to electrode torsion [Dem19b; Rau21], which leads to changes in the orientation of the electrode within the first few days after implantation [Kim10]. Additionally, electrode migration, brain shifts, any trauma or surgical intervention, and the natural course of neurodegenerative diseases may further change the position and orientation of the electrode in the brain [Mor17; Gor21]. Although some studies have indicated that directional electrode orientation is stable and does not exhibit clinically relevant changes on the first postoperative day or over longer periods [Lan21; Dem21b], it is currently unclear and of significant importance when electrode rotations occur and when the final position is reached. Since all existing methods expose patients to ionizing radiation, they hinder further research in this direction and hamper the conduct of long-term clinical trials to resolve such open questions.

Against this background, similar to electrode localization, the method developed within the framework of this dissertation aims to provide an alternative for determining electrode orientation that overcomes the fundamental drawbacks of current orientation detection techniques. In this approach, only the magnetic field induced by the stimulation is measured with magnetic field sensors outside the head, so that patients are not exposed to any radiation. To date, the potential of magnetic field recordings to determine electrode orientation has been investigated only in this thesis. The feasibility of EEG recordings for such questions has not been investigated thus far. Industry representatives and clinicians have a vested interest in treating the patient with a radiation-free approach, which would make the presented method a postoperative modality of choice if it demonstrates clinically reliable accuracies.

2.4 Magnetic Field Measurements

A magnetic field is generated whenever current flows through a conductor, a fact discovered by Hans Christian Orsted (1777–1851) in 1820. The first mathematical formula to describe the relationship between electric current and magnetism was based on experiments conducted in 1820 by French scientists Jean-Baptiste Biot (1774–1862) and Felix Savart (1791–1841) and is known as the Biot-Savart law [Tum11, p. 5]. Both the natural and technical environments of humans generate magnetic fields of many different types and orders of magnitude. The Earth's magnetic field results in magnetic flux densities between 25 and 60 µT, depending on the location. Particularly high values between 1 µT and 1 T can be found in the environment of large electrical engineering facilities such as power plants, transformers, high-voltage transmission lines, and electrically powered machines [Gra95]. Biomagnetic signals generated by human organisms are extremely weak compared to the Earth's magnetic field or to disturbances caused by urban noise. These weak biomagnetic fields are in the order of picotesla and femtotesla in a frequency range from a fraction of one hertz to several kilohertz. The strongest fields are generated by the human heart. The amplitude of the QRS peak in the magnetocardiography is typically a few tenths of picotesla. Biomagnetic signals from the brain are much weaker. Typical evoked fields such as somatosensory, auditory, or visually evoked responses are only several tens or hundreds of femtotesla [Now06, p. 103]. The magnetic field generated by stimulating electrical pulses of DBS is, in fact, not a signal generated by a human organism, but it can be considered to be an artificially generated biomagnetic signal with amplitudes depending on the stimulation setting. The magnetic properties of electrical pulses delivered by DBS systems are investigated within the framework of this dissertation and are presented in the next chapter.

Since very weak biomagnetic signals must be measured in the presence of ambient magnetic noise, highly sensitive sensors as well as a magnetically shielded chamber are needed to reduce the environmental noise below the signal to be measured. In 1968, David Cohen used a copper coil detector to record the first MEG at the University of Illinois [Coh68]. Later, at the Massachusetts Institute of Technology, he built a magnetically shielded chamber to reduce the environmental noise. The chamber had an inner diameter of approximately 2.5 m and consisted of five layers of shielding, three high-µ layers and two aluminum layers. Around the same time, James Zimmerman and colleagues developed the superconducting quantum interference device (SQUID) magnetometer, which uses the Josephson junction to measure weak magnetic fields [Zim70]. It must be cooled to a temperature of four Kelvin with liquid helium and has a sensitivity several hundred times higher than that of a copper coil. Zimmerman brought this detector into Cohen's shielded chamber, and this combination of shielding and detector made possible the first clear measurements of biomagnetic fields. After measuring the heart, Cohen next recorded the brain with a SQUID [Coh72]. For the initial investigations of biomagnetic fields during

the 1970s, numerous laboratories used a single or just a few SQUID magnetometers. To localize the activity in the brain with such a small number of sensors required moving the sensors to take samples at various locations around the head. This was time-consuming and not practicable for routine clinical use. The rapid development of the technology in the 1980s led to multi-channel devices with four channels in 1983, seven channels in 1986, and 24 channels in 1989. Today, modern MEG systems use hundreds of channels to provide whole-head coverage. However, there are two main drawbacks to current SQUID-based MEG systems: fixed sensor positions and high maintenance costs. The investments for the hardware and software as well as the operating costs are currently so high that this technology is available only to research institutions or university hospitals. In recent years, there have been significant advances in the development of new magnetic field sensors that have the potential to overcome these limitations. It has been demonstrated that optically pumped magnetometers (OPMs) have a sensitivity close to that of commercial SQUIDs. Commercially available OPM sensors — for example, the second-generation QuSpin zero-field magnetometer from QuSpin Inc. (Colorado, USA) — have a sensitivity of approximately $10\,\mathrm{fT}/\sqrt{\mathrm{Hz}}$ and operate between 0.1 and 100 Hz. To measure normal oscillatory brain activity, which is commonly categorized into five frequency bands — delta: 0.2–3 Hz, theta: 4–7 Hz, alpha: 8–13 Hz, beta: 14–31 Hz, and gamma: 32–100 Hz — the operating frequency bandwidth of OPMs is perfectly adequate, although it is not wide enough for DBS application. Typically, the frequency of stimulation is often at 130–185 Hz to be clinically effective [Mor02; Ste07; Bro17]. Since the frequency setting is the repetition rate of a single square-wave DBS pulse in one second, signal components are also included in the harmonic frequencies of 130–185 Hz. Within the framework of this dissertation, magnetic field measurements were performed with a fluxgate magnetometer at the Faculty of Engineering of Kiel University and with a clinically used SQUID-based MEG system at the UKD.

Magnetic fields that are measured around the head across many sensors create a magnetic field distribution at the sensor surface level. Such distributions contain important information about active sources within the brain. Physical models are used to represent these field distributions by using current sources in the brain (source model) and the geometrical property of the head (head model). The simplest source model that is used often is the equivalent current dipole model, which describes the activation of a large number of neurons within a small region in the brain and is represented as a point source [Ham93; Bai01; Cov07]. However, an identification problem may arise if too many small regions and their dipoles are required to represent a single large region with coherent activation. These sources need to be represented by more complicated models, such as with multipolar or even distributed models. Head modeling, which is also known as head volume conductor modeling, describes the geometrical, electrical, and magnetic properties of the tissue in the head. The combination of source and head volume conductor models describes the forward model and specifies the current distribution within the brain with

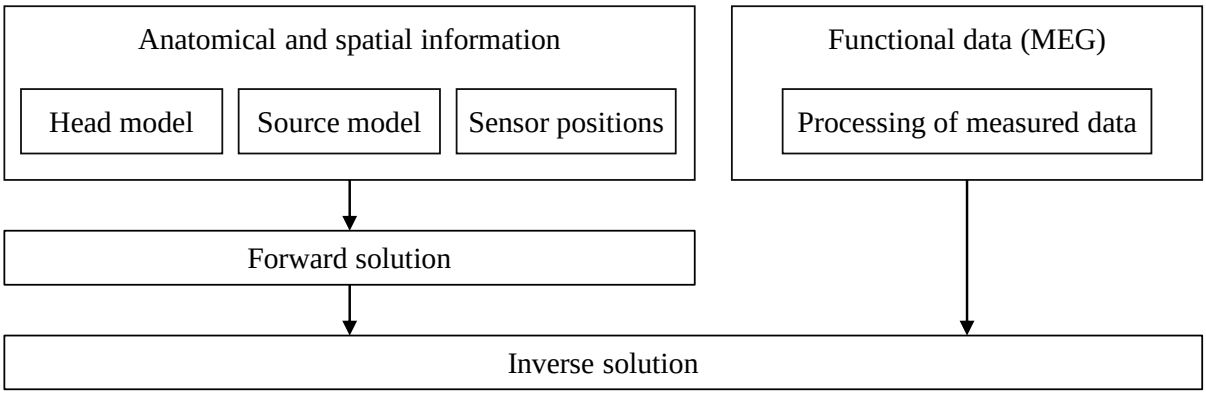

Figure 2.4: Schematic overview of the major steps in source localization. This indicates that the calculation of the inverse solution is based on the outputs of two independent steps: the forward solution — which can be calculated if the head model, source model, and sensor positions are given — and the processing of measured data.

a set of source parameters. In other words, the forward solution provides a model that maps the source parameters to the resulting magnetic fields at the sensor surface level (see Figure 2.4). Depending on the geometry assumed for the volume conductor model, the approaches that lead to a solution for the forward problem are either numerical or analytical [Mos99]. Analytical solutions exist for simplified geometries, such as when the head consists of a single-layer spherical shell with uniform conductivity or a series of nested concentric spheres, each corresponding to one layer. Usually, no more than four layers are assumed, corresponding to the brain, cerebrospinal fluid, skull, and scalp. Assuming that each spherical layer has uniform and isotropic conductivity, there are fast computable analytical solutions to the MEG forward problem. In reality, the head is anisotropic and inhomogeneous, and it has an arbitrary nonspherical shape. For realistic head geometries, numerical approaches such as the boundary element method, finite element method, and finite difference method are used to closely approximate the entire brain. Within the framework of this dissertation, analytically simple modeling approaches were used to approximate the electromagnetic behavior of DBS within phantoms, and numerical finite element method approaches were used for a more precise solution of the forward problem. In conjunction with the actual MEG data measured at specific sensor positions around the head and processed afterwards, the inverse problem can be solved (see Figure 2.4). The goal of inverse modeling is to estimate unknown sources, defined by their position in the brain, that generate the measured data. The accuracy with which a source can be localized is affected by a number of factors, including a head modeling error, a source modeling error, a sensor positioning error, and instrumental or biological noise in the measured data [Whi03]. The standard adopted by [Bai97] states that spatial accuracy should be at least better than 5 mm, although a much higher requirement is necessary for the application studied in this dissertation. There are several inverse modeling algorithms that fall under parametric, nonparametric, and spatial filtering approaches to reconstruct

the location and spectral content of a source in the brain [Bai01; Gre08]. Each approach uses different mathematical, anatomical, or functional constraints. The most traditional approach to inverse modeling in MEG is the parametric dipole model. This method assumes that the data are generated by a small number of current dipoles whose optimal parameters for position, orientation, and amplitude are found using the least-square fitting method so that the difference between the modeled and the measured topography is minimized [Sch86; Ham93; Yam00; Jun05]. In a more advanced class of dipole-based methods, sources are found by using a dipole source to sequentially scan all possible source locations throughout the entire brain volume [Mos92; Zha13]. By determining the goodness-of-fit at each location, information about the location of the source can be derived. These dipole scanning methods have attracted increasing attention, and this method was used to solve the inverse problem within the framework of this dissertation to determine the electrode position and orientation.

The physics of how magnetic fields are generated by the current sources is described by using the quasi-static approximation of Maxwell's equations [Ham93]. The quasi-static condition, which implies that all the currents and fields behave as if they were stationary, is mainly used to describe the volume conductor of the human brain, since the usable frequency spectrum in MEG is typically below a few thousand Hertz [Bai01; Hal07; Gra17]. The electric and magnetic phenomena produced by DBS can be in general described by a unique system of field equations knows as Maxwell's equations [Che89, p. 323]:

$$\text{Gauss' law for electricity:} \qquad \nabla \cdot \vec{D} = \rho \tag{2.1}$$

$$\text{Gauss' law for magnetism:} \qquad \nabla \cdot \vec{B} = 0 \tag{2.2}$$

$$\text{Faraday's law:} \qquad \nabla \times \vec{E} = -\frac{\partial}{\partial t}\vec{B} \tag{2.3}$$

$$\text{Ampere-Maxwell law:} \qquad \nabla \times \vec{H} = \vec{J} + \frac{\partial}{\partial t}\vec{D} \tag{2.4}$$

D is the electric flux density, ρ the electric free charge density, B the magnetic flux density, E the electric field, H the magnetic field, J the electric current density, and ∇ a symbol for the first-order differential operator with respect to the spatial coordinates. The Maxwell's equations describe a variety of electromagnetic phenomena that occur over a wide range of spatial and temporal scales and are difficult to analyze in a general form. In this thesis, the magnetic field B is of particular interest since it is the quantity that will be measured. In general, it is coupled to the electric field E through their time derivatives (see Equations. (2.3) and (2.4)). These equations can be simplified with two approximations if slow electromagnetic fields in the low frequency range (less than a few thousand Hz) are analyzed [Bai01; Hal07; Gra17], as in the case of deep brain stimulation. According to [DiB04], the condition for such approximations can be used when the multiplication

of the size of the physical system and the frequency is much smaller than the speed of light, which is also true for DBS. Firstly, the magnetic induction $\frac{\partial}{\partial t}\vec{B}$ has a negligible effect on the electric field [Plo67; Ros69]. Neglecting the magnetic induction in Faraday's law (see Equation (2.3)) constitutes the electro-quasi-static approximation. Secondly, the macroscopic velocity v of the ions in the brain and the magnetic field of physiological origin are so low that the magnetic component of the Lorentz force $F = q(E + v \times B)$ is negligible [Gra17]. So, the effect of the magnetic field on the motion of free charges is negligible in comparison to the effect of the electric field. The negligence of the magnetic induction and the magnetic component of the Lorentz force leads to a decoupling of the electric and magnetic fields. Since the current density is now independent of the magnetic field, and taking into account the divergence of Equation (2.4), leads to a current continuity statement [Che89, 208 ff.]:

$$\nabla \cdot \vec{J} = 0, \tag{2.5}$$

where J is solenoidal or divergenceless, in other words, the current flows along closed loops. The Maxwell's equations are reduced to the following equations:

$$\text{Gauss' law for electricity:} \quad \nabla \cdot \vec{D} = \rho \tag{2.6}$$

$$\text{Gauss' law for magnetism:} \quad \nabla \cdot \vec{B} = 0 \tag{2.7}$$

$$\text{Faraday's law:} \quad \nabla \times \vec{E} = 0 \tag{2.8}$$

$$\text{Ampere-Maxwell law:} \quad \nabla \times \vec{H} = \vec{J} \tag{2.9}$$

The model with these equations describes a static model, a simplification in which all variations in time are neglected. However, the fields are still functions of time, but given the sources at a certain instant, the fields at that same instant are determined without regard for what the sources of fields were an instant earlier. The four equations of Maxwell together with the equation of continuity and Lorentz force equation form the foundation of electromagnetic theory. The first two, Gauss' law for electricity and Gauss' law for magnetism, describe how the fields vary in space due to the sources and the last two, Faraday's law and Ampere-Maxwell law, describe how induced fields circulate around their respective sources. The magnetic fields circulate around the electric fields while the electric fields circulate around the magnetic fields. The quasi-static approximation changes the last two equations due to the fact that the curl of an electrostatic field is zero, that is, the electric field associated with a set of stationary sources has a curl of zero. In this situation, there is no time-varying magnetic field. For the electric current density J applies:

$$J = J_p(r) + J_v(r) \tag{2.10}$$

$$= J_p(r) + \sigma(r)E(r), \tag{2.11}$$

with the position vector r and the electrical conductivity σ. In the following, the brain is assumed to be isotropic. For this reason, the conductivity becomes a scalar value. The total current density J within the brain consists of two current flows, a primary current J_p related to the original neural activity and the secondary or volume current J_v, that results from the effect of the electric field in the volume by the extracellular charge carriers. Since the electric field has no rotation, as indicated by the quasi-static Maxwell's equations, it can be written as a negative gradient of the electric potential ϕ:

$$E = -\nabla \cdot \phi. \tag{2.12}$$

Thus, the total current density can be rewritten in Equation (2.11), so that it no longer depends on the electric field but on the potential:

$$J = J_p(r) - \sigma(r)\nabla\phi. \tag{2.13}$$

If the divergence is used from the fourth Maxwell's equation (Equation (2.9)), the left side of the expression disappears, since the divergence of a rotation always results in zero. It follows:

$$\nabla J = 0. \tag{2.14}$$

If the divergence is formed from Equation (2.13) and is inserted into Equation (2.14), the result is:

$$\nabla \cdot J_p(r) = \nabla \cdot (\sigma(r)\nabla\phi). \tag{2.15}$$

If the Nabla operator is applied to Equation (2.9) as a cross product, the Poisson equation follows:

$$\Delta B = -\mu_0 \nabla \times J. \tag{2.16}$$

This can be justified as follows: For any vector field v the vector identity is valid with

$$\nabla \times (\nabla \times v) = \nabla(\nabla v) - \Delta v, \tag{2.17}$$

with the Laplace operator $\Delta = \nabla^2$. Since according to the second Maxwell's equation (Equation (2.7)) the divergence of the magnetic flux is zero, the first expression on the right side disappears in Equation (2.17), and Equation (2.16) is obtained. For this Poisson equation, the solution is an integral over the volume V of the head:

$$B(r) = \frac{\mu_0}{4\pi} \int_V \frac{\nabla' \times J(r')}{R} dv' \tag{2.18}$$

$$= \frac{\mu_0}{4\pi} \int_V \frac{\nabla' \times (J_P(r') - \sigma(r')\nabla\phi(r'))}{R} dv'. \tag{2.19}$$

Both in this expression and in the following, $R = r - r'$ and $R = |r - r'|$ were used. To get this result, there has to be demanded, that the potential for r towards infinity disappears.

The expression for the magnetic field can be described as

$$B(r) = B_P(r) + B_v(r), \tag{2.20}$$

with the summands

$$B_P(r) = \frac{\mu_0}{4\pi} \int_V \frac{\nabla' \times J_P(r')}{R} dv' \quad \text{and} \tag{2.21}$$

$$B_v(r) = -\frac{\mu_0}{4\pi} \int_V \frac{\nabla' \times (\sigma(r')\nabla'\phi(r'))}{R} dv'. \tag{2.22}$$

With the vector identity

$$\psi\nabla \times v = v \times \nabla\psi + \nabla \times (\psi v) \tag{2.23}$$

for a scalar field ψ and a vector field v, the second summand $B_v(r)$ becomes

$$B_v(r) = \frac{\mu_0}{4\pi} \left(\int_V J_v(r') \times \nabla' \frac{1}{R} dv' + \int_V \nabla' \times \frac{J_v(r')}{R} dv' \right). \tag{2.24}$$

The second integral in this equation can be expressed with Stokes' theorem $\int_V \nabla \times F dv = \oint_{\partial V} F dr$ as integral over a surface $\oint_{\partial V} J_v(r')/R \cdot n \; dS$. Due to the boundary condition

$$n(r) \cdot (\sigma \nabla \phi(r)) = -n(r) \cdot J_v(r) = 0 \tag{2.25}$$

with $r \in \partial V$, this surface integral is zero where n is the normal vector on the head surface ∂V. This condition expresses that no charge flows out of the head, since the head can be considered isolated and the electric field is tangential to the surface. It finally results in

$$B(r) = B_P(r) - \frac{\mu_0}{4\pi} \int_V \sigma(r')\nabla'\phi(r') \times \nabla' \frac{1}{R} dv' \tag{2.26}$$

as an expression for the magnetic flux density. This is valid for every conductor model. Further, it can be demonstrated that this equation can be simplified for fields in an unbounded homogeneous medium [Sar87]:

$$B(r) = \frac{\mu_0}{4\pi} \left(\frac{(r - r') \times u(r) \cdot Q}{|r - r'|^3} \right) = l(r) \cdot Q, \tag{2.27}$$

where $u(r)$ is the unit orientation and $l(r)$ is the gain vector that relates the intensity of the current flow Q, also called the dipole moment, to the measurement at position r. This equation can be further simplified for different conditions. For the model of a single dipole, denoting the dipole position as L, and observing the ith measurement at sensor

location $R(i)$, the Biot-Savart law can be written as

$$\vec{B}(i) = \frac{\mu_0}{4\pi} \frac{\vec{Q} \times (\vec{R}(i) - \vec{L})}{|\vec{R}(i) - \vec{L}|^3}, \tag{2.28}$$

where $\vec{Q}$ is the dipole moment, $\vec{L}$ is the dipole location, $\vec{R}(i)$ is the ith measurement sensor location, and $\vec{B}(i)$ is the magnetic field at $\vec{R}(i)$. Normally, a magnetic sensor measures only one component of the three-dimensional magnetic field. Thus, only a scalar measurement is made:

$$B(i) = \vec{B}(i) \cdot \hat{s}(i), \tag{2.29}$$

where $\hat{s}(i)$ describes the unit orientation of the ith sensor. Combining the previous two equations leads to

$$B(i) = \frac{\mu_0}{4\pi} \frac{(\vec{R}(i) - \vec{L}) \times \hat{s}(i) \cdot \vec{Q}}{|\vec{R}(i) - \vec{L}|^3} = \vec{g}(i) \cdot \vec{Q}. \tag{2.30}$$

$\vec{g}(i)$ is the gain vector that relates the intensity of the current flow (dipole moment $\vec{Q}$) to the measurement at position $\vec{R}(i)$. This equation can be extended for multiple sensors as follows [Mos92]:

$$\begin{bmatrix} B(1) \\ B(2) \\ \vdots \\ B(m) \end{bmatrix} = \begin{bmatrix} \vec{g}(1) \\ \vec{g}(2) \\ \vdots \\ \vec{g}(m) \end{bmatrix} [\vec{Q}] \Longrightarrow B = GQ, \tag{2.31}$$

where m is the number of sensors and G is the gain matrix or the so-called lead-field matrix that indicates the linear relationship between the dipole moment Q and the magnetic field measurements B.

Chapter 3

Publications

After the brief overview of the fundamentals presented in the previous chapter, this chapter represents the experimental and discussion part of this dissertation. The following six sections of this chapter contain six journal publications that are arranged chronologically by date of publication. Each of the six publications is followed by a brief listing of the key findings and scientific implications of the respective publication for the readers' convenience. An overview of the publications included in this dissertation has already been provided in Figure 1.2 in the introductory chapter.

The first publication examines the magnetic properties of electrical stimulating pulses delivered by DBS systems under both monopolar electrode configurations (with the negative electrode contact in the brain and the positive contact in the neurostimulator case) and bipolar electrode configurations (with the negative and positive electrode contacts in much closer proximity in the brain). Additionally, the feasibility of DBS electrode localization using magnetic field measurements around the head is being investigated. Observations were made with the measurement scanner system constructed in-house in the magnetically shielded chamber at the Faculty of Engineering of Kiel University on a simplified cylindrical head phantom with an integrated conventional four-contact electrode and a voltage-controlled neurostimulator. A single fluxgate magnetometer was used for this purpose.

The second publication addresses mainly the detection of electrode position using magnetic field measurements and investigates the localization accuracy for various electrode positions with increasing depth in the phantom. As in the first publication, the investigations were performed by magnetic field measurements on the cylindrical head phantom with the measurement scanner system constructed in-house inside the magnetically shielded chamber.

In the third publication, the accuracy in detecting the position and the rotational orientation of a directional DBS electrode is investigated using a clinically available SQUID-based MEG device. The investigations were performed at the UKD on the cylindrical head

phantom, with the DBS elements in the phantom used in the previous two publications replaced by a directional electrode and a current-controlled neurostimulator.

The fourth publication presents the minimum requirements that magnetic field sensors must meet to be used for electrode localization and for electrode orientation detection by measuring the magnetic field generated by clinically used DBS settings. The main focus is on the minimum required limit of detection (LOD) and the operating bandwidth that the sensor must have. The investigations are based on measurements performed with the MEG device at the UKD on the cylindrical head phantom with integrated directional DBS system.

The fifth paper is concerned mainly with the detection of electrode orientation by means of magnetic field measurements; it investigates the effects of various types of bipolar directional electrode configurations on the accuracy of orientation detection. As in the previous two publications, the investigations were performed on the cylindrical head phantom with an integrated directional DBS system using the MEG device at the UKD.

In the last publication, a clinically applicable, patient-friendly, and radiation-free method is presented for the magnetic detection of the position and orientation of directional DBS electrodes based on a sequence of MEG measurements under various bipolar electrode configurations. This method has been named MaDoPO (magnetic detection of positions and orientation of directional electrodes). The investigations were performed with MEG measurements at the UKD on a realistic head-torso phantom in which a directional electrode and a current-controlled neurostimulator were placed at appropriate locations.

3.1 The Magnetic Properties of Electrical Pulses Delivered by Deep Brain Stimulation Systems

M. Yalaz, A. Teplyuk, M. Muthuraman, G. Deuschl, and M. Höft, "The Magnetic Properties of Electrical Pulses Delivered by Deep-Brain Stimulation Systems," in *IEEE Transactions on Instrumentation and Measurement*, vol. 69, no. 7, pp. 4303-4313, July 2020, doi: 10.1109/TIM.2019.2945744.

Information about the amount of own contribution to this publication:

Conceptualization	Planning	Implementation	Manuscript preparation
high	high	high	high

© 2020 IEEE. Reprinted, with permission, from M. Yalaz et al., "The Magnetic Properties of Electrical Pulses Delivered by Deep-Brain Stimulation Systems," in *IEEE Transactions on Instrumentation and Measurement*, July 2020. The version of record is available online at https://doi.org/10.1109/TIM.2019.2945744.

In reference to IEEE copyrighted material which is used with permission in this thesis, the IEEE does not endorse any of Kiel University's products or services. Internal or personal use of this material is permitted. If interested in reprinting/republishing IEEE copyrighted material for advertising or promotional purposes or for creating new collective works for resale or redistribution, please go to http://www.ieee.org/publications_standards/publications/rights/rights_link.html to learn how to obtain a License from RightsLink.

IEEE TRANSACTIONS ON INSTRUMENTATION AND MEASUREMENT, ACCEPTED VERSION OF THE ARTICLE PUBLISHED IN THIS JOURNAL.

The Magnetic Properties of Electrical Pulses Delivered by Deep-Brain Stimulation Systems

Mevlüt Yalaz, Alexander Teplyuk, Muthuraman Muthuraman, Günther Deuschl, and Michael Höft, *Senior Member, IEEE*

***Abstract*—The aim of this study is to analyze the magnetic field properties for both monopolar and bipolar electrode configurations of deep brain stimulation electrodes using three dimensional magnetic field measurements and to investigate if the magnetic measurements enable a localization of the electrode as a proof-of-concept. Therefore, a simplified head phantom with an integrated deep brain stimulation electrode was created to measure the magnetic flux densities in all three dimensions with a fluxgate magnetometer over a sensor trajectory of measuring points inside the magnetically shielded chamber. The magnitude of the magnetic flux density for monopolar stimulation and bipolar stimulation are in the nT and pT range for the frequency 160 Hz, depending on the stimulation amplitude and on the distance between sensor and electrode. The field distributions show a linear decline of the magnetic field for the monopolar and a quadratic decline for the bipolar stimulation. We were able to reconstruct the magnetic field using multiple recording sites. As the magnetic field of deep brain stimulation can be measured and its field strength can be reconstructed, it is feasible to estimate the strength of the field within the limits of programmable stimulation parameters and distance between sensor and electrode. The presented results are intended as preliminary work for the further development of electrode localization methods using magnetic measurements. As an example of the feasibility of electrode localization, this paper presents a bipolar measurement that creates a more focused spatial field distribution and results in an accurate localization.**

***Index Terms*—Deep brain stimulation (DBS), fluxgate magnetometer, magnetic field measurement, monopolar bipolar stimulation, neurostimulator.**

I. Introduction

DEEP brain stimulation (DBS) is an established treatment of movement disorders such as Parkinson's disease (PD), dystonia or tremors [1]–[3]. The most common targets are the subthalamic nucleus (STN) for PD, the globus pallidus internus (GPi) for dystonia and the nucleus ventrointermedius internus (Vim) for tremors. During surgery, these targets are determined with stereotactic methods based on the magnetic resonance images (MRI) which are obtained with a stereotactic ring. The electrodes are connected to the neurostimulator that is surgically placed under the skin near the clavicle which delivers the DBS signal according to the patients' needs. The amplitude of the stimulation signal is commonly set between 1 and 4 V, the pulse width between 60 and 250 µs, the frequency between 130 and 185 Hz and the stimulation mode between monopolar and bipolar electrode configuration [4]. The stimulation elicits a corresponding spatial distribution of the stimulation field around the electrodes that causes the extent of the neural activation or the volume of tissue activated (VTA). The size of the VTA during DBS is adapted to improve the clinical benefit of DBS [5], [6], considering the trade-off between minimizing side effects and maximizing clinical improvement. To mathematically model the stimulated field, the exact position of the electrode in the brain must be determined [7], [8]. One neuroimaging approach opportunity is to localize the DBS electrodes via metal artifacts in computed tomography (CT) [9] or post-operative MRI images [10]–[12] or in combination of both [13]. The other way is to locate a single source which is responsible for a certain frequency from the signal by using non-invasive modalities like EEG or MEG. Parametric approaches like dipole-fit methods estimating the source that best explains the measured data can be used [14]. In order to have a satisfactory match of the mathematical model with the considered measurement, a mathematical model estimation must be made which ensures the magnetic field properties analyzed in this paper. To diminish the magnetic noise, a magnetically shielded chamber is required during data acquisition [15], [16].

In this paper, magnetic field measurements for monopolar and bipolar electrode configuration are performed to investigate its magnetic field properties. This may be of interest for different research areas. First, the magnetic properties of DBS are needed for the development of suitable magnetic sensors that operate at room temperature and outside the shielded chamber, e.g. magnetoelectric sensors [17]. Secondly, the distortion of the investigated magnetic field distribution can be used to test the safety of the system against electromagnetic fields generated by various electrical devices. A first experimental study has been published [18]. Furthermore, by knowing the distribution of the magnetic field strength at the scalp-level through the invasive DBS system, an estimation of how strong and in which direction the magnetic field might be stimulated in non-invasive brain stimulation technologies such as transcranial magnetic stimulation (TMS) [19], transcranial direct current stimulation (tDCS) [20], or magnetic field projector (MFP) [21] can be given.

M. Yalaz, A. Teplyuk, and M. Höft are with the Chair of Microwave Engineering, Christian-Albrechts-University, 24143 Kiel, Germany (e-mail: my@tf.uni-kiel.de; alt@tf.uni-kiel.de; mh@tf.uni-kiel.de).

M. Muthuraman is with the Department of Neurology, Johannes Gutenberg University, 55131 Mainz, Germany (e-mail: m.muthura@uni-mainz.de).

G. Deuschl is with the Department of Neurology, Christian-Albrechts-University, 24105 Kiel, Germany (e-mail: g.deuschl@neurologie.uni-kiel.de).

We are mainly interested in locating the DBS electrode with magnetic field measurements. This is intended to be an alternative to conventional magnetic resonance imaging techniques as described above that are affected by metal artifacts causing errors of up to 10.4 mm [22]. Significant discrepancies have also been reported between the electrode centers estimating by CT and MRI. On the other hand, microelectrode recording (MER) during surgery is used to confirm the target location by recording the discharge patterns of single neurons that identify the interested brain structures (i.e. STN, GPi, Vim). Retrospective analysis of the tracking error of the microelectrode was performed between the planned trajectory and the microelectrode tip, giving a total error of 1.2 mm [23]. Nevertheless, MER is time consuming and requires the patient to be awake. From a clinical perspective, identifying the exact target area within the brain is still not yet precisely defined. The exact determination of the target area therefore plays an important role in achieving optimal clinical results. Electrode localization has also been tried as a proof-of-concept with electroencephalography (EEG) recordings on the scalp [24], however, this paper deals with the magnetic side of DBS. Future perspectives include to identify the best contact of the electrode for reaching the anatomically defined stimulation target area in the brain.

II. Methods

A. Head Phantom

A simplified phantom head with the shape of a cylinder as shown in Fig. 1a with dimensions comparable to a human head, as depicted in Fig. 1b, was developed to model the measurement of the magnetic field, and was filled with an isotonic fluid (NaCl 0.9 %) to mimic the electric conductivity of a human brain. The cylinder body is made of acrylic glass, and therefore is neither electrically conductive nor magnetic. The electrode can be moved in the x and y direction by rotating the adjustment wheel (see Fig. 1a and Fig. 2), and in the z direction by pulling up and down the electrode holder and can thereby be placed at any fixed position. Thus, it is possible to measure the exact stereotactic position of the electrode which ensures the accuracy of this model.

B. Stimulation System

The used Medtronic 3387 DBS electrode, as depicted in Fig. 3, consists of a polyurethane outer jacket and has a diameter of 1.27 mm and four independent annular platinum-iridium contacts with 1.5 mm in length and 1.5 mm apart from each other. Two types of stimulation modes are applied which differ in electrical polarity. In case of bipolar stimulation, two contacts of the electrode are activated, one as the cathode (negative pole) and another one as the anode (positive pole), whereas in monopolar stimulation, one of the contacts is programmed as the cathode, while the neurostimulator is used as the anode [25], [26]. Since the stimulator could not be placed in the cylinder easily, a round non-magnetic titanium plate at the bottom of the cylinder is added that represents the neurostimulator as the anode in case of monopolar electrode configuration.

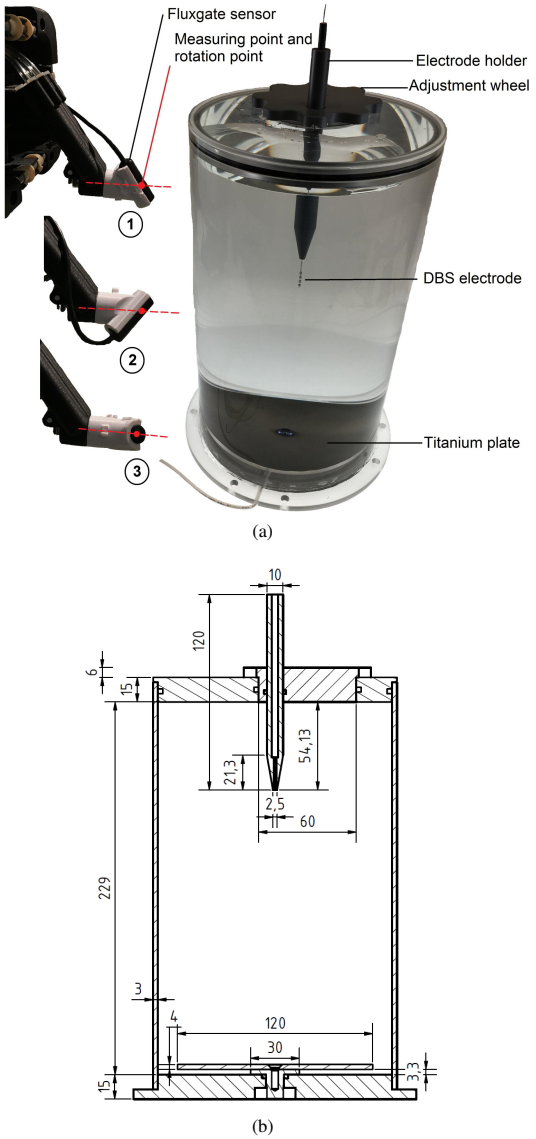

Fig. 1. The upper figure shows the cylindrical phantom head and the fluxgate sensor with its all three orthogonal measuring directions that are used for the measurements. The rotation point of the sensor is also the assumed measuring point. The lower one illustrates the dimensions of this phantom in mm.

C. Recording System

To measure the magneto-electrical properties, the whole recordings took place in a magnetically shielded measuring chamber (Series Ak3B, Vacuumschmelze GmbH). The head scanner inside the chamber was constructed in-house with non-ferromagnetic materials and operates pneumatically to avoid interfering electromagnetic fields due to electrically driven stepping motors. The entire electronic equipment to drive the scanner is located outside the chamber. With this head scanner, an optimized sensor trajectory of variable measuring points around the head phantom with the desired spatial resolution can be programmed.

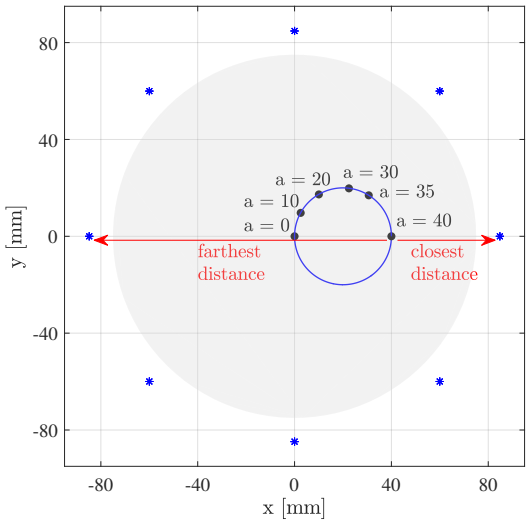

Fig. 2. The top view of the cylinder with the radius of 75 mm (gray circular area). The electrode can be rotated along the inner circle (blue). The distance to the origin defines the variable a, which can be set between $a = 0$ mm and $a = 40$ mm with the corresponding xy coordinates. The blue asterisk markers indicate the positions of the measuring points. The red arrows indicate the closest (45 mm) and farthest (125 mm) measuring point to the position $a = 40$ mm.

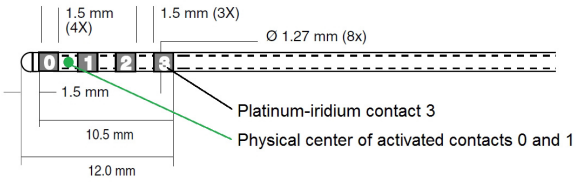

Fig. 3. The dimensions of the Medtronic Model 3387 DBS Electrode [27]. As an example, the physical center point of the bipolar electrode configuration with activated contacts 0 and 1 is marked as a green dot marker.

The attached unidirectional fluxgate magnetometer (Fluxmaster, Stefan Mayer Instruments) is oriented at each measuring point in all three orthogonal directions to get the complete magnetic information at this point by rotation of its sensitive axis, as shown in Fig. 1a. The rotational axis (red dashed line) is aligned to the diagonal axis of the three orthogonal sensing axes (i.e. along vector (1,1,1)'). At first, the first magnetic field component B_1 is measured in direction 1 (vector (1,0,0)'), then direction 2 (vector (0,1,0)') is obtained by +120° rotation of the sensor around the rotation axis by proper mechanical mean driven by air pressure and the second field component B_2 is measured. Finally, the same procedure is performed with direction 3 (vector (0,0,1)'), by further 120° rotation to measure the third field component B_3. This is necessary for calculating the magnitude of the magnetic flux density with $\sqrt{B_1^2 + B_2^2 + B_3^2}$. Since the sensor has a diameter of 10 mm and a length of 30 mm, it is fixed that the point exactly in the middle of the detection coil with a length of 20 mm placed in the front of the sensor represents the measuring point and is thus the rotating point of the sensor. The red point marker in Fig. 1a represents the measuring point that has a distance of 11 mm (half of the detection coil length 10 mm plus protective cover of 1 mm) to the front of the sensor. It has a noise level of typically 20 pT/$\sqrt{\text{Hz}}$ at 1 Hz and a bandwidth of 1 kHz from 0 to 1 kHz. The recorded signals of the fluxgate sensor were amplified with a low-noise preamplifier (Model SR560, Stanford Research Systems) by a factor of 10 for monopolar and 1000 for bipolar electrode configuration before it was recorded with a multifunction data acquisition device (USB-6361, National Instruments) with an A/D converter resolution of 16 bits between the analog input range of ± 10 V and with a maximum sampling rate of 1 MS/s. The sampling rate was set to 40 kHz for the measurements performed in this paper. Care has been taken that the noise contribution of the A/D converter is negligible by the sufficient pre-amplification of the sensor signals. This device is also used to generate biphasic impulses, as generally applied for clinical neurostimulators, by adjusting the stimulation frequency f_s, pulse width of the stimulation t_p and the amplitude A in voltage, as shown in Fig. 4a. A DC component in the signal is avoided by a negative pulse with the same pulsewidth-voltage product.

D. Biot-Savart-Law

This section briefly gives two different equations to calculate the total magnetic field B with the Biot-Savart-Law for two approaches, which are of interest in this paper. The magnetic field for a straight wire can be calculated using the Biot-Savart-Law for a current carrying finite straight wire [28] with the following equation:

$$B(i) = \frac{\mu_0 I}{4\pi D(i)} \Big(\cos(\alpha) - \cos(\beta) \Big), \tag{1}$$

where the wire carries the current I at a distance $D(i)$ to the ith sensor with the identified end points by the angles α and β, $\mu_0/(4\pi)$ is a constant, and $B(i)$ is the magnetic flux density at $D(i)$. We will see that this formula can be used as a good approximation for the monopolar electrode configuration.

The magnetic field for a current dipole can be calculated with the Biot-Savart law for a single current dipole [14]:

$$B(i) = \frac{\mu_0}{4\pi} \frac{(\vec{R}(i) - \vec{L}) \times \hat{s}(i) \cdot \vec{Q}}{|\vec{R}(i) - \vec{L}|^3}, \tag{2}$$

where $\vec{Q}$ is the dipole moment, $\vec{L}$ is the dipole location (represented as a green dot marker in Fig. 3), $\vec{R}(i)$ is the ith sensor location (represented as a red dot marker in Fig. 1a) and $\hat{s}(i)$ is the unit orientation of the ith sensor. It will be shown that this equation fits the bipolar electrode configuration and will be used for electrode localization. At this point, it is assumed that the dipole points in the direction of the negative z-axis, considering that the electrode in the phantom head is arranged parallel to the z-axis and thus the current flows in this direction ($\hat{s} = [0, 0, -1]$). Since we are only interested in the position of the electrode and the dipole orientation is not taken into account for the localization algorithm described in section III-D, it will not be discussed further.

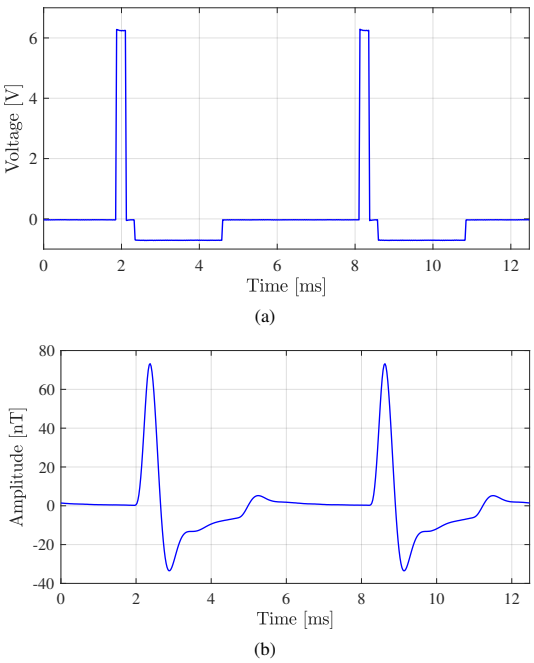

Fig. 4. (a) The created stimulation signal with an amplitude of $A = 6.3$ V, a pulse width of $t_p = 240$ µs and a frequency of $f_s = 160$ Hz. (b) The measured signal with the fluxgate sensor with 80 averaging for monopolar electrode configuration.

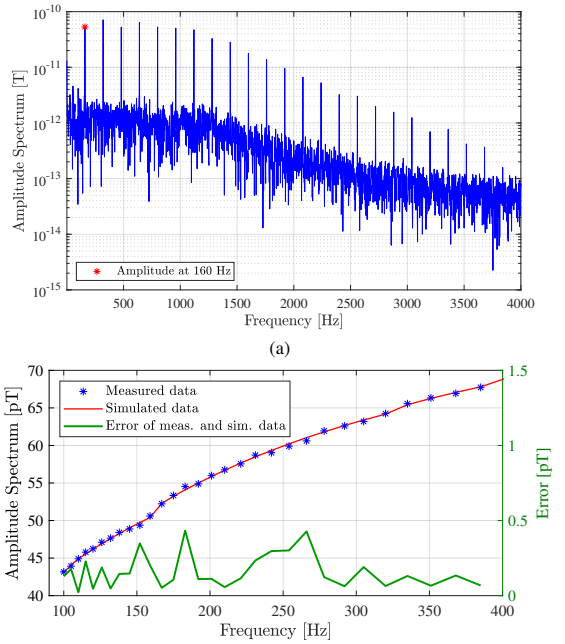

Fig. 5. (a) The amplitude spectrum in T of the stimulation signal with an amplitude of $A = 6.3$ V for bipolar mode is shown. The red asterisk marker indicates the amplitude value at the 160 Hz fundamental frequency. (b) The measured and simulated amplitude values and the error between both values in pT at the fundamental frequency, if it is varied between 100 Hz and 385 Hz for bipolar electrode configuration with a constant stimulation amplitude of 6.3 V.

III. Results

For all the following results, a relatively strong stimulation signal with an amplitude of $A = 6.3$ V, a pulse width of $t_p = 240$ µs and a frequency of $f_s = 160$ Hz, as depicted in Fig. 4a, was used. The motivation of this choice is included in the discussion section.

A. Signal Analysis

In order to examine the shape of the measured deep brain stimulation signal with the fluxgate sensor, the electrode was monopolarly stimulated and the tangential magnetic component was measured one second at a distance of about 45 mm. The measured signal (80 times averaged) is shown in Fig. 4b. The measured signal is already visible in the time domain since the magnetic flux density generated by the monopolar stimulation is relatively strong and has a peak amplitude of about 73 nT. The shape of the recorded signal is due to sensor properties, that has a bandwidth of 1 kHz and thus acts as a low-pass filter.

Furthermore, the electrode was bipolarly stimulated with a constant pulse width of $t_p = 240$ µs and a frequency of $f_s = 160$ Hz. The amplitude spectrum is shown in Fig. 5a for a constant stimulus voltage. Increasing the stimulation voltage between 0.5 V and 7 V showed a linear increase of the resulting magnetic flux density between approx. 5 pT and 50 pT, as can be expected for a homogeneous model with only one conductivity. Nevertheless, an increase in the stimulation frequency at a constant stimulation voltage leads to a non-linear increase of the magnetic field, that was measured and can be seen in Fig. 5b. For this purpose, a constant stimulation amplitude of 6.3 V was selected, the stimulation frequency was changed logarithmically between 100 Hz and 385 Hz, each 60 seconds recording was transformed into the frequency domain using the Welch's method [29] with the Hanning window, and finally the amplitude value from the amplitude spectrum at the correspondingly adjusted fundamental frequency was taken. The increase of the magnetic field over the investigated frequency can be interpreted as an increase of the electrical conductivity between the used contacts for the bipolar electrode configuration over the frequency. The magnitude of the impedance between both contacts was measured and decreases non-linear from about 380 Ω for 100 Hz to 240 Ω for 385 Hz and thus the current gets higher with the same behavior. This finally leads to an increase with the same slope in the magnetic field. The error between the measured data with the fluxgate sensor and the simulated data based on the measured magnitude impedance is less than 0.4 pT for all performed measurements (see Fig. 5b), i.e. a maximum of about one percent inaccuracy of the measured magnetic field values.

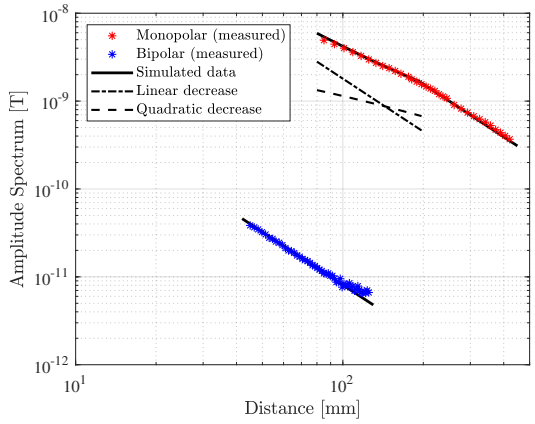

Fig. 6. The decrease of the amplitude spectrum at the fundamental frequency in T in dependency of the distance in mm for both monopolar (blue curve) and bipolar (red curve) electrode configurations. At 45 mm of distance, there is about 40 pT of magnetic field in bipolar mode (red asterisk marker).

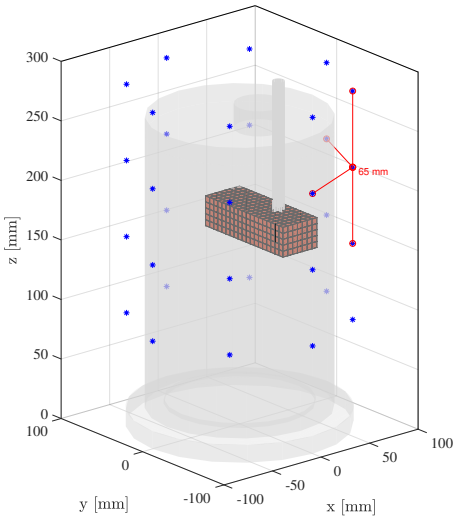

Fig. 7. The cylindrical head model surrounding by 32 measuring points in blue asterisks in a symmetrical measuring system, eight points each at one measuring height. As an example, a part of the whole volume is shown, which has been divided into small voxels with an edge length of 5 mm.

B. Distance Dependency

In order to investigate which field strengths are to be expected in both monopolar and bipolar electrode configurations at which distance, the following measurement was performed. The stimulation parameters as described at the beginning of this chapter were used. The tangential magnetic component was measured with the fluxgate sensor one second for the monopolar and ten seconds for the bipolar mode at the height of the electrode. The measurement distance varied between 85 mm and 421 mm with a step size of 3 mm for the monopolar and between 45 mm and 125 mm with a step size of 1 mm for the bipolar mode. Again, each measured time signal is transformed into the frequency domain using Welch's method, and the amplitude value from the amplitude spectrum at 160 Hz is then taken.

The results are shown in Fig. 6 in a double logarithmic scale. The magnetic field in the monopolar mode (e.g. about 5 nT at a distance of 85 mm) compared to bipolar stimulation (about 10 pT at the same distance) is about more than 100 times stronger. At larger distances, the resulting magnetic field of the bipolar stimulation is strongly affected by the sensor noise, causing fluctuation of the bipolar measured values (blue asterisk markers). Furthermore, the magnetic field of both electrode configuration decreases differently over the distance. It decreases quadratically in the bipolar stimulation mode, and first linearly, then quadratically in the monopolar mode, which can be explained by the current flow in the system and confirms the following assumptions: The current flow between the two middle contacts of the electrode (bipolar), which corresponds to approx. 3 mm, is assumed to be a current dipole at the considered distances between 45 mm and 125 mm, so that the resultant magnetic field decreases quadratically according to Eq. 2, in which the relation $B \propto 1/R^2$ applies. The (calculated) simulated values were inserted as a black line in the figure, that shows the agreement of measured and simulated data. In case of monopolar stimulation, where the current flows over the entire height of the phantom head, the resultant field decreases linearly, according to Eq. 1 in which the field B is directly proportional to $1/D$. And with increasing distance, when it reaches the same order of the phantom dimension, the current flow behaves like a dipole, and the field then starts to decrease quadratically, as some lines previously described.

C. Monopolar and Bipolar Analysis

For the analysis of the magnetic field distribution for both monopolar and bipolar electrode configuration, the following measurement was performed: The stimulation signal as depicted in Fig. 4a has been used for both modes. Since each measurement with different electrode positions marked with black dots in Fig. 2 showed qualitatively the same behavior, the measurement with the electrode position at $a = 40$ mm will be presented here.

In case of monopolar stimulation, the lowest contact of the electrode is chosen to be the cathode (contact 0 in Fig. 3), and in case of bipolar stimulation, the middle two contacts are used as the cathode and the anode (contact 1 and 2 in Fig. 3). The measurement took place at 32 measuring points with a radius of approx. 85 mm, divided over four heights with a distance of 65 mm, as depicted in Fig. 7 with blue asterisk markers. The neighboring measuring points are also 65 mm apart to guarantee a symmetrical measuring system. The measuring points were located at the distance between 45 mm (closest distance) and 125 mm (farthest distance) to the electrode, as shown in Fig. 2. In the monopolar case, the magnetic field is measured for one second at each of these measuring points in all three orthogonal directions, whereas in bipolar case, it was measured for ten seconds. Thus, the total measurement time varies between 10 minutes (monopolar) and 30 minutes

(bipolar), including the movement of the head scanner, the rotation of the sensor, the storage process of the measured data and the one-second break before each recording to remove vibration artifacts in the system.

Each measured time signal is transformed into the frequency domain using the Welch's method, the amplitude value from the amplitude spectrum at the 160 Hz fundamental frequency is taken and the magnitude of the magnetic flux density at each point is calculated, which results in a total of 32 values representing the measured magnetic field distribution. For a better graphical visualization, interpolation between these values is then performed. The result for the field distribution of the monopolar and bipolar electrode configuration can be seen in Fig. 8. The field distribution in the top figure is generated by the current, which flows from the signal generator through the conductors over the entire height of the cylinder and under the cylinder back to the generator. Thus, a relatively large magnetic flux density in the nT-range is generated over the entire measuring surface. The contribution of the field generated by the current in the conductor placed parallel to the cylinder is most evident in contrast to the field generated by the current flowing through the cylinder, which is visible as the red area in the figure. The measured magnetic field distribution of the monopolar stimulation for the same electrode location can thus be calculated theoretically as an approach using the Biot-Savart law for a current carrying finite straight wire with Eq. 1. The calculated result is shown in Fig. 9a, which only considers the field generated by the current in the cylinder and neglects the influence of the signal cable.

The measured field distribution in the bipolar case (see Fig. 8b) is, in contrast to that of the monopolar one, caused only by the current flowing between the two contacts of the electrode, results in about 100 times weaker magnetic flux density in the pT-range. In the blue area, the distance of the measuring points to the electrode is already so large that the magnetic field strength disappears in the noise level of the sensor. The magnetic field caused by the current in the conductor is completely removed, since the current flowing through the conductor to the electrode flows back through the conductor parallel and in close vicinity to the feeding conductor so that their contributions cancel out each other. Hence, the stimulation mode can be modeled as an electrical current dipole. For the calculation of its field distribution, the Biot-Savart law for a single current dipole according to Eq. 2 can be used. The theoretically calculated magnetic field distribution for the same electrode location can be seen in Fig. 9b showing qualitatively the same behavior. The normalized root mean square error (NRMSE) between the measured magnetic field distribution of the bipolar electrode configuration (Fig. 8b) and the simulated magnetic field distribution (Fig. 9b) can be seen in Fig. 9c. The error varies between about 0 and 12 percent, depending on how far the measuring points are placed to the electrode. At short distances, the error is comparatively small (between about 0 and 2 percent), since the magnetic field generated by the stimulation can be measured by the fluxgate sensor. At larger distances the error increases significantly up to 12 percent, due to the fact that the measuring range is limited by the noise level of the fluxgate sensor and the generated magnetic field disappears in the sensor noise.

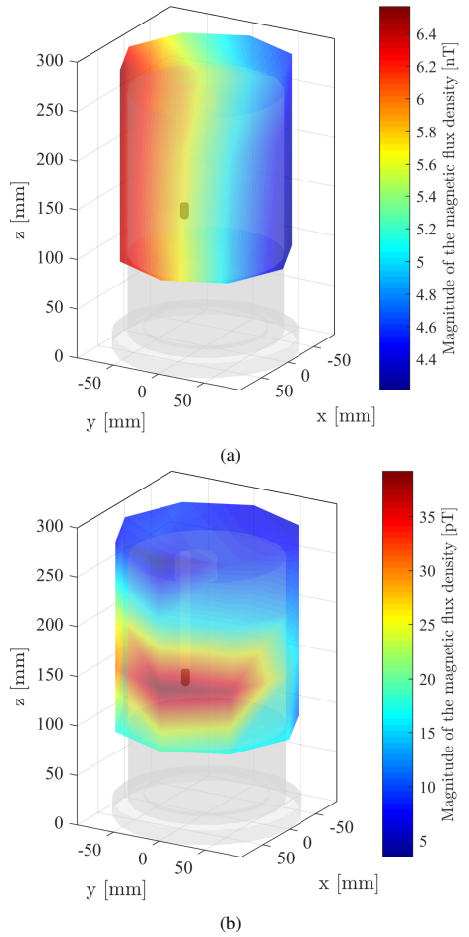

Fig. 8. The measured magnetic field distribution of monopolar (a) and bipolar (b) electrode configuration created by 32 measuring points. The magnitude of the magnetic flux density at each measuring point was calculated and interpolated between the points.

In order to localize the DBS electrode in the cylindrical head model by such magnetic field measurements, it is required to have a concentrated spatial field distribution, as in the case of bipolar stimulation. However, it has to be dealt with very weak magnetic fields in the pT-range. In case of monopolar stimulation, the magnetic field is much stronger, but no information about the electrode height can be obtained. Furthermore the superimposition of the magnetic field through the conductor has also to be considered, which anyway limits the localization accuracy of the electrode.

D. Localization of the Electrode

The bipolar analysis has shown that the model of an electrical current dipole fits the bipolar electrode configuration. The assumption is confirmed by an exemplary successful DBS electrode localization which will be presented in this section. Since the exactly placed electrode does not move, does not rotate and there is only one active source in the model, a

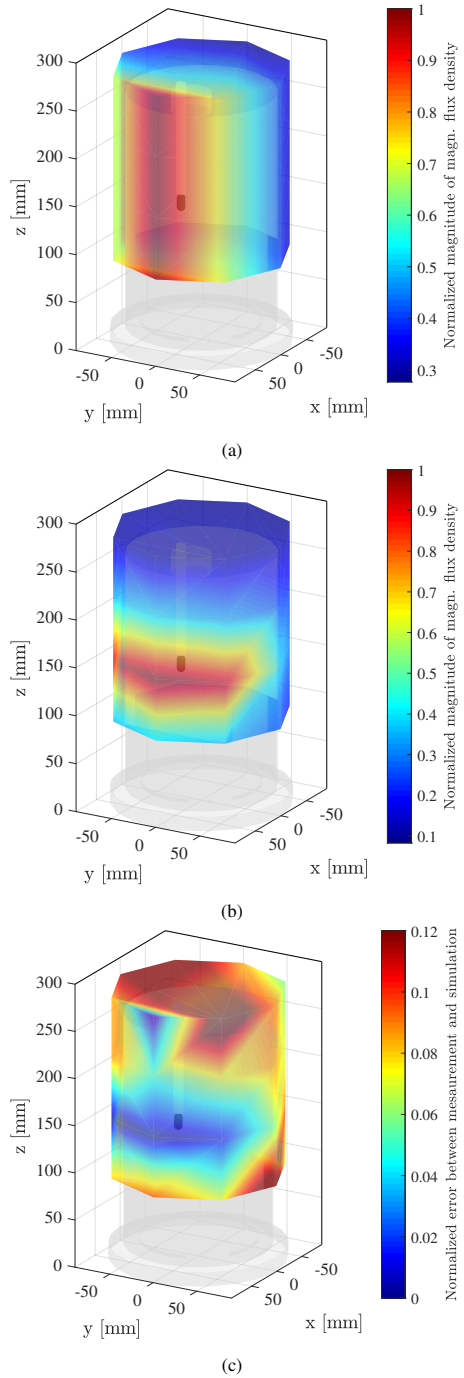

Fig. 9. The theoretically calculated field distribution of monopolar (a) and bipolar (b) electrode configuration with Eq. 1 and Eq. 2 for the same electrode location as in Fig. 8. The normalized magnitude of the magnetic flux density at each simulated point was calculated. (c) The normalized root mean square error of the measured (see Fig. 8b) and simulated (see Fig. 9b) data are shown.

dipole fitting algorithm can be used, which searches for a source that best describes the measured data. The volume to be examined is divided into small voxels and the forward-computed magnetic flux density with Eq. 2 are compared with those calculated from the measured data. The programmed and used dipole-fit algorithm is mainly divided in five algorithm steps:

1) Calculate the magnitude of the magnetic flux density in tesla at each ith measurement of the sensor. Therefore, each measured time signal has to be transformed into the frequency domain and the amplitude in the spectrum at the adjusted stimulation frequency has to be taken. The result will be the measured magnitude of the magnetic flux density $|B_{\mathrm{meas}}|(i)$. It is a vector with the length of $\mathrm{N_{meas}}$ (total number of measuring points i).
2) Consider only the elements of $|B_{\mathrm{meas}}|$ at the measuring points j where the magnetic flux density could be calculated and did not get lost in the noise. The well-known noise level of the used measuring sensor can be selected as a threshold value. Then, normalize the remaining values to their maximum value to get $|B_{\mathrm{meas,norm}}|(j)$. The maximum value is the strongest measured magnetic field, which comes from the measurement at the closest measuring point to the electrode. It is a vector with the length of $\mathrm{N_s}$ (total number of considered measuring points j, $\mathrm{N_s} \leq \mathrm{N_{meas}}$).
3) Divide the region to be examined into small 1x1 mm voxels, where each voxel gets a voxel number and its Cartesian coordinates. Then calculate the expected magnitude of the magnetic flux density in Tesla over the same chosen sensor positions j with Eq. 2 and normalize it to its maximum element in the vector. The result will be the modeled magnetic flux density $|B_{\mathrm{model,norm}}|(j,n)$. It is a matrix with the dimension $\mathrm{N_s} \times \mathrm{N_v}$, where $\mathrm{N_v}$ represents the total number of considered voxels n.
4) Define the dipole-fit cost function and determine the specific error for all voxel n:
$$e(n) = \sum_{j=1}^{\mathrm{N_s}} \Big(|B_{\mathrm{meas,norm}}|(j) - |B_{\mathrm{model,norm}}|(j,n) \Big)^2, \tag{3}$$
where $\mathrm{N_s}$ represents the total number of chosen measuring points in step 2 of the algorithm. $e(n)$ is a vector with the length of $\mathrm{N_v}$.
5) Take the global minimum value of the dipole-fit cost function:
$$\min\Big[e(n)\Big] = e(n_{\mathrm{dipole}}). \tag{4}$$
The voxel n_{dipol} represents the smallest error and is the result of the localization algorithm. The calculated magnetic flux density for this voxel best explains the measured data with the error $e(n_{\mathrm{dipol}})$.

For the exemplary fluxgate measurement to be shown here, the electrode was placed at $a = 40$ mm, it was bipolarly stimulated with the stimulation parameters as described previously, and the lower two contacts are used with the physical center at the Cartesian coordinates $[x_d, y_d, z_d] = [40\ \mathrm{mm},\ 0\ \mathrm{mm},\ 179\ \mathrm{mm}]$. The measuring time at each measuring points was set to ten seconds and a total of 176 measuring points, 22 points at eight heights, was selected. The

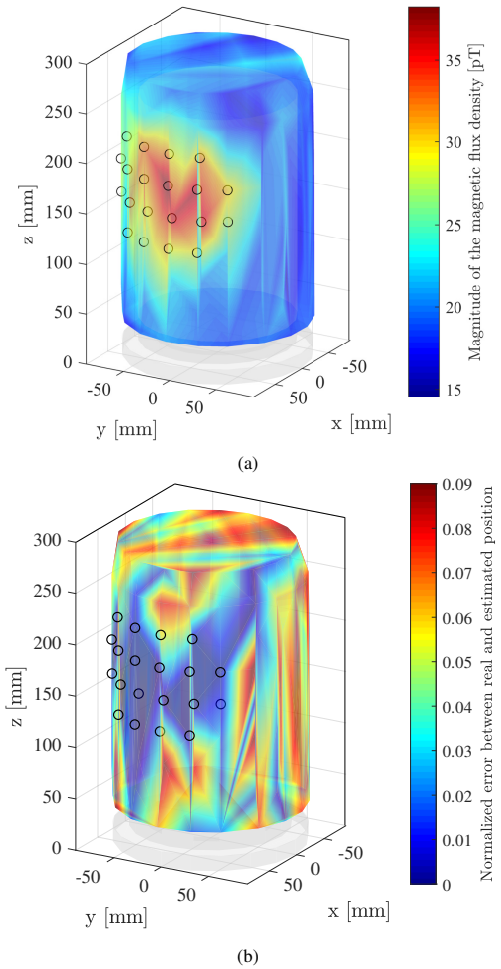

Fig. 10. (a) The measured field distribution of bipolar electrode configuration created by 176 sensor points. The magnitude of the magnetic flux density at each measuring point was calculated and interpolated between the points. The sensor points where the magnetic fields are visible were marked in black circles. (b) The normalized root mean square error (NRMSE) between the real position of the electrode and the position estimated by the localization algorithm.

sensor points were located at the distance between 45 mm and 125 mm to the fixed electrode. The measured field distribution is depicted in Fig. 10a. In step 2 of the algorithm, only 20 of 176 measuring points were considered due to the field shown in blue that was basically the noise level of the fluxgate sensor. The considered measuring points are represented with black circles in Fig. 10. The threshold value chosen here at 30 pT was slightly higher than the sensor noise level to remove measurement inaccuracies and variations just above the noise level. The region was divided into 1 mm³ voxels in which the electrode was searched in x-direction from 19 mm to 50 mm, in y-direction from -31 mm to 60 mm and in z-direction from 173 mm to 194 mm in a total number of about $N_s = 60,000$ voxels. For each of these voxels its voxel number and its Cartesian coordinates are known. The Euclidean distances between these voxels and the real position

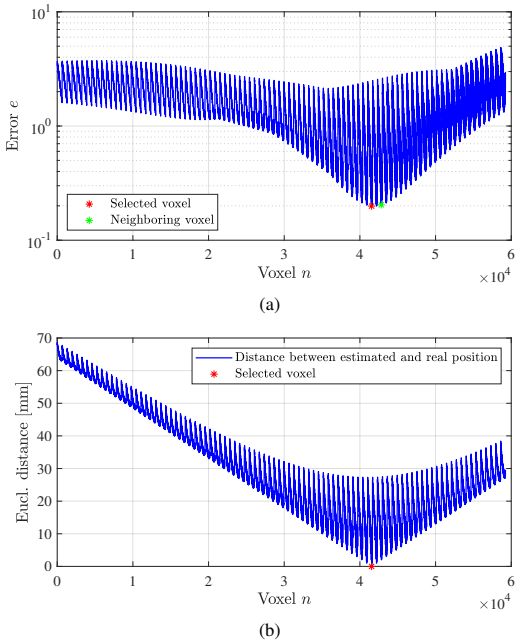

Fig. 11. (a): The calculated error e over all voxel n. The voxel that illustrates the smallest error at the global minimum is selected (red asterisk). The second smallest error is caused by the neighboring voxel (green asterisk). (b) The Euclidean distances in mm over the same voxel n. The selected voxel has a distance of 0 mm to the real position of the electrode.

of the electrode are depicted in Fig. 11b. The region to be examined can be seen in Fig. 7, which was subdivided with voxel edge length of 5 mm. For each voxel, the corresponding error $e(n)$ is calculated with Eq. 3 and is depicted in Fig. 11a. The voxel number $n_{\text{dipole}} = 41,548$ illustrates the smallest error at the global minimum of about $e(n_{\text{dipole}}) = 0.2$ and represents the solution found at the same Cartesian coordinates of the electrode $[x_d, y_d, z_d] = [40 \text{ mm}, 0 \text{ mm}, 179 \text{ mm}]$. So the distance between the position of the physical center of the used bipolar electrode configuration and the voxel that yielded the smallest error in the calculation is 0 mm (see Fig.11b). The normalized root mean square error between the real position of the electrode and the position estimated by the localization algorithm can be seen in Fig. 10b. At the considered measuring points (black circles), the errors are between 0 and 1 percent, which led to an accurate localization. At the other measuring points, errors of up to 10 percent can be seen, which were neglected in step 2 of the algorithm, as they would lead to a shifting of the found position. The direct neighbor voxel ($n_{\text{neighbor}} = 42,199$) with the Cartesian coordinates $[x_n, y_n, z_n] = [41 \text{ mm}, 0 \text{ mm}, 179 \text{ mm}]$, has a distance of 1 mm to the real position and reaches the second smallest error (see Fig. 11a). Since the distribution of the volume into voxels is done by first arranging the voxels in the z-direction, then arranging them in the y-direction and then in the x-direction, jumps occur after the last arranged voxel at the end of each direction to get higher with the distribution plane. Thus, the distance of the voxel to the electrode changes rapidly and such value jumps of the errors occur, as can be

seen in Fig. 11. Therefore, the number of the neighboring voxel $n_{\mathrm{neighbor}} = 42,199$ is not directly adjacent to the found voxel $n_{\mathrm{dipole}} = 41,548$.

The entire measurement took about two hours of time and the computing time was significantly reduced by the second step of the algorithm. It has been shown that the model of an electrical current dipole can be assumed for the bipolar electrode configuration and that localization can be performed with this model assumption at least at an electrode position near to the surface. For a more accurate validation of the localization feasibility, further measurements have to be made, which will be part of our further work.

IV. Discussion

The magnetic field properties for both monopolar and bipolar electrode configuration of a deep brain stimulation electrode was analyzed in this paper with three dimensional magnetic field measurements using the fluxgate sensor as an unidirectional magnetometer. Therefore, the electrode was placed in a cylindrical simplified phantom head that has been developed to match the dimensions of a human head. Such a geometrically well-defined model is needed as a first step in measuring the precise position of the deep brain stimulation electrode. In further steps, it will also be important for electrode reconstruction algorithms for validating the localization accuracy. That was the motivation for the current study.

Since the fluxgate sensor has a frequency bandwidth of 1 kHz, it acts as a low-pass filter during recording and the recorded signal thus mainly includes the applied stimulation frequency of 160 Hz and its next five harmonics (320, 480, 640, 800, 960 in Hz). Nevertheless the shape of the stimulation signal was still clearly visible. The whole analysis in this paper took place in the frequency domain by taking the amplitude value from the amplitude spectrum at the fundamental frequency. It is also possible to take any other harmonic frequency below 1 kHz by using the fluxgate sensor. Other magnetic sensors with a smaller bandwidth detecting one of these frequencies of interest would also be sufficient, e.g. thin-film magnetoelectric sensors (ME sensors) [30], which are being developed within the framework of the Collaborative Research Centre CRC 1261.

The field strengths of the monopolar electrode configuration were in the nT-range and decrease linearly over the considered distance. Since the magnetic field at the measuring points is superimposed by the fields generated by the current flowing through the whole system, the field generated only by the current in the cylinder cannot be determined due to the influence of the signal cable. Therefore, the monopolar stimulation modeled approximation as a current-carrying conductor cannot be used for electrode localization. In addition, there is no information about the height of the electrode (z-coordinate) that already limits the localization possibility. In contrast, the bipolar electrode configuration allows a more focused spatial resolution in the field distribution, which could be estimated by the model of an electrical current dipole and could be used for electrode localization. However, the field strength is 100 times weaker than the field generated by monopolar stimulation, and it decreases quadratically with the distance to the sensor. Therefore, it is feasible to estimate the magnetic field strengths at any desired location within the described limits to enable the electrode localization with magnetic sensor measurements.

While we acknowledge that further work is necessary to achieve a more accurate validation of localization methods, the localization result in this paper shows that the basic dipole fitting algorithm was able to detect the position of the electrode in the simplified cylindrical phantom head. In a more realistic scenario, the following difficulties need to be addressed, and the localization algorithm has to be adapted to that. The real human head with different brain structures is more complicated. This model has to be extracted from high-resolution MR or CT images of the patient. Since the implanted areas of interest are known and the current of the DBS is only flowing in a particular known region, the segmentation of this images can be specified on this region resulting in a higher quality. The localization method must use the resultant segmented head model to divide the entire head into small voxels. Each voxel has its own electrical conductivity, which also differs from our homogeneous model with only one conductive material. The used voltage-controlled stimulation regulates the voltage by changing the current depending on the resistance, which is different in each individual anatomy of the patients. Changes in the current leads to a change of the strength of the magnetic field. Thus, the magnetic field which is calculated in step 3 of the algorithm becomes even more difficult. This problem can be solved by using a newer current-controlled DBS system (e.g. Vercise Cartesia$^{\mathrm{TM}}$ electrode, Boston Scientific Corporation), in which the current can be adjusted to any individual anatomy, which in turn leads to a constant magnetic field. Different conductivities would therefore no longer be a problem for the described algorithm, which is still under investigation in our research. In addition, the angle at implantation of the DBS electrode is also unknown, which was assumed to be vertical in our model. This will lead to a variable orientation of the magnetic field. Since the algorithm, as described here, works with the magnitude of the magnetic field and not with its orientation, the problem can be neglected. Furthermore, the magnetic field measurements with real DBS patients using only one magnetic sensor, measuring around the head point for point, will also be a challenge due to the long measuring time on the one hand and the head movement of the patient during the measurement on the other hand. An array of sensors will reduce the time significantly and the movement of the head can be detected and corrected e.g. with non-magnetic cameras inside the shielded chamber recording the shifting of the head to correct the position of the sensor in relation to the head surface.

The parameters of the used stimulation signal over all performed measurements were set at relatively high values with 6.3 V amplitude and 240 µs pulse width, to take advantage of the phantom head ending up with larger magnetic fields. The same choice of the stimulation amplitude cannot be applied in a real head of a DBS patient as this would not be tolerated by the patient. Since the magnetic field generated by the stimulation is linearly dependent on the stimulation amplitude for the investigated frequency, it can

be assumed that the field strengths caused by the amplitude commonly set between 1 and 4 V in a real head are smaller by a factor of between $6.3/1 = 6.3$ and $6.3/4 = 1.6$ compared to the measured values. This can be interpreted as an estimated calculation in order to get an idea of an approximate magnitude of the generated magnetic fields in real DBS patients, considering that the electrical conductivity of the physiologic saline solution used in the cylindrical head model is comparable to that of a human brain and that the investigated frequency is adjusted in the patient.

V. Conclusion

This study demonstrates that the magnetic field of the deep brain stimulation electrode can be measured with magnetic fluxgate sensors at a distance between 45 mm and 125 mm and there are differences in the magnetic properties of both monopolar and bipolar electrode configurations. The magnetic flux densities are in the pT-range in bipolar stimulation mode and decrease quadratically with distance. In monopolar mode, the fields are in the nT-range and decrease first linearly, then quadratically with distance. Furthermore, it has been shown that measuring with bipolar mode gives us a more focused spatial magnetic field distribution, which is essential for electrode localization, where the stimulation mode can be modeled as an electrical current dipole. As proof of feasibility, we presented a bipolar measurement in which the model assumed in the dipole-fit algorithm accurately localized the electrode. We acknowledge that further work is necessary to achieve a more accurate validation of localization methods and results. Although the monopolar stimulation generates a 100 times larger magnetic field, it is less suited to be used for electrode localization due to the corresponding field distribution, which is the superposition of magnetic fields from the cables, and does not provide any information about the height of the electrode in the head phantom.

Acknowledgment

This work was supported by the German Research Foundation (Deutsche Forschungsgemeinschaft, DFG) through the project B5 and Z2 of the Collaborative Research Centre CRC 1261 *Magnetoelectric Sensors: From Composite Materials to Biomagnetic Diagnostics*.

References

[1] G. Deuschl *et al.*, "A randomized trial of deep-brain stimulation for parkinson's disease," *New England Journal of Medicine*, vol. 355, no. 9, pp. 896–908, 2006.

[2] A. Kupsch *et al.*, "Pallidal deep-brain stimulation in primary generalized or segmental dystonia," *New England Journal of Medicine*, vol. 355, no. 19, pp. 1978–1990, 2006.

[3] J. M. Nazzaro, K. E. Lyons, and R. Pahwa, "Chapter 13 - deep brain stimulation for essential tremor," in *Brain Stimulation*, ser. Handbook of Clinical Neurology, A. M. Lozano and M. Hallett, Eds. Elsevier, 2013, vol. 116, pp. 155 – 166.

[4] S. Hemm and K. Wårdell, "Stereotactic implantation of deep brain stimulation electrodes: A review of technical systems, methods and emerging tools," *Medical and Biological Engineering and Computing*, vol. 48, no. 7, pp. 611–624, 2010.

[5] C. Butson and C. Mcintyre, "The use of stimulation field models for deep brain stimulation programming," *Brain Stimulation*, vol. 20, 06 2015.

[6] C. R. Butson and C. C. McIntyre, "Current steering to control the volume of tissue activated during deep brain stimulation," *Brain Stimulation*, vol. 1, no. 1, pp. 7 – 15, 2008.

[7] C. Schmidt and U. van Rienen, "Modeling the field distribution in deep brain stimulation: The influence of anisotropy of brain tissue," *IEEE transactions on bio-medical engineering*, vol. 59, pp. 1583–92, 03 2012.

[8] ——, "Adaptive estimation of the neural activation extent in computational volume conductor models of deep brain stimulation," *IEEE Transactions on Biomedical Engineering*, vol. 65, no. 8, pp. 1828–1839, Aug 2018.

[9] A. Motevakel and A. Medvedev, "Localization of deep brain stimulation electrodes via metal artifacts in CT images," *2014 36th Annual International Conference of the IEEE Engineering in Medicine and Biology Society, EMBC 2014*, pp. 1055–1058, 2014.

[10] H. P. Sun *et al.*, "Electrode position determined by fused images of preoperative and postoperative magnetic resonance imaging and surgical outcome after subthalamic nucleus deep brain stimulation," *Neurosurgery*, vol. 63, no. 5, pp. 925–936, 2008.

[11] C. Pollo *et al.*, "Localization of electrodes in the subthalamic nucleus on magnetic resonance imaging," *Journal of Neurosurgery*, vol. 106, no. 1, pp. 36–44, 2007. [Online]. Available: http://thejns.org/doi/10.3171/jns.2007.106.1.36

[12] W. O. Contreras Lopez *et al.*, "A series of 80 consecutive cases of dystonia: A neurosurgical treatment algorithm," *Journal of Neural Transmission*, vol. 120, no. 7, pp. 1141–1142, 2013.

[13] J. Y. Lee *et al.*, "Is MRI a reliable tool to locate the electrode after deep brain stimulation surgery? Comparison study of CT and MRI for the localization of electrodes after DBS," *Acta Neurochirurgica*, vol. 152, no. 12, pp. 2029–2036, 2010.

[14] J. C. Mosher, P. S. Lewis, and R. M. Leahy, "Multiple Dipole Modeling and Localization from Spatio-Temporal MEG Data," *IEEE Transactions on Biomedical Engineering*, vol. 39, no. 6, pp. 541–557, 1992.

[15] P. Hansen, *MEG an introduction to methods*. New York Oxford: Oxford University Press, 2010.

[16] J. W. Wheless *et al.*, "Magnetoencephalography (MEG) and magnetic source imaging (MSI)," *Neurologist*, vol. 10, no. 3, pp. 138–153, 2004.

[17] P. Hayes *et al.*, "Electrically modulated magnetoelectric sensors," *Applied Physics Letters*, vol. 108, p. 182902, 05 2016.

[18] X. Jun, L. Luming, and H. Hongwei, "Primary experimental study on safety of deep brain stimulation in rf electromagnetic field," in *2009 Annual International Conference of the IEEE Engineering in Medicine and Biology Society*, Sep. 2009, pp. 3091–3094.

[19] E. M. Wassermann and T. Zimmermann, "Transcranial magnetic brain stimulation: Therapeutic promises and scientific gaps," *Pharmacology & Therapeutics*, vol. 133, no. 1, pp. 98 – 107, 2012.

[20] M. A. Nitsche *et al.*, "Transcranial direct current stimulation: State of the art 2008," *Brain Stimulation*, vol. 1, no. 3, pp. 206 – 223, 2008.

[21] J. Fan *et al.*, "Magnetic field projector for deep brain stimulation," *IEEE Transactions on Magnetics*, vol. 51, no. 11, pp. 1–4, Nov 2015.

[22] C. Pollo *et al.*, "Magnetic resonance artifact induced by the electrode activa 3389: an in vitro and in vivo study," *Acta Neurochirurgica*, vol. 146, no. 2, pp. 161–164, Feb 2004.

[23] B. Brahimaj, R. B. Kochanski, and S. Sani, "Microelectrode accuracy in deep brain stimulation surgery," *Journal of Clinical Neuroscience*, vol. 50, pp. 58 – 61, 2018.

[24] M. I. Iacono *et al.*, "A study on the feasibility of the deep brain stimulation (dbs) electrode localization based on scalp electric potential recordings," *Frontiers in Physiology*, vol. 9, p. 1788, 2019.

[25] J. Volkmann *et al.*, "Introduction to the programming of deep brain stimulators," *Movement Disorders*, vol. 17, no. SUPPL. 3, 2002.

[26] J. Volkmann, E. Moro, and R. Pahwa, "Basic algorithms for the programming of deep brain stimulation in Parkinson's disease," *Movement Disorders*, vol. 21, no. SUPPL. 14, pp. 284–289, 2006.

[27] J. Buhlmann *et al.*, "Modeling of a Segmented Electrode for Desynchronizing Deep Brain Stimulation," *Frontiers in Neuroengineering*, vol. 4, no. December, pp. 1–8, 2011. [Online]. Available: http://journal.frontiersin.org/article/10.3389/fneng.2011.00015/abstract

[28] J. A. Miranda, "Magnetic field calculation for arbitrarily shaped planar wires," *American Journal of Physics*, vol. 68, no. 3, pp. 254–258, 2000. [Online]. Available: http://aapt.scitation.org/doi/10.1119/1.19418

[29] P. Welch, "The use of fast fourier transform for the estimation of power spectra: A method based on time averaging over short, modified periodograms," *IEEE Transactions on Audio and Electroacoustics*, vol. 15, no. 2, pp. 70–73, Jun 1967.

[30] R. Jahns *et al.*, "Magnetoelectric sensors for biomagnetic measurements," in *2011 IEEE International Symposium on Medical Measurements and Applications*, May 2011, pp. 107–110.

Key Findings and Scientific Implications

- The magnetic field generated by high-stimulation parameter settings of DBS can be measured with a fluxgate magnetometer.
- Voltage-controlled stimulation leads to a proportional dependency between the stimulation amplitude and the magnetic field if the impedance of the electrode-tissue interface and, therefore, the current delivered to the tissue remain constant.
- Differences in magnetic properties between monopolar and bipolar electrode configuration exist.
- The monopolar electrode configuration is not suitable for electrode localization, although it produces a magnetic field approximately 100 times larger than the magnetic field generated by the bipolar configuration.
- The bipolar electrode configuration causes a concentrated spatial magnetic field distribution on the measurement sensor surface, leading to better localization of the electrodes.
- The behavior of the magnetic field generated by the bipolar electrode configuration can be approximated by the model of an electric current dipole.
- The position of the electrode can be determined from the measured magnetic field generated by the bipolar electrode configuration.

3.2 Dipole Fit Localization of the Deep Brain Stimulation Electrode Using 3D Magnetic Field Measurements

M. Yalaz, A. Teplyuk, G. Deuschl, and M. Höft, "Dipole Fit Localization of the Deep Brain Stimulation Electrode Using 3D Magnetic Field Measurements," in *IEEE Sensors Journal*, vol. 20, no. 16, pp. 9550-9557, August 2020, doi: 10.1109/JSEN.2020.2988067.

Information about the amount of own contribution to this publication:

Conceptualization	Planning	Implementation	Manuscript preparation
high	high	high	high

© 2020 IEEE. Reprinted, with permission, from M. Yalaz et al., "Dipole Fit Localization of the Deep Brain Stimulation Electrode Using 3D Magnetic Field Measurements," in *IEEE Sensors Journal*, August 2020. The version of record is available online at https://doi.org/10.1109/JSEN.2020.2988067.

In reference to IEEE copyrighted material which is used with permission in this thesis, the IEEE does not endorse any of Kiel University's products or services. Internal or personal use of this material is permitted. If interested in reprinting/republishing IEEE copyrighted material for advertising or promotional purposes or for creating new collective works for resale or redistribution, please go to http://www.ieee.org/publications_standards/publications/rights/rights_link.html to learn how to obtain a License from RightsLink.

IEEE Sensors Council IEEE SENSORS JOURNAL, ACCEPTED VERSION OF THE ARTICLE PUBLISHED IN THIS JOURNAL 1 of 8

Dipole Fit Localization of the Deep Brain Stimulation Electrode using 3D Magnetic Field Measurements

Mevlüt Yalaz, Alexander Teplyuk, *Associate Member, IEEE*, Günther Deuschl, Michael Höft, *Senior Member, IEEE*

***Abstract*— The aim of this study is to localize the electrode of the deep brain stimulation with three dimensional magnetic field measurements by applying the dipole fitting approach. The deep brain stimulation electrode was positioned successively at five increasing depths with well-known positions in a cylindrical head phantom and the magnetic field distribution was measured with a fluxgate magnetometer around the phantom. At each measuring point, the total magnetic field was measured by rotating the sensor in all three orthogonal directions. Finite element method was used to model the volume conduction of the phantom with its exact dimensions and electromagnetic simulations were performed to calculate the magnetic field distribution at the same measuring points around the phantom. The dipole fitting approach was then used to localize the position of the electrode by means of minimizing the normalized root mean square error between measured and calculated data. The results show an average localization accuracy of less than 1 mm over all performed measurements for both near surface and deep positions. Small deviations in the results can be explained by the measuring accuracy of the used fluxgate sensor. It can be concluded that the deep brain stimulation electrode can be precisely localized by three dimensional magnetic field measurements by using an accurate head volume conduction model and by applying the dipole fitting approach. The presented results are intended as preparatory work for real magnetic field measurements with patients implanted with deep brain stimulation electrodes.**

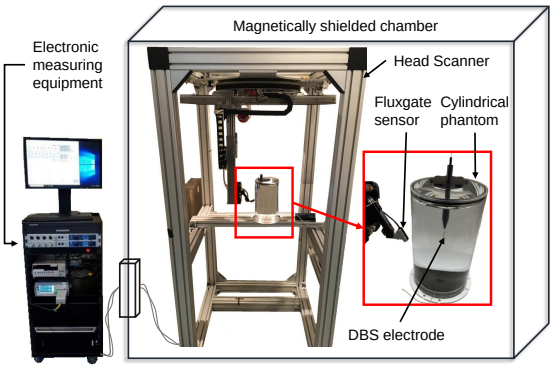

***Index Terms*— Deep brain stimulation (DBS), dipole fitting, electrode localization, finite element analysis, fluxgate magnetometer, magnetic field measurement, head volume conductor model.**

I. Introduction

DEEP brain stimulation (DBS) is a neurosurgical procedure used to treat patients with approved neurological and movement disorders such as Parkinson's disease (PD), dystonia, epilepsy, obsessive-compulsive disorders and tremors. During surgery, small electrodes are implanted in specific areas (subthalamic nucleus, globus pallidus or thalamus) on both sides of the brain depending on the symptoms to be treated, and are connected by long wires with a battery-powered neurostimulator placed under the skin near the clavicle. It delivers the DBS signal according to the patients' need with amplitudes between 1 and 4 V, pulse widths between 60 and 250 µs and frequencies from 130 to 185 Hz [1]. By the end of 2010, more than 80,000 patients have been treated with DBS worldwide [2] and the current number of the operation is more than 150,000 [3]. This huge number shows that DBS becoming more important over the time, but the neurobiological mechanisms of actions of DBS are not yet fully understood and the exact identification of the target area within the brain is still not yet precisely defined [4], [5]. Thus, the precise localization of the electrode position in the brain after DBS implantation provides important data to confirm the relationship between the electrode and the target. This helps to explain intended or unexpected effects. It is also essential to achieve optimal clinical outcome of the DBS treatment.

This paper deals with the localization of the deep brain stimulation electrode with magnetic field measurements, which is intended to be an alternative method to conventional neuroimaging techniques. The neuroimaging approach localizes the DBS electrode by visual inspection via metal artifacts in computed tomography (CT), post-operative magnetic resonance imaging (MRI), or in combination of both. However,

M. Yalaz, A. Teplyuk, and M. Höft are with the Chair of Microwave Engineering, Christian-Albrechts-University, 24143 Kiel, Germany (e-mail: my@tf.uni-kiel.de; alt@tf.uni-kiel.de; mh@tf.uni-kiel.de).

G. Deuschl is with the Department of Neurology, Christian-Albrechts-University, 24105 Kiel, Germany (e-mail: g.deuschl@neurologie.uni-kiel.de).

the images (mainly from MRI) are affected by metal artifacts which cause localization errors of up to 10.4 mm [6]. In addition, significant discrepancies were reported between the electrode centers estimated by CT and MRI and it is still being investigated which method is the better option [7]. Another imaging technique, the transcranial sonography (TCS), is also being investigated for post-operative electrode localization. First results have already been presented [8]. Furthermore, it is also shown, that the results for the electrode localization with neuroimaging data is software dependent, where differences were observed between four widely used software programs [9]. Accordingly, electroencephalography (EEG) and magnetoencephalography (MEG) provide alternative imaging modalities for measuring the stimulation induced brain activity, basically the artifacts generated by the DBS electrodes, to detect the position of the implanted electrodes. Studies showed the feasibility of DBS electrode localization with EEG recordings [10], [11], whereby a maximum error of about 15 mm was reported. The commercial state-of-the-art MEG systems consist of a certain amount of superconducting quantum interference devices (SQUIDs), that are placed and arranged in fixed positions so that they are mainly sensitive to tangentially and insensitive to radially oriented sources. We have used an affordable and easier to operate fluxgate sensor that was rotated in all three orthogonal directions of space to get the complete magnetic information at this point. This can be understood as a sensitivity of the sensor to arbitrarily oriented sources.

In our previous work, we have presented shortly as a proof-of-concept that electrode localization can be realized with magnetic field distribution measurements based on the investigated magnetic properties of DBS [12]. This paper mainly deals with the detection of the electrode in more detail and investigates the localization accuracy for different electrode positions and fewer measuring points by using a more realistic head volume conductor model. The bipolar electrode configuration with a given pair of two active contacts on the electrode, one as the anode (positive pole) and another one as the cathode (negative pole), must continue to be used as it generates more focused spatial magnetic field distribution that is essential for electrode localization. As an approximation, we modeled the bipolar mode of DBS as a dipole source that is located at the physical center of both activated electrode contacts and calculated theoretically the expected magnetic values with the simplified Biot-Savart law for an electrical current dipole [12]. However, this model applies to an infinite homogeneous space and neglects the modeling of the volume conduction. In this paper, a finite element mehtod (FEM) volume conduction model of the phantom head is created based on the exact dimensions of the phantom by using COMSOL Multiphysics (solving the forward problem). Subsequently, the dipole fitting approach is used to search for a single source and estimates the source that best explains the measured data by means of minimizing a defined cost function (solving the inverse problem). If the measured data can be explained by a single dipole, it can usually be localized robustly [13].

The motivation and future perspectives include the development of a non-invasive and non-radiation measuring system to measure the position of the DBS electrode and its orientation (rotation) in the brain when segmented electrodes are implanted to identify the best contact of the electrode for reaching the anatomically defined stimulation target area in the brain.

II. Methods

A. Experimental Design

Since the magnetic flux densities for the bipolar electrode configuration of DBS are in the pT range, all of the recordings took place in a magnetically shielded measuring chamber (Series Ak3B, Vacuumschmelze GmbH) to diminish the magnetic noise. The figure in the abstract shows qualitatively the entire measurement environment in which magnetic field measurements are performed. The head scanner, which is constructed in-house and is placed inside the chamber, operates pneumatically and moves the attached unidirectional magnetic sensor (Fluxmaster, Stefan Mayer Instruments) to any previously defined sensor points. At these points, the magnetic field can be measured in all three orthogonal directions by rotation of its sensitive axis to get the complete magnetic information at this point. The motivation and the advantages of adapting this sensor for magnetic field measurements are included in the discussion section. The sensor points can be distributed around the developed simplified cylindrical phantom head (diameter of 150 mm), which is filled with saline solution. The deep brain stimulation electrode (Model 3387, Medtronic) can be moved in all three x, y, and z direction at any fixed and well-known position. The entire electronic equipment is located outside the chamber. The recorded signals of the magnetic sensor were amplified with a low-noise preamplifier (Model SR560, Stanford Research Systems) by a factor of 1000 and were then recorded with a multifunction data acquisition device (USB-6361, National Instruments). Care has been taken that the noise contribution of the A/D converter is negligible by the sufficient pre-amplification of the sensor signals. This device is also used to generate biphasic impulses, as generally applied for clinical neurostimulators. A more detailed description of the measuring equipment and the measuring procedure can be found in [12].

B. Magnetic Field Measurement

Magnetic field recordings were performed with five different positions of the electrode in the head phantom, which differed in the distance to the origin of the cylindrical phantom (see Fig. 1a). The distance is defined by the variable a, which can be set between a = 20, 25, 30, 35 and 40 mm (see Fig. 1b). Since the electrode was adjusted to a fixed height (z = 152 mm), the values only changed in the x and y coordinates. For each measurement, the bipolar electrode configuration with the lower pair of active contacts and the same stimulation signal with an amplitude of $A = 6.3$ V, a pulse width of $t_p = 240$ µs and a frequency of $f_s = 160$ Hz were used. The measurements took place at 32 measuring points with a radius of 89.6 mm, eight points each at one of four measuring heights (88, 152, 216 and 280 mm) to guarantee a symmetrical measuring system (see Fig. 1a). The motivation was that at least one pair of measuring points

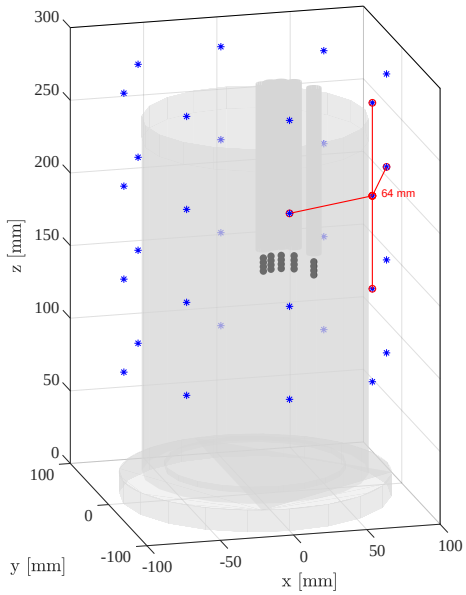

(a)

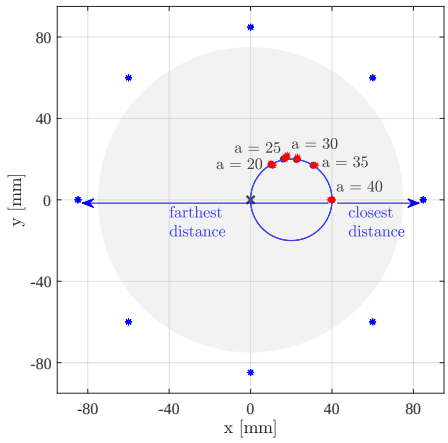

(b)

Fig. 1. (a) The cylindrical head phantom surrounded by 32 measuring points (blue asterisk markers) in a symmetrical measuring system is shown. The distance between two neighboring measuring points is 64 mm. Five different positions of the DBS electrode in the phantom can be seen. The four circles on top of each other (in dark grey) represent the four contacts of the electrode, whereby only the lower two contacts are used. (b) The top view of the cylinder with the radius of 75 mm (gray circular area) is shown. The electrode can be rotated along the inner circle (blue). The DBS electrode was placed at a = 20, 25, 30, 35, and 40 mm with the corresponding xy coordinates. The values describe the distance to the origin (gray cross), so that a = 40 mm represents the position closest to the cylinder surface and a = 20 mm the deepest position in the phantom. The blue asterisk markers indicate the positions of the measuring points. The blue arrows indicate the closest (∼50 mm) and farthest (∼130 mm) measuring point to the exemplary position a = 40 mm. The red asterisk markers represent the results of electrode localization described in section III.

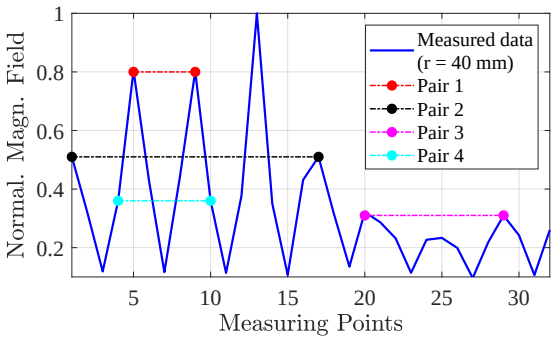

Fig. 2. The measured and normalized magnitudes of the magnetic field at all 32 measuring points are shown. The electrode was located at a = 40 mm. The highest magnetic field was measured at point 13, that represents the closest position to the electrode. Due to the symmetrical measuring system, same magnetic fields are measured at the corresponding points of each presented pair. For reasons of clarity, only four measurement pairs were shown (pair 2-4).

was located at the same distance from the electrode, so that the same magnitude of the magnetic field must be present at these points. In this way, the measuring accuracy of the sensor could be investigated in a simple way. The magnetic field at each position was measured for 10 seconds in all three orthogonal directions with the fluxgate sensor to calculate the magnitude of the magnetic field. Each 10 seconds recording was divided into small stimulation periods with a length of $T_s = 1/f_s = 6.25$ ms in the case of 160 Hz stimulation frequency, and averaged. Thus, the total measured signal power by the sensor is considered and by averaging the signal-to-noise ratio (SNR) is also improved by $\sqrt{n}$ with a total of $n = 1{,}600$ averages [14]. The averaged signal, i.e. an averaged single DBS period, represents the best condition for considering its maximum value as it represents the value with the highest SNR. The calculation of the magnitude by the corresponding three maximum values at each measuring point results in a total of 32 values representing the measured magnetic field distribution for the performed measurement. A measurement example for the electrode position a = 40 mm is given in Fig. 2. Measuring point 13 represents the sensor position with the closest distance to the electrode, at which the maximum field was measured. The points 5 and 9 (pair 1 in red) and the corresponding points for the other exemplary pairs are equidistant due to the symmetrical measuring system. The same magnetic fields were measured at these points, which differ slightly with the measuring accuracy of the magnetic sensor that was used (0.5% according to the data sheet).

The processing step that was applied in our previous work was to analyze a certain DBS frequency from the measured signal ignoring the rest of the signal. Therefore, each measured time signal was transformed into the frequency domain and the amplitude value from the amplitude spectrum e.g. at the correspondingly adjusted fundamental frequency was taken. This drastically worsened the SNR, but we have shown in practice that even a sensor with a narrow bandwidth (e.g. magneto-electric sensors) could be used for electrode localization. Since one frequency component contains only about 3% of the whole

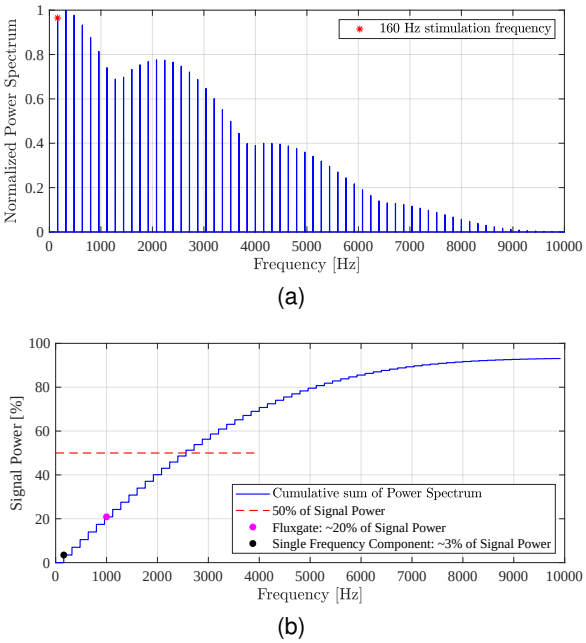

Fig. 3. (a) The normalized power spectrum of a measured DBS signal with a stimulation frequency of $f_s = 160$ Hz is shown. The adjusted repetition frequency and its harmonics can be seen clearly. (b) A curve with the cumulative sum of the power spectrum is shown. The fluxgate sensor that operates between 1 Hz and 1 kHz measures ∼20% of the signal power, whereas a single frequency component contains ∼3% of the power.

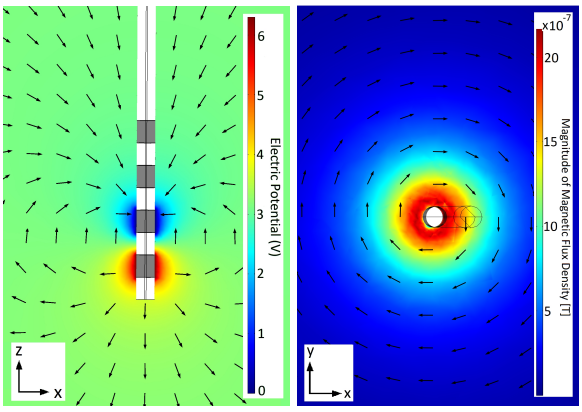

Fig. 4. (a) The colored background represents the electrical potential between 0 and 6.3 V. The lowest contact of the electrode is modelled as the cathode and the contact above it as the anode. The normalized arrows describe the current flow. (b) The spherical decay of the magnitude of the magnetic flux density based on the electrical result is shown with the colored background. The alignment of the magnetic field lines is represented by the arrows.

DBS signal power (see Fig. 3), the desired magnetic values become more robust when there is an increase in frequency components considered. However, it is usually limited by the operation bandwidth of the used magnetic sensor, that is 1 kHz for the fluxgate sensor in this case.

C. Forward and Inverse Problem

The electromagnetic simulations were based on a head model that was created within COMSOL Multiphysics with the exact sizes of the cylindrical head phantom and DBS electrode. The materials for each phantom and electrode structure were taken directly from the built-in material library and a uniform electrical conductivity σ, relative permeability μ_r, and relative permittivity ϵ_r for each structure were given. The cylinder body and the outer jacket of the Medtronic electrode were modeled with acrylic plastic ($\sigma \approx 0$ S/m, $\mu_r = 1$, $\epsilon_r = 4.2$), the four independent annular contacts with platinum-iridium ($\sigma = 10^6$ S/m, $\mu_r = 1$, $\epsilon_r = 1$), and the content of the phantom with saline solution ($\sigma = 1.6$ S/m, $\mu_r = 1$, $\epsilon_r = 80$). The values were taken from the literature. The phantom, including the electrode, is placed inside an overall cylindrical geometry with a radius of 89.6 mm and a height of 300 mm. This geometry was created so that the real measuring points are distributed on the surface of the entire geometry. The utilized mesh consists of extra fine tetrahedral elements. A bipolar electrode configuration with the two lower contacts of the electrode was considered, one modeled as cathode and the other as anode. For this, the terminal boundary condition of voltage type was used with a value of 6.3 V for the cathode and the ground boundary condition for the anode. Three-dimensional (3D) finite-element method (FEM) electromagnetic simulations were then performed using the Magnetic and Electric Fields (mef) interface of the AC/DC module and the magnetic flux densities outside the phantom on the surface of the entire cylindrical geometry (radius of 89.6 mm) were calculated where the measuring points were located. The free space between the phantom and the sensor points was modeled as air ($\sigma \approx 0$ S/m, $\mu_r = 1$, $\epsilon_r = 1$). Fig. 4 shows the electromagnetic result within the phantom for an arbitrary electrode position. The arrows on the left side show the current flow between the activated contacts of the electrode (xz-plane) and on the right side the alignment of the magnetic field according to the right-hand rule (xy-plane). In order to shorten the computation time for the simulations, the electrode was successively moved in all Cartesian coordinates in the region of interest (ROI) between $x \in \{0, 50\}$, $y \in \{-10, 30\}$, and $z \in \{150, 160\}$ with a step size of 1 mm and the simulated magnetic fields B_{model} were saved. The result of the electromagnetic simulation with the normalized magnitude of the magnetic flux density for the electrode position $a = 35$ mm can be seen in Fig. 5. The changes of the model (e.g. the displacement of the electrode) and the subsequent analysis (e.g. postprocessing and electrode localization) are carried out with MATLAB. The physical center of both activated electrode contacts is assumed to be the source and represented by n.

Since there is only one active source in the experiment and it does not move and rotate, the dipole fitting approach is best suited for searching for a source n_{dipole} that best explains the measured data B_{meas}. For each of the simulated electrode positions n, the normalized root mean square error (NRMSE) was calculated as follows to represent the cost function of the

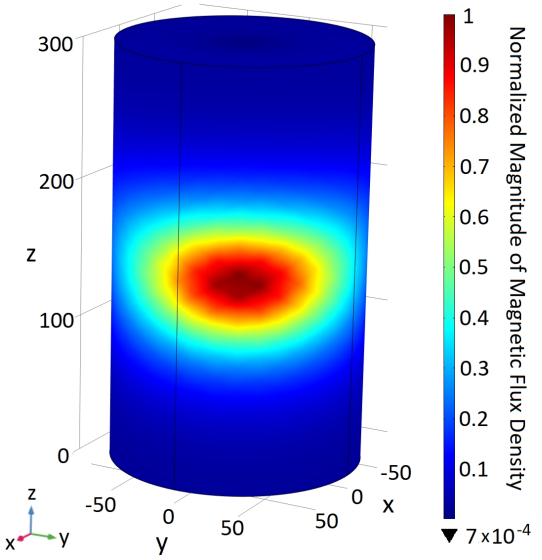

Fig. 5. The magnetic field distribution at the cylindrical geometry surface (radius of 89.6 mm and height of 300 mm) with the normalized magnitude of the magnetic flux density is shown. That is the result of the 3D FEM electromagnetic simulation for the exemplary electrode position a = 35 mm. The real measuring points (see again Fig. 1) are also distributed at 32 well-known positions on the same surface. The modeled and measured data are used for electrode localization, where a concentrated spatial field distribution as shown in this figure is required.

dipole-fit algorithm:

$$e(n) = \frac{1}{\mathrm{N_s}} \sum_{i=1}^{\mathrm{N_s}} \left(\frac{|B_{\mathrm{meas,i}}|}{\max\left[|B_{\mathrm{meas,i}}|\right]} - \frac{|B_{\mathrm{model,i}}|(n)}{\max\left[|B_{\mathrm{model,i}}|(n)\right]} \right)^2, \tag{1}$$

where $\mathrm{N_s}$ represents the total number of given measuring points, $|B_{\mathrm{meas}}|$ the measured magnitude of the magnetic flux density and $|B_{\mathrm{model}}|$ the modeled magnitude values. The minimum value of this cost function

$$\min\Big[e(n)\Big] = e(n_{\mathrm{dipole}}) \tag{2}$$

represents the smallest error and the corresponding voxel n_{dipole} is the found source and the result of the localization algorithm. Thus, the calculated magnetic flux densities at the given measuring points for this voxel best explain the measured magnetic flux densities with the NRMSE $e(n_{\mathrm{dipole}})$.

III. Localization Results

In order to validate the magnetic localization accuracy, the same measurement was performed five times at each considered electrode position at a = 20, 25, 30, 35, and 40 mm ending up with a total of 25 measurements. The total measurement time for each recording took about 30 minutes, including the movement of the head scanner, the rotation of the sensor, the storage process of the measured data, and the break of one second before each recording to remove vibration artifacts in the system. The real Cartesian coordinates of those electrode locations in the phantom head and the calculated Cartesian coordinates from the measured magnetic data can be seen in Table I. The localization results, i.e. the xy coordinates of the localized sources, are inserted in Fig. 1b as red asterisk markers. The following two contents can be taken from the table and figure. First, the localization accuracy, which is represented by the calculated Euclidean distances (error) between the real and calculated position, neither increases nor decreases the closer the electrode is placed to the surface of the model. The mean Euclidean distance is even less than 1 mm between the real source and the calculated source for almost all electrode positions. This can be justified by the fact that, on the one hand, the head volume conduction model reflects the cylindrical phantom model and that the measuring time of 10 seconds for each recording was sufficient for the sensitivity of the fluxgate sensor. If the measuring time is chosen too short, the magnetic fields generated by deeper sources (e.g. a = 20 mm) will be noisy much earlier than by sources located near the surface (e.g. a = 40 mm) due to the rapid drop in the magnetic field. However, this is also depending on the sensor characteristics (bandwidth, sensitivity) of the magnetometer. Secondly, there are also small differences in the localization results for the associated five measurements. The slight deviations for these electrode positions can be explained with the tolerance range of the measuring accuracy of the fluxgate sensor. According to the data sheet, the sensor has an accuracy of 0.5%, which is further reduced by the sum over all 32 measuring points in Eq. 1. Thus, the sum increases the measuring inaccuracy, which then leads to slight electrode localization displacements that already occur at $e(n) \approx 1\%$.

IV. Discussion

The localization of the deep brain stimulation electrode with magnetic field measurements adds a new possibility to conventional methods with neuroimaging approaches and, has in addition, the following advantages during and after DBS surgery. The duration of surgery is increased significantly due to MRI or CT acquisition; this is due to the patient being put under general anesthesia for DBS targeting. It is not yet possible to locate the target brain structure in real time with neuroimaging and microelectrode recordings (MER) and is therefore still in research [15]. The approach described in this paper has the potential to realize non-invasive technology for guiding such a DBS surgery with quick installation, high safety, easy usability and low cost if portable magnetic sensor arrays are developed. The post-operative localization of the electrode is used for an optimal treatment of the DBS patient based on optimal adjustment of the stimulation parameters for the DBS pulse. In this paper, we have shown at least with a simplified head phantom that it is possible to localize the electrode by measuring the typically generated DBS artifact caused by the DBS pulse. The magnetic fields for the bipolar electrode configuration are in the pT range and mainly superimpose the fields that are generated by brain activity (fT range). Nevertheless, it has to be used with very weak magnetic fields.

We have achieved a mean localization error of less than 1 mm for almost all electrode locations ($a = 40, 35, 30$, and 20 mm), regardless of how deep the electrode was placed in

TABLE I

LOCALIZATION RESULTS OF EACH PERFORMED MEASUREMENT REPRESENTED WITH THE EUCLIDEAN DISTANCES BETWEEN THE REAL ELECTRODE POSITION AND THE CALCULATED POSITION FROM THE MEASURED DATA (THE MEAN VALUE IN THE LAST ROW). THE OTHER ENTRIES DESCRIBE THE CARTESIAN COORDINATES OF THE REAL AND CALCULATED ELECTRODE POSITION.

Electrode position [mm]	a = 40	a = 35	a = 30	a = 25	a = 20
Real Cartesian coordinates $[x_1, y_1, z_1]$ in the phantom head in mm	[40, 0, 152]	[31, 17, 152]	[23, 20, 152]	[16, 20, 152]	[10, 17, 152]
Calculated Cartesian coordinates $[x_2, y_2, z_2]$ from the measured data in mm of the ...					
... first measurement	[39, 0, 151]	[32, 17, 151]	[23, 20, 151]	[17, 21, 152]	[11, 17, 152]
... second measurement	[40, 0, 151]	[31, 17, 152]	[23, 20, 152]	[18, 22, 152]	[10, 17, 151]
... third measurement	[40, 0, 152]	[31, 17, 151]	[23, 20, 150]	[18, 21, 152]	[10, 18, 152]
... fourth measurement	[40, 0, 152]	[31, 17, 152]	[23, 21, 151]	[17, 21, 151]	[11, 17, 152]
... fifth measurement	[40, 0, 151]	[31, 17, 151]	[23, 20, 152]	[17, 20, 152]	[10, 17, 152]
Mean Euclidean distance between real and calculated position [mm]	0.68	0.68	0.88	1.13	0.8

the phantom and an error about 0.8 mm over all 25 performed measurements. The results were achieved by the following measurement and simulation procedure that will be further discussed:

- Using the fluxgate magnetometer for three dimensional magnetic field measurements.
- Measuring at 32 sensor points with symmetrical sensor distribution with 10 seconds recording each direction.
- Calculating the magnitude of the magnetic flux density at each measuring point.
- Creating a proper FEM volume conduction model of the phantom based on its well-known dimensions.
- Solving the forward problem by doing a FEM based electromagnetic simulation.
- Using the dipole fitting approach to localize the DBS electrode with a cost function defined as the normalized root mean square error.

Each of these listed points has more or less a direct influence and impact on the achieved localization results. The system noise level in the magnetically shielded chamber was given by the noise level of the used magnetic fluxgate sensor. Its sensitivity ($20\ \mathrm{pT}/\sqrt{\mathrm{Hz}}$) and bandwidth (from 0 to 1 kHz) were sufficient for the detection of the magnetic field generated by the used stimulation settings. Similar localization results can be achieved by using a sensor with a lower bandwidth but higher sensitivity or even lower sensitivity over a higher bandwidth, e.g. magnetoelectric (ME) or surface acoustic wave based magnetic sensors, which are being developed within the framework of the Collaborative Research Centre CRC 1261. The signal power is distributed over a large frequency bandwidth (see Fig. 3). Other advantages of the sensor are the low acquisition costs especially if several sensors are to be combined into a sensor array and low operation costs for performing routine measurements compared e.g. to conventional MEG systems with SQUID sensors, which include their operation at cryogenic temperatures. Furthermore, the fluxgate sensor is a compact and robust sensor that can be easily integrated into our measuring system, which rotates the sensor in all three spatial directions. This means, that all three components of the magnetic field can be measured and the system is not blind to a particular direction.

The number of measuring points was chosen so that it can also be used for measurements with real DBS patients. Each performed measurement took about 30 minutes, that is still acceptable to the patient. In the simplified system containing one dipole source in the model, the magnetic values from 32 measuring points were sufficient for the dipole localization accuracy. Nevertheless, increasing the number of measuring points will increase the spatial resolution of the measured magnetic field distribution ending up with a more robust localization. Increasing the recording time at each measuring point allows longer averaging and thus to an even more robust signal period, from which the maximum amplitude can be taken. For a 10 second recording, an average of 1,600 DBS periods results, since a repetition rate of 160 Hz has been set. Thus, the well-known driving waveform of the signal allows a drastic improvement of the SNR.

The angle at implantation of the DBS electrode during surgery is also unknown, which was assumed to be vertical along the z-axis in our model due to a-priori knowledge. This will lead to a variable orientation of the magnetic field in reality. Accordingly, not only a variable position of the electrode, but also a variable orientation of the electrode must be taken into account during modeling.

The volume conduction model determines how the source within the brain, that is the DBS electrode within the phantom in our case, is visible on the magnetic sensors. The model was created by using the well-known dimensions of the cylindrical head phantom ending up with an accurate description of the geometry of the phantom. It was not considered in our previous work based on the assumption that the normal tissue is nonmagnetic and the permeability is constant across the tissues of the head and free space. Nevertheless, the law of Biot-Savart states that all currents in the model contribute to the external magnetic field, so this model therefore considers in addition the volume (ohmic) currents produced by the same source. Fig. 6 shows the comparison between both models along the horizontal and vertical lines. Even though the assumption of an infinite homogeneous model represents a good approximation, the model shows inaccuracies outside the phantom. The further the measuring point is located from the phantom, the greater is the inaccuracy. For example, an average localization accuracy of more than 2 mm was achieved for the electrode position a = 20 with the same magnetic

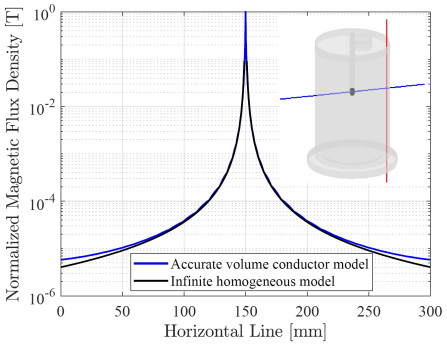

(a)

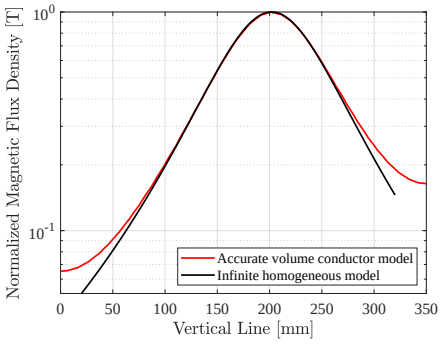

(b)

Fig. 6. (a) Simulated normalized magnetic flux density over the horizontal line (blue line) by assuming infinite homogeneous model (black curve) and by using an accurate volume conductor model (blue curve). (b) Simulated values over the vertical line (red line) for the same models.

measurements, although this will not be discussed in detail here. Electromagnetic simulations were performed to solve the Maxwell's equations and simulate the external magnetic field at the sensor level.

The dipole fitting algorithm is best suited for this kind of localization challenge where only a single dipole is searched for. The NRMSE was used as a cost function, that is frequently used to compare estimated and measured data. Also, other cost functions like correlation coefficients (CC) and different localization algorithms can be considered, whereby the comparison of different cost functions and source reconstruction algorithms were not the main part of this work.

Conclusion

We presented a new method for non-invasive and non-radiative localization of the deep brain stimulation electrode by means of three dimensional magnetic field measurements that were performed using a simplified cylindrical phantom head with an integrated DBS electrode. The magnetic field distribution around the phantom was measured with the fluxgate magnetometer and calculated by using finite element method electromagnetic simulations. The dipole fitting approach is then used to minimize the NRMSE between the measured and calculated values. Our findings showed that the electrode was localized with an average accuracy of less than 1 mm over all performed measurements. The performance of the localization method was not limited by an incorrect model assumption or the presence of noise. Only the measuring accuracy of the used magnetic sensor caused slight deviations in the localization results. Thus, this paper motivates and represents the main step toward a measurement with real DBS patients by using the same measurement and simulation procedure.

Acknowledgment

This work was supported by the German Research Foundation (Deutsche Forschungsgemeinschaft, DFG) through the project B5 of the Collaborative Research Centre CRC 1261 *Magnetoelectric Sensors: From Composite Materials to Biomagnetic Diagnostics*.

References

[1] S. Hemm and K. Wårdell, "Stereotactic implantation of deep brain stimulation electrodes: A review of technical systems, methods and emerging tools," *Medical and Biological Engineering and Computing*, vol. 48, no. 7, pp. 611–624, 2010.

[2] A. Sarem-Aslani and K. Mullett, "Industrial Perspective on Deep Brain Stimulation: History, Current State, and Future Developments," *Frontiers in integrative neuroscience*, vol. 5, p. 46, 09 2011.

[3] L. R. Sankery, P. J. Ford, A. G. Machado, L. J. Hoeksema, R. V. Samala, and D. J. Harris, "Deep Brain Stimulation at End of Life: Clinical and Ethical Considerations," *Palliative Medicine*, 08 2019.

[4] A. M. Lozano, N. Lipsman, H. Bergman, P. Brown, S. Chabardes, J. W. Chang, K. Matthews, C. C. McIntyre, T. E. Schlaepfer, M. Schulder, Y. Temel, J. Volkmann, and J. K. Krauss, "Deep brain stimulation: current challenges and future directions," *Nat Rev Neurol*, vol. 15, pp. 148–160, 03 2019.

[5] C. J. Hartmann, S. Fliegen, S. J. Groiss, L. Wojtecki, and A. Schnitzler, "An update on best practice of deep brain stimulation in Parkinson's disease," *Ther Adv Neurol Disord.*, 03 2019.

[6] C. Pollo, J.-G. Villemure, F. Vingerhoets, J. Ghika, P. Maeder, and R. Meuli, "Magnetic resonance artifact induced by the electrode activa 3389: an in vitro and in vivo study," *Acta Neurochirurgica*, vol. 146, no. 2, pp. 161–164, Feb 2004.

[7] J. R. Ellenbogen, R. Tuura, and K. Ashkan, "Localisation of DBS Electrodes Post-Implantation, to CT or MRI? Which Is the Best Option?" *Stereotact Funct Neurosurg*, vol. 96, pp. 347–348, 2018.

[8] L. Ispierto, J. Muñoz, J. Cladellas, P. Cuadras, J. Capellades, P. Latorre, A. Dávalos, T. Vancamp, and R. Alvarez, "Post-Operative Localization of Deep Brain Stimulation Electrodes in the Subthalamus Using Transcranial Sonography: DBS ELECTRODE LOCALIZATION USING TCS," *Neuromodulation*, vol. 21, pp. 574–581, 08 2018.

[9] J. Engelhardt, D. Guehl, N. Damon-Perrière, O. Branchard, P. Burbaud, and E. Cuny, "Localization of Deep Brain Stimulation Electrode by Image Registration Is Software Dependent: A Comparative Study between Four Widely Used Software Programs," *Stereotact Funct Neurosurg*, vol. 96, pp. 364–369, 2018.

[10] M. I. Iacono, S. R. Atefi, L. Mainardi, H. C. Walker, L. M. Angelone, and G. Bonmassar, "A Study on the Feasibility of the Deep Brain Stimulation (DBS) Electrode Localization Based on Scalp Electric Potential Recordings," *Frontiers in Physiology*, vol. 9, p. 1788, 2019.

[11] K. G. Mideksa, A. Singh, N. Hoogenboom, H. Hellriegel, H. Krause, A. Schnitzler, G. Deuschl, J. Raethjen, G. Schmidt, and M. Muthuraman, "Comparison of imaging modalities and source-localization algorithms in locating the induced activity during deep brain stimulation of the STN," *38th Annual International Conference of the IEEE Engineering in Medicine and Biology Society (EMBC)*, pp. 105–108, Aug 2016.

[12] M. Yalaz, A. Teplyuk, M. Muthuraman, G. Deuschl, and M. Höft, "The Magnetic Properties of Electrical Pulses delivered by Deep Brain Stimulation Systems," *IEEE Transactions on Instrumentation and Measurement*, pp. 1–1, 2019.

[13] M. S. Hämäläinen, "Functional localization based on measurements with a whole-head magnetometer system," *Brain Topography*, vol. 7, no. 4, pp. 283–289, Jun 1995. [Online]. Available: https://doi.org/10.1007/BF01195254

[14] W. van Drongelen, "Chapter 4 - signal averaging," in *Signal Processing for Neuroscientists (Second Edition)*, second edition ed., W. van Drongelen, Ed. Academic Press, 2018, pp. 59 – 80. [Online]. Available: http://www.sciencedirect.com/science/article/pii/B9780128104828000047

[15] A. Tepper, M. C. Heinrich, L. Schiaffino, A. R. Munoz, A. Gutierrez, and J. G. Martinez, "Selection of the Optimal Algorithm for Real-Time Estimation of Beta Band Power during DBS Surgeries in Patients with Parkinson's Disease," *Computational Intelligence and Neuroscience*, vol. 2017, 2017.

Key Findings and Scientific Implications

- The DBS signal consists of strong spectral peaks at the stimulation frequency and at its harmonics, such that a single frequency component represents only an estimated 3% of the total DBS signal power, while components up to 1 kHz and 10 kHz correspond to approximately 20% and more than 90% of the signal power, respectively.
- The underlying source model used to estimate expected magnetic fields at the measurement surface (forward problem) is crucial for the accuracy of electrode localization.
- The electric current dipole model, which is valid for an infinite homogeneous space, neglecting the modeling of the volume conduction, should be replaced by a precise electromagnetic finite element model to improve detection accuracy.
- The approach of fitting measured and the modeled data using the normalized root mean square error as a cost function are most appropriate for electrode localization (inverse problem).
- The electrode can be localized with an average accuracy of less than 1 mm regardless of the depth of the electrode in the phantom.

3.3 DBS Electrode Localization and Rotational Orientation Detection Using SQUID-Based Magnetoencephalography

M. Yalaz, M. S. Noor, C. C. McIntyre, M. Butz, A. Schnitzler, G. Deuschl, and M. Höft, "DBS electrode localization and rotational orientation detection using SQUID-based magnetoencephalography," in *Journal of Neural Engineering*, vol. 18, no. 2, p. 026021, March 2021, doi: 10.1088/1741-2552/abe099.

Information about the amount of own contribution to this publication:

Conceptualization	Planning	Implementation	Manuscript preparation
high	high	high	high

© 2021 IOP Publishing Ltd. Reproduced with permission. All rights reserved. This is the Accepted Manuscript version of an article accepted for publication in Journal of Neural Engineering. IOP Publishing Ltd is not responsible for any errors or omissions in this version of the manuscript or any version derived from it. The version of record is available online at https://doi.org/10.1088/1741-2552/abe099.

JOURNAL OF NEURAL ENGINEERING, ACCEPTED VERSION OF THE ARTICLE 1 of 22

IOP Publishing

DBS Electrode Localization and Rotational Orientation Detection using SQUID-based Magnetoencephalography

Mevlüt Yalaz[1], M. Sohail Noor[2], Cameron C. McIntyre[2], Markus Butz[3], Alfons Schnitzler[3], Günther Deuschl[4], and Michael Höft[1]

[1] Chair of Microwave Engineering, Christian-Albrechts-Universität zu Kiel, 24143 Kiel, Germany
[2] Department of Biomedical Engineering, Case Western Reserve University, Cleveland, OH, United States
[3] Institute of Clinical Neuroscience and Medical Psychology, Heinrich-Heine-Universität Düsseldorf, 40225 Düsseldorf, Germany
[4] Department of Neurology, Christian-Albrechts-Universität zu Kiel, 24105 Kiel, Germany

Abstract. The aim of the present study was to investigate the accuracy of localization and rotational orientation detection of a directional deep brain stimulation (DBS) electrode using a state-of-the-art magnetoencephalography (MEG) scanner. A directional DBS electrode along with its stimulator was integrated into a head phantom and placed inside the MEG sensor array. The electrode was comprised of six directional and two omnidirectional contacts. Measurements were performed while stimulating with different contacts and parameters in the phantom. Finite element modeling and fitting approach were used to compute electrode position and orientation. The electrode was localized with a mean accuracy of 2.2 mm while orientation was determined with a mean accuracy of 11°. The limitation in detection accuracy was due to the lower measurement precision of the MEG system. Considering an ideal measurement condition, these values represent the lower bound of accuracy that can be achieved in patients. However, a future magnetic measuring system with higher precision will potentially detect location and orientation of a DBS electrode with an even greater accuracy.

Keywords: Deep brain stimulation, MEG, SQUID, directional DBS electrode, magnetic field measurement, electrode localization, rotational orientation detection.

1. Introduction

Deep brain stimulation (DBS) is a surgical procedure used for the treatment of a variety of movement disorders such as Parkinson's disease, essential tremor, and dystonia [1] and is being studied for use in many other neurological conditions. Currently, more than 200,000 patients have been implanted with a DBS system worldwide. The surgery involves implanting a stimulating electrode (comprising of a linear array of stimulating contacts) into a specific target region of the patient's brain, which is connected to a

battery-powered neurostimulator implanted in the chest near the collarbone. Recently, new DBS electrode designs have become available with segmented contacts (split into three segments along the circumference of the electrode) which allows steering of the electric fields in a desired direction [2, 3, 4]. First studies indicate improved therapeutic effects and lower side-effect thresholds compared to electrodes with standard ring contacts. However, the long-term clinical benefits of directional electrodes need to be investigated further. To use the full potential of this technology, correct localization and rotational orientation of the electrode in the anatomical brain structures must be determined for interpreting the observed stimulation effects and to inform and guide programming.

To date, no generally accepted protocol for electrode localization has been established. Current approaches for electrode localization are based on the fusion of pre- and postoperative neuroimaging data, e.g. postoperative computed tomography (CT) with preoperative magnetic resonance imaging (MRI). All images are affected by metal artifacts, so for low-quality images the localization errors are increased. Furthermore, significant discrepancies were reported between electrode centers estimated by CT and MRI, and differences in localization results were observed between various widely used software programs [5, 6]. Moreover, CT also exposes patients to ionizing radiations and MRI cannot always be conducted due to safety concerns. Accordingly, electroencephalography (EEG) and magnetoencephalography (MEG) provide alternative imaging modalities to detect electrode position by measuring the stimulation induced DBS artifacts. Earlier studies have already demonstrated the feasibility of electrode localization with EEG recordings, whereby a maximum error of about 15 mm was reported [7]. The feasibility and potential of MEG recordings for DBS electrode localization has not yet been investigated to the best of our knowledge.

Similar to electrode localization, no established means are presently available for non-invasively reviewing the electrode orientation. Current methods to determine electrode orientation, e.g. with X-rays, standard CT, flat-panel CT, and rotational fluoroscopy [8, 9, 10], all rely on high-quality images, since artifact patterns must be calculated from these images based on the electrode's orientation marker. Although these approaches are considered to be precise enough for high-quality images, patients are dosed with ionizing radiation in all these methods. Additionally, the feasibility of determining electrode orientation beyond mere localization by alternative imaging modalities such as EEG or MEG has not yet been investigated.

The aim of this paper is to assess a non-radiative method to determine the location and rotational orientation of a DBS electrode in a phantom using a state-of-the-art MEG scanner, which consists of a number of highly sensitive Superconducting QUantum Interference Devices (SQUID). These sensors, with a noise spectral density of approximately 3 $\mathrm{fT}/\sqrt{\mathrm{Hz}}$, are best suited to measure the magnetic fields generated by DBS. The magnetic fields produced by DBS electrodes are in the pT range, while those generated by normal brain activity are in the fT range. This is why the later has a negligible effect on the field generated by the electrode and can be ignored.

First, we placed the electrode at predefined positions in the phantom, programmed the neurostimulator with electrode configuration settings specified in advance, placed the phantom within the MEG sensor array, and measured the magnetic field distribution. We then developed a precise electromagnetic Finite Element Model (FEM) to compute the magnetic fields produced at these positions with different electrode positions and orientations. A fitting approach was then used to find the model that minimized the error between simulated and measured data. The location and orientation of the electrode in the found model determined the result of position and orientation detection. In our previous works [11, 12], we have already investigated the characteristics of magnetic fields generated by a DBS electrode and have shown that an electrode can be localized with an average accuracy of less than 1 mm by measuring the magnetic field distribution around the phantom. However, we used a single fluxgate magnetometer (Fluxmaster, Stefan Mayer Instruments) for the recordings, generated a boosted DBS signal artificially over a multifunction data acquisition device (USB-6361, National Instruments), and used our in-house constructed measurement system. The fluxgate sensor had a noise level of 20 $\mathrm{pT}/\sqrt{\mathrm{Hz}}$ and an operating frequency bandwidth of 1 kHz.

The present work investigates the feasibility of localization and rotational orientation detection of a DBS electrode as implanted in clinical routine with a MEG scanner. This method may enable long-term studies to investigate any displacement and rotation of the electrode over time without exposing patients to radiation risk of CT or X-ray imaging. Electrode migration, i.e. an unintended postoperative displacement of the DBS electrode, on the one hand and, on the other hand, electrode rotation can be observed in clinical practice and poses a challenge [13, 14]. If the electrode continues to rotate after implantation, direct postoperative imaging may be inadequate to obtain the rotation for stimulation settings. The first clinical study [15] addressing this problem revealed large deviations from the intended implantation direction. Deviations of more than 30° occurred in 41% of cases and more than 60° in 11% of cases. Only postoperative CT imaging, which is part of the patient's routine clinical care, was used to avoid exposing the patient to radiation unnecessarily. Another clinical study indicated no change in direction within the first two weeks of implantation [16]. Here, in addition to postoperative CT imaging, only a single measurement was performed with rotational fluoroscopy due to the same reason. However, it is still of significant importance to establish whether directional electrodes continue to rotate and by how much. Our method could be carried out without hesitation in continuous intervals as often as desired without exposing patients to radiation at all.

2. Methods

2.1. Head Phantom

The cylindrical head phantom used in this study is depicted in Fig. 1a. It was slightly changed and adapted for this work compared to our earlier studies in [11] and

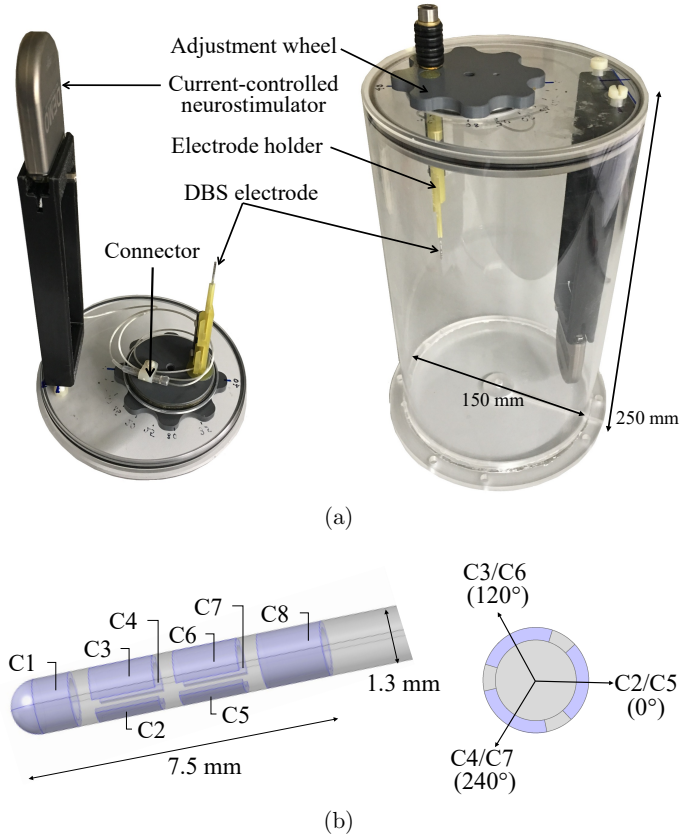

Figure 1. (a) Cylindrical phantom head with integrated current-controlled DBS neurostimulator (Vercise™ PC) and directional electrode (Vercise Cartesia™). The electrode is connected to the stimulator via the DBS connector and can be moved along a circle by rotating the adjustment wheel. (b) Modeled geometry of the directional DBS electrode. Contact C1 and C8 are full-ring contacts, and the others are contacts with equally spaced segments, each spanning 120˚ of the circumference.

[12]. The cylinder body with dimensions comparable with a human head (diameter of 150 mm, height of 250 mm) is made of acrylic glass and is, therefore, neither electrically conductive nor magnetic. It was filled with an isotonic fluid (NaCl 0.9%) to mimic the electric conductivity of a human brain. We used a DBS system by Boston Scientific consisting of a current-controlled DBS neurostimulator (Vercise™ PC) and a directional electrode (Versice Cartesia™) as used in the clinical routine. The DBS system was integrated and fixed into the phantom. The DBS electrode can be moved along a circle in the xy-plane by rotating the adjustment wheel and was placed at five different positions; each with a different distance 'a' to the phantom's origin (40, 30, 20, 10, 0 mm). a = 0 mm represents the deepest position at the origin of the phantom, whereas a = 40 mm represents the position nearest to the phantom surface (phantom radius is 75 mm). The vertical position of the electrode remained fixed

during these measurements. The electrode is connected to the neurostimulator via an extension wire and connector. In most previous works, the magnetic field around the DBS electrodes was severely contaminated by the presence of artifacts related to ferromagnetic extension wires. These wires were made of stainless steel and generated artifacts in the MEG signals [17, 18, 19]. We used non-ferromagnetic extension wires made of platinum-iridium to avoid such artifact [20]. Moreover, we used non-magnetic material for all other components used in the phantom. The screws on top of the electrode holder were made of titanium, while the adjustment wheel and the holders for the electrode and neurostimulator casing were made of plastic. Unintentionally, the ferrule under the titanium screw was made of ferromagnetic material and caused artifact at the corresponding sensor points. The structure of the directional DBS electrode is shown in Fig. 1b. It comprised eight individually controlled platinum-iridium contacts (C1-C8), in which the two middle contact levels were segmented into three contacts each spanning 120° of the circumference. Any combination of these contacts can be activated to steer the stimulation current direction. The outer jacket is made of polyurethane. The dimensions of the electrode are as follows: diameter of 1.3 mm, contact length of 1.5 mm, and a vertical spacing between adjacent contacts of 0.5 mm.

2.2. MEG Preparation

Before starting the actual MEG recording, several preparatory steps were performed. Four head position indicator (HPI) coils were attached to the surface of the head phantom and a round template with three landmarks (referred as nasion, right pre-auricular, and left pre-auricular) was fixed on the cylinder cap. Then, a point digitizer (Fastrak, Polhemus) was used to localize anatomical fiducial points (nasion, left and right pre-auricular) and HPI coils. Furthermore, 150 additional points around the phantom were localized to improve the accuracy of the spanned coordinate system of the phantom. Fig. 2a shows the phantom during the digitization process; the glasses represent the reference, and one of the two receivers used for digitization. The digitized locations of the anatomical landmarks in [x, y, z] directions are as follows:

- Nasion: [0, 74.9 mm, 0]
- Right pre-auricular: [74.7 mm, 0, 0]
- Left pre-auricular: [-75.1 mm, 0, 0]

The cap of the cylindrical phantom lied exactly on the xy-plane, the longitudinal axis of the cylinder on the z-axis, and the origin of the coordinate system was in the center of the cylinder's circular cap. The radius of the cylindrical phantom was 75 mm, and the digitization process was performed with an accuracy of ±0.3 mm (given by the error of right pre-auricular). The locations of HPI coils, landmarks, additional points, and the position and orientation of the electrode were all expressed in the phantom coordinate frame. The phantom placement in the MEG scanner can be seen in Fig. 2b. The MEG sensors were in the MEG coordinate system. Before each recording, MEG sensor

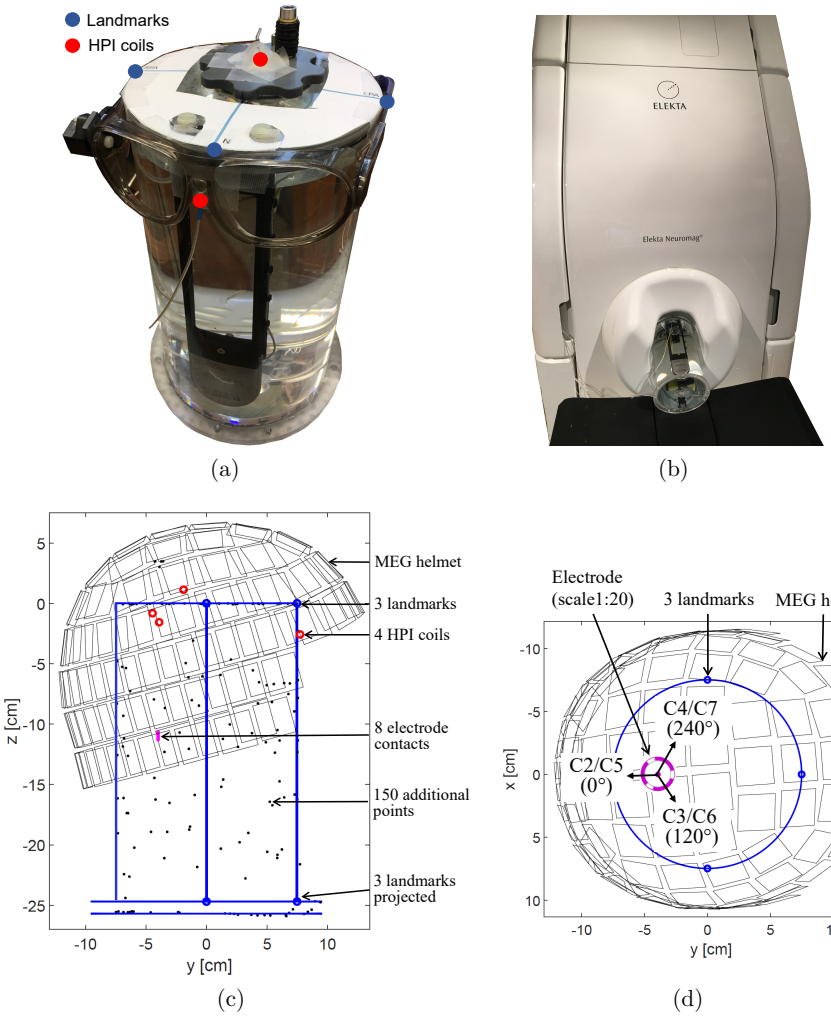

Figure 2. (a) Phantom during MEG preparation. Four head position indicator (HPI) coils are taped onto the phantom's surface to detect its position with respect to the MEG sensor array before recording (two HPI coils can be seen). Their positions, together with the anatomical fiducials (nasion, left and right pre-auricular points) and further additional points around the phantom surface are digitized by placing the tracker (located in the middle of both glasses) on the phantom's surface and by using the digitizer pen. (b) Phantom inside the MEG scanner. (c) Side view of the phantom in the MEG sensor array with all the digitized points. The blue circles represent the three anatomical landmarks, the red circles represent the four HPI coils, and the black dots show the additional points around the surface of the phantom. In addition, the position of the electrode (a = 40 mm) in the phantom is depicted as an example. (d) Top view of the phantom illustrating the orientation of each segmented electrode contact at electrode position a = 40 mm.

positions were automatically determined in phantom coordinates. The relationship between MEG and phantom coordinates was determined by applying current with a particular frequency to the HPI coils and determining their positions with respect to the MEG sensor array. This step was performed by the MEG system itself, which already had the positions of the HPI coils in phantom coordinates. Fig. 2c illustrates the positioning of the MEG helmet in the phantom coordinate system from side view and shows all digitized points. The coordinates of all five electrode positions were therefore known in advance, and only the position of the MEG sensor array with respect to the phantom was to be determined by the MEG system before the first measurement. Fig. 2d shows the top view of the phantom with respect to the MEG sensor array and illustrates the orientation of each segmented electrode contact (C2-C7) at electrode position $a = 40$ mm.

2.3. Data Acquisition

The electrical stimulation comprised of biphasic rectangular pulses with a stimulus pulse phase and a passive charge-balancing phase. The parameters of stimulation used are mentioned in Table 1. MEG data was collected with an Elekta Neuromag VectorView® MEG scanner at the Universitätsklinikum Düsseldorf (UKD) in Düsseldorf. The scanner comprises of 306 individual channels, corresponding to 102 magnetometers and 204 gradiometers. It can be noted that only the magnetometer data was used in this study. The noise level according to the datasheet is about 3 $\mathrm{fT}/\sqrt{\mathrm{Hz}}$ for both magnetometers and gradiometers. The acquisition parameters of the MEG scanner were set as follows: The sampling rate was set to its maximum of 5 kHz. The low-pass filter was set to the highest possible value of 1660 Hz and the cut-off frequency of the high-pass filter was set to direct current (no high-pass filtering) in order to obtain measurements of the DBS signal with the maximum allowed acquisition bandwidth. The duration of each measurement was three minutes. A total of 38 measurements with bipolar electrode configurations were taken (see Table 1), with different activated electrode contacts (1-8: contact numbers, first number: anode, second number: cathode), stimulation parameters (amplitude, pulse width, frequency), and electrode positions within the phantom. Before each recording of the first 29 measurements, the phantom was removed from the MEG scanner, the position of the electrode was changed by rotating the adjustment wheel and the phantom was placed back again. It was not possible to place the phantom at the exact same position in the MEG every time, so the estimation of the phantom position in the scanner had to be performed each time by the MEG system, as described in detail in the previous section. A direct comparison between the localization and rotational orientation results across these 29 measurements can therefore not be drawn. However, in the 30th measurement, the electrode position was set once to $a = 40$ mm and was not changed until the end. Here, the obtained results could be compared with each other.

For the sake of clarity, the table is divided into five groups. In the first group,

Table 1. Performed MEG measurements (1-8: activated contacts).

Group	Num.	Bipolar configuration	Ampl. [mA]	Pulse [μs]	Freq. [Hz]	Position [mm]
1	1-5	1 vs 234	11.9	100	170	40,30,20,10,0
2	6-10	1 vs 234	11	60	130	40,30,20,10,0
	11-15	234 vs 567	11	60	130	40,30,20,10,0
	16-20	567 vs 8	11	60	130	40,30,20,10,0
3	21-23	1 vs 2	11	60	130	40,30,20
	24-26	1 vs 3	11	60	130	40,30,20
	27-29	1 vs 4	11	60	130	40,30,20
4	30	1 vs 2	11	60	130	40
	31	1 vs 3	11	60	130	40
	32	1 vs 4	11	60	130	40
5	33	1 vs 234	3	60	130	40
	34	234 vs 567	3	60	130	40
	35	567 vs 8	3	60	130	40
	36	1 vs 234	1.5	60	130	40
	37	234 vs 567	1.5	60	130	40
	38	567 vs 8	1.5	60	130	40

the bipolar electrode configuration with the maximum possible stimulation parameters was set. In the second group, measurements were performed with the activation of contacts at different electrode heights and positions. The third and fourth group provide directional stimulation with the activation of the tip of the electrode (contact C1) against an individual segmented contact (C2-C4). Notice that the phantom was not moved during the measurements in the fourth group and afterwards. In the fifth group, the stimulation amplitude was reduced to a value as used in clinical routine, i.e. 3 or 1.5 mA. The good quality of recorded data was ensured by an empty room measurement prior to the start of the experiment and by visual inspection of about 1 min of MEG recording before each measurement. Electrode localization was performed for measurements with non-directional stimulation (groups 1, 2, and 5), and rotational orientation detection was performed for measurements with directional stimulation (groups 3 and 4).

2.4. Signal Processing

The processing steps of the MEG measurements are depicted in Fig. 3. For each measurement, we obtained 102 time signals, one from each MEG sensor. The measured data was imported into MATLAB® (Version R2018a) and preprocessed using the FieldTrip toolbox [21]. Each time signal was 180 s long and high-pass filtered (6th order Butterworth) with a cutoff frequency of 60 Hz without signal loss since the signal contains higher frequencies (stimulation frequency f_0 and its harmonics) as shown in

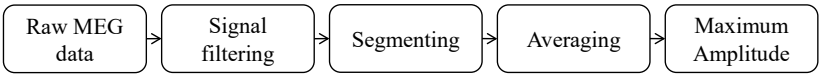

Figure 3. Each measured MEG signal is high-pass filtered with 60 Hz cutoff frequency, segmented, and averaged to a single period with $N = 180\ \mathrm{s} \cdot f_0$ averages. Then, the maximum amplitude value is taken.

Table 1. Each signal was divided into short segments of length equal to the inverse of stimulation frequency, e.g. for 170 Hz stimulation $\mathrm{T}_s = 1/f_s = 5.88$ ms (first five measurements in Table 1) and $\mathrm{T}_s = 7,69$ ms for 130 Hz of stimulation (remaining measurements in Table 1). These segments were then averaged which improved the signal-to-noise ratio (SNR) by $\sqrt{N}$, where $N = 180\ \mathrm{s} \cdot f_0$. The maximum value from this averaged time segment is then taken for each MEG sensor, resulting in a total of 102 values representing the maximum magnetic field $\mathrm{B}_{\mathrm{meas,i}}$ measured by each sensor at location i. Since these were phantom measurements, the measured MEG signals were not contaminated by biological artifacts such as cardiac muscle, skeletal muscles, or eye movements. Thus, the measurements with a phantom represent an ideal case. The ambient noise solely consisted of the power line interference, which only affected non-important frequencies (50 Hz and harmonics). The only magnetic noise in our MEG recordings arose from a non-biological source, i.e. from the ferromagnetic ferrule, which was placed under the screw, that over time became magnetized and generated an artificial magnetic field. This artifact was modeled in the electromagnetic simulations using the known position and dimensions of the ferrule and was subtracted from the measured data. The results are given in Section 3.2.

2.5. Localization and rotational orientation determination

Finite element modeling (FEM) and model-fitting approach were used to determine location and rotational orientation of the DBS electrode in the phantom. Using FEM, the magnetic field was calculated at measurement points i with different electrode positions p and rotations r. The values calculated by the model are represented by $\mathrm{B}_{\mathrm{model},i}(p, r)$. That is, a single model with a given electrode position p_1 and electrode rotation r_1 resulted in 102 modeled values corresponding to a total of 102 measurement points. Modeled data with different electrode positions was used for electrode localization that was performed for measurements with non-directional stimulation (groups 1, 2, and 5 in Table 1). The corresponding contacts of the electrode were activated in the model resulting in a symmetrical flow of current along the length of the electrode. Modeled data with different electrode rotations was used to perform orientation detection using measurements with directional stimulation (groups 3 and 4 in Table 1). The bottom contact C1 (the tip) of the electrode was activated against one of the segmented contacts C2, C3, or C4. This led to a current flow that was steered in a direction compared to the non-directional stimulation. The model is described in

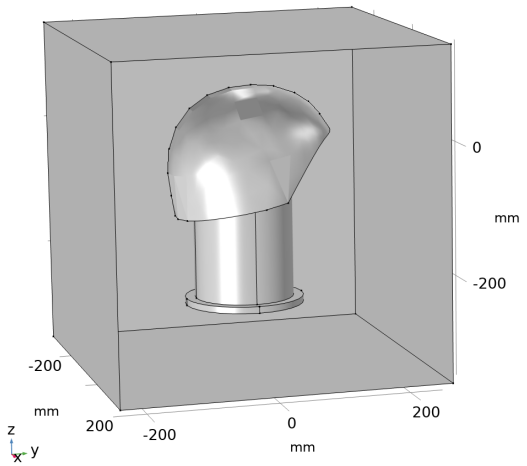

Figure 4. Diagram of the used finite element model with its dimensions. It includes the cylindrical phantom that is filled with saline solution, the directional DBS electrode placed inside the phantom, and the helmet-shaped MEG sensor surface. These structures are surrounded by a cuboid air box with a length of 500 mm.

detail in the next paragraph. A fitting approach was then used that searched for the model that best fit the measured and preprocessed data $B_{meas,i}$, which was described in the previous subsection. Therefor, the algorithm calculated the normalized root mean square error (NRMSE) between each modeled and measured data, and determined the model with the smallest error. From the selected model $B_{model,i}(p_{best}, r_{best})$, p_{best} was the computed electrode position and r_{best} the computed electrode orientation. The error in electrode localization was calculated with the Euclidean distance between p_{best} and p_{real}, the real known position of the electrode in the phantom. The error in determining the electrode orientation was calculated using the angle between r_{best} and r_{real}, the real known orientation of the electrode in the phantom.

FEM electromagnetic simulations were based on a model created in COMSOL Multiphysics®, as shown in Fig. 4. For each structure in the model, the corresponding material was taken directly from the built-in material library and value of a uniform electrical conductivity σ, relative permeability μ_r, and relative permittivity ϵ_r were assigned. The electrode was placed parallel to the longitudinal axis of the cylinder. The cylinder body and the outer jacket of the electrode were modeled with acrylic plastic ($\sigma \approx 0$ S/m, $\mu_r = 1$, $\epsilon_r = 4.2$), the eight independent electrode contacts with platinum-iridium ($\sigma = 10^6$ S/m, $\mu_r = 1$, $\epsilon_r = 1$), and the content of the phantom with saline solution ($\sigma = 1.6$ S/m, $\mu_r = 1$, $\epsilon_r = 80$). These values were taken from the literature. The phantom including the modeled electrode was surrounded by a cuboid box with a length of 500 mm that is filled with air ($\sigma \approx 0$ S/m, $\mu_r = 1$, $\epsilon_r = 1$). The MEG helmet was modeled as a surface and all measurement points were located on that surface. Tetrahedral mesh of 'Extra Fine' resolution was utilized. To model the bipolar electrode configurations, the 'Terminal' boundary condition of 'Current Type'

was used for the cathode and the 'Ground' boundary condition was used for the anode. Simulations were performed using the 'Magnetic and Electric Fields (mef)' interface of the 'AC/DC module' of COMSOL and magnetic flux densities in x, y, and z direction (B_x, B_y, and B_z) on the surface of the MEG helmet were calculated. In this experiment, SQUID sensors (fixed in the helmet) measured the magnetic field perpendicular to the helmet surface. To find the magnetic field $B_{model,i}$ perpendicular to the helmet surface in the simulation, we used the dot product $B_{model,i} = \vec{B}_i \cdot \vec{s}(i)$, where $\vec{s}(i)$ is the unit vector perpendicular to the helmet at the sensor location i and $B_i = B_x + B_y + B_z$.

In the model, the electrode was successively moved in the phantom with a step size of 1 mm (in all x, y, and z directions) and the magnetic field was calculated at each position. This data was used to analyze measurements with non-directional stimulation. The fitting approach found the electrode position which resulted in minimum NRMSE with the measured data. To analyze directional stimulation measurements, the electrode was successively rotated along its own axis with an angle step of 1° and the produced magnetic field was found for each step. Again, the fitting approach found the orientation that minimized the NRMSE. To improve detection accuracy, contiguous measurements could be evaluated together using a-priori information of electrode geometry. When determining electrode position, measurements with different levels of activated contacts along the electrode (lower, middle, upper level stimulation) were used, and the distance between adjacent levels was known to be 2 mm. When determining electrode rotation, measurements with different directional segments were used, and the angle between adjacent segments was known to be 120°. In contrast to the analysis of a single measurement, where the fitting approach determined only a single model which gave minimum NRMSE, when analyzing contiguous measurements (i.e., three measurements with stimulation electrode at different level or direction), the fitting algorithm determined three contiguous models (i.e., three related models with stimulation level separated by 2 mm or direction separated by 120°) whose calculated values minimized the sum of the individual NRMSE with the corresponding measured values. The results based on consideration of multiple measurements are presented in Section 3.5.

3. Results

3.1. Magnetic field strengths

The magnetic flux densities obtained from the time signals are summarized in Table 2. The maximum amplitudes from all sensors from all measurements in group 2 and 5 were considered. From the data shown in the table, we can conclude the following two points:

- Decreasing the stimulation amplitude leads to a proportional decrease in the magnetic field.
- The expected mean magnetic fields from MEG measurements in DBS patients with bipolar stimulation amplitude of 1.5 to 3 mA will be in average in the range of 1 to 2 pT.

Table 2. Measured magnetic flux densities.

Amplitude [mA], Pulse width [μs], Frequency [Hz]	Stats of values obtained from time signal from all sensors [pT]		
	Min	Mean	Max
12, 100, 170	2.4	25	65
11, 60, 130	2.0	7.6	24
3, 60, 130	0.6	2	6.6
1.5, 60, 130	0.3	1	3.3

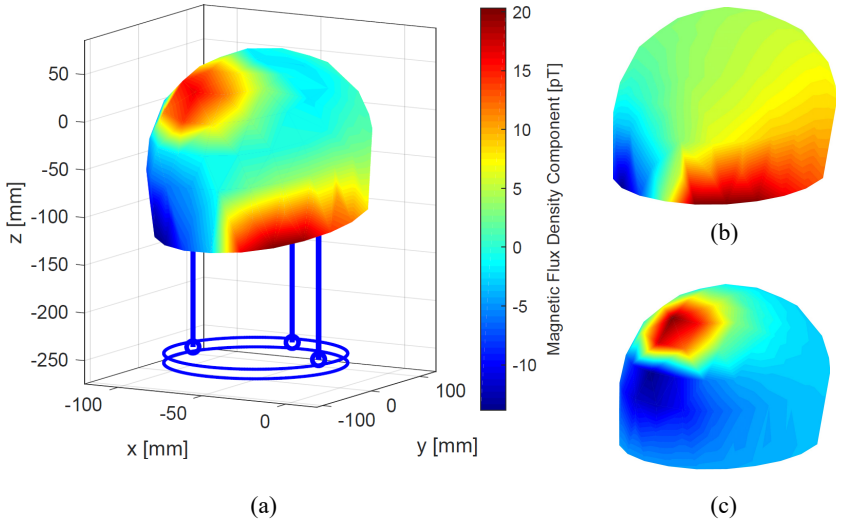

Figure 5. (a) Measured magnetic field distribution at the MEG helmet surface for measurement #11. The maximum amplitude from the averaged signal at each measuring point is calculated and interpolated between the points. The red and blue area in the lower part represents the magnetic field generated by the electrode and the circular red area in the top the artifact of the ferromagnetic ferrule. (b) Normalized modeled magnetic field distribution generated by the bipolar electrode configuration and (c) by the artifact of the ferromagnetic circular ferrule as the result of the electromagnetic simulation. The addition of both models represents the entire model.

3.2. Measured and modeled magnetic field distribution

The magnetic field distribution for measurement #11 (non-directional) can be seen in Fig. 5a. Since we had data for only 102 points across the surface, we used interpolation to get a surface plot. This figure represents a typical measured field distribution for bipolar recordings. It shows the magnetic field that is generated by the current flowing between the activated contacts (see Fig. 5b) and the undesired field that is created due to the magnetization of the ferromagnetic ferrule (see Fig. 5c). Our phantom was made of non-magnetic materials (titanium screws and plastic parts). As already mentioned in Section 2.4, this ferrule described the only magnetic noise which produced an artificial

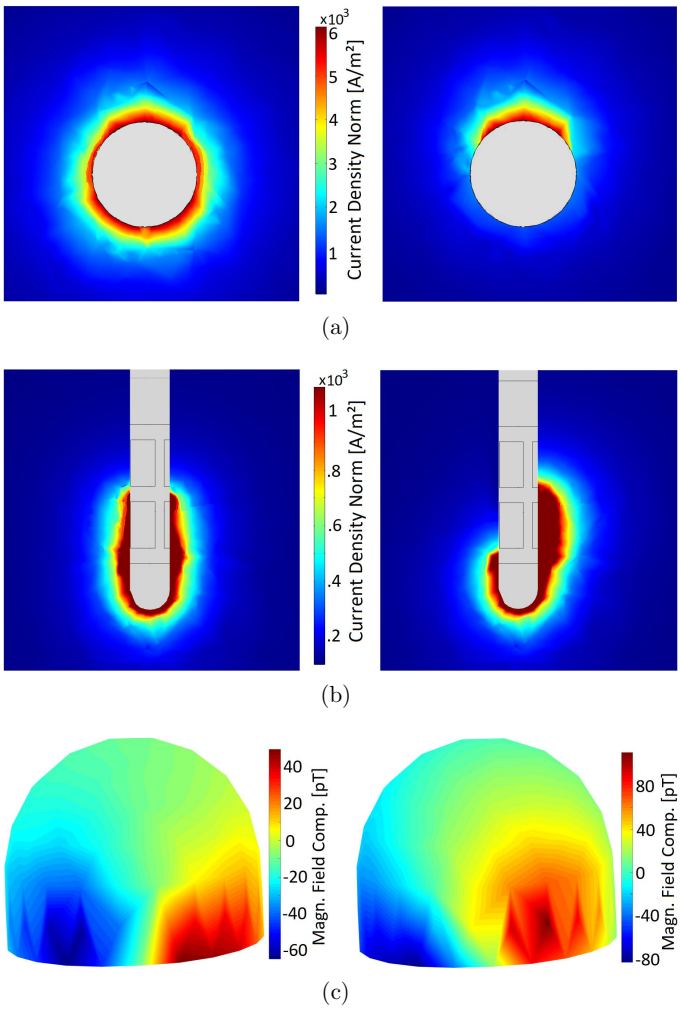

Figure 6. Electromagnetic simulation results of a non-directional (left column) and directional (right column) stimulation. The magnitude of the current density is visualized from the top view (a) and side view (b) of the electrode. With non-directional stimulation, the current flows symmetrically along the electrode, which generates the corresponding magnetic field distribution (c). With directional stimulation, the current flows diagonally, which causes a different field distribution that is used to determine the rotational orientation of the electrode in the phantom.

magnetic field. This artifact was observed in each measurement and was removed by modeling (in electromagnetic simulations) and by subtracting it from the measured data.

Fig. 6 compares the electromagnetic simulation results of a non-directional (left column) and directional (right column) stimulation. Fig. 6a and Fig. 6b displays the top and side view of the electrode with the current density generated due to the active contacts. In the non-directional case, the current flows symmetrically along the electrode and in the directional case, it is asymmetrical. The asymmetry in the current flow also

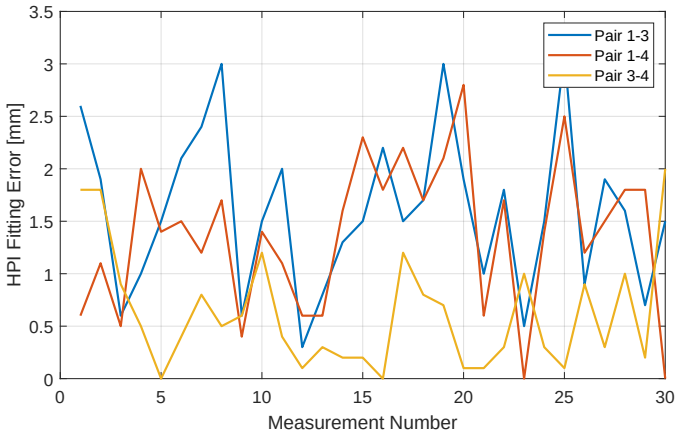

Figure 7. Error in the distances between HPI coils measured by the MEG scanner prior to each measurement. The pairs with coil number 2 showed high HPI fitting errors and were therefore not considered. The mean error of the fitting results is 1.6 mm for pair 1-3, 1.4 mm for pair 1-4, and 0.6 mm for pair 3-4.

causes an asymmetry in the magnetic field distribution (see right side of Fig. 6c) which determines the rotational orientation of the electrode.

We did not observe an effect of the connector, excess electrode wire, and neurostimulator on the measured magnetic field. This may be because the return current in the connector and wire cancels the field generated by the current flowing in the other direction (bipolar configuration). The current flowing within the neurostimulator may not be symmetrical and could have generated some magnetic field, but this is difficult to isolate and measure.

3.3. System measurement accuracy

Before the results of electrode localization and orientation determination are presented in the following sections, this section investigates the overall measurement accuracy since it describes the spatial resolution of the entire system. The system measurement accuracy depended on the inaccuracy of the following measuring steps:

- The phantom was constructed in-house and had an accuracy in sub-millimeter range (±0.1 mm).
- The digitizer device showed an accuracy of ±0.3 mm (see Section 2.2).
- The position of the HPI coils on the phantom surface, localized internally by the MEG system, provided the accuracy of the initial phantom position determination. The distances between the fitted coil positions and the digitized points are compared in Fig. 7, which shows the HPI fitting errors for all performed measurements. The average error was ±1.6 mm for the pair 1-3, 1.4 mm for the pair 1-4, and 0.6 mm for the pair 3-4. The pairs with coil number 2 had larger fitting errors and were therefore not considered by the MEG system.

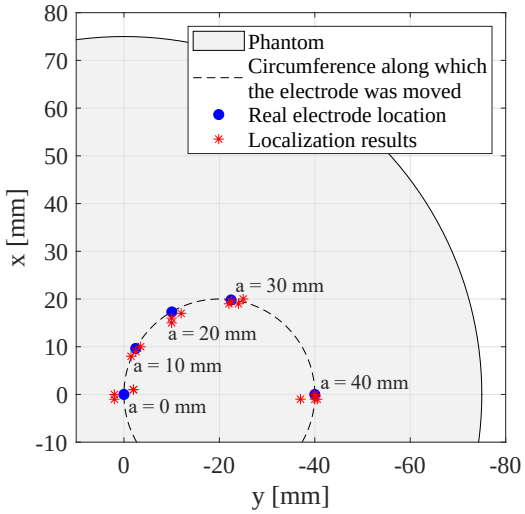

Figure 8. Top view of the cylindrical phantom with 75 mm radius. The electrode can be placed at any location on the inner circle (dashed line) by rotating the adjustment wheel. In this work, the electrode was placed at five different positions indicated by blue dots. Red asterisks illustrate electrode locations found by magnetic measurements.

The sum of all inaccuracies leads to a value of ±2 mm and describes the spatial resolution of the entire system. This value is taken into account in the electrode localization and rotation determination in the next sections. The dominant error is caused by the estimation of the phantom position by the MEG scanner.

3.4. Results using single measurement

In this section, the results of electrode localization and rotational orientation determination from the first three groups in Table 1 are presented. Note that after each measurement in these groups, the phantom was taken out of the MEG scanner to reposition the electrode and could not be placed exactly in the same position with respect to the MEG scanner and, thus, the measurements conducted in these groups cannot be compared. Therefore, each measurement had to be analyzed separately.

3.4.1. Localization: Electrode localization was performed for the first 20 measurements in Table 1. In these measurements with non-directional stimulation electrode position (in the xy-plane), the level of activated contacts along the z-axis was varied. The real electrode locations and the localization results from the measured magnetic data are depicted in Fig. 8. It shows the top view of the cylindrical phantom which has a radius of 75 mm. Five blue dots represent the five electrode placements (a = 40, 30, 20, 10, 0 mm) used in this work. The locations of the DBS electrode found using MEG are illustrated by red asterisks. This deviation is similar at all electrode positions which suggests that the localization accuracy is not affected by the proximity of the electrode

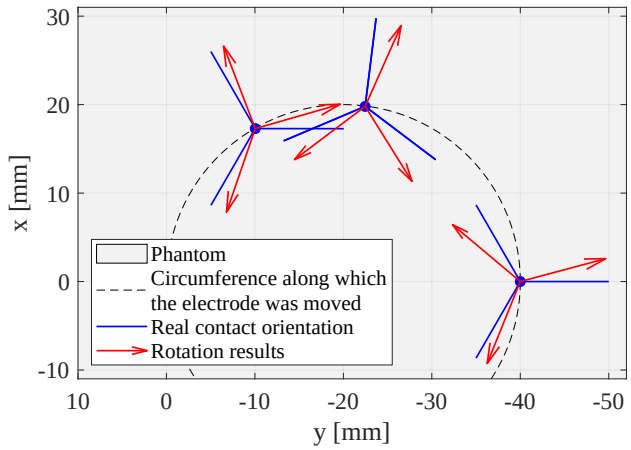

Figure 9. Top view of the cylindrical phantom. The electrode was placed at three different positions in the phantom represented by blue dots. Blue lines describe real orientations of each segmented contact and red arrows represent computed rotation results. The mean accuracy of rotation determination is around 15˚ on average.

to the phantom surface and to the sensor array. A similar distribution of localization results was observed for activated contacts at different electrode levels. The localization accuracy (represented by the Euclidean distance between real and computed electrode position) is calculated to be around 3 mm on average.

3.4.2. Orientation detection: The rotational orientation of the DBS electrode was found for measurements 21 to 29. Directional current was applied in the phantom in different directions using bipolar stimulation by activating contact C1 as anode and segmented contacts C2, C3, and C4 one-by-one as cathode. Real orientation of each segmented contact at three different electrode positions in the phantom, as well as the rotation results from the measured data are depicted in Fig. 9. It displays the top view of the phantom, where blue lines represent real orientations of each segment and red arrows orientations estimated by magnetic field measurements. Computed orientations are located close to the corresponding real orientations. The detection accuracy was calculated to be around 15˚.

3.5. Results using multiple measurements

In this section, the results of electrode localization and rotational orientation determination from the last two measurement groups in Table 1 are presented. The position of the phantom remained the same across these measurements since it was not taken out of the MEG scanner to reposition the electrode. Since the distance between adjacent contacts of the electrode (which is 2 mm) and the angle between adjacent segmented contacts (which is 120˚) is known, measurements at different stimulation heights and directions can be considered together to improve detection accuracy.

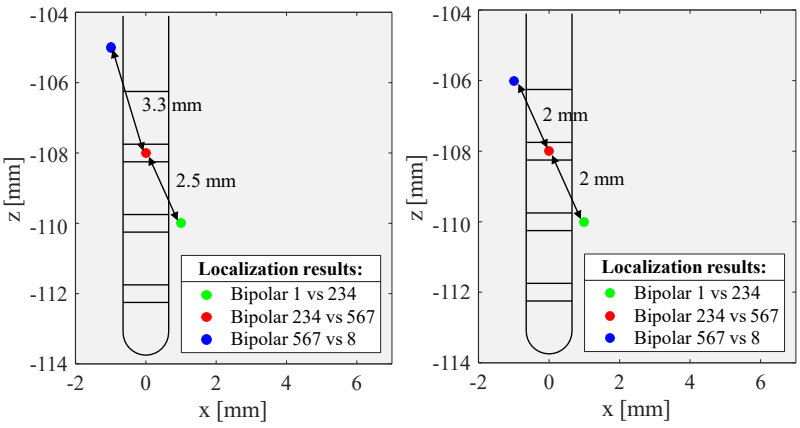

Figure 10. Localization results for different levels of activated contacts along the electrode (a) by considering each position separately and (b) by considering each position together while constraining solutions to known distances between adjacent positions.

3.5.1. Localization: Electrode localization was performed for the measurements 33 to 35 and 36 to 38, where the phantom was not moved during measurements. Fig. 10a depicts the localization results for measurements 33 to 35 with colored points. Different colors represent different levels of activated contacts along the electrode, where green refers to the lower, red to the middle, and blue refers to the upper level. The positions of localized sources reveal an average localization error of 2.8 mm, which is closer to the accuracy obtained in the previous section. Since the position of each electrode level was estimated separately, the distance between adjacent points in the figure deviated significantly from 2 mm. If the a-priori known distance is applied as a condition for localization as delineated in Fig. 10b, the result improves slightly to the value 2.2 mm. Moreover, it can be seen that localized points are not arranged along the electrode but along a different axis. This error is mainly due to the inaccurate estimation of the phantom position in the MEG scanner. When looking at the figure, it already becomes clear that the localization accuracy could be further improved if the localized points would be slightly shifted in negative z-direction and tilted in the xz-plane. This observation suggests that a slight readjustment of the MEG sensor array, i.e. an improvement of the system spatial resolution, would significantly improve the localization accuracy.

3.5.2. Orientation detection: The determination of the rotational orientation of the directional electrode was performed for measurements 30 to 32. The electrode was directionally stimulated in the phantom by activating the tip of the electrode against all segmented contacts successively. The obtained rotation results are shown in Fig. 11a

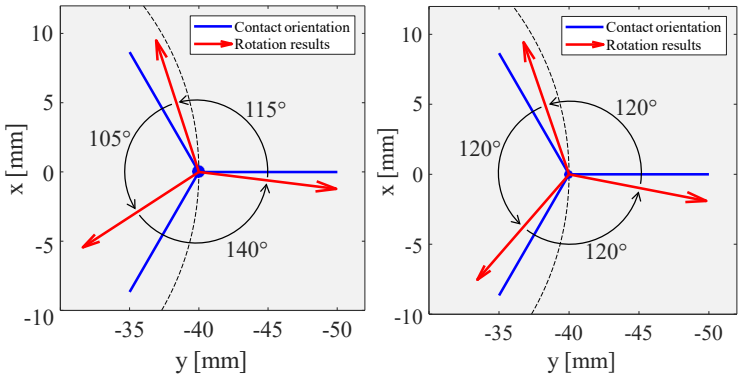

Figure 11. Rotational orientation results for each segmented electrode contact (a) by considering each orientation separately and (b) by considering each orientation together while constraining solutions to known angels between adjacent orientations.

with red arrows, while the blue lines indicate real orientations of the segments. The accuracy of rotation determination is calculated to an average of 15°, which corresponds exactly to the accuracy obtained in the previous section for different electrode positions. The orientation for each segment was estimated separately. If the a-priori known angle is applied as a condition for rotation detection, the result improves slightly to a value of 11°, as illustrated in Fig. 11b. This error is mainly due to the inaccurate estimation of the phantom position in the MEG scanner. A minimization of this error can be achieved by a more precise measuring system.

4. Discussion

In this paper, a new method to determine the position and the rotational orientation of a DBS electrode by using magnetic field measurements with SQUID sensors was presented. These measurements were valuable for us because they were performed on a MEG scanner in a clinical setting in comparison to our previous work, which was based on an in-house constructed measurement system with a single sensor. Employing clinically used DBS stimulation parameters of 1.5 mA/3 mA amplitude, 60 μs pulse width, 130 Hz frequency, and bipolar configuration, a magnetic field of 1/2 pT on average was measured. This value represents the minimum requirement for the sensitivity of magnetic field sensors for this type of application. However, the SNR of the measured signal can be drastically improved by segmenting the signal into time periods equivalent to the stimulation time period and then by averaging over these segments.

To date, no generally accepted protocol for DBS electrode localization is available. Localization of a DBS electrode in patients using MEG presents an alternative method to the currently employed neuroimaging approaches, in which the electrode is localized by visual inspection of metal artifacts. These neuroimaging techniques have their

own limitations, which were briefly discussed in the introduction and in detail in our previous work [12]. In our method presented here, the stimulation current produced a strong magnetic field (in the pT range), significantly larger than the field generated by human brain activity (in the fT range), and was measured by MEG sensors. The DBS electrode in the phantom could be reliably localized with an accuracy of about 3 mm over all performed measurements, each measurement being considered separately for localization. The accuracy could be improved to around 2.2 mm by using multiple measurements and applying a-priori known distance between adjacent contacts as a condition for localization. These accuracies were limited due to the imprecise estimation of the phantom position by the MEG device. This suggests that the localization accuracy can be significantly improved further if the spatial resolution of the MEG scanner is also improved.

Similar to electrode localization, no established protocol to ascertain the electrode orientation is currently available. The determination of the rotational orientation of the electrode using MEG describes an alternative method to the existing radiation-based methods. Segmented contacts of a directional electrode can allow generation of an electric field in a desired direction. This new technology requires the knowledge of the exact electrode orientation in the brain in order to fully exploit its benefit. In all other methods currently available, patients are exposed to radiation. The method presented here is completely harmless and safe for patients. The orientation of each electrode's directional contact was determined with an average accuracy of 15°, whereby each measurement was used separately for the determination. However, this error could be reduced to about 11° by using multiple measurements and applying the a-priori known angle between adjacent segments as a condition for orientation detection. Again, the accuracy was mainly limited by the spatial resolution of the MEG scanner, which suggests that a significant improvement in determining electrode orientation can be achieved if the measurement accuracy is improved.

A non-radiative and non-invasive method for the precise determination of a DBS electrode's position and rotation constitutes an important development in stereotaxic neurosurgery and DBS therapy. The results presented in this paper demonstrate that a MEG scanner can detect the position and orientation of a segmented electrode in a cylindrical phantom with decent accuracy, and a higher accuracy can be achieved if the scanner is made more precise. We are aware that our measurements were made under an ideal condition and that the accuracy will decline in real patients due to movements associated with breathing and cardiac activity. Moreover, a heterogeneous patient-specific FEM head model will be required. Nevertheless, the desired localization accuracy can be achieved using a more precise MEG scanner. At present, MEG scanners use a fixed helmet-shaped sensor array, relative to which the head can move. Emerging technical developments using optically pumped magnetometers may lead to cap-shaped MEG sensor arrays that will move with the head [22], i.e. no relative movement between head and sensors, and can adapt to the individual head shape. In that case, sufficient accuracy in determining the position and rotation of the electrode can be achieved.

Therefore, the results presented here suggest that, in principle, a non-invasive and radiation-free electrode localization and orientation detection is possible using MEG, and new technical developments will foster this endeavor.

5. Conclusion

We have presented a novel non-invasive and non-radiative method to determine location and rotational orientation of a DBS electrode using MEG. Magnetic field around the phantom was measured with a clinically used MEG scanner and calculated using precise electromagnetic FEM model. A fitting approach was then used to minimize the error between measured and modeled values. Our method localized the DBS electrode with an accuracy of about 2.2 mm and its orientation with an accuracy of 11° regardless of the electrode location in the phantom. The spatial resolution of the MEG scanner was the main limiting factor for these lower accuracies. If more precise MEG systems are available, allowing precise determination of the phantom position in the MEG scanner, these accuracies will be improved significantly.

Acknowledgment

This work was supported by the German Research Foundation (Deutsche Forschungsgemeinschaft, DFG) through the project T1 of the Collaborative Research Centre CRC 1261 *Magnetoelectric Sensors: From Composite Materials to Biomagnetic Diagnostics*. Furthermore, we would like to express our very great appreciation to the group of Prof. Schnitzler from the Heinrich-Heine-University Düsseldorf, in particular to Levent Kandemir and Holger Krause, for their support in performing the MEG measurements.

References

[1] P. Krack, J. Volkmann, G. Tinkhauser, and G. Deuschl, "Deep Brain Stimulation in Movement Disorders: From Experimental Surgery to Evidence-Based Therapy," *Movement Disorders*, vol. 34, 10 2019.

[2] C. R. Butson and C. C. McIntyre, "Current steering to control the volume of tissue activated during deep brain stimulation," *Brain Stimulation*, vol. 1, no. 1, pp. 7 – 15, 2008.

[3] F. Steigerwald, L. Müller, S. Johannes, C. Matthies, and J. Volkmann, "Directional deep brain stimulation of the subthalamic nucleus: A pilot study using a novel neurostimulation device," *Movement Disorders*, vol. 31, no. 8, pp. 1240–1243, 2016.

[4] P. Krack, J. Volkmann, G. Tinkhauser, and G. Deuschl, "Deep Brain Stimulation in Movement Disorders: From Experimental Surgery to Evidence-Based Therapy," *Movement Disorders*, vol. 34, no. 12, pp. 1795–1810, 2019.

[5] J. R. Ellenbogen, R. Tuura, and K. Ashkan, "Localisation of DBS Electrodes Post-Implantation, to CT or MRI? Which Is the Best Option?" *Stereotact Funct Neurosurg*, vol. 96, pp. 347–348, 10 2018.

[6] J. Engelhardt, D. Guehl, N. Damon-Perrière, O. Branchard, P. Burbaud, and E. Cuny, "Localization of Deep Brain Stimulation Electrode by Image Registration Is Software Dependent: A Comparative Study between Four Widely Used Software Programs," *Stereotact Funct Neurosurg*, vol. 96, pp. 364–369, 12 2018.

[7] M. I. Iacono, S. R. Atefi, L. Mainardi, H. C. Walker, L. M. Angelone, and G. Bonmassar, "A Study on the Feasibility of the Deep Brain Stimulation (DBS) Electrode Localization Based on Scalp Electric Potential Recordings," *Frontiers in Physiology*, vol. 9, p. 1788, 2019.

[8] P. Reinacher, M. Krüger, V. Coenen, M. Shah, R. Roelz, C. Jenkner, and K. Egger, "Determining the Orientation of Directional Deep Brain Stimulation Electrodes Using 3D Rotational Fluoroscopy," *American Journal of Neuroradiology*, vol. 38, no. 6, pp. 1111–1116, 2017.

[9] S. Hunsche, C. Neudorfer, F. E. Majdoub, M. Maarouf, and D. Sauner, "Determining the Rotational Orientation of Directional Deep Brain Stimulation Leads Employing Flat-Panel Computed Tomography," *Operative Neurosurgery*, vol. 16, no. 4, pp. 465–470, 06 2018.

[10] A. Sitz, M. Hoevels, A. Hellerbach, A. Gierich, K. Luyken, T. A. Dembek, M. Klehr, J. Wirths, V. Visser-Vandewalle, and H. Treuer, "Determining the orientation angle of directional leads for deep brain stimulation using computed tomography and digital x-ray imaging: A phantom study," *Medical Physics*, vol. 44, no. 9, pp. 4463–4473, 2017.

[11] M. Yalaz, A. Teplyuk, M. Muthuraman, G. Deuschl, and M. Höft, "The Magnetic Properties of Electrical Pulses Delivered by Deep-Brain Stimulation Systems," *IEEE Transactions on Instrumentation and Measurement*, vol. 69, no. 7, pp. 4303–4313, 2020.

[12] M. Yalaz, A. Teplyuk, G. Deuschl, and M. Höft, "Dipole Fit Localization of the Deep Brain Stimulation Electrode Using 3D Magnetic Field Measurements," *IEEE Sensors Journal*, vol. 20, no. 16, pp. 9550–9557, 2020.

[13] T. Morishita, J. Hilliard, M. Okun, D. Neal, K. Nestor, D. Peace, A. Hozouri, M. Davidson, F. Bova, J. Sporrer, G. Oyama, and K. Foote, "Postoperative lead migration in deep brain stimulation surgery: Incidence, risk factors, and clinical impact," *PLOS ONE*, vol. 12, p. e0183711, 09 2017.

[14] J.-g. Choi, S.-H. Lee, Y.-M. Shon, and B.-C. Son, "Long-Term Migration of a Deep Brain Stimulation (DBS) Lead in the Third Ventricle Caused by Cerebral Atrophy in a Patient with Anterior Thalamic Nucleus DBS," *Journal of Epilepsy Research*, vol. 5, pp. 96–100, 12 2015.

[15] T. Dembek, M. Hoevels, A. Hellerbach, A. Horn, J. Petry-Schmelzer, J. Borggrefe, J. Wirths, H. Dafsari, M. Barbe, V. Visser-Vandewalle, and H. Treuer, "Directional DBS leads show large deviations from their intended implantation orientation," *Parkinsonism & Related Disorders*, vol. 67, pp. 117–121, 08 2019.

[16] M. Krüger, Y. Naseri, F. Cavalloni, P. Reinacher, G. Kägi, J. Weber, D. Brogle, O. Bozinov, S. Hägele-Link, and F. Brugger, "Do directional deep brain stimulation leads rotate after implantation?" *Acta neurochirurgica*, 09 2020.

[17] V. Litvak, A. Eusebio, A. Jha, R. Oostenveld, G. R. Barnes, W. D. Penny, L. Zrinzo, M. I. Hariz, P. Limousin, K. J. Friston, and P. Brown, "Optimized beamforming for simultaneous MEG and intracranial local field potential recordings in deep brain stimulation patients," *NeuroImage*, vol. 50, no. 4, pp. 1578 – 1588, 2010.

[18] V. Litvak, A. Jha, A. Eusebio, R. Oostenveld, T. Foltynie, P. Limousin, L. Zrinzo, M. I. Hariz, K. Friston, and P. Brown, "Resting oscillatory cortico-subthalamic connectivity in patients with Parkinson's disease," *Brain*, vol. 134, no. 2, pp. 359–374, 12 2010.

[19] A. Oswal, A. Jha, S. Neal, A. Reid, D. Bradbury, P. Aston, P. Limousin, T. Foltynie, L. Zrinzo, P. Brown, and V. Litvak, "Analysis of simultaneous MEG and intracranial LFP recordings during Deep Brain Stimulation: a protocol and experimental validation," *Journal of Neuroscience Methods*, vol. 261, pp. 29 – 46, 2016.

[20] J. Hirschmann, T. Özkurt, M. Butz, M. Homburger, S. Elben, C. Hartmann, J. Vesper, L. Wojtecki, and A. Schnitzler, "Distinct oscillatory STN-cortical loops revealed by simultaneous MEG and local field potential recordings in patients with Parkinson's disease," *NeuroImage*, vol. 55, no. 3, pp. 1159 – 1168, 2011.

[21] R. Oostenveld, P. Fries, E. Maris, and J.-M. Schoffelen, "FieldTrip: Open Source Software for Advanced Analysis of MEG, EEG, and Invasive Electrophysiological Data," *Computational intelligence and neuroscience*, vol. 2011, p. 156869, 01 2011.

[22] R. M. Hill, E. Boto, M. Rea, N. Holmes, J. Leggett, L. A. Coles, M. Papastavrou, S. K. Everton, B. A. Hunt, D. Sims, J. Osborne, V. Shah, R. Bowtell, and M. J. Brookes, "Multi-channel whole-head OPM-MEG: Helmet design and a comparison with a conventional system," *NeuroImage*, vol. 219, p. 116995, 2020.

Key Findings and Scientific Implications

- The magnetic field generated by clinically applied stimulation parameter settings of DBS can be measured with a clinically used SQUID-based MEG.
- Unlike voltage-controlled DBS, current-controlled stimulation provides a proportional dependency between the stimulation amplitude and the magnetic field independent of the impedance of the electrode-tissue interface, because the current delivered to the tissue is regulated by the electrode impedance.
- Measurements with a bipolar omnidirectional stimulation mode, in which one level of the electrode is activated against another level (conventional ring stimulation), can be used to determine electrode position.
- Measurements with a bipolar directional stimulation mode, in which the tip of the electrode is activated against one of the three segmented contacts at the next higher level of the electrode, can be used to determine electrode orientation.
- The electrode can be localized with an average accuracy of approximately 3 mm and the orientation can be detected with an average accuracy of an estimated 15° when considering a single measurement with omnidirectional and directional stimulation, respectively.
- The accuracy of electrode localization and orientation detection depends on the number of measurements, which differ for omnidirectional electrode configurations in the activation of contact pairs along the height of the electrode and for directional electrode configurations in the activation of contact pairs around the electrode.
- The detection error can be minimized to 2.2 mm for electrode localization and to 11° for electrode orientation detection when considering a sequence of three contiguous measurements under omnidirectional and directional stimulation modes, respectively.
- The detection accuracy is limited mainly by the spatial resolution of the MEG system, which is given by the imprecise estimation of measurement positions with respect to the head location.

3.4 Investigation of Magnetoelectric Sensor Requirements for Deep Brain Stimulation Electrode Localization and Rotational Orientation Detection

M. Yalaz, G. Deuschl, M. Butz, A. Schnitzler, A.-K. Helmers, and M. Höft, "Investigation of Magnetoelectric Sensor Requirements for Deep Brain Stimulation Electrode Localization and Rotational Orientation Detection," in *Sensors*, vol. 21, no. 7, art. no. 2527, April 2021, doi: 10.3390/s21072527.

Information about the amount of own contribution to this publication:

Conceptualization	Planning	Implementation	Manuscript preparation
high	high	high	high

© 2021 by the authors. This article is an open access article distributed under the terms and conditions of the Creative Commons Attribution (CC BY) license (https://creativecommons.org/licenses/by/4.0/), which permits unrestricted use, distribution, and reproduction in any medium. The version of record is available online at https://doi.org/10.3390/s21072527.

sensors

MDPI

Article

Investigation of Magnetoelectric Sensor Requirements for Deep Brain Stimulation Electrode Localization and Rotational Orientation Detection

Mevlüt Yalaz [1,*], Günther Deuschl [2], Markus Butz [3], Alfons Schnitzler [3], Ann-Kristin Helmers [4] and Michael Höft [1]

[1] Chair of Microwave Engineering, Christian-Albrechts-Universität zu Kiel, 24143 Kiel, Germany; mh@tf.uni-kiel.de
[2] Department of Neurology, Christian-Albrechts-Universität zu Kiel, 24105 Kiel, Germany; g.deuschl@neurologie.uni-kiel.de
[3] Institute of Clinical Neuroscience and Medical Psychology, Medical Faculty, Heinrich Heine Universität Düsseldorf, 40225 Düsseldorf, Germany; markus.butz@hhu.de (M.B.); alfons.schnitzler@hhu.de (A.S.)
[4] Department of Neurosurgery, Christian-Albrechts-Universität zu Kiel, 24105 Kiel, Germany; Ann-Kristin.Helmers@uksh.de
* Correspondence: my@tf.uni-kiel.de; Tel.: +49-431-880-6167

Abstract: Correct position and orientation of a directional deep brain stimulation (DBS) electrode in the patient's brain must be known to fully exploit its benefit in guiding stimulation programming. Magnetoelectric (ME) sensors can play a critical role here. The aim of this study was to determine the minimum required limit of detection (LOD) of a ME sensor that can be used for this application by measuring the magnetic field induced by DBS. For this experiment, a commercial DBS system was integrated into a head phantom and placed inside of a state-of-the-art Superconducting Quantum Interference Device (SQUID)-based magnetoencephalography system. Measurements were performed and analyzed with digital signal processing. Investigations have shown that the minimum required detection limit depends on various factors such as: measurement distance to electrode, bandwidth of magnetic sensor, stimulation amplitude, stimulation pulse width, and measurement duration. For a sensor that detects only a single DBS frequency (stimulation frequency or its harmonics), a LOD of at least 0.04 pT/Hz$^{0.5}$ is required for 3 mA stimulation amplitude and 60 µs pulse width. This LOD value increases by an order of magnitude to 0.4 pT/Hz$^{0.5}$ for a 1 kHz, and by approximately two orders to 3 pT/Hz$^{0.5}$ for a 10 kHz sensor bandwidth. By averaging, the LOD can be reduced by at least another 2 orders of magnitude with a measurement duration of a few minutes.

Keywords: magnetoelectric sensor; SQUID; MEG; deep brain stimulation (DBS); directional DBS electrode; magnetic field measurement; electrode localization; rotational orientation detection

check for updates

Citation: Yalaz, M.; Deuschl, G.; Butz, M.; Schnitzler, A.; Helmers, A.-K.; Höft, M. Investigation of Magnetoelectric Sensor Requirements for Deep Brain Stimulation Electrode Localization and Rotational Orientation Detection. *Sensors* **2021**, *21*, 2527. https://doi.org/10.3390/s21072527

Academic Editor: Ruben Specogna

Received: 5 March 2021
Accepted: 30 March 2021
Published: 4 April 2021

Publisher's Note: MDPI stays neutral with regard to jurisdictional claims in published maps and institutional affiliations.

Copyright: © 2021 by the authors. Licensee MDPI, Basel, Switzerland. This article is an open access article distributed under the terms and conditions of the Creative Commons Attribution (CC BY) license (https://creativecommons.org/licenses/by/4.0/).

1. Introduction

Deep brain stimulation (DBS) is an elective surgical procedure in which electrodes are implanted in specific areas of the brain. It has become an evidence based therapy for Parkinson's disease with fluctuating mobility [1,2] and has become applicable to treat many other diseases [3]. The stimulating electrodes constantly deliver electrical impulses to target brain regions to control abnormal brain activity. The impulses are generated by a neurostimulator that is implanted under the skin (below the clavicle) and is connected by extension wires to the electrodes. In current clinical practice, each patient receives an individualized stimulation setting in which specific parameters are set based on clinician experience and readjusted based on clinically observed outcome parameters, i.e., symptom suppression such as tremor reduction. Thus, programming of the implanted pulse generator (IPG) or neurostimulator is a time-consuming, iterative, and trial-and-error based process [4–7]. DBS continues to be the subject of intensive fundamental and clinical

research [8,9]. The number of diseases for which DBS is emerging as a potentially effective therapeutic measure is steadily growing. Continuous technical advancements in DBS systems, as well as improvements in medical imaging techniques, are also contributing to the immense development potential of this treatment modality. The overall goal is to provide the patient with an optimal therapy.

One of the revolutionary developments in recent years has been the development of directional electrode technology with segmented contacts (split into three segments along the circumference of the electrode) to steer the stimulation volume in a predefined direction. This has shown to improve the therapeutic effect and lower side effect thresholds when compared to electrodes with standard ring contacts [10–12]. To exploit the full potential of this technology and enable image-guided directional stimulation, detailed knowledge of the precise location and orientation of the electrode in the anatomical brain structures is required. To date, no generally established means are available for non-invasive electrode localization and rotational orientation detection. Currently, detection approaches are all based on neuroimaging data, e.g., the fusion of postoperative computed tomography (CT) with preoperative magnetic resonance imaging (MRI) to localize the electrode [13,14] or the detection of artifact patterns from X-rays, CT, and rotational fluoroscopy to determine electrode orientation [15–17]. These neuroimaging techniques are all associated with various limitations, and have been discussed in detail in previous works [18]. Recently, our group has developed and presented a new non-invasive and non-radiative method to determine the position and the rotational orientation of a DBS electrode by using magnetic field measurements [19]. To date, this method has been tested on head phantoms with an in-house constructed measurement system with a single Fluxgate sensor (20 $pT/Hz^{0.5}$ between 0 and 1 kHz) [18,20] and with a state-of-the-art magnetoencephalography (MEG) scanner in a clinical setting based on Superconducting Quantum Interference Device (SQUID) sensors (3 $fT/Hz^{0.5}$ between 0 and 1660 Hz) [19]. To do this, the neurostimulator was programmed with the following electrode configuration settings:

- Bipolar non-directional electrode configuration (ring stimulation) with the activation of contacts at different electrode heights for electrode localization and
- bipolar directional electrode configuration with the activation of the tip of the electrode against an individual segmented contact for electrode orientation detection.

Subsequently, the magnetic field induced by the stimulation was measured around the phantom or patient's head at multiple measurement points and the position and rotation of the electrode was inferred using suitable forward models and localization algorithms. Our method localized the DBS electrode with an accuracy of about 2.2 mm and determined its orientation with an accuracy of 11°, regardless of the electrode location in the phantom. These accuracies were mainly limited by the imprecise position estimation of the phantom with respect to the measurement points (SQUID sensors). This indicates that the accuracies in position and orientation detection can be significantly improved if the measurement procedure is enhanced, i.e., if the position of the phantom and the measurement points can be accurately transferred into a uniform coordinate system. New technical developments are moving towards cap-shaped MEG sensor arrays [21,22] that move with the patient's head (i.e., no relative movement between head and sensors) and can be adapted to the individual's head shape. It would have the potential to overcome this limitation and could become a breakthrough in neurology, as they would achieve sufficient accuracy for this application. This could help in interpreting observed stimulation effects and in guiding time-consuming stimulation programming. These new systems make use of significant advances in the development of magnetic sensors that have the potential to overcome the limitation of current generation of MEG devices. Optically pumped magnetometers (OPMs) have been demonstrated to have sensitivities approaching the gold standard, those of commercial SQUIDs (10 $fT/Hz^{0.5}$ between 0 and 100 Hz) [23] making them suitable for OPM-MEG development. However, these sensors still have too narrow of a bandwidth for use in DBS applications due to the presence of much higher frequencies (stimulation frequency and harmonics). It is reported that ME sensor approaches offer

a high potential for this application since the resonance frequency of an ME sensor can be tuned to the stimulation frequency or its higher harmonics to measure the artificial magnetic signal of DBS [24–26]. However, such resonant, narrow-band ME sensors measure only a single frequency component of the entire broadband DBS signal, therefore, higher sensor sensitivity is required. Surface acoustic wave (SAW) sensors, which operate over a wide bandwidth of 50 kHz, may be more promising because they can pick up all frequency components of the signal [27]. Therefore, a high sensor sensitivity, as provided by a SQUID sensor, is not required. The objective of this work is to provide the minimum requirements that the magnetic field sensors must meet in order to be used for electrode localization and electrode orientation detection. The main focus is on the required operating frequency bandwidth and detection limit of the sensor.

2. Materials and Methods

2.1. Experimental Design

The head phantom used in this study is depicted in Figure 1a. The cylinder body with dimensions that are comparable with a human head (diameter of 150 mm, height of 250 mm) was made of acrylic glass and was, therefore, neither electrically conductive nor magnetic. It was filled with an isotonic fluid (NaCl 0.9%) to mimic the electric conductivity of a human brain. We used a DBS system by Boston Scientific Inc. (Boston Scientific, Marlborough, MA, USA) consisting of a current-controlled DBS neurostimulator (Vercise™ PC) and a directional electrode (Versice Cartesia™) as used in clinical routines. This system is based on stimulation with traditional rectangular pulses including a stimulus pulse phase and a passive charge-balancing phase. It was integrated and fixed into the phantom. Moreover, we used non-magnetic material for all other components used in the phantom. The screws on top of the electrode holder were made of titanium, while the adjustment wheel and the holders for the electrode and neurostimulator casing were made of plastic. The structure of the directional DBS electrode is shown in Figure 1b. It is comprised of eight individually controlled platinum-iridium contacts (C1–C8), in which the two middle contact levels were segmented into three contacts each spanning 120° of the circumference. Any combination of these contacts can be activated to steer the stimulation current direction. The outer jacket is made of polyurethane. MEG data were collected with an Elekta Neuromag VectorView® MEG scanner at the Universitätsklinikum Düsseldorf (UKD, Düsseldorf, Germany) in Düsseldorf. Figure 1c depicts how the phantom was positioned within the MEG sensor array.

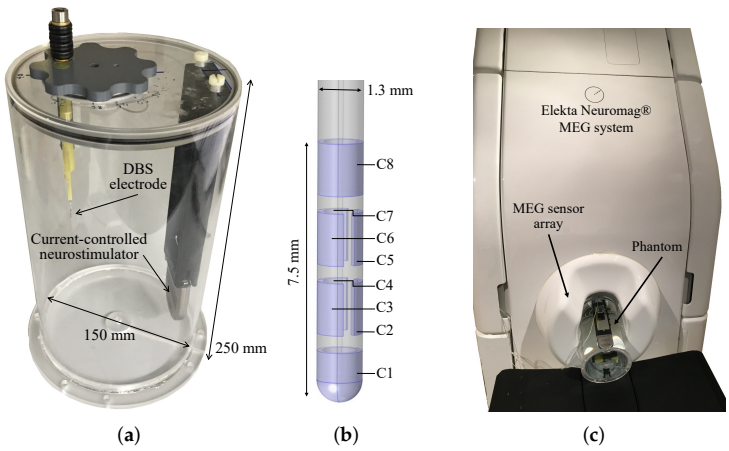

Figure 1. (**a**) The cylindrical phantom with the integrated deep brain stimulation (DBS) system which consists of a current-controlled neurostimulator and directional electrode by Boston Scientific. (**b**) The geometry of directional electrode and its contact numbers. (**c**) The phantom inside the MEG scanner.

2.2. Data Acquisition

The MEG scanner was comprised of 306 individual sensors, corresponding to 102 magnetometers and 204 gradiometers arranged as 102 sensor triplets. Only the magnetometer data were used in this study. The noise level according to the datasheet was about 3 $\mathrm{fT}/\sqrt{\mathrm{Hz}}$ for both magnetometers and gradiometers. The acquisition parameters of the MEG scanner were set as follows: The sampling rate was set to its maximum of 5 kHz. The low-pass filter was set to the highest possible value of 1660 Hz and the cut-off frequency of the high-pass filter was selected to direct current (no high-pass filtering) in order to obtain measurements of the DBS signal with the maximum allowed acquisition bandwidth. The duration of each measurement was three minutes. A total of nine measurements were taken (see Table 1) with different activated electrode contacts (1–8: contact numbers, first number: anode, second number: cathode) and stimulation parameters (amplitude, pulse width, frequency). The first three measurements were performed in bipolar mode with activation of contacts at different electrode heights with 3 mA of stimulation amplitude. The next three measurements were performed with 1.5 mA stimulation. The last three measurements were made under monopolar electrode configuration. The applied values (3 or 1.5 mA, 130 Hz, 60 µs) are values used in clinical routine. Since these were phantom measurements, the measured MEG signals were not contaminated by biological artifacts such as cardiac muscle, skeletal muscles, or eye movements. Thus, the measurements with a phantom represent an ideal case. The ambient noise solely consisted of the power line interference, which only affected non-important frequencies (50 Hz and harmonics). The distance between the electrode and MEG sensors varies between 7 cm (sensor closest to the electrode) and 15 cm (sensor farthest from the electrode). These distances are also to be expected in real patient measurements. The good quality of recorded data was ensured by an 'empty room' measurement prior to the start of the experiment and by visual inspection of approximately 1 min of MEG recording before each measurement.

Table 1. Tabulation of the MEG measurements.

Num.	Configuration	Contacts: (−) vs. (+)	Amplitude [mA]	Pulse [µs]	Frequency [Hz]
1	Bipolar	1 vs. 234	3	60	130
2	Bipolar	234 vs. 567	3	60	130
3	Bipolar	567 vs. 8	3	60	130
4	Bipolar	1 vs. 234	1.5	60	130
5	Bipolar	234 vs. 567	1.5	60	130
6	Bipolar	567 vs. 8	1.5	60	130
7	Monopolar	1 vs. Case	1.5	60	130
8	Monopolar	234 vs. Case	1.5	60	130
9	Monopolar	8 vs. Case	1.5	60	130

2.3. Signal Processing

The processing steps of the MEG measurements are depicted in Figure 2. For each measurement, we obtained 102 time signals, one from each MEG sensor. The measured data was imported into MATLAB® (Version R2018a) and preprocessed using the FieldTrip toolbox [28]. Each time signal was high-pass filtered (6th order Butterworth) with a cutoff frequency of 60 Hz and without signal loss, since the signal contains higher frequencies (stimulation frequency of 130 Hz and its harmonics). Each signal was divided into short segments of length equal to the inverse of stimulation frequency ($T_s = 1/f_s = 7.69$ ms). These segments were then averaged which improved the signal-to-noise ratio (SNR) by $\sqrt{N}$, where $N = 180\ \mathrm{s} \times 130\ \mathrm{Hz} = 23{,}400$. The maximum value from this averaged time segment is then taken for each MEG sensor, resulting in a total of 102 values representing the measured field distribution around the phantom. In addition, each high-pass filtered time signal was also transformed into the frequency domain using the Welch's method [29]

with a Hanning window, and the amplitude value was taken from the spectrum at 130 Hz stimulation frequency and at its harmonics. Since the MEG system measured at a sampling rate of 5 kHz, a total of 18 harmonics ranging from 260 to 2470 Hz could be considered, although only the first 11 harmonics ranging from 260 to 1560 Hz could be measured without attenuation due to the 1660 Hz low-pass filter used in the MEG device. Therefore, in addition to 102 values obtained from the time signal, each measurement was also represented by 102 values obtained from each of the 19 frequencies in the frequency signal. The maximum amplitude from the averaged time signal was composed of the total acquisition bandwidth, which was limited to 1660 Hz by the MEG system. This amplitude value can be interpreted as the result of a measurement with a magnetic sensor with 1660 Hz bandwidth. A single amplitude in the spectrum considers only a single frequency component of the DBS signal, so this amplitude value can be interpreted as the result of a measurement performed with a narrow-band sensor that is sensitive only at the corresponding frequency.

Since magnetic sensors always exhibit noise as a function of frequency, the term density spectrum was used in this paper when investigating the minimum required detection limit. The power density spectrum has as its physical dimension the squared physical unit of the observed quantity per Hz. The amplitude density spectrum, which is the square root of the power density spectrum, has as its physical dimension the physical unit of the observed quantity per $\sqrt{\text{Hz}}$ [30]. In this work, the term measured quantity refers to a magnetic flux density to be measured with the physical dimension Tesla. For the case that an amplitude density spectrum has as physical unit the dimension of the measured quantity per $\sqrt{\text{Hz}}$, it is called the noise level or the limit of detection (LOD) of the sensor with the unit $\text{T}/\sqrt{\text{Hz}}$. This results from the quotient of the amplitude noise density $[\text{V}/\sqrt{\text{Hz}}]$ and the sensitivity [V/T] of the sensor. The frequency bandwidth of a sensor describes a white noise behavior between the lower and upper cutoff frequency with the same noise level or LOD value.

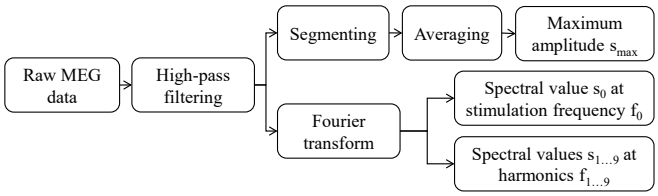

Figure 2. Each measured MEG signal is high-pass filtered with 60 Hz cutoff frequency, segmented, and averaged to a single DBS time period. Then, the maximum amplitude value is taken. The filtered time signal is also transformed into the frequency domain and the spectral values at stimulation frequency f_0 and at its harmonics $f_{1...18}$ are taken.

3. Results

3.1. Presence of Magnetic Flux Densities in the Time Domain

The range of measured magnetic flux densities in the time domain is shown in Figure 3a for both applied bipolar electrode configurations. This figure demonstrates preprocessed and averaged signals of a single DBS period with 7.69 ms length (equals to the inverse of 130 Hz stimulation frequency), in which the maximum amplitudes were marked. For 3 mA bipolar mode, the maximum measured field at the sensor closest to the electrode (7 cm) was 6.6 pT and the maximum measured field at the sensor farthest away (15 cm) was 0.8 pT. All other measured field strengths were between these two values. For 1.5 mA bipolar mode, exactly half the values obtained at 3 mA were measured. The sampling rate of the MEG system limited the resolution of the signal over time. Marked amplitudes with asterisks and triangles in Figure 3a were entered in Table 2 under frequency bandwidth '0–1660 Hz', because the acquisition bandwidth was limited by the MEG system at 1660 Hz. Measured results with monopolar electrode configuration were also added to the table but not included in the figure, since monopolar mode caused much larger fields

(between 5 and 195 pT) that would stretch the figure. Figure 3b visualizes the result of how the maximum amplitude in time domain changed when sensors with different signal bandwidths were used. The set electrode configuration with 1.5 mA, 130 Hz, and 60 µs was measured electrically at the activated electrode contacts with 170 kHz sampling rate (black curve). A good agreement with the theoretical signal (red curve) can be seen, which had significantly more frequency components in the signal and thus perfectly represents the rectangular wave pulse. The maximum amplitude corresponds to 1.35 mA, since 90% of the applied stimulation amplitude is used for the stimulus pulse and 10% of the stimulation amplitude for the passive charge-balancing phase. The electrically measured signal was low-pass filtered with decreasing cut-off frequency and the maximum amplitude of the signal was taken in each case. Three additional curves are added to this figure which represent 5 kHz, 1660 Hz, and 1 kHz cut-off frequency. Maximum amplitudes were marked with black asterisks and, for more clarity, three more markers for 8 kHz, 10 kHz, and 500 Hz are added. It can be seen that the amplitude of the signal actually increases at very wide frequency bandwidths (10 to 85 kHz), but then as the bandwidth decreases, much fewer frequency components of the signal are considered which leads to amplitude reduction. For comparison, a magnetically measured signal (the exemplary signal measured at a large distance from the signals shown in Figure 3a was chosen) was inserted into a second y-axis. The pattern of the magnetically measured curve corresponded to the pattern of the electrically measured signal low-pass filtered with 1660 Hz. The maximum amplitude with 0.3 pT height changed when considering different sensor bandwidths; the amplitude became approximately 5 times larger with a 10 kHz bandwidth, and 1.6 and 17 times smaller with a 1 kHz and a 150 Hz bandwidth, respectively. The calculated values are given in Figure 2.

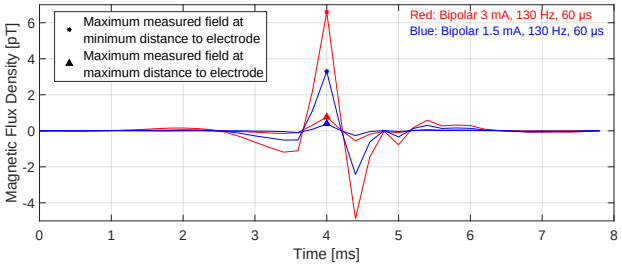

(**a**)

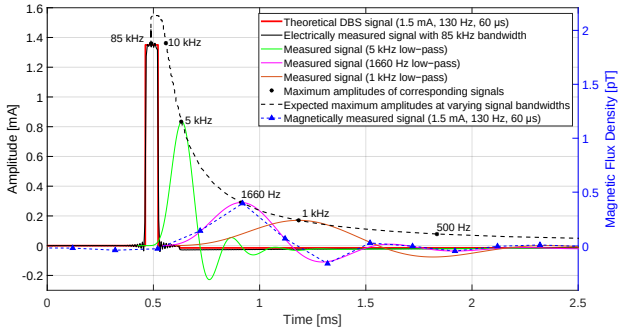

(**b**)

Figure 3. (**a**) The measured, preprocessed, and averaged time signal of a single DBS period for both bipolar configuration types, each considering an MEG sensor farthest from the electrode (small field) and a sensor closest to the electrode (larger field). The maximum amplitudes are marked with asterisk and triangle symbols, which represent the values with the highest SNR. (**b**) The DBS time signals in theory, electrically measured, and with different frequency bandwidths. The fewer frequency components there are in the signal, the smaller the maximum amplitude gets. The behavior of a magnetically measured signal exactly matches that of the electrically measured field with 1660 Hz low-pass.

Table 2. The measured magnetic flux densities from all MEG sensors.

Config.	Ampl. [mA], Pulse [µs], Freq. [Hz]	Available Magnetic Flux Densities [pT] within Bandwidth							
		0–10 kHz		0–1660 Hz		0–1 kHz		130 Hz	
		Min	Max	Min	Max	Min	Max	Min	Max
Bipolar	3.0, 60, 130	3.8	30	0.8	6.6	0.5	3.9	0.036	0.38
	1.5, 60, 130	1.9	15	0.4	3.3	1.9	10	0.018	0.19
Monopolar	1.5, 60, 130	-	-	5	195	-	-	1	20

3.2. Presence of Magnetic Flux Densities in the Frequency Domain

The range of measured magnetic flux densities in the frequency domain is illustrated in Figure 4a for the applied monopolar and for both applied bipolar electrode configurations. Markers represent the height of spectral values with a stimulation frequency of 130 Hz and the 18 corresponding harmonics ranging from 260 to 2470 Hz. The maximum frequency was limited by the sampling rate. The measured spectrum at the sensor closest to the electrode (7 cm) was marked by asterisks symbols and the spectrum at the sensor farthest away (15 cm) is marked by triangle symbols. All other measured spectra were between both markers. For 1.5 mA bipolar mode, exactly half the spectral values obtained at 3 mA were measured, i.e., 18 fT at the fundamental frequency for 1.5 mA stimulation and 36 fT for 3 mA stimulation. The decrease of spectral values after 1660 Hz is due to the system bandwidth. The flux densities in monopolar mode were much higher compared to the densities in bipolar mode with the same setting, this is because in bipolar mode, the reverse current in the connector and its corresponding wire canceled the field generated by the current flowing in the other direction, whereas in monopolar configuration, all current elements from the neurostimulator to the electrode within the cable and back within the saline solution contributed to the magnetic field. Therefore, the monopolar configuration could not be used to determine the position and rotation of the electrode. The measured spectral values at 130 Hz fundamental frequency corresponded exactly to the maximum amplitude in the 150 Hz low-pass filtered signal in the time domain. Corresponding values have been inserted in Table 2 under '130 Hz'. The spectrum of the ambient noise signal (with an equivalent noise bandwidth of 0.09) can be seen in Figure 4a. The corresponding measurement was performed without the phantom in the MEG. An increase in the noise floor was observed after placing the phantom into the MEG scanner without activating the stimulation current. This occurred because the neurostimulator was powered and was in stand-by-mode. Nevertheless, the background noise over all frequencies, especially over the frequencies of interest, was so low that the magnetic field generated by the stimulation was not affected. Figure 4b depicts the behavior of spectral values over the frequency of electrically measured, magnetically measured, and theoretical DBS signal. A good agreement between the theoretical signal (red curve) and the electrically measured signal (black curve) can be seen for frequencies up to 20 kHz. When the pulse width of stimulation increased to e.g., 120 or 240 µs, the magnitude spectrum loops became thinner and higher. In other words, the zeros move close to the origin (compare zeros at the frequencies 1/60, 1/120, and 1/240 Hz) and the spectral values became larger. Furthermore, the spectra of electrically measured signals with cut-off frequencies of 5 kHz, 1660 Hz, and 1 kHz were exhibited to this figure. The smaller the bandwidth, the fewer frequency components of the signal were measured. As a comparison, a magnetically measured spectrum (exemplary the spectrum measured at 15 cm distance to the DBS electrode as shown in Figure 4a is chosen) was inserted into a second y-axis. The course of the magnetically measured curve over the frequency corresponds to the course of the electrically measured spectrum low-pass filtered with 1660 Hz. At the fundamental frequency, a value of 18 fT was measured for 1.5 mA stimulation and 60 µs pulse width, which becomes twice and four times as large for double and quadruple pulse width, respectively.

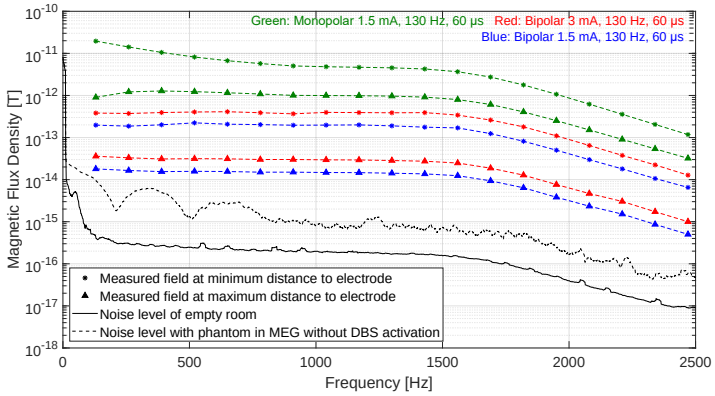

(**a**)

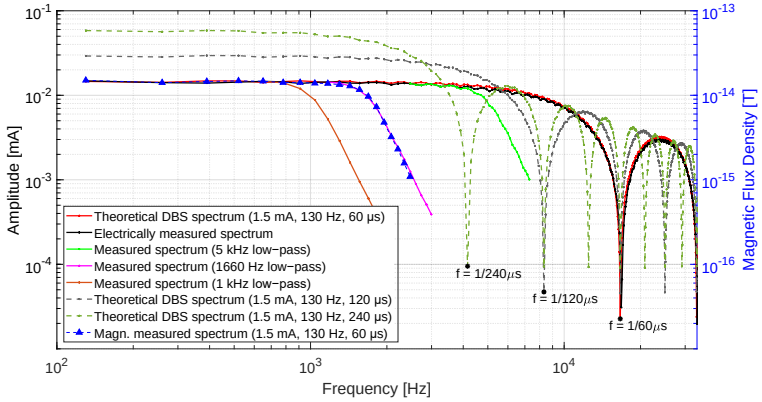

(**b**)

Figure 4. (**a**) The spectrum of the measured fields for the monopolar and both bipolar electrode configurations. The spectral values with 130 Hz stimulation frequency and at its corresponding harmonics are marked. In each case, an MEG sensor farthest from the electrode (small field) and a sensor closest to the electrode (larger field) were considered. (**b**) The DBS spectra in theory, electrically measured, and with different frequency bandwidths. The lower the bandwidth, the less frequency components of the DBS signal are considered. The behavior of a magnetically measured spectrum corresponds exactly to that of the electrically measured spectrum with 1660 Hz low-pass.

3.3. The Required Frequency Bandwidth of Magnetic Sensor

To determine the position and the rotational orientation of a DBS electrode in the phantom or patient head, the measurement data needed to be normalized to the maximum measured field closest to the electrode. In this manner, the magnetic field distribution around the phantom or patient head was normalized. This section investigates whether the behavior of the required magnetic field distribution across sensors depended on the frequency bandwidth of the sensor, i.e., whether the normalized behavior changed when more or less frequency components of the stimulation signal were measured. For that, we normalized the computed data of measurement number 1 in time and frequency domain according to Figure 2 across sensors. This allowed for a fair comparison and contrast of the data. Figure 5 provides the determined values for all 102 sensors obtained in time (by maximum value from averaged signal) and frequency domain (spectral value at third harmonic 520 Hz). The time values included frequency components up to 1660 Hz (limited by the MEG system), while the frequency values included only a single frequency component of the signal. The normalized root mean square error (NRMSE) between both data, which describes the quality of the similarity of both data, was 0.07% in this case.

Errors in % for other frequencies 130, 260, 390, 650, 780, 910, 1040, 1170, 1300 Hz are 0.16, 0.18, 0.09, 0.07, 0.08, 0.09, 0.1, 0.11, 0.13 respectively and the average error is 0.11%. Thus, the difference in values obtained with respect to the frequency and time values was negligible, since a measurement accuracy of 0.5% showed no electrode localization displacement [18] and all of the calculated error values are below 0.5%. Nevertheless, slight differences of the errors in the figure could be described by the following points: resolution of digitized time signals during measurement, filtering of signals during digital signal processing, and amplitude spectrum estimation during frequency domain transformation. This result demonstrated that the same behavior of magnetic field distribution around the phantom could be observed either by considering maximum amplitude in the time domain or single spectral amplitude at one of the DBS frequencies. Thus, for the determination of electrode position and rotation, the magnetic field generated by DBS could be measured both with a narrow-band sensor sensitive only at one of the DBS frequencies and with a broadband sensor with a higher bandwidth. However, it should be noted that the signal amplitudes became drastically smaller with decreasing bandwidth (see previous section) and thus the noise level of the sensor must have been significantly improved. This is part of the next section.

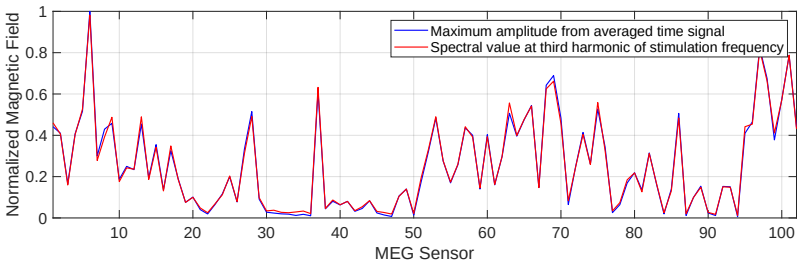

Figure 5. The comparison between normalized measured magnetic field values calculated in the time domain (maximum amplitude from averaged signal) and the frequency domain (spectral value at the third harmonic frequency of 130 Hz stimulation) for measurement number 1. The NRMS error between data is 0.07% and therefore negligible.

3.4. The Required Limit of Detection

This section investigates what minimum limit of detection (LOD) a sensor must have to measure the magnetic field produced during stimulation in order to perform electrode localization and rotational orientation detection. White noise was assumed for sensors so that the LOD value was identical for all spectral components. Since flicker noise (1/f-noise) is only noticeable at low frequencies and the first frequency of interest is the much higher stimulation frequency, this assumption represented a good approximation. For an even more detailed investigation, however, one should consider the LOD frequency behavior of a real sensor. The blue curve in Figure 6 shows the increase in measured maximum signal amplitude in double logarithmic scale for the bipolar electrode configuration with 1.5 mA amplitude, 130 Hz stimulation frequency, and 60 µs pulse width, and represents the same curve in black dashed line from Figure 3b. This curve was chosen as the reference curve for LOD investigations because it represented the expected amplitudes at maximum distance from the DBS electrode; and for accurate electrode localization, all magnetic fields around the phantom or patients' head should be measured, including more distant attenuated fields such as those from the curve. It resulted in a signal-to-noise ratio (SNR) of one. According to this curve, a LOD of at least 0.02 $pT/Hz^{0.5}$ was required if the sensor had an operating bandwidth that detected only the fundamental frequency component of the stimulation signal, e.g., if the sensor was sensitive between 100 and 150 Hz. The LOD requirement decreased by an order of magnitude to 0.2 $pT/Hz^{0.5}$ for a sensor with 1 kHz bandwidth and by about two orders of magnitude to 1.5 $pT/Hz^{0.5}$ for 10 kHz bandwidth. The LOD curve could be correspondingly degraded by a factor of two (red curve) for

twice the stimulation amplitude if it could be administered to the patient, since increasing the stimulation amplitude led to a proportional increase in the magnetic field. The LOD curve could be further increased by longer recording and averaging. A measurement of 1 minute resulted in a total of 130 Hz × 60 s = 7800 DBS periods and 10 minutes in 130 Hz × 60 s × 10 = 78,000 periods, which can be averaged. Since noise occurred stochastically, the standard deviation of the noise signal only grew by a factor of $\sqrt{N}$ when N single time periods were summed, and in relation, the signal grew by a factor of N. The SNR related to the signal amplitudes increased by $N/\sqrt{N} = \sqrt{N}$, which follows from the central limit theorem. Therefore, for 3 mA stimulation amplitude, a narrow-band sensor (sensitive at the fundamental frequency) could have a LOD of approximately 3 pT/Hz$^{0.5}$ for 1 min of recording (dark green) and approximately 10 pT/Hz$^{0.5}$ for 10 min of recording (red dashed). According to our physicians, a measurement time of 10 min in the MEG scanner is reasonable for the patient. The magnetic field could be increased again by a factor of 2 or 4 in the low frequencies when the stimulation pulse width was increased from 60 µs to 120 or 240 µs, however, only few patients would tolerate this. The corresponding LOD could thus be reduced for sensors with narrow and limited bandwidth (magenta curve and black curve), whereas the pulse width for the LOD had no effect for sensors with a bandwidth of 10 kHz or more.

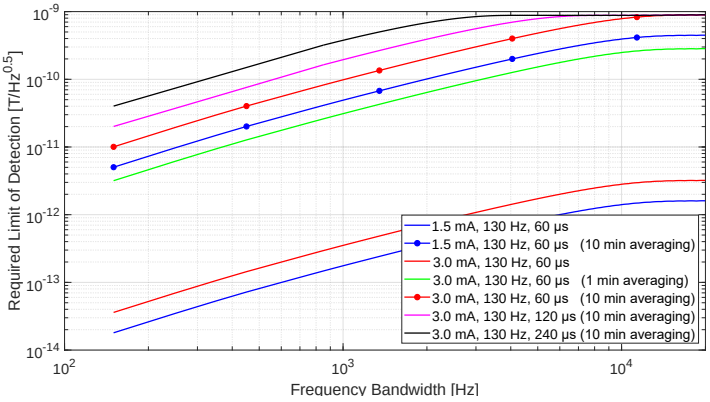

Figure 6. The required limit of detection (LOD) curves with respect to frequency bandwidth of a sensor for different bipolar electrode configuration types and measurement duration. As an example, the minimum required LOD with 150 Hz bandwidth is around 20 fT/Hz$^{0.5}$ for 1.5 mA amplitude, 60 µs pulse width, and 130 Hz frequency without averaging. The noise level of a sensor can be 1 nT/Hz$^{0.5}$ between 130 Hz and 10 kHz for 3 mA amplitude, 60 µs pulse width, and 130 Hz frequency with 10 min of averaging.

4. Discussion

In this paper, the required sensing characteristics of magnetic field sensors needed to measure the magnetic field induced by DBS were investigated in order to determine the position and rotation of a directional DBS electrode. The work focused mainly on the minimum requirements to answer the question of what minimum frequency bandwidth and minimum detection limit a sensor must have so that the magnetic field remains measurable at measurement points at a realistic distance from the electrode. The investigations were performed in a state-of-the-art SQUID-based MEG scanner. SQUID sensors are still the gold standard of measuring magnetic fields, i.e., the most sensitive magnetic field sensors, with which resolutions in the femto Tesla range can be achieved. Such a high sensitivity is not necessary for this application because the stimulation current generates a magnetic field much larger than the magnetic field generated by human brain activity. Thus, this application represents a potential area for future sensor development, (magnetoelectric or surface acoustic wave sensors) by both industry and research institutes.

Our recently presented method [19] for determining electrode position and electrode rotation with magnetic field measurements is intended to provide an alternative to conventional neuroimaging techniques. The neuroimaging approach localizes the DBS electrode by visual inspection via metal artifacts of the electrode contacts on postoperative CT or MRI. The rotation of the electrode is determined by visual inspection over artifacts created by the radiopaque marker over the electrode contacts on X-rays, standard CT, flat-panel CT, or rotational fluoroscopy. All currently available methods expose the patient to radiation. The method based on magnetic field measurements is harmless (non-radiative and non-invasive) and safe for the patient. This simply involves programming and setting up the neurostimulator with the bipolar electrode configuration and appropriate choice of stimulation parameters to generate a defined magnetic field. The magnetic field distribution can then be measured around the patient's head or phantom and used with precise forward modeling and localization algorithms to derive electrode position and rotation.

The investigations in this paper were performed with SQUID measurements in a clinical MEG scanner using a head phantom with dimensions comparable to a human head and clinically used DBS stimulation parameters. First, the presence of the magnetic field was analyzed in both the time domain and the frequency domain. The following observations were made:

- For 1.5 mA, 130 Hz, and 60 µs bipolar mode, the maximum measured field in the time domain at the sensor closest to the electrode (7 cm) was 3.3 pT and the maximum measured field at the farthest sensor (15 cm) was 0.4 pT. The measured amplitude in the frequency domain at the stimulation frequency was 0.2 pT for the sensor closest to the electrode and the spectral value at the sensor farthest away was 18 fT.
- An increase in the stimulation amplitude from 1.5 to 3 mA (with pulse width and frequency remaining the same) leads to a proportional increase in the magnetic field amplitude in both the time and frequency domain.
- The maximum amplitude of the magnetic field in the time domain (that is generated by the broadband stimulus signal) depends on the given frequency bandwidth of the sensor or system. Since the SQUID sensor acts like a low-pass filter due to the system frequency bandwidth (0–1660 Hz limited by the MEG system), the maximum amplitude is attenuated by −13 dB (20% amplitude compared to a broadband amplitude).
- Measured magnetic field amplitudes in the frequency domain at the stimulation frequency and at its harmonics up to 1660 Hz are approximately equal in height. The spectral values decrease due to the system bandwidth of 1660 Hz.
- An increase in the stimulation pulse width from 60 to 120 µs (amplitude and frequency remain the same) results in an increase in spectral values at lower frequencies (even doubling up to 1 kHz), while the main magnitude loop in the spectrum comes closer to the origin and higher. The maximum amplitude in the time domain also increases with increasing stimulation pulse width. The same behavior applies to the maximum amplitude in the time domain.

The same behavior between the measured and the normalized fields at 102 points around the phantom could be observed whether the maximum amplitude in the time domain or a single spectral amplitude at one of the DBS frequencies (stimulation frequency or its harmonics) was considered. Therefore, from the methodological perspective of electrode localization, it makes no difference with which bandwidth and which frequency component is measured, but care should be taken to measure at a lower frequency (e.g., components between 130 Hz and 3 kHz for 60 µs pulse width or between 130 Hz and 1.5 kHz for 120 µs pulse width), because the height of the magnetic field slowly decreases with respect to frequency and its dependence on stimulation pulse width. Of course, this only applies to a sensor that has sufficient sensitivity. Otherwise, however, the signal amplitudes become drastically smaller with decreasing bandwidth and thus the detection limit of the sensor must be significantly improved. The minimum required detection limit depends on the strength of the magnetic field to be detected, which in turn depends on

various factors such as measurement distance to the electrode, bandwidth of the magnetic sensor, stimulation amplitude, and stimulation pulse width. The stimulation parameters are already given in a patient (1.5 to 3 mA and 60 µs), even if the amplitude and pulse width can be slightly increased for a short measurement period. Since all magnetic fields around the patient's head should be measured for precise electrode localization and especially for the determination of electrode rotation, 15 cm was taken as a reference value for the distance. Thus, the required detection limit depends mainly on the bandwidth of the magnetic sensor. For example, a LOD of at least 0.04 $pT/Hz^{0.5}$ is required for 3 mA, 130 Hz, and 60 µs stimulation if the sensor has an operating bandwidth that captures only the fundamental frequency component of the stimulation signal. The LOD requirement drops by an order of magnitude (to 0.4 $pT/Hz^{0.5}$) for a sensor with a 1 kHz bandwidth and by approximately two orders of magnitude (to 3 $pT/Hz^{0.5}$) for a 10 kHz bandwidth. In addition, a longer measurement duration can reduce the noise of the sensor by averaging (SNR increases with the square root of the number of averages when the noise is white noise), so that for a 10-minute measurement (easily tolerable for a patient), a LOD of 10 $pT/Hz^{0.5}$ is sufficient for a narrow-band sensor which is sensitive only at the fundamental frequency (100 $pT/Hz^{0.5}$ for a 1 kHz bandwidth, and 1 $nT/Hz^{0.5}$ for a 10 kHz bandwidth). Further digital signal processing can improve the SNR. Here we can mention the matched filter, which is a method to detect a known signal that is embedded in noise [31,32]. The stimulation signal is well-known since it is set in advance on the neurostimulator. The filter maximizes the SNR of the stimulation signal being detected with respect to the noise. However, this was not part of the work presented at this time.

In addition to the sensor requirements that have been investigated in this correspondence, there are often common demands on sensors, such as operation at ambient temperature without cooling, reduced sensor dimensions, low-power consumption, and high dynamic magnetic field range. However, these are not essential for the measurement of the DBS magnetic field. Therefore, the standard conditions that have been used for the sensors in our experiment suggest that the development of a non-radiative and non-invasive method that is capable of precise determination of the position and rotation of a DBS electrode are suitable, and represent an important development in DBS therapy.

5. Conclusions

This work has investigated the minimum limit of detection (LOD) a magnetic sensor must have in order to be used to measure the magnetic field generated by DBS. In order to determine this, magnetic measurements were performed with a state-of-the-art SQUID-based MEG scanner and analyzed. The results have shown that the required LOD depends mainly on the frequency bandwidth of the sensor and on the measurement duration, since other factors, such as the applied DBS stimulation parameters and the measurement distances to the electrode, are predetermined. For a narrow-band sensor that is sensitive only at the stimulation frequency or at its corresponding harmonics, a LOD of at least 0.04 $pT/Hz^{0.5}$ is required for 3 mA and 60 µs stimulation. This LOD value increases by an order of magnitude for a sensor with a 1 kHz bandwidth and by approximately two orders of magnitude for a broadband sensor with a 10 kHz bandwidth. With recording times of a few minutes and averaging, this value can be increased by another two orders of magnitude.

Author Contributions: conceptualization, M.Y. and G.D.; methodology, M.Y., M.H., A.-K.H., and M.B.; software, M.Y.; validation, M.Y. and M.B.; formal analysis, M.Y., G.D., and M.H.; investigation, M.Y.; resources, M.Y., M.H., A.-K.H., and A.S.; data acquisition, M.B. and A.S.; writing—original draft preparation, M.Y.; writing—review and editing, G.D., M.B., A.S., A.-K.H., and M.H.; visualization, M.Y.; supervision, G.D. and M.H.; project administration, G.D., M.H. and A.S. All authors have read and agreed to the published version of the manuscript.

Funding: This work was supported by the German Research Foundation (Deutsche Forschungsgemeinschaft, DFG) through the project T1 of the Collaborative Research Centre CRC 1261 'Magnetoelectric Sensors: From Composite Materials to Biomagnetic Diagnostics'.

Institutional Review Board Statement: Not applicable.

Informed Consent Statement: Not applicable.

Data Availability Statement: Not applicable.

Acknowledgments: We would like to express our very great appreciation to the group of Schnitzler from the Heinrich-Heine-University Düsseldorf, in particular to Levent Kandemir and Holger Krause, for their support in performing the MEG measurements.

Conflicts of Interest: The funders had no role in the design of the study; in the collection, analyses, or interpretation of data; in the writing of the manuscript, or in the decision to publish the results.

References

1. Limousin, P.; Foltynie, T. Long-term outcomes of deep brain stimulation in Parkinson disease. *Nat. Rev. Neurol.* **2019**, *15*, 234–242. [CrossRef] [PubMed]
2. Schuepbach, W.M.M.; Rau, J.; Knudsen, K.; Volkmann, J.; Krack, P.; Timmermann, L.; Hälbig, T.D.; Hesekamp, H.; Navarro, S.M.; Meier, N.; et al. Neurostimulation for Parkinson's disease with early motor complications. *N. Engl. J. Med.* **2013**, *368*, 610–622. [CrossRef] [PubMed]
3. Krack, P.; Volkmann, J.; Tinkhauser, G.; Deuschl, G. Deep Brain Stimulation in Movement Disorders: From Experimental Surgery to Evidence-Based Therapy. *Mov. Disord.* **2019**, *34*, 1795–1810. [CrossRef] [PubMed]
4. Lozano, A.M.; Lipsman, N.; Bergman, H.; Brown, P.; Chabardes, S.; Chang, J.W.; Matthews, K.; McIntyre, C.C.; Schlaepfer, T.E.; Schulder, M.; et al. Deep brain stimulation: Current challenges and future directions. *Nat. Rev. Neurol.* **2019**, *15*, 148–160. [CrossRef] [PubMed]
5. Wagle Shukla, A.; Zeilman, P.; Fernandez, H.; Bajwa, J.A.; Mehanna, R. DBS Programming: An Evolving Approach for Patients with Parkinson's Disease. *Parkinsons Dis.* **2017**, *2017*, 8492619. [CrossRef] [PubMed]
6. Volkmann, J.; Herzog, J.; Kopper, F.; Deuschl, G. Introduction to the programming of deep brain stimulators. *Mov. Disord.* **2002**, *17* (Suppl. S3), S181–S187. [CrossRef] [PubMed]
7. Picillo, M.; Lozano, A.M.; Kou, N.; Munhoz, R.P.; Fasano, A. Programming Deep Brain Stimulation for Tremor and Dystonia: The Toronto Western Hospital Algorithms. *Brain Stimul.* **2016**, *9*, 438–452. [CrossRef]
8. Muthuraman, M.; Bange, M.; Koirala, N.; Ciolac, D.; Pintea, B.; Glaser, M.; Tinkhauser, G.; Brown, P.; Deuschl, G.; Groppa, S. Cross-frequency coupling between gamma oscillations and deep brain stimulation frequency in Parkinson's disease. *Brain* **2020**, *143*, 3393–3407. [CrossRef]
9. Stoker, V.; Krack, P.; Tonder, L.; Barnett, G.; Durand-Zaleski, I.; Schnitzler, A.; Houeto, J.L.; Timmermann, L.; Rau, J.; Schade-Brittinger, C.; et al. Deep Brain Stimulation Impact on Social and Occupational Functioning in Parkinson's Disease with Early Motor Complications. *Mov. Disord. Clin. Pract.* **2020**, *7*, 672–680. [CrossRef]
10. Steigerwald, F.; Matthies, C.; Volkmann, J. Directional Deep Brain Stimulation. *Neurotherapeutics* **2019**, *16*, 100–104. [CrossRef]
11. Merola, A.; Romagnolo, A.; Krishna, V.; Pallavaram, S.; Carcieri, S.; Goetz, S.; Mandybur, G.; Duker, A.P.; Dalm, B.; Rolston, J.D.; et al. Current Directions in Deep Brain Stimulation for Parkinson's Disease—Directing Current to Maximize Clinical Benefit. *Neurol. Ther.* **2020**, *9*, 25–41. [CrossRef] [PubMed]
12. Kramme, J.; Dembek, T.A.; Treuer, H.; Dafsari, H.S.; Barbe, M.T.; Wirths, J.; Visser-Vandewalle, V. Potentials and Limitations of Directional Deep Brain Stimulation: A Simulation Approach. *Stereotact. Funct. Neurosurg.* **2021**, *99*, 65–74. [CrossRef] [PubMed]
13. Engelhardt, J.; Guehl, D.; Damon-Perrière, N.; Branchard, O.; Burbaud, P.; Cuny, E. Localization of Deep Brain Stimulation Electrode by Image Registration Is Software Dependent: A Comparative Study between Four Widely Used Software Programs. *Stereotact. Funct. Neurosurg.* **2018**, *96*, 364–369. [CrossRef] [PubMed]
14. Ellenbogen, J.; Tuura, R.; Ashkan, K. Localisation of DBS Electrodes Post-Implantation, to CT or MRI? Which Is the Best Option? *Stereotact. Funct. Neurosurg.* **2018**, *96*, 347–348. [CrossRef] [PubMed]
15. Lange, F.; Steigerwald, F.; Engel, D.; Malzacher, T.; Neun, T.; Fricke, P.; Volkmann, J.; Matthies, C.; Capetian, P. Longitudinal Assessment of Rotation Angles after Implantation of Directional Deep Brain Stimulation Leads. *Stereotact. Funct. Neurosurg.* **2020**. [CrossRef] [PubMed]
16. Hunsche, S.; Neudorfer, C.; Majdoub, F.E.; Maarouf, M.; Sauner, D. Determining the Rotational Orientation of Directional Deep Brain Stimulation Leads Employing Flat-Panel Computed Tomography. *Oper. Neurosurg.* **2019**, *16*, 465–470. [CrossRef] [PubMed]
17. Reinacher, P.C.; Krüger, M.T.; Coenen, V.A.; Shah, M.; Roelz, R.; Jenkner, C.; Egger, K. Determining the Orientation of Directional Deep Brain Stimulation Electrodes Using 3D Rotational Fluoroscopy. *AJNR Am. J. Neuroradiol.* **2017**, *38*, 1111–1116. [CrossRef]
18. Yalaz, M.; Teplyuk, A.; Deuschl, G.; Höft, M. Dipole Fit Localization of the Deep Brain Stimulation Electrode Using 3D Magnetic Field Measurements. *IEEE Sens. J.* **2020**, *20*, 9550–9557. [CrossRef]
19. Yalaz, M.; Noor, S.; McIntyre, C.; Butz, M.; Schnitzler, A.; Deuschl, G.; Höft, M. DBS electrode localization and rotational orientation detection using SQUID-based magnetoencephalography. *J. Neural. Eng.* **2021**. [CrossRef]
20. Yalaz, M.; Teplyuk, A.; Muthuraman, M.; Deuschl, G.; Höft, M. The Magnetic Properties of Electrical Pulses Delivered by Deep-Brain Stimulation Systems. *IEEE Trans. Instrum. Meas.* **2020**, *69*, 4303–4313. [CrossRef]

21. Boto, E.; Holmes, N.; Leggett, J.; Roberts, G.; Shah, V.; Meyer, S.S.; Muñoz, L.D.; Mullinger, K.J.; Tierney, T.M.; Bestmann, S.; et al. Moving magnetoencephalography towards real-world applications with a wearable system. *Nature* **2018**, *555*, 657–661. [CrossRef] [PubMed]
22. Hill, R.M.; Boto, E.; Rea, M.; Holmes, N.; Leggett, J.; Coles, L.A.; Papastavrou, M.; Everton, S.K.; Hunt, B.A.; Sims, D.; et al. Multi-channel whole-head OPM-MEG: Helmet design and a comparison with a conventional system. *NeuroImage* **2020**, *219*, 116995. [CrossRef] [PubMed]
23. Tierney, T.M.; Holmes, N.; Mellor, S.; López, J.D.; Roberts, G.; Hill, R.M.; Boto, E.; Leggett, J.; Shah, V.; Brookes, M.J.; et al. Optically pumped magnetometers: From quantum origins to multi-channel magnetoencephalography. *NeuroImage* **2019**, *199*, 598–608. [CrossRef] [PubMed]
24. Su, J.; Niekiel, F.; Fichtner, S.; Kirchhof, C.; Meyners, D.; Quandt, E.; Wagner, B.; Lofink, F. Frequency Tunable Resonant Magnetoelectric Sensors for the Detection of Weak Magnetic Field. *J. Micromech. Microeng.* **2020**, *30*. [CrossRef]
25. Salzer, S.; Jahns, R.; Piorra, A.; Teliban, I.; Reermann, J.; Höft, M.; Quandt, E.; Knöchel, R. Tuning fork for noise suppression in magnetoelectric sensors. *Sens. Actuators A Phys.* **2016**, *237*, 91–95. [CrossRef]
26. Su, J.; Niekiel, F.; Fichtner, S.; Thormaehlen, L.; Kirchhof, C.; Meyners, D.; Quandt, E.; Wagner, B.; Lofink, F. AlScN-based MEMS magnetoelectric sensor. *Appl. Phys. Lett.* **2020**, *117*, 132903. [CrossRef]
27. Kittmann, A.; Durdaut, P.; Zabel, S.; Reermann, J.; Schmalz, J.; Spetzler, B.; Meyners, D.; Sun, N.X.; McCord, J.; Gerken, M.; et al. Wide Band Low Noise Love Wave Magnetic Field Sensor System. *Sci. Rep.* **2018**, *8*, 278. [CrossRef] [PubMed]
28. Oostenveld, R.; Fries, P.; Maris, E.; Schoffelen, J.M. Open source software for advanced analysis of MEG, EEG, and invasive electrophysiological data. *Comput. Intell. Neurosci.* **2011**, *2011*, 156869. [CrossRef]
29. Welch, P. The use of fast Fourier transform for the estimation of power spectra: A method based on time averaging over short, modified periodograms. *IEEE Trans. Audio Electroacoust.* **1967**, *15*, 70–73. [CrossRef]
30. Heinzel, G.; Rüdiger, A.; Schilling, R. *Spectrum and Spectral Density Estimation by the Discrete Fourier transform (DFT), Including a Comprehensive List of Window Functions and Some New Flat-Top Windows*; Max-Planck-Institut für Gravitationsphysik (Albert-Einstein-Institut): Hannover, Germany. Available online: http://hdl.handle.net/11858/00-001M-0000-0013-557A-5 (accessed on 15 February 2002).
31. Wu, N. Using a Matched Filter to Improve SNR of Radio Maps. *Astron. Data Anal. Softw. Syst.* **1992**, *25*, 291.
32. Sun, Y.; Farzan, F.; Dominguez, L.G.; Barr, M.S.; Giacobbe, P.; Lozano, A.M.; Wong, W.; Daskalakis, Z.J. A novel method for removal of deep brain stimulation artifact from electroencephalography. *J. Neurosci. Methods* **2014**, *237*, 33–40. [CrossRef] [PubMed]

Key Findings and Scientific Implications

- The required minimum detection limit of a magnetic sensor depends on several factors but mainly on the operating frequency bandwidth of the sensor, since other factors — such as the strength of the magnetic field to be detected — are predetermined to a certain extent.
- From the methodological perspective of electrode localization and orientation detection, it does not matter which bandwidth the sensor has and which frequency component of the stimulation signal is measured, as long as the sensor bandwidth includes at least one frequency component of the stimulation signal and the magnetic field can be reliably measured.
- The narrower the frequency bandwidth of a magnetic sensor, the higher the minimum detection limit requirements of the sensor. Conversely, the wider the bandwidth of a sensor, the lower the detection limit requirements of the sensor.
- An LOD of at least $0.04\,\mathrm{pT/Hz^{0.5}}$ is required for clinically used stimulation parameter settings and realistic distances between the stimulating electrode and the sensor, which is sensitive only to the stimulation frequency.
- The LOD requirement decreases by one order of magnitude to an estimated $0.4\,\mathrm{pT/Hz^{0.5}}$ for a sensor with a bandwidth of 1 kHz (between 0 and 1 kHz) and by approximately two orders of magnitude to $3\,\mathrm{pT/Hz^{0.5}}$ for a sensor with a bandwidth of 10 kHz (between 0 and 10 kHz).
- The LOD requirement decreases by another two orders of magnitude for recording times of a few minutes if the averaging of periodic stimulation pulses is performed.

3.5 Determining the Rotational Orientation of Directional Deep Brain Stimulation Electrodes Using Magnetoencephalography

M. Yalaz, G. Deuschl, M. S. Noor, M. Butz, A. Schnitzler, A.-K. Helmers, and M. Höft, "Determining the rotational orientation of directional deep brain stimulation electrodes using magnetoencephalography," in *Journal of Neural Engineering*, vol. 18, no. 5, p. 056056, October 2021, doi: 10.1088/1741-2552/ac2c4d.

Information about the amount of own contribution to this publication:

Conceptualization	Planning	Implementation	Manuscript preparation
high	high	high	high

© 2021 IOP Publishing Ltd. Reproduced with permission. All rights reserved. This is the Accepted Manuscript version of an article accepted for publication in Journal of Neural Engineering. IOP Publishing Ltd is not responsible for any errors or omissions in this version of the manuscript or any version derived from it. The version of record is available online at https://doi.org/10.1088/1741-2552/ac2c4d.

JOURNAL OF NEURAL ENGINEERING, ACCEPTED VERSION OF THE ARTICLE 1 of 22

IOP Publishing

Determining the Rotational Orientation of Directional Deep Brain Stimulation Electrodes using Magnetoencephalography

Mevlüt Yalaz[1], Günther Deuschl[2], M. Sohail Noor[3], Markus Butz[4], Alfons Schnitzler[4], Ann-Kristin Helmers[5], and Michael Höft[1]

[1] Chair of Microwave Engineering, Christian-Albrechts-Universität zu Kiel, 24143 Kiel, Germany
[2] Department of Neurology, Christian-Albrechts-Universität zu Kiel, 24105 Kiel, Germany
[3] Department of Biomedical Engineering, Case Western Reserve University, Cleveland, OH, United States
[4] Institute of Clinical Neuroscience and Medical Psychology, Heinrich-Heine-Universität Düsseldorf, 40225 Düsseldorf, Germany
[5] Department of Neurosurgery, Christian-Albrechts-Universität zu Kiel, 24105 Kiel, Germany

Abstract. *Objective.* The aim of the present study was to evaluate the effect of different electrode configurations on the accuracy of determining the rotational orientation of the directional DBS electrode with our previously published MEG-based method. *Approach.* A directional DBS electrode, along with its implantable pulse generator, was integrated into a head phantom and placed within the MEG sensor array. Predefined bipolar electrode configurations, based on activation of different directional and omnidirectional contacts of the electrode, were set to generate a defined magnetic field during stimulation. This magnetic field was then measured with MEG. Finite element modeling and model fitting approach were used to calculate electrode orientation. *Main results.* The accuracy of electrode orientation detection depended on the electrode configuration: The vertical configuration (activation of two directional contacts arranged one above the other) achieved an average accuracy of only about 41°. The diagonal configuration (activation of the electrode tip and a single directional contact at the next higher level of the electrode) achieved an accuracy of 13°, while the horizontal electrode configuration (activation of two adjacent directional contacts at the same electrode level) achieved the best accuracy of 6°. The accuracy of orientation detection of the DBS electrode depends on the change in spatial distribution of the magnetic field with the rotation of the electrode along its own axis. In the vertical configuration, rotation of the electrode has a small effect on the magnetic field distribution, while in the diagonal or horizontal configuration, electrode rotation has a significant effect on the magnetic field distribution. *Significance.* Our work suggests that in order to determine rotational orientation of a DBS electrode using MEG, horizontal configuration should be used as it provides the most accurate results compared to other possible configurations.

Keywords: Deep brain stimulation, magnetoencephalography, SQUID, directional DBS electrode, electrode configuration, magnetic field measurement, rotational orientation detection.

1. Introduction

Deep brain stimulation (DBS) is a surgical procedure used to treat a variety of movement disorders such as Parkinson's disease, essential tremor, and dystonia, and is being investigated for use in many other neurological disorders [1, 2, 3]. Currently, more than 200,000 patients worldwide have been implanted with a DBS system. During surgery, a stimulating electrode (consisting of a linear array of stimulating contacts) is implanted in a specific target region of the patients' brain, which is connected to a battery-powered implanted pulse generator (IPG) in the chest near the collarbone.

Recently, new DBS directional electrode designs with segmented contacts (divided into three segments along the circumference of the electrode) have become available allowing control of the electric fields in a desired direction [4, 5]. Initial and current studies indicate improved therapeutic effects and lower side effect thresholds compared with electrodes with standard ring contacts [6, 7]. However, the long-term clinical utility of directional electrodes is still under investigation. To realize the full potential of this technology, the correct localization and rotational orientation of the electrode in the patient-specific neuroanatomy must be determined in order to interpret the observed stimulation effects on the patient meaningfully, and to guide and facilitate the programming of the neurostimulator. Although no generally accepted protocol for electrode localization has been established to date, solely approaches based on fusion of pre- and postoperative neuroimaging data are available [8, 9]. Moreover, alternative imaging modalities such as electroencephalography (EEG) and magnetoencephalography (MEG) are currently being explored [10, 11, 12, 13].

Our previous work [13] has demonstrated the feasibility of localizing and detecting electrode orientation using MEG. The current work investigates the accuracy with which rotational orientation can be determined as there are currently no established means of determining the rotational orientation of the electrode in the patients' brain. Current methods for determining electrode orientation are using stereotactic x-rays, standard computed tomography (CT), flat-panel CT, and rotational fluoroscopy [14, 15, 16]. They all rely on high quality images because specific artifact patterns must be calculated from these images based on radiopaque orientation markers which are located dorsally to the electrode contacts. However, the underlying symmetrical artifact of the electrode exhibits a 180° symmetry, which limits orientation detection to two possible solutions. Neither imaging technique is currently able to resolve this ambiguity without further measurements. Existing software tools, such as the DiODe algorithm integrated in the open-source Lead-DBS toolbox [17] and the commercial Elements® Lead Localization software package, rely on the intended orientation and assume that a deviation of more than ±90° is very unlikely. If such a deviation occurs in clinical practice, it may lead to errors in the analysis of stimulation effects and to incorrect choice of stimulation parameters. Recently, solutions to the ambiguity of artifact symmetry have been proposed, but additional x-ray images are required to resolve 100% of cases [18, 19]. In addition, all of the existing methods expose patients to ionizing

radiation, which is clearly suboptimal and completely hampers further research in this direction and the conduct of long-term clinical trials. Unfortunately, it has been demonstrated that there is still ongoing displacement and rotation of the electrode in the subsequent days after electrode implantation due to lead torsion and lead migration [20, 21, 22, 23, 24], and any trauma or surgical intervention may further change the position and orientation. Although other clinical studies have shown no directional change after the first postoperative day [25], it is still of great importance to determine if and how much directional electrodes move and continue to rotate. Therefore, EEG or MEG, which are non-invasive and non-radiative, provide alternative imaging modalities for detecting electrode orientation by measuring stimulation-induced DBS magnetic fields that overcome the underlying drawbacks of current postoperative imaging methods without exposing patients to radiation at all. The objective of this work is to evaluate the effect of different electrode configuration on the accuracy of determining the rotational orientation of the directional DBS electrode with our previously published MEG-based method [13].

2. Methods

First, we placed the electrode at a well-known position in the phantom and programmed the IPG or neurostimulator with predefined bipolar electrode configuration settings, which we divided into three configuration types (vertical, diagonal, and horizontal electrode configuration) with different current flow direction. Then, we placed the phantom within the MEG sensor array and measured the magnetic field distribution generated during stimulation. For data analysis, we developed an accurate finite element electromagnetic model to compute the expected magnetic fields generated at the MEG sensor locations, with each electrode orientation accounted for in the model. A model-fitting approach was used in the following to find the model that minimized the error between simulated and measured data. The orientation of the electrode in the found model determined the orientation detection result. In this way, the work provides insight into the accuracies achievable in orientation determination and which electrode configuration type is the most promising among the investigated cases for use in such problems.

2.1. Head Phantom

The head phantom used in this study is depicted in Fig. 1a. It is the similar model as used in our previous works [12, 13]. The cylindrical body with dimensions comparable to a human head (diameter 150 mm, height 250 mm) was made of acrylic glass and was therefore neither electrically conductive nor magnetic. It was filled with an isotonic fluid (NaCl 0.9%) to mimic the electrical conductivity of a human brain. A DBS system by Boston Scientific Inc. (Boston Scientific, Marlborough, MA, USA), consisting of a current-controlled IPG (Vercise™ PC) and a directional electrode (Versice

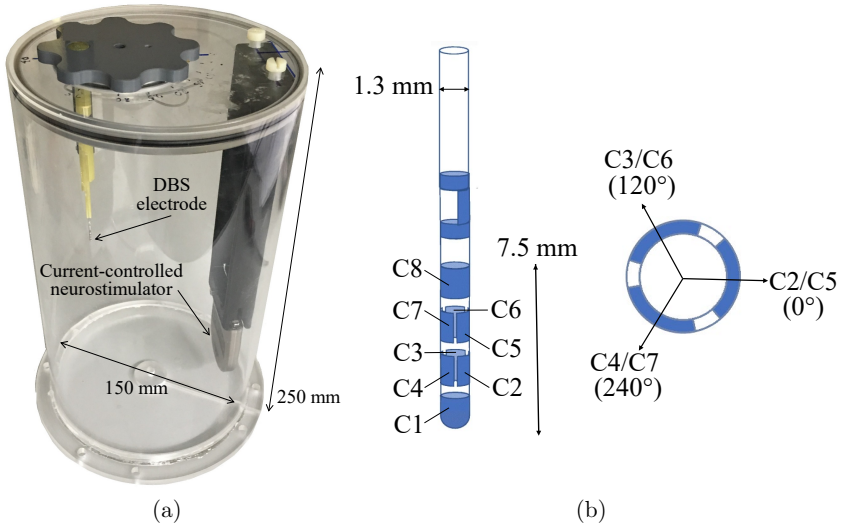

Figure 1. (a) Cylindrical phantom with integrated current-controlled neurostimulator (Vercise™ PC) and directional electrode (Vercise Cartesia™). **(b)** Directional DBS electrode in side view (left) and top view (right). Contact C1 and C8 are full-ring contacts, and the others are contacts with equally spaced segments, each spanning 120° of the circumference.

Cartesia™), was used as it is in routine clinical use. This system is based on stimulation with conventional rectangular pulses that include a stimulation pulse phase and a passive charge-balancing phase. The electrode has been integrated and fixed exactly at 35 mm depth in the phantom. In addition, we used non-magnetic material for all other components used in the phantom. The structure of the directional DBS electrode is illustrated in Fig. 1b in side view (left) and top view (right). It consists of eight individually actuated platinum-iridium contacts (C1-C8), with the two middle contact levels divided into three contacts, each spanning 120° of the circumference. Any combination of these contacts can be activated to steer the stimulation current direction. This technology, which is also known as Multiple Independent Current-Controlled (MICC) technology, has allowed us to set any desired electrode configuration. Therewith, the direction of the current flow in the phantom could be influenced and a known magnetic field can be generated, which was subsequently measured with the MEG system. Three different configuration types were investigated in the framework of this study, which will be discussed in more detail in Section 2.3.

2.2. MEG Preparation

Several preparatory steps were performed before starting the actual MEG recording. Four head position indicator (HPI) coils were attached to the surface of the head phantom, and a circular template with three landmarks (designated as nasion, right pre-auricular, and left pre-auricular) was attached to the circular cap of the cylinder.

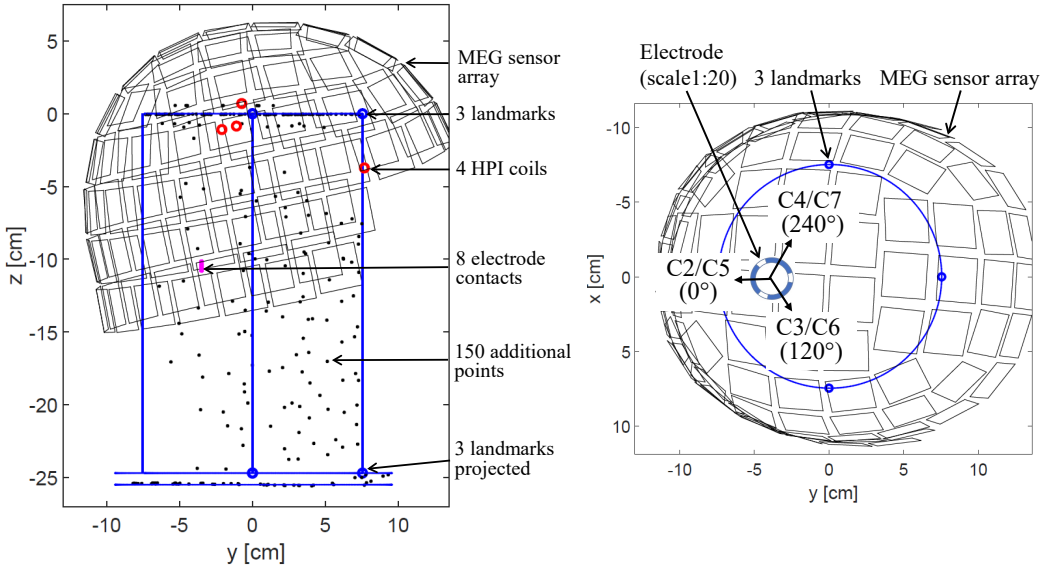

(a) (b)

Figure 2. (a) Side view of the cylindrical phantom in the helmet-shaped MEG sensor array including the real position of the electrode, and positions of the landmarks, HPI coils, and additional points. **(b)** Top view of the phantom in the MEG illustrating the orientation of each segmented electrode contact.

Then, a point digitizer (Fastrak, Polhemus) was used to localize anatomical reference points (nasion, left pre-auricular, and right pre-auricular) and HPI coils. Furthermore, 300 additional points were localized around the phantom to improve the accuracy of the spanned coordinate system of the phantom. The digitized positions of the anatomical landmarks on the cylinder cap in [x, y, z] direction were as follows:

- Nasion: [0, 75.52 mm, 0]
- Right pre-auricular: [74.51 mm, 0, 0]
- Left pre-auricular: [-75.11 mm, 0, 0]

The radius of the cylindrical phantom was 75 mm, so the digitizing process was performed with an accuracy of 0.5 mm (given by the error of nasion and right pre-auricular). As a result of the digitization process, the cap of the cylindrical phantom was exactly on the xy-plane, the longitudinal axis of the cylinder was on the z-axis, and the origin of the coordinate system was at the center of the cylinder cap (see Fig. 2). This figure also illustrates all digitized points, and the known position and orientation of the electrode fixed in the phantom. We define the orientation of electrode contacts C2 and C5 as angle 0°, which points exactly into the negative y-axis. The angle for contacts C3 and C6 is 120°, and for contacts C4 and C7 is 240° (as also demonstrated in Fig. 1b). The phantom was then placed into the MEG scanner and the positions of the MEG sensors were automatically determined in phantom coordinates by the MEG system

Table 1. Performed MEG measurements.

Configuration	Number	Contacts: (-) vs. (+)
Vertical	#1	C2 vs. C5
	#2	C3 vs. C6
	#3	C4 vs. C7
Diagonal	#4	C1 vs. C2
	#5	C1 vs. C3
	#6	C1 vs. C4
Horizontal	#7	C2 vs. C3
	#8	C3 vs. C4
	#9	C4 vs. C2

itself. The relationship between the MEG coordinate system and phantom coordinate system was determined by applying current at a specific frequency to the HPI coils and determining their positions with respect to the MEG sensor array. Fig. 2a illustrates the determined position of the helmet-shaped MEG sensor array with respect to the phantom in the side view (left) and the top view (right). The errors in the distances between the fitted coil positions and the digitized positions were as follows: Pair 1-2: 1.1 mm; Pair 1-3: 0.8 mm; Pair 1-4: 0.6 mm; Pair 2-3: 1.0 mm; Pair 2-4: 0.3 mm; Pair 3-4: 0.2 mm. Thus, the accuracy in position estimation of the phantom in the MEG scanner was limited to 1.1 mm given by the error between pair 1-2. The sum of all inaccuracies in the system, 0.1 mm (phantom construction) + 0.5 mm (digitization) + 1.1 mm (HPI fitting), resulted in a value of 1.7 mm which described the spatial resolution of the overall system. It is worth mentioning here that the digitizing step and the HPI fitting step were performed here until a reasonable accuracy was achieved. This value limited the accuracy in determining the position of the electrode in the phantom in our previous work [13] and is therefore also considered in determining the orientation of the electrode in this work.

2.3. Data Acquisition

MEG data was collected using an Elekta Neuromag VectorView® MEG scanner at the Universitätsklinikum Düsseldorf (UKD) in Düsseldorf (Germany). The scanner consisted of 306 individual channels corresponding to 102 highly sensitive Superconducting QUantum Interference Devices (SQUID) magnetometers and 204 SQUID gradiometers. It should be noted that only the magnetometer data was used in this study. The noise level of the magnetometer sensors was measured at the beginning of the MEG recordings as part of a reference measurement at approximately 3 $\mathrm{fT}/\sqrt{\mathrm{Hz}}$ (as also specified in the data sheet). These sensors are ideally suited to measure the magnetic fields generated during stimulation. The acquisition parameters of the MEG scanner were set as follows: The sampling rate was set to its maximum of 5 kHz. The low-pass filter was set to its highest possible value of 1660 Hz and the cutoff frequency

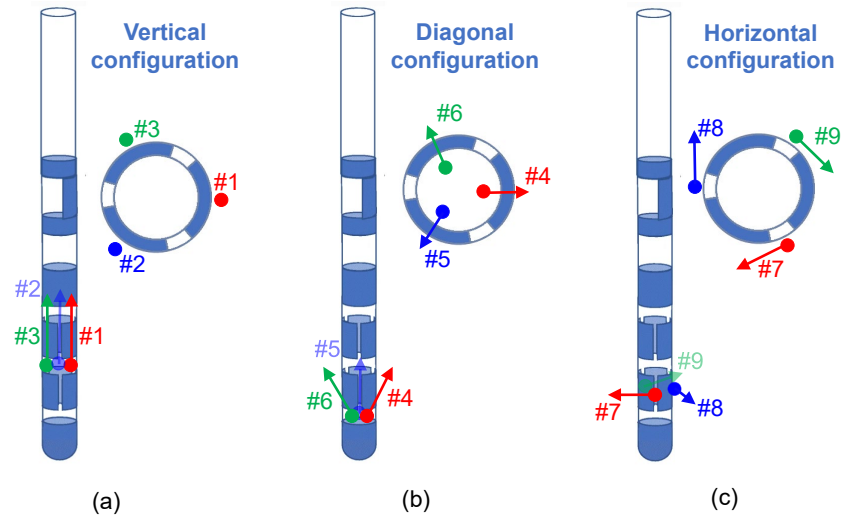

Figure 3. Illustration of electrode configurations used for the nine MEG recordings. Three different electrode configurations were used for three different recordings, resulting in a total of nine recordings: **(a)** vertical (MEG recordings #1, #2, #3), **(b)** diagonal (MEG recordings #4, #5, #6), and **(c)** horizontal (MEG recordings #7, #8, #9), which differ by the physical center of stimulation (thick colored dots) and the direction of current flow (colored arrows).

of the high-pass filter was set to DC (no high-pass filtering) to obtain measurements of the DBS signal with the maximum allowable acquisition bandwidth. The duration of each measurement was three minutes. A total of 9 measurements were performed using bipolar electrode configurations with 3 mA stimulation amplitude, 60 µs stimulation pulse width, and 130 Hz stimulation frequency. These applied values are normally used in clinical routine. The measurements differed by the activated electrode contacts (see Table 1), which we divided into three vertical, diagonal, and horizontal configuration types. The numbers C1 to C8 in the table stand for the electrode contact numbers according to Fig. 1b, where the first number defines the cathode and the second number the anode. The motivation for the choice of the applied electrode configurations is illustrated in Fig. 3 and can be briefly described in a simplified way as follows: In the 'vertical' electrode configuration, the physical center of the stimulation (shown with thick colored dots) is exactly between the activated directional electrode contacts, e.g., between contacts C2 and C5 in the first measurement, with the current flowing from the cathode to the anode and, thus, having a vertical current flow direction along the longitudinal axis of the electrode (indicated by the colored arrows). In the 'diagonal' configuration, the physical center of the stimulation is located deeper in the electrode, e.g. between contacts C1 and C2 in the fourth measurement, and the current flowing from the cathode to the anode here exhibits a diagonal current flow direction. In the 'horizontal' configuration, the physical center of stimulation lies exactly between adjacent segmented contacts, e.g., between contacts C2 and C3 in the seventh

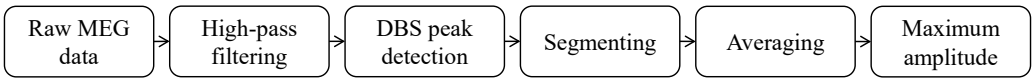

Figure 4. Signal processing pipeline: Each measured MEG signal is high-pass filtered with 60 Hz cutoff frequency, segmented into short DBS periods (according to the locations of DBS peaks detected by a peak detection algorithm), and averaged to a single period. The maximum amplitude value is then taken.

measurement, and the current flowing from the cathode to the anode here exhibits a horizontal current flow direction (perpendicular to the longitudinal axis of the electrode). The current, whose direction is defined by the corresponding configuration, generates a defined magnetic field. The magnetic field distribution can be measured around the phantom and used with precise electromagnetic simulations and detection algorithms to derive the orientation of the electrode.

Since this study involved phantom measurements, the measured MEG signals were not contaminated by biological artifacts such as cardiac muscle, skeletal muscle, or eye movements. Therefore, the measurements with the phantom represented the ideal case. Ambient noise consisted solely of the power line interference, which affected non-important frequencies only (50 Hz and its harmonics). The distance between the electrode and the MEG sensors varied between 7 cm (sensor closest to the electrode) and 15 cm (sensor farthest from the electrode). These distances are also to be expected in real patient measurements. Good quality of the recorded data was ensured by a blank measurement before the start of the experiment and by visual inspection of approximately 1 min of MEG recording before each measurement.

2.4. Signal Processing

The processing steps of the MEG measurements are visualized in Fig. 4. For each measurement, we obtained 102 time signals, one from each MEG magnetometer. The measured data was imported into MATLAB® (version R2018a) and preprocessed using the FieldTrip toolbox [26]. Each time signal was 180 s long and was high-pass filtered with a 6th order Butterworth filter with a cutoff frequency of 60 Hz without signal loss, since the stimulation signal contained higher frequencies (stimulation frequency of 130 Hz and its harmonics). Then, a peak detection algorithm was used to detect the location of successive DBS peaks in the time signal and, in the next step, to divide each signal into individual DBS segments. These segments were then averaged, which significantly improved the signal-to-noise ratio (SNR) by $\sqrt{N}$, where $N = 180\ \mathrm{s} \cdot 130\ \mathrm{s}^{-1}$ averages. The maximum value from this averaged time segment is then taken for each MEG magnetometer, resulting in a total of 102 values $\mathrm{B}_{\mathrm{meas}}$ representing the measured magnetic field distribution of the corresponding MEG recording.

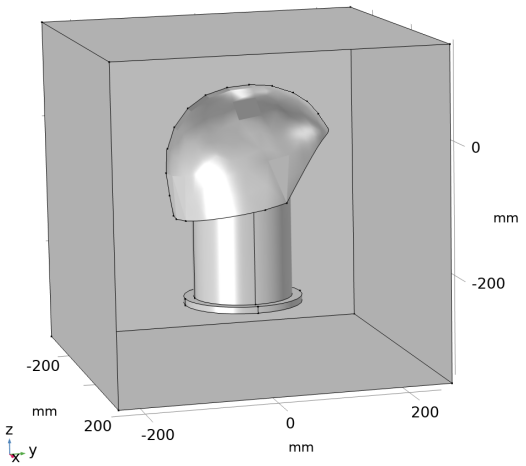

Figure 5. Finite element model with its dimensions. It includes the cylindrical phantom that is filled with saline solution, the directional DBS electrode placed inside the phantom, and the helmet-shaped MEG sensor surface. These structures are surrounded by a cuboid air box with a length of 500 mm.

2.5. Finite Element Model

Finite element method electromagnetic simulations were based on a model created in COMSOL Multiphysics®, as depicted in Fig. 5. For each structure in the model, the corresponding material was taken directly from the built-in material library and values of a uniform electrical conductivity σ, relative permeability μ_r, and relative permittivity ϵ_r were assigned. The cylinder body and the outer jacket of the electrode were modeled with acrylic plastic ($\sigma \approx 0$ S/m, $\mu_r = 1$, $\epsilon_r = 4.2$), the eight independent electrode contacts with platinum-iridium ($\sigma = 10^6$ S/m, $\mu_r = 1$, $\epsilon_r = 1$), and the content of the phantom with saline solution ($\sigma = 1.6$ S/m, $\mu_r = 1$, $\epsilon_r = 80$) [27, 28, 29, 30]. The phantom including the directional electrode (placed in the model according to the digitization step described in Section 2.2) was surrounded by a cuboid box with a length of 500 mm that is filled with air ($\sigma \approx 0$ S/m, $\mu_r = 1$, $\epsilon_r = 1$). The MEG helmet was modeled as a surface (placed in the model according to the HPI fitting step described in Section 2.2) and all measurement points were located on that surface. Tetrahedral mesh of 'Extra Fine' resolution was utilized. To model the corresponding bipolar electrode configurations from Table 1, the 'Terminal' boundary condition of 'Current Type' was used for the cathode and the 'Ground' boundary condition was used for the anode. Simulations were performed using the 'Magnetic and Electric Fields (mef)' interface of the 'AC/DC module' of COMSOL and magnetic flux densities in x, y, and z direction (B_x, B_y, and B_z) on the surface of the MEG helmet were calculated. In this experiment, the magnetometers (fixed in the MEG helmet) measured the magnetic field perpendicular to the helmet surface. To compute the magnetic field $B_{\text{model},i}$ perpendicular to the helmet surface in the simulation, we used the dot product

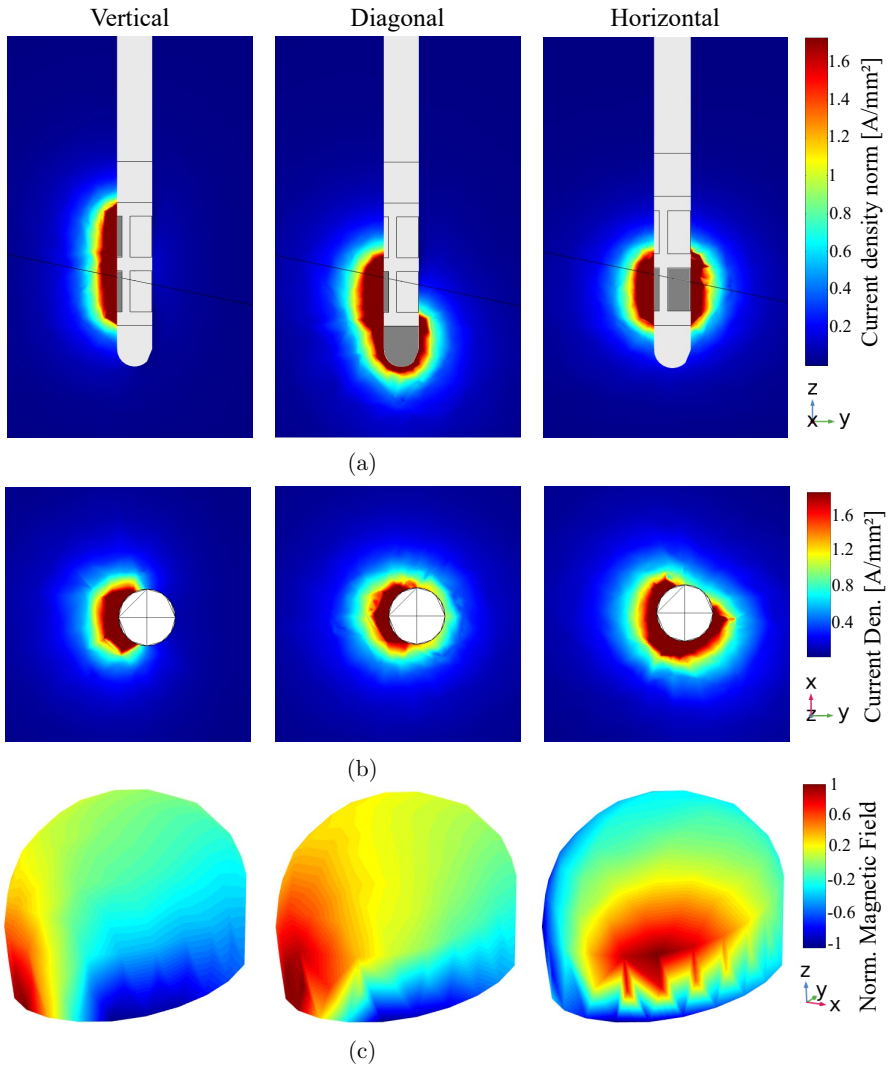

Figure 6. Electromagnetic simulation results of a vertical (left column), diagonal (middle column), and horizontal (right column) electrode configuration. The norm of the current density is visualized from **(a)** the side view and **(b)** the top view. **(c)** Generated magnetic field distribution.

$B_{\text{model},i} = \vec{B}_i \cdot \vec{s}(i)$, where $\vec{s}(i)$ is the unit vector perpendicular to the helmet at the sensor location i and $B_i = B_x + B_y + B_z$.

Fig. 6 compares the electromagnetic simulation results of a vertical (left column), diagonal (middle column), and horizontal (right column) electrode configuration considered in the framework of this work. Fig. 6a and 6b displays the side and top view of the electrode with the norm of the current density generated due to the activated contacts in the model (marked with dark gray). In the vertical configuration, the current flows vertically along the longitudinal axis of the electrode from the cathode

to the anode; in the diagonal configuration, the direction of current flow exhibits a diagonal behavior; and in the horizontal configuration, the current flows perpendicularly to the longitudinal axis of the electrode. The corresponding magnetic field distribution generated by the current can be seen in Fig. 6c. In the vertical case, the magnetic field distribution has a symmetrical shape (due to the symmetrical current flow), while in the diagonal case the field distribution is asymmetrical and tilted in the direction of the diagonal current flow. In the horizontal case, the magnetic field is even tilted by 90° compared to the vertical case.

2.6. Method for Detection of Electrode Orientation

Finite element (FE) modeling and model fitting were used to determine the rotational orientation of the directional DBS electrode in the phantom. As described in the previous section, FE modeling was used to calculate expected magnetic field values at the measurement positions using the electrode configuration to be analyzed with consideration of all electrode orientations. The values calculated by the model were represented by $\mathrm{B}_{\mathrm{model,config}}(r)$, where r represents the rotation of the electrode from 1° to 360° with 1° steps and the index 'config' represents the corresponding vertical, diagonal, or horizontal electrode configuration. Each individual simulation resulted in 102 modeled values corresponding to a total of 102 measurement points. Next, a model-fitting approach was used that searched for the simulated data that best fit the measured data $\mathrm{B}_{\mathrm{meas}}$ (introduced in Section 2.3). To do this, the fitting algorithm calculated the Goodness of Fit (GoF) between each modeled and measured data using the normalized root mean square error (NRMSE) as a cost function as follows:

$$GoF_{\mathrm{meas}}(r) = 1 - \frac{||\mathrm{B}_{\mathrm{model,config}}(r) - \mathrm{B}_{\mathrm{meas}}||}{||\mathrm{B}_{\mathrm{model,config}}(r) - \mathrm{mean}(\mathrm{B}_{\mathrm{model,config}}(r))||}, \quad (1)$$

with a value of one indicating a perfect fit and || the 2-norm of a vector. The model that obtained the largest value for GoF is the result of the orientation detection for the particular analyzed measurement. The error in determining the electrode orientation was calculated using the absolute angle between the electrode orientation in the found model and the real known orientation of the electrode in the phantom. To improve detection accuracy, all three contiguous measurements in the different electrode configurations (see Table 1) were evaluated together using *a priori* information of the electrode geometry. The angle between adjacent segments was known to be 120°. Thus, the cost function could be set up as follows:

$$GoF(r) = GoF_{\mathrm{meas1}}(r) + GoF_{\mathrm{meas2}}(r + 120°) + GoF_{\mathrm{meas3}}(r + 240°), \quad (2)$$

where the GoF of the second measurement is calculated with the electrode rotated by 120° in the model, and the GoF of the third measurement is calculated with the electrode rotated by 240° in the model.

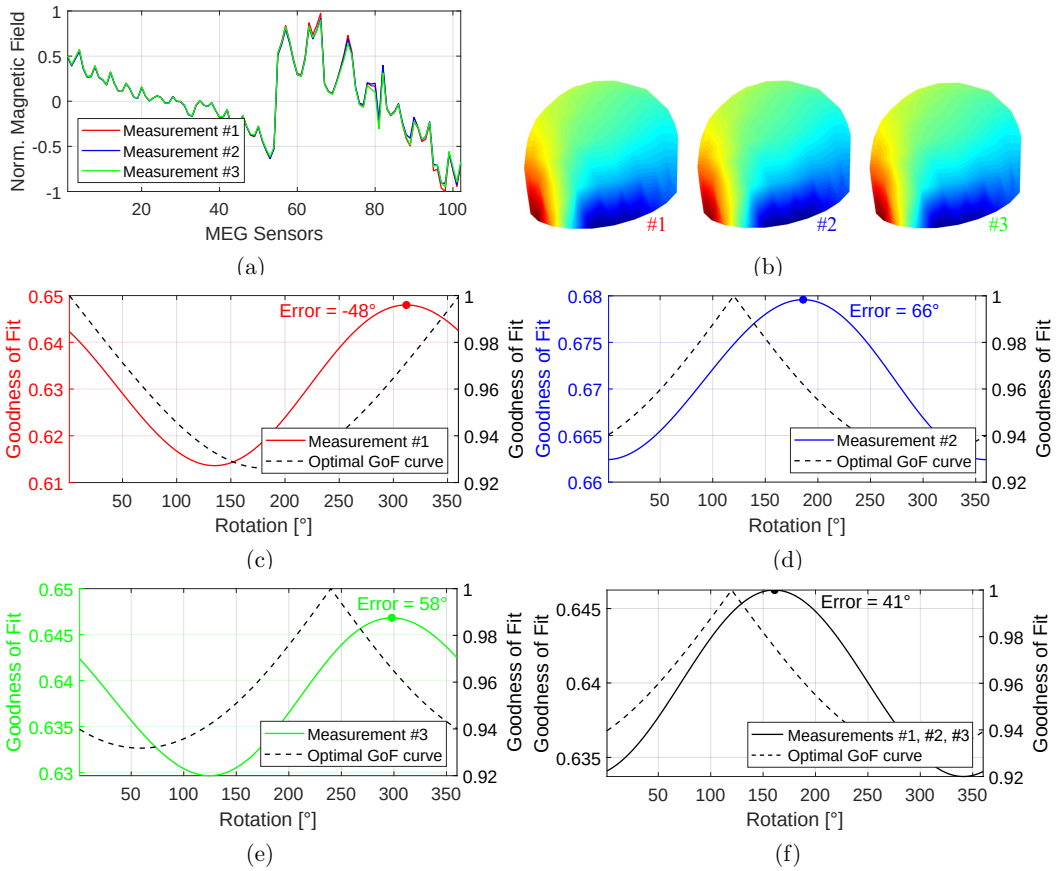

Figure 7. Vertical electrode configuration: **(a)** Magnetic field measured by the MEG sensors in measurements #1, #2, and #3. **(b)** Visualization of the magnetic field distribution. **(c)-(e)** Goodness of fit between measured data and data modeled with all rotations of the electrode considering single measurement. **(f)** Goodness of fit between measured data and data modeled with all rotations of the electrode considering all three measurements together. The maximum GoF is marked in each case.

3. Results

3.1. Vertical Electrode Configuration

In this section, the orientation detection results of the DBS electrode in the phantom for the measurements #1 to #3 are presented. Vertical current flow along the electrode was applied in the phantom using bipolar stimulation by activating a segmented contact C2, C3, or C4 as the cathode and the corresponding segment on the next higher level of the electrode (C5, C6, or C7) as the anode. The data measured by the MEG sensors in all three measurements and the corresponding visualization of the magnetic field distribution are depicted in Fig. 7a and 7b. We did not observe any influence of the DBS connector, the excess electrode wire, and the IPG on the measured magnetic field.

The reason for this may be that the returning current flow in the wire cancels the field generated by the forward current flow (bipolar electrode configuration). The measured data differed only slightly from each other, with no difference visually apparent in the field distributions, which was noticeable in the rotation determination. The orientation of the segmented contact C2/C5 could be determined with an accuracy of 48° (see Fig. 7c), since the detection algorithm found the maximum fit between measurement #1 and the model at an electrode rotation of 312° (the real orientation of C2/C5 is 0° or 360° according to Fig. 1b and 2b). The orientation of segment C3/C6 could be determined by measurement #2 with an accuracy of 66° (found rotation 186° instead of the real rotation of 120° as in Fig. 7d), and the orientation of segment C4/C7 could be determined by measurement #3 with an accuracy of 58° (found rotation 298° instead of the real rotation of 240° as in Fig. 7e). Even if a maximum value of each GoF curve was present, this value differed slightly from the GoF values of neighboring or other rotations (e.g., values between approximately 0.61 and 0.65 were present in the first measurement). Thus, the computed values with other electrode rotations in the model also achieved comparable agreement with the measured data. If the *a priori* known angle between the segments is applied as a condition for rotation detection, joint consideration of the measurements improved the detection accuracy to a value of 41° (found rotation 161° instead of the real rotation of 120°), as illustrated in Fig. 7f. The observed errors are mainly due to the inaccurate estimation of the phantom position in the MEG scanner, which was discussed in Section 2.2. Furthermore, since the difference between the three measured data is very minimal, even a small inaccuracy in the measurements, simulations, and measurement setup leads to detection errors. Minimization of this error can be achieved by a more accurate measurement system, i.e., if the position of the phantom and the measurement points can be accurately transferred into a uniform coordinate system.

3.2. Diagonal Electrode Configuration

This section reports the results of orientation detection of the DBS electrode in the phantom for the measurements #4 to #6. Diagonal current was applied in the phantom in different directions using bipolar stimulation by activating contact C1 as cathode and segmented contacts C2, C3, and C4 one-by-one as anode. Fig. 8a shows the measured data of these three measurements at the MEG sensors and Fig. 8b the corresponding visualization of the magnetic field distribution. Compared to the vertical configuration, where the measured data differed only slightly from each other, the measured data here differed in part considerably, so that differences in the field distributions can also be recognized visually. This was noticeable in the orientation detection with a higher accuracy. The orientation of the segmented contact C2/C5 could be determined with an accuracy of 23° (see Fig. 8c), since the detection algorithm found the maximum fit between measurement #4 and the model at an electrode rotation of 23° (the real orientation of C2/C5 is 0° or 360° according to Fig. 1b and 2b). The orientation of segment C3/C6 could be determined by measurement #5 with an accuracy of 16° (found

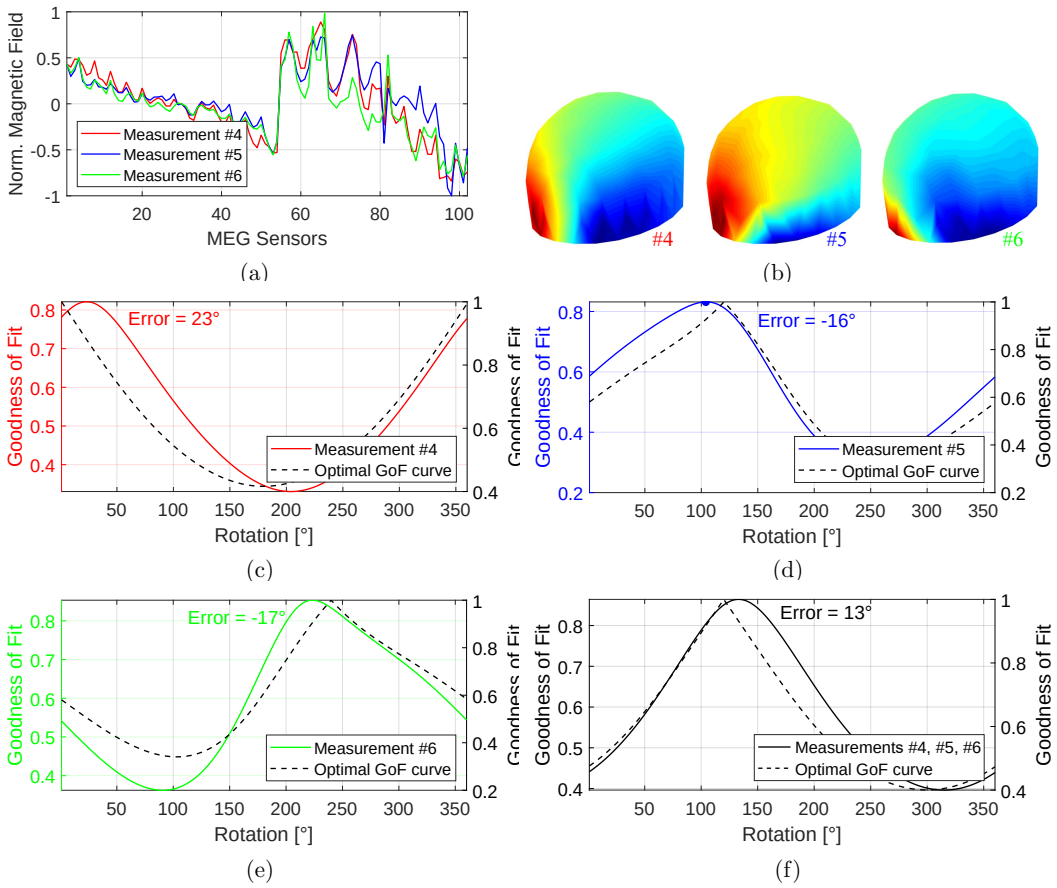

Figure 8. Diagonal electrode configuration: **(a)** Magnetic field measured by the MEG sensors in measurements #4, #5, and #6. **(b)** Visualization of the magnetic field distribution. **(c)-(e)** Goodness of fit between measured data and data modeled with all rotations of the electrode considering single measurement. **(f)** Goodness of fit between measured data and data modeled with all rotations of the electrode considering all three measurements together. The maximum GoF is marked in each case.

rotation 104° instead of the real rotation of 120° as in Fig. 8d), and the orientation of segment C4/C7 could be determined by measurement #6 with an accuracy of 17° (found rotation 223° instead of the real rotation of 240° as in Fig. 8e). The maximum value of each determined GoF curve is greater than 0.8, indicating a good fit between measured and modeled data compared to the vertical configuration with values around 0.65. The range of calculated GoF values (e.g., values between approximately 0.3 and 0.8 were available for the fourth measurement) was comparatively larger, so that the maximum GoF value differed from the values calculated for adjacent or other rotations. If the *a priori* known angle between the segments is applied as a condition for rotation detection, joint consideration of the measurements improved the detection accuracy to a value of 13° (found rotation 133° instead of the real rotation of 120°), as illustrated

in Fig. 8f. Similar to the vertical configuration, the observed errors can be mainly attributed to the inaccurate estimation of the phantom position in the MEG scanner. We have reported similar results with the same electrode configuration in our previous work [13]. Small inaccuracies in the measurements, simulations, and measurement setup can still be tolerated with this type of electrode configuration. However, minimization of the observed errors can be achieved by a more accurate measurement system.

3.3. Horizontal Electrode Configuration

This section presents the results of orientation detection of the DBS electrode in the phantom for measurements #7 to #9. Horizontal current perpendicular to the longitudinal axis of the electrode was applied in the phantom in different directions using bipolar stimulation by activating a segmented contact against an adjacent segment on the same level of the electrode, i.e. C2 against C3, C3 against C4, and C4 against C2. Fig. 9a shows the measured data of these three measurements at the MEG sensors and Fig. 9b the corresponding visualization of the produced magnetic field distribution. Compared to the other two configuration types, the measured data here differed considerably from each other, so that large differences in the field distributions can also be seen visually. This was noticeable in orientation detection with an even higher accuracy. The orientation of the segmented contact C2/C5 could be determined with an accuracy of 13° (see Fig. 9c), since the detection algorithm found the maximum fit between measurement #7 and the model at an electrode rotation of 73° (the real orientation of C2/C5 is 60° according to Fig. 1b and 2b). The orientation of segment C3/C6 could be determined by measurement #8 with an accuracy of 11° (found rotation 169° instead of the real rotation of 180° as in Fig. 9d), and the orientation of segment C4/C7 could be determined by measurement #9 with an accuracy of 15° (found rotation 285° instead of the real rotation of 300° as in Fig. 9e). The maximum value of each determined GoF curve is about 0.9, indicating even better agreement between measured and modeled data compared to the diagonal configuration. The range of calculated GoF values (e.g., values between -1.2 and 0.9 were available for the seventh measurement) was again larger, so that the maximum GoF value differed significantly from the values calculated for adjacent or other rotations. By considering all three measurements together, the detection accuracy is improved to a value of 6°, as illustrated in Fig. 9f. This value represents the best result obtained in this work. The inaccurate estimation of the phantom position in the MEG scanner can again be considered as the reason for this small error. Here, however, small inaccuracies in the measurements, simulations, and measurement setup have little to no influence on the orientation detection results, making this type of electrode configuration the most promising among all investigated configurations.

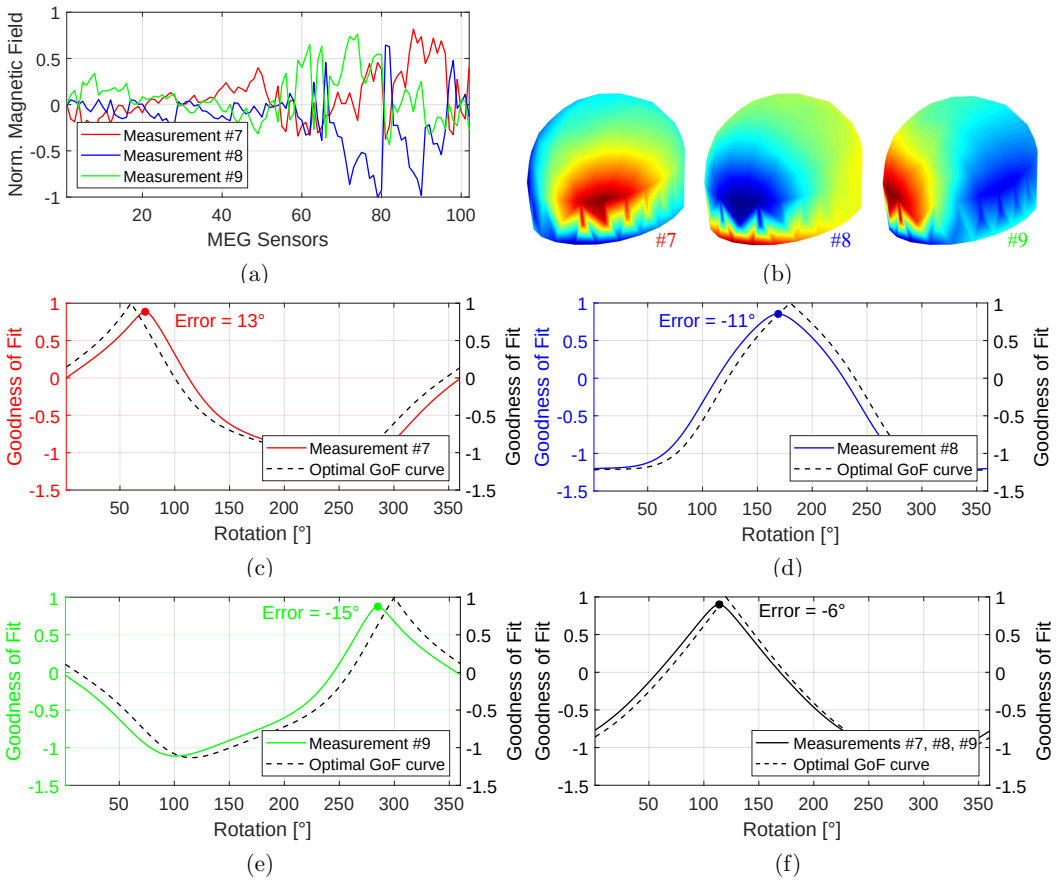

Figure 9. Horizontal electrode configuration: **(a)** Magnetic field measured by the MEG sensors in measurements #7, #8, and #9. (b) Visualization of the magnetic field distribution. **(c)-(e)** Goodness of fit between measured data and data modeled with all rotations of the electrode considering single measurement. **(f)** Goodness of fit between measured data and data modeled with all rotations of the electrode considering all three measurements together. The maximum GoF is marked in each case.

4. Discussion

In this study, we have investigated the orientation detection accuracy of a directional DBS electrode in a phantom using magnetic field measurements by a state-of-the-art SQUID-based MEG device. The presented method for determining electrode orientation provides an alternative to conventional neuroimaging techniques in which electrode orientation is determined by visual inspection over artifacts created by the radiopaque marker of the electrode using x-rays, standard CT, flat-panel CT, or rotational fluoroscopy. However, the underlying artifacts exhibit a 180° symmetry, and neither imaging technique is currently able to resolve this ambiguity without further measurements. In addition, all of these currently available methods expose the patient to radiation. The presented detection method which is based on magnetic field

measurements is harmless and safe for the patient (non-invasive and non-radiative), which may be interesting for clinical application. For this purpose, the IPG is programmed and set up with the bipolar electrode configuration (employing clinically used DBS stimulation parameters) and the appropriate choice of activated contacts to generate a defined magnetic field. The magnetic field distribution can then be measured around the phantom or patient's head, and used with precise finite element modeling and detection algorithms to derive electrode orientation.

Segmented contacts of a directional electrode can enable the generation of an electric field in a desired direction. In order to use this new technology with all its advantages, the knowledge of the exact electrode orientation in the brain is required. Three different electrode configuration types (adjustable using directional electrode technology) were investigated for their accuracy in determining electrode orientation. These configurations differed in the activation of different directional and omnidirectional contacts of the electrode and, thus, in the direction of current flow in the phantom. The following accuracies were obtained, which depended on the type of stimulation:

- In the vertical electrode configuration (activation of a segmented contact against the corresponding segment on the next higher level of the electrode), a vertical current flow is caused along the longitudinal axis of the electrode. The orientation of each directional contact was determined with an average accuracy of approximately 60°, with each measurement used separately for the detection. However, this error could be reduced to approximately 40° by using three contiguous measurements and applying the *a priori* known angle between adjacent segments as a condition for orientation detection.
- In the diagonal electrode configuration (activation of the tip of the electrode against a segmented contact on the next higher level of the electrode), a diagonal current flow in the phantom is caused. The orientation of each directional contact was determined with an average accuracy of approximately 20°, with each measurement used separately for the detection. However, this error could be reduced to 13° by using three contiguous measurements.
- In the horizontal electrode configuration (activation of a segmented contact against an adjacent segment on the same level of the electrode), a horizontal current flow perpendicular to the longitudinal axis of the electrode is caused. The orientation of each directional contact was determined with an average accuracy of 13°, with each measurement used separately for the detection. This error could be reduced to 6° by using three contiguous measurements.

The inaccuracies in orientation detection were caused by the sum of several inaccuracies in the system, including inaccuracies in the measurements, the signal processing pipeline of the measured data, the simulations, and the measurement procedure. All these issues affected the observed accuracies of the investigated electrode configurations to different degrees, with the vertical configuration being the most affected and the horizontal

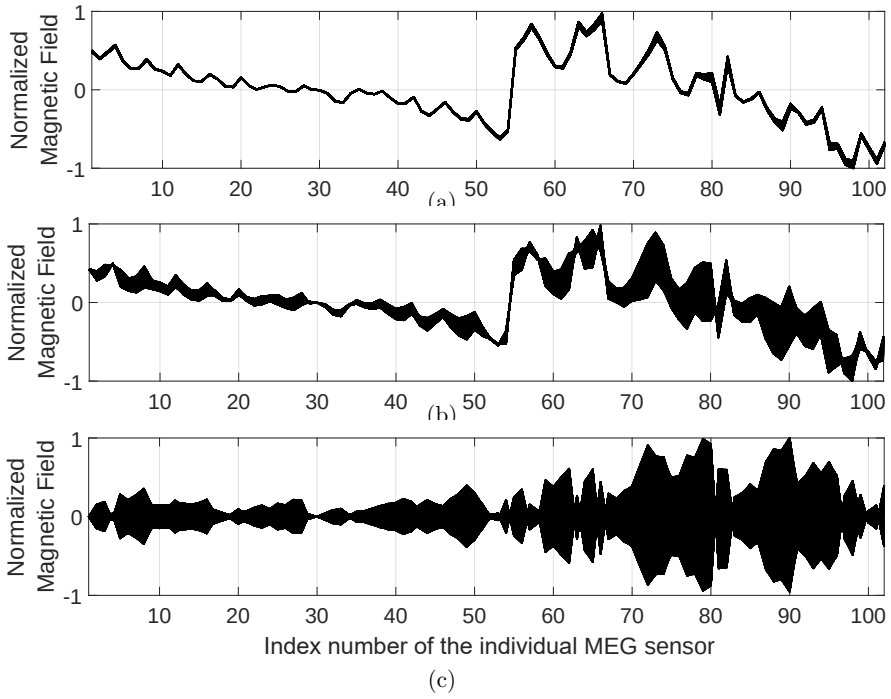

Figure 10. Modeled magnetic field at each sensor location for each rotation of the electrode in the phantom with **(a)** vertical, **(b)** diagonal, and **(c)** horizontal electrode configuration. Each figure contains 360 black curves, where one curve corresponds to one electrode orientation in the model.

configuration the least affected. This can also be observed in Fig. 10, which gives an overview of all modeled values (calculated magnetic field values at measurement points using electromagnetic simulations) for each rotation of the electrode in the phantom. That is, each figure contains 360 curves, where one curve corresponds to one electrode rotation. In the vertical electrode configuration (Fig. 10a), the results of all modeled data for each electrode rotation in the phantom are very similar to each other, so that any inaccuracy in the system would already lead to detection errors. The modeled values in the diagonal (and horizontal) electrode configuration for each electrode rotation in the phantom differ from each other significantly, i.e., so a small inaccuracy in the system had little to no effect on the detection accuracy. Based on the observed accuracies, it can be claimed that the horizontal electrode configuration is the most promising configuration type among all investigated configurations to determine the electrode orientation with magnetic field measurements by a modern MEG. The 180° ambiguity in the solutions, as is the case with postoperative imaging techniques, does not exist with the presented method.

The non-radiative method for determining the rotational orientation of a directional DBS electrode using magnetic field measurements appears to be promising. The accuracies obtained in our work were mainly limited by the inaccurate position

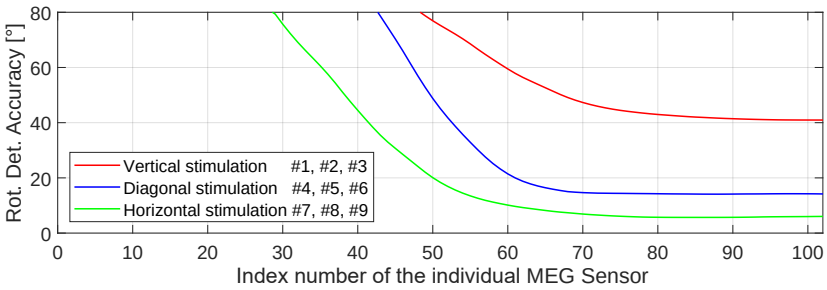

Figure 11. Accuracy of electrode orientation detection with respect to the number of MEG sensors for all three configuration types. Contiguous measurements were considered together to improve detection accuracy.

estimation of the phantom with respect to the measurement points. This suggests that detection accuracies can be (significantly) improved if the measurement procedure is improved, i.e., if the position of the phantom and the measurement points can be precisely transferred into a uniform coordinate system. Recent technical developments are moving toward cap-shaped MEG sensor arrays that move with the patient's head (i.e., no relative movement between head and sensors) and can be adapted to the individual head shape [31, 32]. They would have the potential to overcome the observed limitation in detecting electrode orientation and could become a breakthrough in neurology by achieving sufficient accuracy for this application. Optically pumped magnetometers (OPMs) have been shown to have sensitivities approaching the gold standard of commercial SQUIDs, making them suitable for OP-MEG development [32, 33]. Although these sensors still have too low a bandwidth for use in DBS applications due to the presence of much higher frequencies (stimulation frequency and its harmonics), the IPG allows a lower stimulation frequency to be set and, according to our physicians, poses no problem in reducing the stimulation frequency in patients for the duration of the measurement in order to perform multiple recordings required for the detection of electrode position and orientation. In our recent work [34], we investigated the minimum requirements that magnetic field sensors must meet in order to be used for electrode localization and electrode orientation detection. A high sensor sensitivity, as provided by a SQUID sensor, is not required. Further investigations have demonstrated that such a high number of 102 magnetometers, as provided by the MEG device, is also not essential to achieve decent accuracies. Fig. 11 visualizes the accuracy in detecting electrode orientation as a function of the number of MEG sensors for all three configuration types (smoothed curves). The number of sensors was uniformly reduced by 1 sensor in each step and the detection procedure was performed. The curves reveal that for the diagonal and for the horizontal electrode configuration also 70 and 80 sensors, respectively, are sufficient to achieve the same accuracy as with 102 sensors. With a lower number of sensors, the error increases.

5. Conclusion

In this work, accuracies in detecting the rotational orientation of a directional DBS electrode using MEG were investigated. Three different bipolar electrode configurations were analyzed. Each configuration caused the electric current to flow in a different direction in the phantom. Precise finite element electromagnetic modeling and a detection algorithm were then used to derive the orientation of the electrode. Vertical configuration achieved a detection accuracy of only 41°, diagonal configuration achieved an accuracy of 13°, while horizontal configuration achieved an accuracy of 6°. The latter proved to be the most promising electrode configuration type. Although 6° accuracy is not ideal, many clinicians would accept this inaccuracy when gaining the benefit of a non-radiative assessment method. Furthermore, this inaccuracy will be further reduced if more precise cap-shaped MEG sensor array is used.

Acknowledgment

This work was supported by the German Research Foundation (Deutsche Forschungsgemeinschaft, DFG) through the project T1 of the Collaborative Research Centre CRC 1261 *Magnetoelectric Sensors: From Composite Materials to Biomagnetic Diagnostics*.

References

[1] F. Hitti, A. Ramayya, B. McShane, A. Yang, K. Vaughan, and G. Baltuch, "Long-term outcomes following deep brain stimulation for parkinson's disease," *Journal of Neurosurgery*, vol. 132, pp. 1–6, 01 2019.

[2] M. Schüpbach, J. Rau, K. Knudsen, J. Volkmann, P. Krack, L. Timmermann, T. Hälbig, H. Hesekamp, S. Navarro, N. Meier, D. Falk, H. M. Mehdorn, S. Paschen, M. Maarouf, M. Barbe, G. Fink, A. Kupsch, D. Gruber, G.-H. Schneider, and G. Deuschl, "Neurostimulation for parkinson's disease with early motor complications," *New England Journal of Medicine*, vol. 368, pp. 610–22, 02 2013.

[3] P. Krack, J. Volkmann, G. Tinkhauser, and G. Deuschl, "Deep Brain Stimulation in Movement Disorders: From Experimental Surgery to Evidence-Based Therapy," *Movement Disorders*, vol. 34, no. 12, pp. 1795–1810, 2019.

[4] C. R. Butson and C. C. McIntyre, "Current steering to control the volume of tissue activated during deep brain stimulation," *Brain Stimulation*, vol. 1, no. 1, pp. 7 – 15, 2008.

[5] F. Steigerwald, L. Müller, S. Johannes, C. Matthies, and J. Volkmann, "Directional deep brain stimulation of the subthalamic nucleus: A pilot study using a novel neurostimulation device," *Movement Disorders*, vol. 31, no. 8, pp. 1240–1243, 2016.

[6] C. Pollo, A. Kaelin-Lang, M. F. Oertel, L. Stieglitz, E. Taub, P. Fuhr, A. M. Lozano, A. Raabe, and M. Schüpbach, "Directional deep brain stimulation: an intraoperative double-blind pilot study," *Brain*, vol. 137, no. 7, pp. 2015–2026, 05 2014.

[7] A. Schnitzler, P. Mir, M. Brodsky, L. Verhagen, S. Groppa, R. Alvarez, A. Evans, M. Blazquez, S. Nagel, J. Pilitsis, M. Pötter-Nerger, W. Tse, L. Almeida, N. Tomycz, J. Jimenez-Shahed, W. Libionka, F. Carrillo, C. Hartmann, S. Groiss, and f. Investigators, "Directional Deep Brain Stimulation for Parkinson's Disease: Results of an International Crossover Study With Randomized, Double-Blind Primary Endpoint," *Neuromodulation*, 05 2021.

[8] A. Horn, N. Li, T. A. Dembek, A. Kappel, C. Boulay, S. Ewert, A. Tietze, A. Husch, T. Perera, W.-J. Neumann, M. Reisert, H. Si, R. Oostenveld, C. Rorden, F.-C. Yeh, Q. Fang, T. M. Herrington, J. Vorwerk, and A. A. Kühn, "Lead-DBS v2: Towards a comprehensive pipeline for deep brain stimulation imaging," *NeuroImage*, vol. 184, pp. 293–316, 2019.

[9] J. Engelhardt, D. Guehl, N. Damon-PerriÃ¨re, O. Branchard, P. Burbaud, and E. Cuny, "Localization of Deep Brain Stimulation Electrode by Image Registration Is Software Dependent: A Comparative Study between Four Widely Used Software Programs," *Stereotactic and Functional Neurosurgery*, vol. 96, pp. 364–369, 12 2018.

[10] M. I. Iacono, S. R. Atefi, L. Mainardi, H. C. Walker, L. M. Angelone, and G. Bonmassar, "A Study on the Feasibility of the Deep Brain Stimulation (DBS) Electrode Localization Based on Scalp Electric Potential Recordings," *Frontiers in Physiology*, vol. 9, p. 1788, 2019.

[11] M. Yalaz, A. Teplyuk, M. Muthuraman, G. Deuschl, and M. Höft, "The Magnetic Properties of Electrical Pulses Delivered by Deep-Brain Stimulation Systems," *IEEE Transactions on Instrumentation and Measurement*, vol. 69, no. 7, pp. 4303–4313, 2020.

[12] M. Yalaz, A. Teplyuk, G. Deuschl, and M. Höft, "Dipole Fit Localization of the Deep Brain Stimulation Electrode Using 3D Magnetic Field Measurements," *IEEE Sensors Journal*, vol. 20, no. 16, pp. 9550–9557, 2020.

[13] M. Yalaz, M. S. Noor, C. C. McIntyre, M. Butz, A. Schnitzler, G. Deuschl, and M. Höft, "DBS electrode localization and rotational orientation detection using SQUID-based magnetoencephalography," *Journal of Neural Engineering*, vol. 18, no. 2, p. 026021, mar 2021.

[14] P. Reinacher, M. Krüger, V. Coenen, M. Shah, R. Roelz, C. Jenkner, and K. Egger, "Determining the Orientation of Directional Deep Brain Stimulation Electrodes Using 3D Rotational Fluoroscopy," *American Journal of Neuroradiology*, vol. 38, no. 6, pp. 1111–1116, 2017.

[15] S. Hunsche, C. Neudorfer, F. E. Majdoub, M. Maarouf, and D. Sauner, "Determining the Rotational Orientation of Directional Deep Brain Stimulation Leads Employing Flat-Panel Computed Tomography," *Operative Neurosurgery*, vol. 16, no. 4, pp. 465–470, 06 2018.

[16] A. Sitz, M. Hoevels, A. Hellerbach, A. Gierich, K. Luyken, T. A. Dembek, M. Klehr, J. Wirths, V. Visser-Vandewalle, and H. Treuer, "Determining the orientation angle of directional leads for deep brain stimulation using computed tomography and digital x-ray imaging: A phantom study," *Medical Physics*, vol. 44, no. 9, pp. 4463–4473, 2017.

[17] A. Hellerbach, T. Dembek, M. Hoevels, J. Holz, A. Gierich, K. Luyken, M. Barbe, J. Wirths, V. Visser-Vandewalle, and H. Treuer, "Diode: Directional orientation detection of segmented deep brain stimulation leads: A sequential algorithm based on ct imaging," *Stereotactic and Functional Neurosurgery*, vol. 96, pp. 335–341, 01 2018.

[18] T. Dembek, A. Hellerbach, H. Jergas, M. Eichner, J. Wirths, H. Dafsari, M. Barbe, V. Visser-Vandewalle, and H. Treuer, "DiODe v2: Unambiguous and fully-automated detection of directional DBS lead orientation," 07 2021.

[19] R. Kurtev-Rittstieg, S. Achatz, A. Nourinia, and S. Mittermeyer, "Orientation of Directional Deep Brain Stimulation Leads on CT: Resolving the Ambiguity," *bioRxiv*, 2020.

[20] Y. H. Kim, H. J. Kim, C. Kim, D. Kim, B. Jeon, and S. Paek, "Comparison of electrode location between immediate postoperative day and 6 months after bilateral subthalamic nucleus deep brain stimulation," *Acta Neurochirurgica*, vol. 152, pp. 2037–2045, 2010.

[21] T. Morishita, J. Hilliard, M. Okun, D. Neal, K. Nestor, D. Peace, A. Hozouri, M. Davidson, F. Bova, J. Sporrer, G. Oyama, and K. Foote, "Postoperative lead migration in deep brain stimulation surgery: Incidence, risk factors, and clinical impact," *PLOS ONE*, vol. 12, p. e0183711, 09 2017.

[22] T. Dembek, M. Hoevels, A. Hellerbach, A. Horn, J. Petry-Schmelzer, J. Borggrefe, J. Wirths, H. Dafsari, M. Barbe, V. Visser-Vandewalle, and H. Treuer, "Directional DBS leads show large deviations from their intended implantation orientation," *Parkinsonism & Related Disorders*, vol. 67, pp. 117–121, 08 2019.

[23] A. Rau, H. Urbach, V. Coenen, K. Egger, and P. Reinacher, "Deep brain stimulation electrodes

may rotate after implantation - an animal study," *Neurosurgical Review*, vol. 44, pp. 2349–2353, 08 2021.

[24] N. Göransson, J. Johansson, K. Wårdell, and P. Zsigmond, "Postoperative Lead Movement after Deep Brain Stimulation Surgery and the Change of Stimulation Volume," *Stereotactic and functional neurosurgery*, vol. 99, pp. 221–229, 2021.

[25] F. Lange, F. Steigerwald, D. Engel, T. Malzacher, T. Neun, P. Fricke, J. Volkmann, C. Matthies, and P. Capetian, "Longitudinal Assessment of Rotation Angles after Implantation of Directional Deep Brain Stimulation Leads," *Stereotactic and Functional Neurosurgery*, vol. 99, pp. 1–9, 09 2020.

[26] R. Oostenveld, P. Fries, E. Maris, and J.-M. Schoffelen, "FieldTrip: Open Source Software for Advanced Analysis of MEG, EEG, and Invasive Electrophysiological Data," *Computational intelligence and neuroscience*, vol. 2011, p. 156869, 01 2011.

[27] B. Teplitzky, L. Zitella, Y. Xiao, and M. Johnson, "Model-Based Comparison of Deep Brain Stimulation Array Functionality with Varying Number of Radial Electrodes and Machine Learning Feature Sets," *Frontiers in Computational Neuroscience*, vol. 10, p. 58, 06 2016.

[28] E. Lewis, "The practical salinity scale 1978 and its antecedents," *IEEE Journal of Oceanic Engineering*, vol. 5, no. 1, pp. 3–8, 1980.

[29] E. ToolBox. (2010) Relative Permittivity - the Dielectric Constant. (accessed: 11.08.2021). [Online]. Available: https://www.engineeringtoolbox.com/relative-permittivity-d_1660.html

[30] ——. (2016) Permeability. (accessed: 11.08.2021). [Online]. Available: https://www.engineeringtoolbox.com/permeability-d_1923.html

[31] E. Boto, N. Holmes, J. Leggett, G. Roberts, V. Shah, S. Meyer, L. Muñoz, K. Mullinger, T. Tierney, S. Bestmann, G. Barnes, R. Bowtell, and M. Brookes, "Moving magnetoencephalography towards real-world applications with a wearable system," *Nature*, vol. 555, p. 657–661, 03 2018.

[32] R. M. Hill, E. Boto, M. Rea, N. Holmes, J. Leggett, L. A. Coles, M. Papastavrou, S. K. Everton, B. A. Hunt, D. Sims, J. Osborne, V. Shah, R. Bowtell, and M. J. Brookes, "Multi-channel whole-head OPM-MEG: Helmet design and a comparison with a conventional system," *NeuroImage*, vol. 219, p. 116995, 2020.

[33] E. J. Pratt, M. Ledbetter, R. Jiménez-Martínez, B. Shapiro, A. Solon, G. Z. Iwata, S. Garber, J. Gormley, D. Decker, D. Delgadillo, A. T. Dellis, J. Phillips, G. Sundar, J. Leung, J. Coyne, M. McKinley, G. Lopez, S. Homan, L. Marsh, M. Zhang, V. Maurice, B. Siepser, T. Giovannoli, B. Leverett, G. Lerner, S. Seidman, V. DeLuna, K. Wright-Freeman, J. Kates-Harbeck, T. Lasser, H. Mohseni, T. Sharp, A. Zorzos, A. H. Lara, A. Kouhzadi, A. Ojeda, P. Chopra, Z. Bednarke, M. Henninger, and J. K. Alford, "Kernel Flux: a whole-head 432-magnetometer optically-pumped magnetoencephalography (OP-MEG) system for brain activity imaging during natural human experiences," in *Optical and Quantum Sensing and Precision Metrology*, vol. 11700, International Society for Optics and Photonics. SPIE, 2021, pp. 162 – 179.

[34] M. Yalaz, G. Deuschl, M. Butz, A. Schnitzler, A.-K. Helmers, and M. Höft, "Investigation of magnetoelectric sensor requirements for deep brain stimulation electrode localization and rotational orientation detection," *Sensors*, vol. 21, no. 7, 2021.

Key Findings and Scientific Implications

- The multiple independent current-controlled technology of available neurostimulators allows the current flow through each contact to be individually controlled, so that any bipolar electrode configuration can be set.
- Each bipolar directional electrode configuration differs in the activation of various segmented contact pairs and generates its own topographical pattern in the magnetic field distribution on the sensor surface level.
- The accuracy of electrode orientation detection is highly dependent on the type of directional bipolar electrode configuration used.
- The activation of a segmented contact against an adjacent segment at the same level of the electrode proves to be the most promising electrode configuration type for electrode orientation detection.
- The orientation of the electrode can be determined with an average accuracy of approximately 13° when a single measurement is performed with the activation of two adjacent segmented contacts at the same level of the electrode.
- The detection error in electrode orientation detection can be minimized to 6° if a sequence of three measurements, each with activation of a pair of segmented contacts around the electrode, is considered.

3.6 MaDoPO: Magnetic Detection of Positions and Orientations of Segmented Deep Brain Stimulation Electrodes: A Radiation-Free Method Based on Magnetoencephalography

M. Yalaz, N. Maling, G. Deuschl, L. M. Juárez-Paz, M. Butz, A. Schnitzler, A.-K. Helmers, and M. Höft, "MaDoPO: Magnetic Detection of Positions and Orientations of Segmented Deep Brain Stimulation Electrodes: A Radiation-free Method based on Magnetoencephalography," in *Brain Sciences*, vol. 12, no. 1, art. no. 86, January 2022, doi: 10.3390/brainsci12010086.

Information about the amount of own contribution to this publication:

Conceptualization	Planning	Implementation	Manuscript preparation
high	high	high	high

© 2022 by the authors. This article is an open access article distributed under the terms and conditions of the Creative Commons Attribution (CC BY) license (https://creativecommons.org/licenses/by/4.0/), which permits unrestricted use, distribution, and reproduction in any medium. The version of record is available online at https://doi.org/10.3390/brainsci12010086.

brain sciences

MDPI

Article

MaDoPO: Magnetic Detection of Positions and Orientations of Segmented Deep Brain Stimulation Electrodes: A Radiation-Free Method Based on Magnetoencephalography

Mevlüt Yalaz [1,*], Nicholas Maling [2], Günther Deuschl [3], León M. Juárez-Paz [2], Markus Butz [4], Alfons Schnitzler [4], Ann-Kristin Helmers [5] and Michael Höft [1]

[1] Microwave Engineering, Christian-Albrechts-Universität zu Kiel, 24143 Kiel, Germany; mh@tf.uni-kiel.de
[2] Boston Scientific Corporation, Santa Clarita, CA 91355, USA; Nicholas.Maling@bsci.com (N.M.); Leon.JuarezPaz@bsci.com (L.M.J.-P.)
[3] Department of Neurology, Christian-Albrechts-Universität zu Kiel, 24105 Kiel, Germany; g.deuschl@neurologie.uni-kiel.de
[4] Institute of Clinical Neuroscience and Medical Psychology, Medical Faculty, Heinrich-Heine-Universität Düsseldorf, 40225 Düsseldorf, Germany; butzm@hhu.de (M.B.); alfons.schnitzler@hhu.de (A.S.)
[5] Department of Neurosurgery, Christian-Albrechts-Universität zu Kiel, 24105 Kiel, Germany; Ann-Kristin.Helmers@uksh.de
* Correspondence: my@tf.uni-kiel.de

Abstract: Background: Current approaches to detect the positions and orientations of directional deep brain stimulation (DBS) electrodes rely on radiative imaging data. In this study, we aim to present an improved version of a radiation-free method for magnetic detection of the position and the orientation (MaDoPO) of directional electrodes based on a series of magnetoencephalography (MEG) measurements and a possible future solution for optimized results using emerging on-scalp MEG systems. Methods: A directional DBS system was positioned into a realistic head–torso phantom and placed in the MEG scanner. A total of 24 measurements of 180 s each were performed with different predefined electrode configurations. Finite element modeling and model fitting were used to determine the position and orientation of the electrode in the phantom. Related measurements were fitted simultaneously, constraining solutions to the a priori known geometry of the electrode. Results were compared with the results of the high-quality CT imaging of the phantom. Results: The accuracy in electrode localization and orientation detection depended on the number of combined measurements. The localization error was minimized to 2.02 mm by considering six measurements with different non-directional bipolar electrode configurations. Another six measurements with directional bipolar stimulations minimized the orientation error to 4°. These values are mainly limited due to the spatial resolution of the MEG. Moreover, accuracies were investigated as a function of measurement time, number of sensors, and measurement direction of the sensors in order to define an optimized MEG device for this application. Conclusion: Although MEG introduces inaccuracies in the detection of the position and orientation of the electrode, these can be accepted when evaluating the benefits of a radiation-free method. Inaccuracies can be further reduced by the use of on-scalp MEG sensor arrays, which may find their way into clinics in the foreseeable future.

Keywords: deep brain stimulation; magnetoencephalography; segmented DBS electrode; bipolar electrode configuration; localization; rotational orientation detection

check for updates

Citation: Yalaz, M.; Maling, N.; Deuschl, G.; Juárez-Paz, L.M.; Butz, M.; Schnitzler, A.; Helmers, A.-K.; Höft, M. MaDoPO: Magnetic Detection of Positions and Orientations of Segmented Deep Brain Stimulation Electrodes: A Radiation-Free Method Based on Magnetoencephalography. *Brain Sci.* **2022**, *12*, 86. https://doi.org/10.3390/brainsci12010086

Academic Editor: Giovanni Pellegrino

Received: 10 December 2021
Accepted: 6 January 2022
Published: 8 January 2022

Publisher's Note: MDPI stays neutral with regard to jurisdictional claims in published maps and institutional affiliations.

Copyright: © 2022 by the authors. Licensee MDPI, Basel, Switzerland. This article is an open access article distributed under the terms and conditions of the Creative Commons Attribution (CC BY) license (https://creativecommons.org/licenses/by/4.0/).

1. Introduction

Deep brain stimulation (DBS) is a neurosurgical procedure in which electrodes are placed within the brain to electrically stimulate specific target areas, thereby modulating dysregulated neural circuits [1]. Due to the relative safety, therapeutic efficacy, and post-surgically modifiable nature of DBS, it has become a common surgical procedure over

the past three decades. To date, it is estimated that over 200,000 patients have been implanted in over 700 centers worldwide [2,3]. While DBS is most commonly used to treat movement disorders, such as Parkinson's disease and essential tremor, it is increasingly being investigated for its therapeutic potential regarding a range of other brain diseases, including conditions such as neuropathic pain and epilepsy. Estimating the volume of tissue activated (VTA) has demonstrated clinical advantages in programming efficacy [4] and provides a method for optimizing stimulation while avoiding side effects. Conventional DBS electrodes, which have a linear array of ring contacts, offer limited control over an approximately spherical VTA. Directional electrodes with contacts divided into three segments along the circumference of the electrode offer the possibility to steer the VTA inside the target in a desired stimulation direction to prevent the current from spreading to adjacent fibers or nuclei [5,6]. Clinical studies have reported improved therapeutic effects and lower side effect thresholds for directional DBS [7,8]. To realize the full potential of this directional stimulation technology, the correct position and orientation of the electrode in the patient-specific neuroanatomy must be precisely determined in order to meaningfully interpret the observed stimulation's effects on the individual patient and to guide and facilitate neurostimulator programming.

Current approaches to electrode localization rely on the fusion of pre- and postoperative neuroimaging data. All images are subject to metal artifacts, which increase localization errors in poor quality images. In addition, significant discrepancies between electrode centers estimated by computed tomography (CT) and magnetic resonance imaging (MRI) have been reported, and differences in localization results between different widely used software programs have been noted [9–11]. Furthermore, CT exposes patients to ionizing radiation, whereas MRI cannot always be performed for safety reasons. Similar limitations also exist in electrode orientation detection. Current methods for determining electrode orientation include anteroposterior and lateral X-rays, standard CT, flat-panel CT, and rotational fluoroscopy [12–14]. Techniques using X-rays and CT rely on high-quality images because specific artifact patterns generated by the radiopaque orientation markers, which are located dorsal to the electrode contacts, must be calculated from these images. However, the underlying symmetric artifact has 180° symmetry, which limits orientation detection to two possible solutions. Neither imaging technique is currently capable of resolving this ambiguity without further measurements. Recently, solutions to the ambiguity of artifact symmetry have been proposed, but additional X-ray images are required to resolve 100% of cases [15,16]. Rotational 3D fluoroscopy seems to be a promising alternative [12], but all existing methods for orientation detection expose patients to ionizing radiation, which may be detrimental to patients. In addition, electrode migration, electrode torsion, and any trauma or surgical intervention may cause undesired electrode displacement and rotation, requiring the patient to be re-exposed to radiation or X-ray imaging. This would hinder further research into whether and to what extent directional electrodes move and continue to rotate after implantation, and long-term clinical studies may therefore be very difficult to conduct.

Alternative imaging techniques, such as electroencephalography (EEG) and magnetoencephalography (MEG), provide alternative imaging modalities for determining electrode positions and orientations by measuring stimulation-induced DBS magnetic fields, which overcome the fundamental drawbacks of current postoperative imaging techniques without exposing patients to radiation at all. The feasibility of DBS electrode localization based on scalp EEG has already been demonstrated, but localization errors of more than 10 mm have been reported [17]. The potential of MEG recordings to detect electrode position and orientation has been demonstrated in our previous research [18–22]. In this study, we present an improved and patient-oriented method for the radiation-free detection of electrode positions and orientations using a series of measurements with a conventional SQUID-based MEG. This method has been given the name MaDoPO (Magnetic Detection of Position and Orientation). For this study, a head–torso phantom with realistic dimensions was constructed, and the DBS electrode was placed at a realistic position in

the phantom's head. Postoperative CT was performed to determine the position and orientation of the electrode using state-of-the-art neuroimaging approaches and to compare them with those obtained from MEG recordings. A series of measurements were made with the MEG system under different directional and non-directional bipolar electrode configurations to find the measurement sequence that achieved clinically reliable accuracy with the smallest number of recordings. Although SQUID-MEG systems are not widely available, new technologies toward variable on-scalp or cap-shaped MEGs, which are currently the subject of intense research [23–25], will make magnetic detection of electrode positions and orientations feasible in daily routines. Whether such novel systems could improve detection accuracy is also being investigated in this study.

2. Materials and Methods

Figure 1 provides an overview of the sequence of data generation steps performed within this study. Once the realistic head phantom was constructed, preoperative imaging (both MRI and CT) was performed. Then, the DBS system, consisting of a directional electrode and a current-controlled implanted pulse generator (IPG), was inserted and fixed inside the phantom. A DBS neurosurgeon determined the position of the small opening on the head's surface for insertion of the electrode and the depth of electrode placement. Postoperative imaging (both MRI and CT) was then performed. These steps were performed at the Faculty of Engineering (construction of the phantom) and at the Faculty of Medicine (imaging) at Kiel University. The series of MEG measurements with different electrode configurations were performed at the Faculty of Medicine in Düsseldorf University, where a control CT was also performed directly afterwards to check and exclude possible displacement of the electrode. Preoperative imaging was used to create a 3D model of the phantom for precise electromagnetic modeling. Postoperative imaging was used to localize the electrode and determine the electrode's orientation (using state-of-the-art commercial Guide™ XT software) and to compare the results obtained with those of our MEG-based MaDoPO method. The individual steps from Figure 1 are described in more detail in the following subsections.

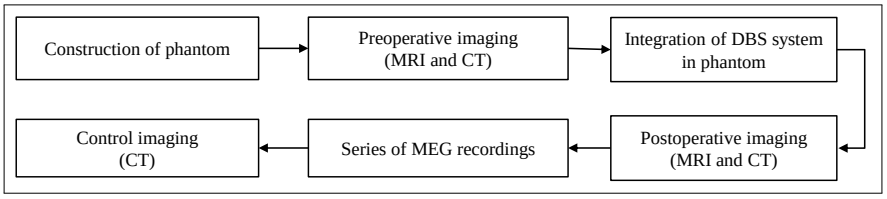

Figure 1. Steps performed to generate imaging and MEG measurement data as part of this study. Preoperative imaging was used to create a 3D model of the phantom. Postoperative imaging was used to determine electrode positions and orientations using a state-of-the-art approach. Localization and orientation detection results from MEG recordings were compared with those from postoperative imaging.

2.1. Phantom Design

The phantom designed for this study is depicted in Figure 2a, which includes both the head and the torso to approximate a human body. The dimensions of this phantom were as follows: 55 cm height, 35 cm width, and 25 cm depth. The phantom was made of acrylic glass and was therefore neither electrically conductive nor magnetic. It was filled with approximately 18 liters of isotonic fluid (NaCl 0.9%) through the only opening on the phantom, which was used to provide electrical conductivity between electrode contacts and the implanted pulse generator (IPG). Five fiducial markers (PINPOINT-128, Beekley Medical®) were placed at three anatomical landmark points (nasion, right pre-auricular (RPA), and left pre-auricular(LPA)) and on the top and back of the phantom to ensure accurate co-registration between the different modalities. The phantom, as it appeared following DBS intervention, is illustrated in Figure 2b.

A DBS system from the Boston Scientific Corporation (Boston Scientific, Marlborough, MA, USA), consisting of a current-controlled IPG (Vercise™ PC) and a directional electrode (Versice Cartesia™), was chosen, as it is currently in routine clinical use. This system is based on stimulation with rectangular pulses comprising a stimulation pulse phase and a passive charge-balancing phase. The position of the burr hole, the position and implantation angle of the electrode, the position of the connector and IPG, the course of the wire, and the drilling of the excess lead wire were determined by our DBS neurosurgeons and taped in the appropriate locations. To prevent the electrode from moving inside the phantom, it was glued into a transparent, rigid plastic tube glued in the burr hole, with only the electrode contacts and the CT radiopaque marker on the electrode protruding from the top of the phantom.

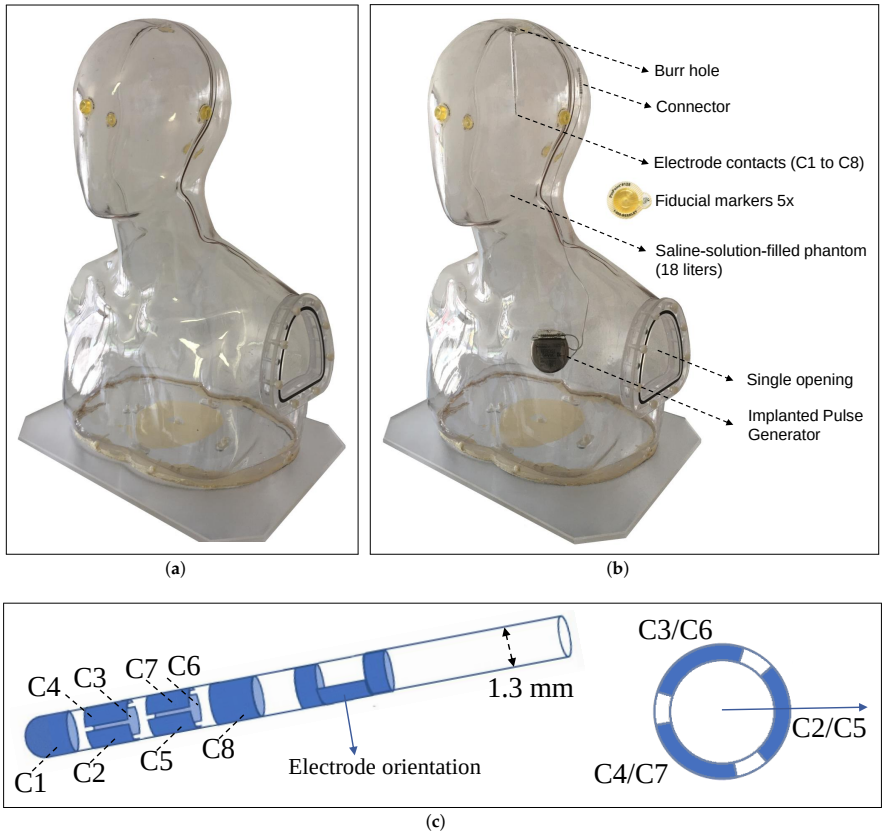

Figure 2. (**a**) Phantom with five fiducial markers attached to the surface of the phantom's head before DBS intervention. (**b**) Phantom with integrated DBS system consisting of a directional electrode, extension, and Implanted Pulse Generator. (**c**) Directional electrode in side view (left) and bottom view (right), showing the eight numbered contacts (C1–C8), and how the middle two contact levels are divided into three equally spaced segments. The arrow indicates electrode orientation.

The directional electrode consists of eight individually controlled platinum–iridium contacts (C1–C8), with the two middle contact levels divided into three segments, each covering 90° of the circumference (with 30° spacing between adjacent segments) as shown in Figure 2c. Any combination of these contacts can be activated to control the direction of the stimulation current. This technology, also known as Multiple Independent Current-Controlled (MICC) technology, has allowed us to precisely assign current amplitudes to

the contacts regardless of impedance differences [26] and to set any desired electrode configuration inside the phantom. In this study, we investigated four different types of configurations that differed in the direction of the current flow and, therefore, in the distribution of the magnetic field. More details are discussed under 'MEG Data Acquisition' in Section 2.4.

2.2. Neuroimaging of the Phantom

Before the DBS system was integrated into the phantom, MRI and CT examinations of the phantom were performed as normal for patients. The upper row in Figure 3 shows the preoperative CT of the phantom in axial, sagittal, and coronal view. The shape and geometry of the head and the position of the fiducial markers are clearly visible. From these images, an accurate 3D model of the phantom was created by segmenting the surface of the phantom's head, which was used to create a precise electromagnetic model. Details of this can be found under 'Modeling' in Section 2.7. These images were also used by our DBS neurosurgeons to plan the DBS surgery, both the position of the burr hole on the surface of the phantom's head and the final position of the electrode to be implanted were determined. Thus, it can be assumed that the position and implantation angle of the electrode match those of real DBS patients. The lower row in Figure 3 depicts the postoperative CT in the three dimensions. The transparent plastic tube through which the electrode was passed can be seen in Figure 3c. Postoperative imaging was performed according to Brainlab AG (Munich, Germany) scanning recommendations to ensure precise detection of DBS electrode position and orientation using commercial, state-of-the-art Guide™ XT software. After transportation and MEG measurements, a control CT of the phantom was performed to detect any displacement or rotation of the electrode during the study using the same software. No displacement or rotation was detected.

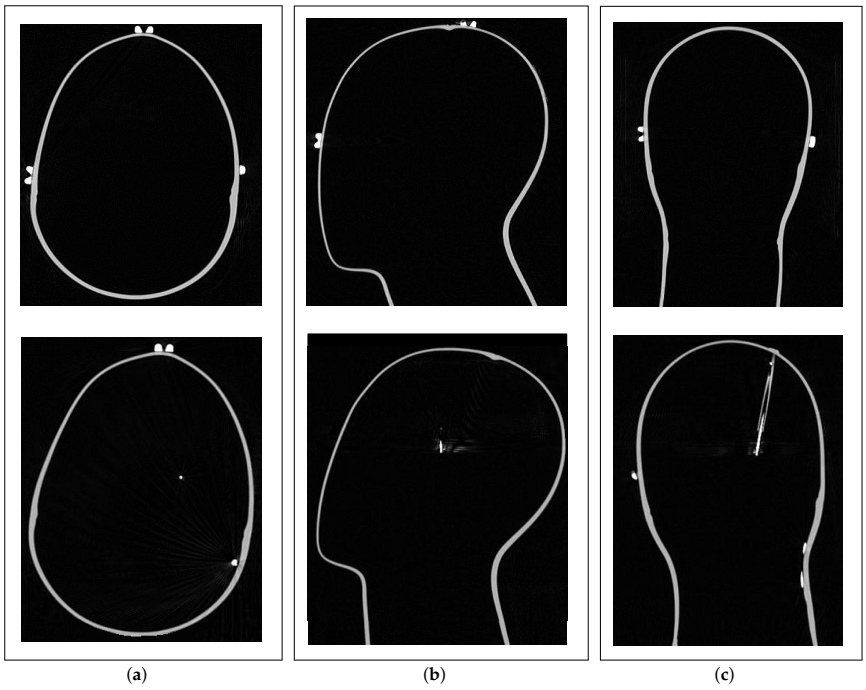

Figure 3. (**a**) Axial, (**b**) sagittal, and (**c**) coronal views of preoperative (upper row) and postoperative (lower row) CT imaging of the phantom. Preoperative imaging was used to create a 3D model of the phantom for an accurate electromagnetic model. Postoperative imaging was used to compare the results in electrode position and orientation detection with results from magnetic detection.

2.3. MEG Preparation

Several preparatory steps were performed before starting the actual MEG recordings. Four head position indicator (HPI) coils were placed at recommended positions on the surface of the phantom's head, i.e., two coils behind the ears and two coils on the upper forehead. The most commonly used digitizing system (Fastrak, Polhemus Inc., Colchester, VT, USA) was then used to first localize anatomical reference points, i.e., the center holes of Nasion, RPA, and LPA fiducial markers, and subsequently the HPI coils. The digitizing system uses an alternating current electromagnetic transmitter and receiver to digitize the positions of the points in space. The device has a static position accuracy of 0.8 mm and an orientation accuracy of 0.15° [27]. Furthermore, 500 additional points were localized around the phantom to improve co-registration accuracy with imaging. The phantom was then placed in the MEG scanner and not moved until the end of the measurements as illustrated in Figure 4a,b. In such conventional MEG scanners, the positions and orientations of the MEG sensors relative to each other are fixed and known beforehand, so that only the localization of the phantom relative to the sensor array is required. Excitation of the HPI coils at different times and frequencies and detection of the distribution of the magnetic fields they generate by the MEG system allowed localization of the coils relative to the MEG sensor array. The minimum errors in the distances between the fitted coil positions and the digitized positions were as follows: HPI pair 2–3: −0.6 mm, HPI pair 2–4: −0.4 mm, and HPI pair 3–4: 0.4 mm. HPI pairs with coil 1 were not considered by the MEG system due to implausible fitting results. From these errors, it can be concluded that the accuracy in detection of the phantom position in the MEG scanner was limited to 0.6 mm, which was given by the error between the HPI pair 2–3. The sum of all inaccuracies in the system, ±0.8 mm (digitization accuracy) and ±0.6 mm (HPI fitting accuracy), resulted in a value of ±1.4 mm, which described the spatial resolution of the MEG system. This value described a crucial factor with respect to electrode localization and orientation detection, as it limits detection accuracies.

(**a**) (**b**) (**c**)

Figure 4. (**a**) Phantom placed on patient bed in the MEG scanner. (**b**) Phantom head within the MEG sensor array. Lower part of the electrode, IPG, and coil cables are visible. (**c**) Programming of the IPG using a programming device.

2.4. MEG Data Acquisition

MEG data were collected using the Elekta Neuromag VectorView® MEG scanner. The scanner consisted of 306 individual channels corresponding to 102 high-sensitivity Superconducting QUantum Interference Device (SQUID) magnetometers and 204 SQUID gradiometers. Only the magnetometer data were used in this study. The noise level of the magnetometer sensors was measured at approximately 3 $fT/\sqrt{Hz}$ (as also indicated in the data sheet) at the beginning of the MEG recordings as part of a reference measurement. These sensors were ideally suited to measure the magnetic fields generated during electrical stimulation, which were in the range of a few picoTesla. The acquisition parameters of the MEG scanner were set as follows: The sampling rate was set to its maximum of 5 kHz. The low-pass filter was set to its highest possible value of 1660 Hz, and the cutoff frequency of the high-pass filter was set to DC (no high-pass filtering) to measure the magnetic field generated by the stimulation with the maximum allowable acquisition bandwidth, since the DBS signal included the adjusted stimulation frequency and its next harmonic frequencies. The duration of each measurement was 180 s. A total of 24 measurements were taken using bipolar electrode configurations with clinically used DBS stimulation parameters with 3 mA amplitude, 60 µs pulse width, and 130 Hz frequency (Figure 4c). These values are normally used in routine clinical practice. The performed measurements differed by the activated electrode contacts as listed in Table 1, which we divided into four vertical, diagonal, horizontal, and symmetrical configuration types. The numbers C1 to C8 in the table represent the electrode contact numbers (according to Figure 2c), where the first number represents the cathode and the second number represents the anode. The motivation for the choice of used electrode configurations is summarized in Figure 5 and can be motivated as follows: The first six measurements (#01–#06) described all possible measurements performed with non-directional electrode configurations, in which all three segmented contacts on the two middle levels of the electrode were activated with the same amount of current to allow conventional ring stimulation (a 33/33/33 ratio of current is guaranteed by MICC technology). These measurements were used to investigate electrode localization. In the 'vertical' electrode configuration, the physical center of stimulation (represented by thick colored dots) lay exactly between activated contacts, e.g., between contacts C1 and C234 in the first measurement, with the stimulation current flowing from the cathode to the anode, thus exhibiting a vertical current flow direction along the longitudinal axis of the electrode (indicated by the colored arrows). The remaining measurements, performed with different directional electrode configurations (#07–#24), were used to investigate electrode orientation detection. In the 'diagonal' configuration, the physical center of stimulation was located deeper within the electrode, e.g., between contacts C1 and C2 in measurement #07, and the current flow from the cathode to the anode there exhibited a diagonal current flow direction. In the 'horizontal' configuration, the physical center of stimulation lay exactly between adjacent segmented contacts, e.g., between contacts C2 and C3 in measurement #13, and the current flowing from the cathode to the anode there exhibited a horizontal current flow direction (perpendicular to the longitudinal axis of the electrode). In the 'symmetrical' configuration, two adjacent segments were stimulated in a 50/50 ratio against the third segment on the same level of the electrode so that the current flow propagates symmetrically around the electrode from both cathode contacts to the anode contact (perpendicular to the longitudinal axis). The current, the direction of which was defined by the corresponding configuration, generated a defined magnetic field. The magnetic field distribution was measured around the phantom by the MEG sensor array and used with precise electromagnetic simulations and detection algorithms to derive electrode positions and orientations. Since the measurements in this study were performed under ideal conditions with a phantom, the measured MEG signals were not contaminated by subject-related biological artifacts, such as cardiac activity, skeletal muscles, eyes, head, and body movements. Ambient noise consisted solely of power line interference, which affected only insignificant frequencies (50 Hz and harmonics).

Table 1. Performed MEG measurements.

Electrode Localization		Electrode Orientation Detection					
Vertical Configuration		Diagonal Config.		Horizontal Config.		Symmetrical Config.	
No.	Contacts: (−) vs. (+)	No.	Contacts: (−) vs. (+)	No.	Contacts: (−) vs. (+)	No.	Contacts: (−) vs. (+)
#01	C1 vs. C234	#07	C1 vs. C2	#13	C2 vs. C3	#19	C23 vs. C4
#02	C234 vs. C567	#08	C1 vs. C3	#14	C3 vs. C4	#20	C34 vs. C2
#03	C567 vs. C8	#09	C1 vs. C4	#15	C4 vs. C2	#21	C42 vs. C3
#04	C1 vs. C567	#10	C5 vs. C8	#16	C5 vs. C6	#22	C56 vs. C7
#05	C234 vs. C8	#11	C6 vs. C8	#17	C6 vs. C7	#23	C67 vs. C5
#06	C1 vs. C8	#12	C7 vs. C8	#18	C7 vs. C5	#24	C75 vs. C6

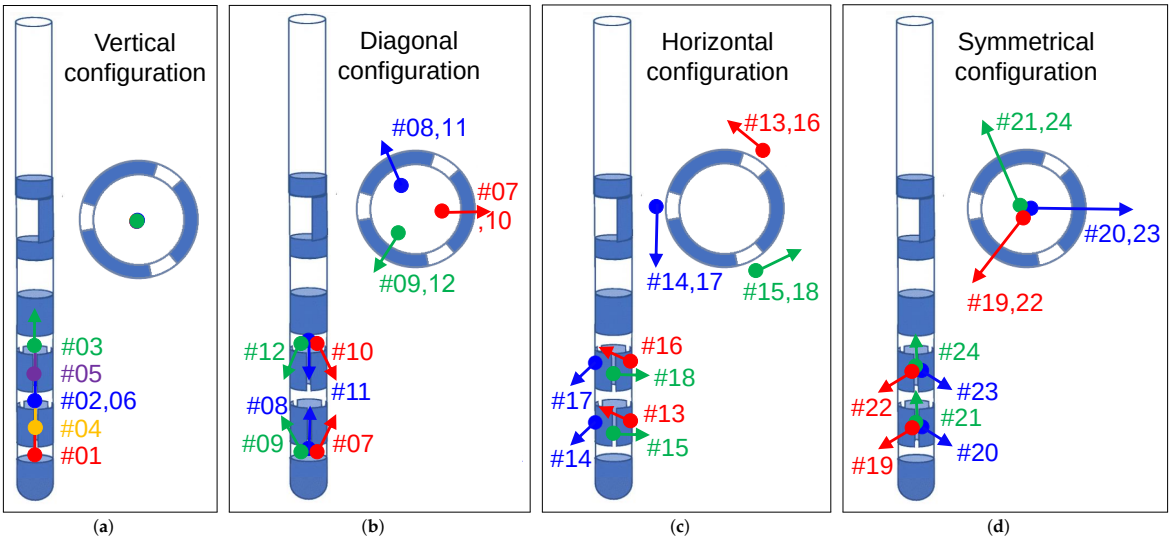

Figure 5. Four different electrode configuration types were analyzed: (**a**) vertical, (**b**) diagonal, (**c**) horizontal, and (**d**) symmetrical electrode configurations, which differ in the physical center of stimulation (thick colored dots) and the direction of current flow (colored arrows).

2.5. The Pipeline of the MaDoPO Method

Figure 6 provides an overview of the procedure for MEG-based localization of the electrode and detection of the electrode orientation in the phantom, which could also be performed in real-patient analysis. First, the preoperative imaging (CT in this case) was imported into 3D Slicer software, which is a free open-source medical imaging software. The surface-based segmentation was performed using this software, first by applying the 'threshold segmentation' function to obtain the preliminary results of the automatic segmentation. Then, manual correction was performed slice by slice, and the result was finally smoothed. After that, a 3D model of the phantom was created and was saved as a STL (STereoLithography) file, a triangulated representation of a 3D model. The file contained the following mesh information: vertices 2,537,752, faces 5,076,736, and storage space approximately 250 MB. Since the mesh resolution was too high for this application, which would have resulted in far too much computation time for modeling, the model was

imported into MeshLab, an open source system for processing and editing 3D meshes, and decimated by remeshing. This resulted in the following mesh information: 20,353 vertices, 40,702 faces, and approximately 2 MB of storage space. This file was first imported into MATLAB software to perform a pre-localization of the electrode. In this process, the created 3D model, generated based on CT data, and thus defined in CT coordinates, had to be transformed into the coordinate system of the MEG system. As mentioned in Section 2.3, the coordinate system in which the MEG sensors were expressed was defined based on three anatomical landmarks identified on the phantom's head (Nasion, LPA, and RPA). FieldTrip Toolbox was used to co-register the anatomical image with the MEG sensor array, which was performed using the 'ft_volumerealign' function [28]. However, the positions of the anatomical landmarks in the CT data had to be given as inputs, which could be accurately localized by the center hole of the attached fiducial markers. The aim of pre-localization was to estimate the position of the electrode in a short time and to narrow down the volume for post-localization by defining the region of interest (ROI). For this purpose, it was sufficient to create a simplified model (i.e, a model of an electric current dipole). Then, the 3D model was imported into the COMSOL software and aligned to the MEG coordinate system based on the translation and rotation results of the co-registration performed previously. An accurate finite element electromagnetic model was created and used together with processed MEG recordings for electrode post-localization and orientation detection. The main steps are described in detail in the following sections. As illustrated with dashed lines in Figure 6, future perspectives of our method include the integration of the localization and orientation detection results into the open-source Lead-DBS software [29,30] to use its implemented features, such as 3D visualization of the electrode within patient-specific anatomy, modeling of the volume of tissue activated based on the applied stimulation parameters, and structural–functional connectivity analysis if needed.

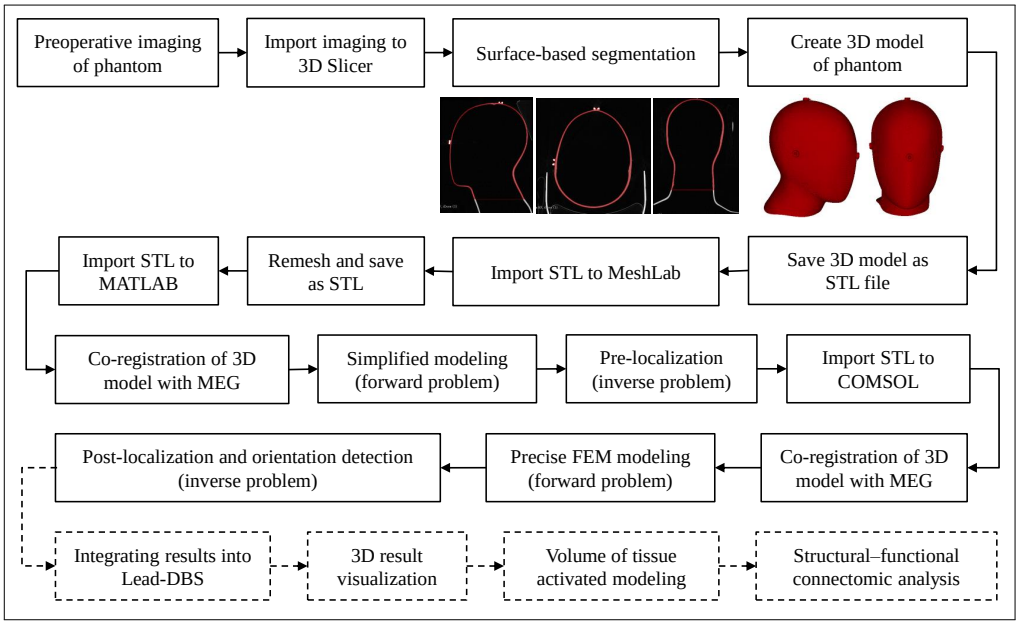

Figure 6. Steps in the modeling process: Preoperative CT is imported into 3D Slicer software, where surface-based segmentation is performed to create the 3D model of the phantom. The model is decimated by remeshing it using MeshLab software. The model is then imported into the appropriate software for modeling.

2.6. Signal Processing of Measured Data

The processing steps used on the measured MEG data are provided as an analysis pipeline in Figure 7. For each measurement, we obtained 102 time signals, one from each MEG sensor. The measured data were imported into MATLAB (version R2018a) and pre-processed using the FieldTrip toolbox [28]. Each time signal, which was 180 s long, was high-pass filtered using a sixth-order Butterworth filter with a cutoff frequency of 60 Hz without losing signal components, since the stimulation signal contained much higher frequencies (stimulation frequency of 130 Hz and its harmonics). Then, a peak detection algorithm was used to detect the location of successive DBS peaks in the time signal, and, in the next step, each signal was divided into individual DBS time segments. These segments were then averaged, which significantly improved the signal-to-noise ratio (SNR) by $\sqrt{N}$ with $N = 180\ \mathrm{s} \cdot 130\ \mathrm{s}^{-1}$ averages. The maximum value from this averaged time segment (at a specific time point with the largest SNR) was then taken for each MEG sensor, resulting in a total of 102 values, with $\mathrm{B}_{\mathrm{meas}}$ representing the measured magnetic field distribution of the corresponding MEG recording. Since the overall background noise over all frequencies and especially over the frequencies of interest (stimulation frequency and its harmonics) was so low that the magnetic field generated by the stimulation could be easily measured, no further signal processing steps such as artifact rejection methods (e.g., signal space separation) needed to be used.

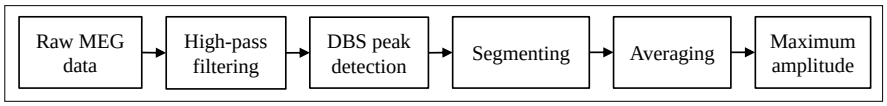

Figure 7. Signal processing pipeline: Each measured MEG signal was high-pass filtered with a 60 Hz cutoff frequency, segmented into short DBS periods (according to the locations of DBS peaks detected by a peak detection algorithm), and averaged to a single time period. The maximum amplitude value was then taken.

2.7. Modeling

A simplified model was used for electrode pre-localization and precise finite element electromagnetic model was used for electrode post-localization and orientation detection.

2.7.1. Simplified Model

The simplified model includes the model of an electric current dipole, which can be calculated using the following Biot–Savart law [31]:

$$\mathrm{B}_{\mathrm{pre,model}}(pd, ad) = \frac{\mu_0}{4\pi} \frac{(\vec{R} - \vec{L}_{pd}) \times \hat{s} \cdot \vec{Q}}{|\vec{R} - \vec{L}_{pd}|^3}, \quad (1)$$

where pd is the dipole position, ad is the dipole orientation, $\vec{Q}$ is the dipole moment with $\vec{Q} = I \cdot \hat{s}_{ad}$, I is the stimulation current, $\hat{s}_{ad}$ is the direction of current flow, $\vec{L}$ is the dipole location, $\vec{R}$ is the sensor location, and $\hat{s}$ is the unit orientation of the sensor. The entire volume of the phantom's head was divided into a regular coarse grid with a size of $90 \times 90 \times 90$ mm and a resolution of 10 mm, resulting in a total number of $N_{pd} = 1000$ dipole positions. For each dipole position, a dipole orientation oriented in the z-direction was tilted in the x- and y-directions in 5° steps between 0° and 30° and rotated in 45° steps on a circle between 0° and 360°, resulting in a total number of approximately $N_{ad} = 70$ dipole orientations. For each different position–orientation pair, the magnetic field was calculated using the above equation. In previous papers [18,19], we have demonstrated that this dipole model, which applies to an infinite homogeneous space and neglects the modeling of the volume conduction, describes a good approximation for the bipolar electrode configuration depicted in Figure 5 within realistic distances between electrode and MEG sensors. Although this model cannot be used for precise

millimeter-accurate localization (since it is only a simplification of the real world), it is sufficient for pre-localization to estimate in which area the electrode is approximately located without much computational time, so that the actual millimeter-accurate search can be performed with the precise electromagnetic finite element model, which requires much more effort and computational time. Post-localization is performed within the ROI with dimensions 29 × 29 × 29 mm with 1 mm resolution, whose position is defined by the result of pre-localization. The associated simulations of the dipole model were performed using MATLAB.

2.7.2. The Finite Element Electromagnetic Model

The electromagnetic finite element simulations were performed based on a model created in COMSOL Multiphysics®, which is shown in Figure 8. For each structure in the model, the corresponding material was taken directly from the built-in material library, and values were assigned for uniform electrical conductivity σ, relative permeability μ_r, and relative permittivity ϵ_r. The phantom and the outer jacket of the electrode were modeled with acrylic plastic ($\sigma \approx 0$ S/m, $\mu_r = 1$, $\epsilon_r = 4.2$), the eight independent electrode contacts with platinum–iridium ($\sigma = 10^6$ S/m, $\mu_r = 1$, $\epsilon_r = 1$), and the content of the phantom with saline solution ($\sigma = 1.6$ S/m, $\mu_r = 1$, $\epsilon_r = 80$). The phantom, whose 3D model was imported into COMSOL and moved to the MEG-based position according to the MEG-CT co-registration result, and the modeled directional electrode were surrounded by a cuboid box with a length of 500 mm filled with air ($\sigma \approx 0$ S/m, $\mu_r = 1$, $\epsilon_r = 1$). The MEG helmet was modeled as a surface and all measurement points were placed on that surface. A tetrahedral mesh with 'Extra Fine' resolution was used. To model the bipolar electrode configurations from Table 1, the boundary condition 'Terminal' of 'Current Type' was used for the cathode and the boundary condition 'Ground' was used for the anode. The simulations were performed using the 'Magnetic and Electric Fields (mef)' interface of the 'AC/DC module' of COMSOL. Figure 9 illustrates the electromagnetic simulation results of the vertical, diagonal, horizontal and symmetrical electrode configuration considered in this work. The corresponding magnetic field distribution is color coded, and the direction of current flow is marked by white arrows. The magnetic flux densities in the *x*-, *y*-, and *z*-directions (B_x, B_y, and B_z) on the surface of the MEG helmet were calculated. In this experiment, the MEG sensors measured the normal field component of the magnetic field perpendicular to the helmet surface. To determine the magnetic field $B_{\text{post,model}}(pe, ae, ce)$ perpendicular to the helmet surface in the simulation, the dot product $B_{\text{post,model}} = \vec{B} \cdot \vec{s}$ was calculated, where $\vec{s}$ is the unit vector perpendicular to the helmet and $B = B_x + B_y + B_z$. Thus, the modeled magnetic field depended on the position of the electrode *pe*, the orientation of the electrode *ae*, and the applied electrode configuration *ce*, with the electrode taking only the positions in 1 mm steps in the predefined ROI with the dimensions 29 × 29 × 29 mm (number of electrode positions in the model N_{pe} = 27,000). For electrode post-localization of each electrode configuration considered in this study, the position of the electrode was moved within the predefined ROI in the model in 1 mm steps, and the expected magnetic field values at the MEG sensor positions were calculated. In determining electrode orientation, it was assumed that electrode localization had already been performed and that the position of the electrode was precisely known. In the model, therefore, the electrode was placed at the appropriate location and rotated around its own longitudinal axis in 1° steps, allowing a total of $N_{rot} = 360$ orientations. The expected magnetic field, $B_{\text{model}}(rot, ce)$, depended only on the rotation of the electrode, *rot*, and on the electrode configuration, *ce*.

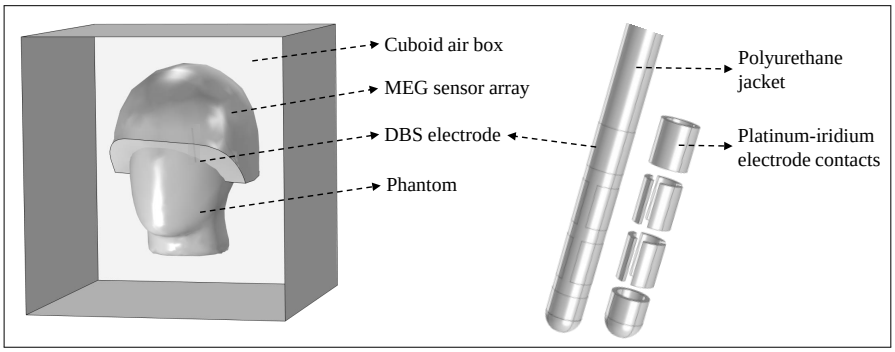

Figure 8. Finite element electromagnetic model. It includes the phantom filled with saline solution, the directional electrode placed inside the phantom, and the helmet-shaped MEG sensor surface. These structures are surrounded by a cuboid air box.

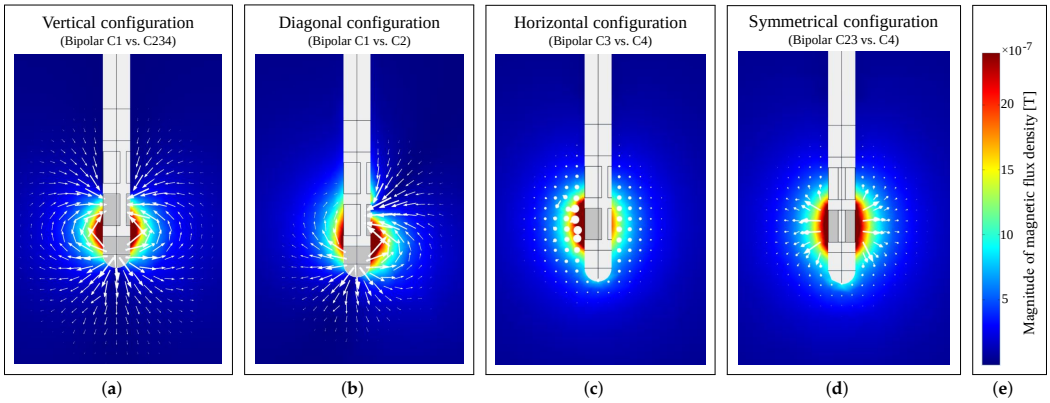

Figure 9. Electromagnetic simulation results of a (**a**) vertical, (**b**) diagonal, (**c**) horizontal, and (**d**) symmetrical electrode configuration, in which the magnetic field is shown in color and the direction of current flow is shown with white arrows. (**e**) Color legend applies to all images.

2.8. The Method Used for Electrode Localization

For electrode localization, the measured and processed values, according to the signal processing pipeline in Figure 7, were compared with the modeled values. As stated, all modeled data described the magnetic field values that would be measured by the MEG sensor array if the electrode occupied the defined position in the phantom. To ensure comparability between measured and modeled data, the data were normalized to the respective absolute maximum values beforehand and the Goodness of Fit (GoF) was calculated between each measured and modeled data point using the normalized root mean square error (NRMSE) as a cost function using Equations (2) and (3) for pre-localization and post-localization, respectively, as follows:

$$\mathrm{GoF}_{\mathrm{meas},x} = 1 - \frac{||\mathrm{B}_{\mathrm{pre,model}}(pd, ad) - \mathrm{B}_{\mathrm{meas},x}||}{||\mathrm{B}_{\mathrm{pre,model}}(pd, ad) - \mathrm{mean}(\mathrm{B}_{\mathrm{pre,model}}(pd, ad))||} \quad (2)$$

$$\mathrm{GoF}_{\mathrm{meas},x} = 1 - \frac{||\mathrm{B}_{\mathrm{post,model}}(pe, ae, ce) - \mathrm{B}_{\mathrm{meas},x}||}{||\mathrm{B}_{\mathrm{post,model}}(pe, ae, ce) - \mathrm{mean}(\mathrm{B}_{\mathrm{post,model}}(pe, ae, ce))||}, \quad (3)$$

where a GoF value of 1 indicates a perfect fit, and $||.||$ is the 2-norm of a vector. The estimated electrode position was then given with the minimum NRMSE value or the maximum GoF value for the particular measurement x. The electrode localization error was calculated using the Euclidean distance between the estimated electrode position in the model and the real, known position of the electrode in the phantom, which was determined using a state-of-the-art neuroimaging approach. To improve localization accuracy, all measurements with non-directional electrode configuration (measurements with vertical electrode configuration from Table 1) were fitted and evaluated together, since the solution of the inverse problem could be constrained by providing a priori known information about the electrode geometry (i.e., the distance between different contacts of the electrode):

$$\mathrm{GoF} = 1/6 \cdot \sum_{x=1}^{6} \mathrm{GoF}_{\mathrm{meas},x} \rightarrow \min. \quad (4)$$

The electrode localization results from the magnetic detection were compared with the co-registered results obtained from postoperative CT imaging using GuideXT software. It should be noted that localization errors may occur due to the discretization of the localization area. The Euclidean distance between both results is defined as the localization error. If the sensor is not directly on a defined grid point, the localization error is at least the distance between the nearest grid point and the location of the sensor. To solve this problem, a higher resolution is required. However, this would lead to a drastic increase in computational complexity during post-localization. A lower initial grid resolution during pre-localization was used to keep the computational complexity low (a few minutes). Precise electromagnetic modeling with a resolution of 1 mm within the ROI for post-localization required a pure computational time of approximately two weeks, i.e., a resolution of 0.5 mm would increase the computational time by a factor of eight (equivalent to 16 weeks). Simulations were performed on a 64-bit computer configured with anIntel core i7, 3.6 GHz processor with 32 GB RAM.

2.9. The Method Used for Electrode Orientation Detection

Similar to electrode localization, for electrode orientation detection, the measured and processed values are compared with the modeled values. Each modeled data point describes the magnetic field values that would be measured by the MEG sensor array if the electrode occupied its defined orientation within the phantom. To ensure comparability between the measured and modeled data, the data were normalized to their respective absolute maximum values beforehand, and the GoF was calculated between each measured and modeled data point using the NRMSE as a cost function, as follows:

$$\mathrm{GoF}_{\mathrm{meas},x} = 1 - \frac{||\mathrm{B}_{\mathrm{model}}(rot, ce) - \mathrm{B}_{\mathrm{meas},x}||}{||\mathrm{B}_{\mathrm{model}}(rot, ce) - \mathrm{mean}(\mathrm{B}_{\mathrm{model}}(rot, ce))||}. \quad (5)$$

The estimated result for the electrode orientation was then given by the minimum NRMSE value or by the maximum GoF value for the particular measurement x. The error in determining the electrode orientation was calculated using the absolute angle between the electrode orientation in the found model and the real known orientation of the electrode in the phantom obtained by the state-of-the-art neuroimaging approach. To improve electrode orientation detection accuracy, different measurements with directional electrode configuration were fitted and evaluated together, since the solution of the fitting approach could be constrained by providing a priori known information about the electrode geometry and corresponding electrode configurations (i.e., the angle between each segmented contact of the electrode):

Considering measurements within same electrode configuration:

$$\mathrm{GoF}_{\mathrm{config}} = 1/\mathrm{N}_{config} \cdot \sum_{x=1}^{\mathrm{N}_{config}} \mathrm{GoF}_{\mathrm{meas},x} \rightarrow \min. \quad (6)$$

Considering measurements within multiple electrode configurations:

$$\mathrm{GoF_{multip}} = 1/\mathrm{N}_{multip} \cdot \sum_{x=1}^{\mathrm{N}_{multip}} \mathrm{GoF_{config},}_{x} \rightarrow \min. \quad (7)$$

Considering all performed measurements:

$$\mathrm{GoF_{total}} = 1/\mathrm{N}_{total} \cdot \sum_{x=1}^{\mathrm{N}_{total}} \mathrm{GoF_{multip},}_{x} \rightarrow \min. \quad (8)$$

The results of the electrode orientation detection with magnetic measurements were compared with the results of postoperative CT imaging using GuideXT software. For this purpose, in the software, an anterior to posterior commisure (AC-PC) line was first defined, with the AC point determined by localizing the center hole of the nasion fiducial marker and the PC point determined by the center hole of the back fiducial marker. Relative to the mid-commisural (MC) point, the orientation of the electrode was then determined, with both 99° and −89° being the results of orientation detection. The difference in absolute angle between both real and calculated orientation is defined as the orientation detection error.

3. Electrode Localization Results

The following Cartesian coordinates of the electrode were determined within the MEG coordinate system by the state-of-the-art approach: Electrode tip [−13.8; 14; 4] mm, mid points of C1 [−14; 14.2; 4.6] mm; C234 [−14.5; 14.9; 6.5] mm, C567 [−14.9; 15.5; 8.3] mm, and C8 [−15.4; 16.1; 10.2] mm.

3.1. Electrode Pre- and Post-Localization

For electrode pre-localization, a volume with dimensions 90 × 90 × 90 mm was first defined in the phantom's head with a coarse resolution of 10 mm, as shown in Figure 10a. Then, the processed measured data from the first measurement in Table 1 were compared with the modeled data from the dipole model with the GoF value for each (numbered) grid point calculated according to Equation (2). The grid point numbered 464, with coordinates [x; y; z] = [−10; 10; 10] mm yielded the maximum GoF value of approximately 0.78 among all 1000 dipole positions as shown in Figure 10b. Since this was a rough estimate, a cuboid of 30 mm length was placed around the localized grid point that defined the ROI for the following precise post-localization of the electrode. For this purpose, the consideration of a single measurement was sufficient. Then, the modeled electrode was moved within the ROI (see Figure 10c) in the precise electromagnetic model with 1 mm steps, and the GoF value was calculated based on the joint consideration of all non-directional measurements using Equation (4). The electrode position (or the position of the electrode tip), numbered 8689 with the coordinates [−15; 15; 4] mm, obtained the maximum GoF value of slightly above 0.8, which described the result of electrode localization (see Figure 10d). A comparison with the real electrode position revealed the following localization errors: Electrode tip 1.65 mm, C1 1.8 mm, C234 2.01 mm, C567 2.26 mm, and C8 2.39 mm, providing an averaged error of 2.02 mm. It can be argued that the localization error of approximately 2 mm was due to several inaccuracies in the system, with the spatial resolution of the MEG scanner being the largest contributor. Assuming a MEG spatial resolution error of 1.4 mm, as described in detail in Section 2.3, it can be concluded that the remaining error of approximately 0.6 mm arose appropriately elsewhere during the localization process, for example, due to inaccuracies in the measurements (noise) and simulations (material parameters).

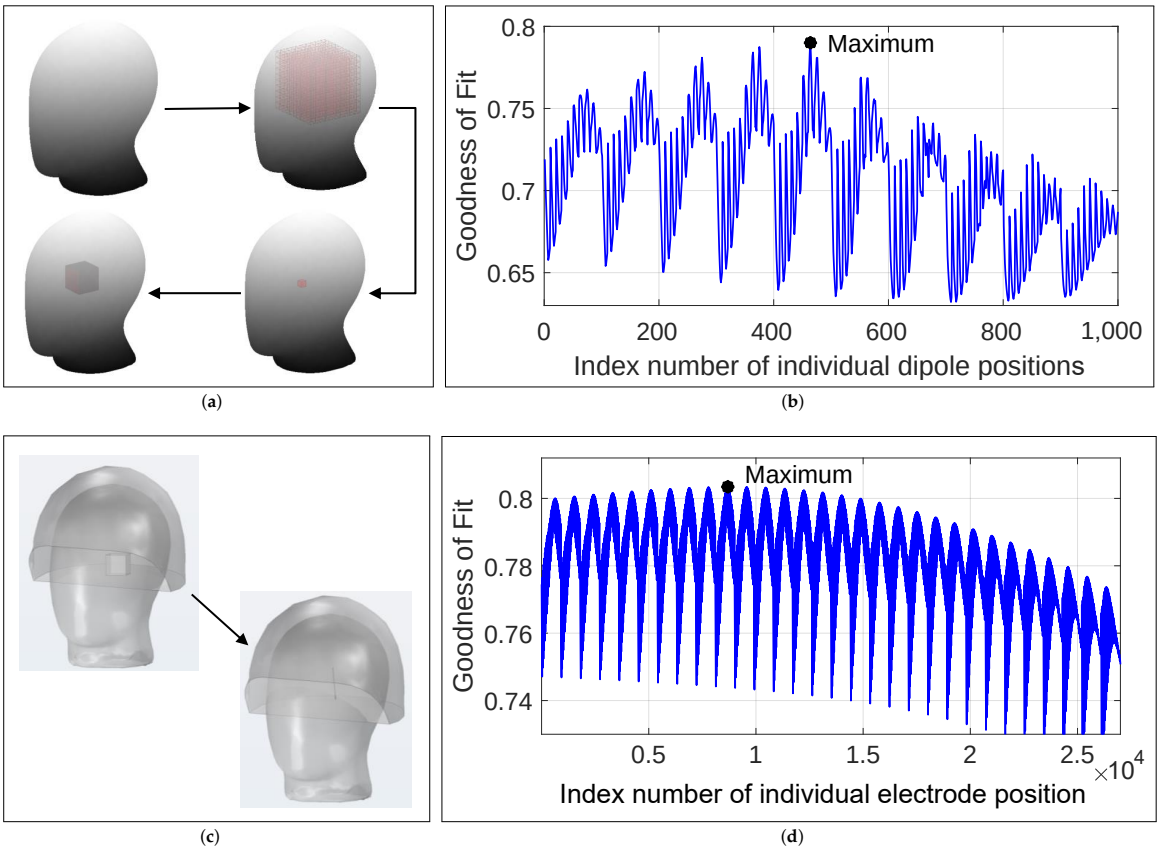

Figure 10. (**a**,**c**): Schematic representation of the procedure for pre- and post-localization of the electrode. (**b**,**d**): GoF values between modeled and measured data, with 1000 positions for the dipole in the simplified dipole model and 27,000 positions for the electrode in the electromagnetic model.

3.2. Localization Accuracy and Number of Sensors

The localization accuracy depended on the number of MEG sensors and their local distribution on the sensor surface as illustrated in Figure 11b. The conventional MEG helmet system provided high spatial resolution of the magnetic field with 102 magnetometers sampling the field distribution. If the number of sensors on the sensor surface was reduced uniformly (uniform sensor distribution), 80 sensors were also sufficient to achieve the same localization result as with 102 sensors, but the localization error increased when less than 80 sensors were considered. However, if the sensors were reduced unevenly depending on the distance of the sensor to the electrode (the sensor with the largest distance was reduced first), even 40 sensors were sufficient to achieve the same localization result. This result indicates that a concentrated distribution of sensors near the electrode is preferable to a uniform sensor distribution around the head.

3.3. Localization Accuracy and Number of Recordings

The localization accuracy depended on the number of measurements considered in the localization process (Figure 11c). A single measurement with a bipolar non-directional electrode configuration resulted in a maximum error of approximately 3.5 to 4 mm, while considering all possible measurements with bipolar non-directional stimulation (six measurements in total) caused a mean error of 2.02 mm. Three specific measurements with a bipolar non-directional configuration at each of the three electrode levels (C1 vs. C234,

C234 vs. C567, C567 vs. C8) resulted in an error of 2.25 mm, so that the remaining three measurements had their accuracies improved by only 0.23 mm.

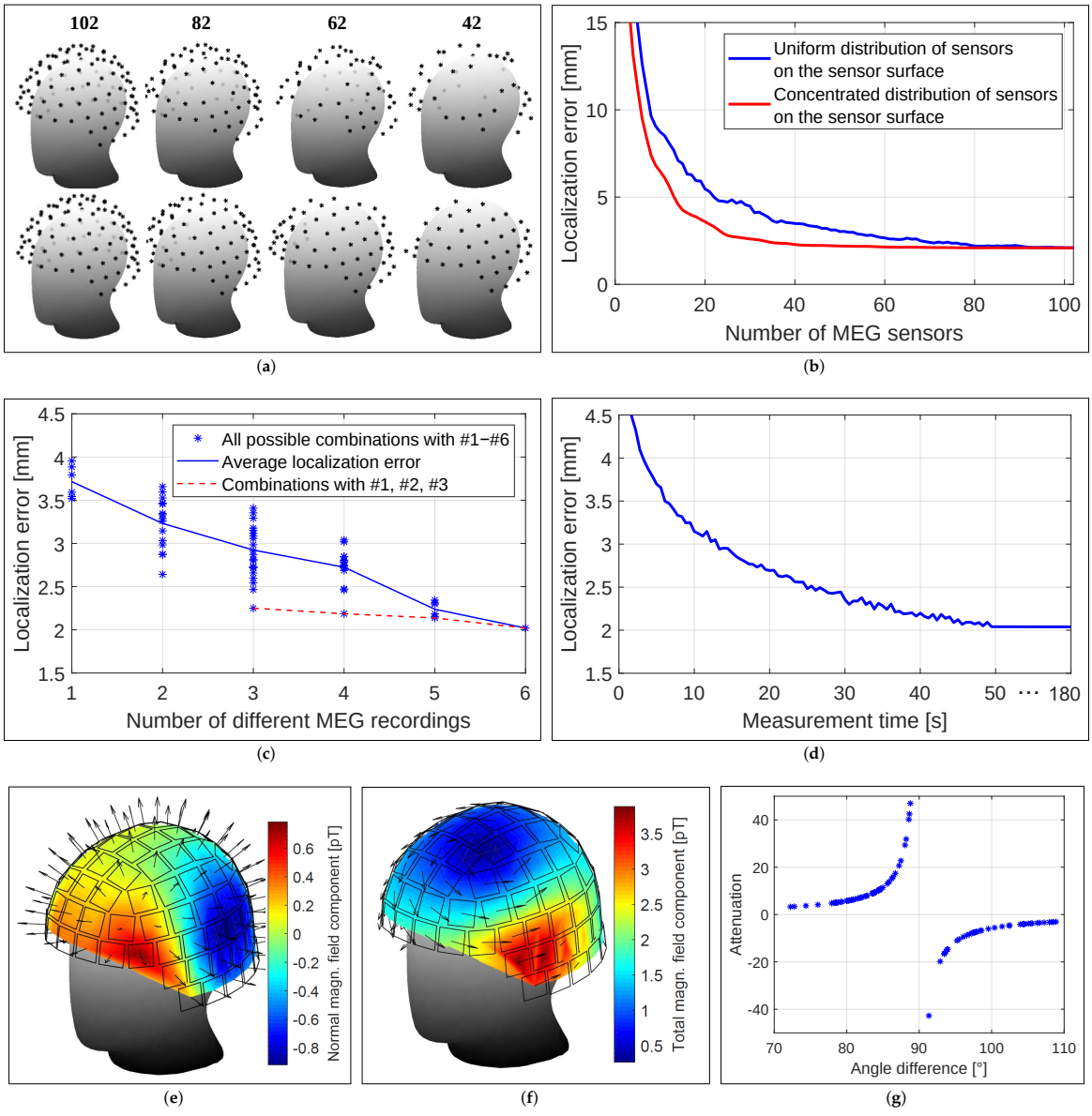

Figure 11. (**a**) Distribution of different numbers of MEG sensors on the sensor surface. Localization error as a function of (**b**) the number of MEG sensors and their distributions, (**c**) the number of MEG recordings with different non-directional stimulation modes, and (**d**) the recording time for each measurement. (**e**) Measured magnetic field distributions with a non-directional stimulation configuration. Arrows indicate the orientation of the MEG sensors. (**f**) Expected magnetic field distribution for the magnitude of the magnetic field. Arrows indicate the direction of the magnetic field. (**g**) Attenuation of measured magnetic fields due to the angle between the orientation of the MEG sensor and that of the magnetic field.

3.4. Localization Accuracy and Measurement Time

The localization accuracy depended on the measurement duration and SNR (Figure 11d). Shortening the measurement duration from 180 s (SNR gain of 21.8 dB after 23,400 averages) to 50 s (SNR gain of 19 dB after 6500 averages) resulted in no loss of localization accuracy. Shortening the measurement duration to approximately 13 s (SNR gain of 16.1 dB after 1700 averages) caused only a 1 mm degradation in accuracy. Further investigation revealed that a SNR of 20 dB (i.e., where the signal is two orders of magnitude larger than the noise) resulted in no loss of localization accuracy, whereas a SNR of 10 dB (i.e., where the signal is only one order of magnitude larger than the noise) resulted in an additional error of 1 mm.

3.5. Localization Accuracy and Sensor Orientation

The localization accuracy depended on the orientation of the MEG sensors. Bipolar non-directional electrode configurations produced a magnetic field that had mainly a tangential field component at the sensor surface, which can be seen as arrows in Figure 11f. However, each MEG sensor measured the normal field component, marked as arrows in Figure 11e, resulting in the measurement of an attenuated magnetic field, with attenuation ranging from a factor of 3 (4.7 dB) to 50 (17 dB), depending on the angle between the sensor orientation and the direction of the magnetic field between 70° and 110° as shown in Figure 11g. On average, a SNR gain of approximately 8.6 dB would be achieved, resulting in a significant reduction in measurement and averaging time of less than 10 s.

4. Electrode Orientation Detection Results

As stated in Section 2.9, the orientation of the electrode was determined to both 99° and −89° relative to the AC-PC line. With a single magnetic measurement with any directional electrode configuration, it was possible to determine that 99° corresponds to the actual orientation of the electrode.

4.1. Diagonal Electrode Configuration

The electrode orientation detection results of measurements with diagonal electrode configurations (i.e., measurements #7–#12) are depicted in Figure 12a. When considering individual measurements, an average accuracy of 16° was achieved with a maximum GoF value of approximately 0.8 (see colored curves). The GoF curves exhibited relatively flat behavior near the maximum, additionally allowing neighboring orientations to be considered as solutions in case of slight measurement or modeling errors. When three contiguous measurements were considered, the maximum GoF value increased to approximately 0.827, and an accuracy of 12° (determined 111° instead of 99°) was achieved. Consideration of three additional measurements resulted in a slight increase of the GoF value to approximately 0.83, and an accuracy of 10° to a slight improvement of orientation detection was achieved.

4.2. Horizontal Electrode Configuration

The electrode orientation detection results of measurements with horizontal electrode configurations (i.e., measurements #13–#18) are shown in Figure 12b. When considering individual measurements, an average accuracy of 11° was achieved with maximum GoF values of approximately 0.8. When three contiguous measurements were considered, an accuracy of 6° (determined to be 93° instead of 99°) was achieved, and the maximum GoF value increased to approximately 0.85. Consideration of three additional measurements resulted in only a slight improvement (maximum GoF value of 0.86 and 5° accuracy).

4.3. Symmetrical Electrode Configuration

The electrode orientation detection results of measurements with symmetrical electrode configurations (i.e., measurements #19–#24) are provided in Figure 12c. When considering individual measurements, an average accuracy of 15° was achieved with GoF values of approximately 0.8, with two potential outliers visible at approximately 130°. Disregard-

ing the two outliers, an average accuracy similar to that of the horizontal configuration was observed (as expected). Since GoF curves show flat behavior around the maximum, adjacent orientations may be considered as solutions (due to measurement or modeling errors), resulting in outliers (as in this case). With three contiguous measurements, an accuracy of 8° (determined to be 91° instead of 99°) was achieved and the maximum GoF value increased to approximately 0.86. Consideration of three additional measurements resulted in only a slight improvement (maximum GoF value of 0.87 and 6° accuracy).

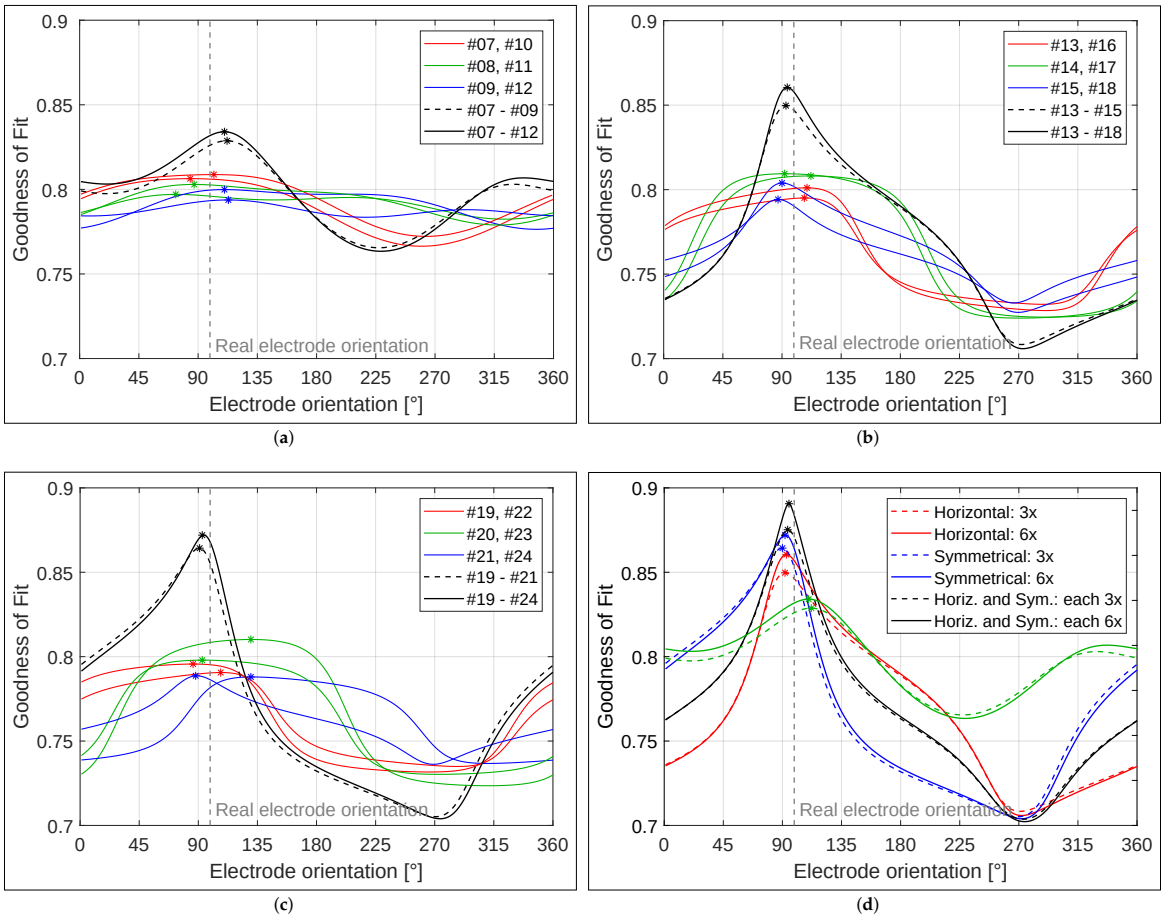

Figure 12. Results of electrode orientation detection for measurements with (**a**) diagonal, (**b**) horizontal, and (**c**) symmetrical electrode configurations. (**d**) Results for measurements with both horizontal and symmetrical electrode configurations.

4.4. Horizontal and Symmetrical Electrode Configuration

The electrode orientation detection results considering three and six contiguous measurements for each of the three investigated electrode configurations are summarized in Figure 12d (colored solid and dashed lines). In addition, that figure presents the result of the combined consideration of the symmetrical and horizontal electrode configurations, since the combinations of both configuration types obtained the best results among all possible combinations with the diagonal configuration. The range of GoF values for the diagonal configuration was relatively flat (between 0.77 and 0.83), because the rotation of the electrode in the model had little effect on the change of the magnetic field distribu-

tion compared to other configuration types. It was found that the maximum GoF value increased to approximately 0.88–0.89 when the horizontal and symmetrical configurations were considered, depending on the number of measurements considered. An accuracy of 4° and 3° in orientation detection was achieved when three and all six measurements from each configuration were selected, respectively. This indicates that, with a total of six measurements (three each from two different configurations), an accuracy of 4° was achieved and another six measurements (three each from both configuration types) resulted in only a slight improvement of 1° in accuracy. Consideration of additional measurements with the diagonal electrode configuration did not provide any additional benefit.

It was found that the horizontal and symmetrical electrode configurations provided similar results and that the combination of both types provided the best result among all possible combinations. This can be explained by the fact that both types complement each other in the direction of the current flow as illustrated in Figure 13, so that a finer sampling of the magnetic field distribution could be observed. With three measurements from each of the two configuration types, the magnetic field distribution could be measured with a resolution of 30° around the electrode. Multiple Independent Current Control (MICC) technology was developed for fine control of the stimulation position to provide very precise electrical signals through controllable current delivery and to tailor therapy to the individual patient. Thus, this technology can ensure current delivery through the electrode in any direction with the desired resolution [26]. For example, the red arrow in Figure 13 marks the current direction for a bipolar electrode configuration in which contacts C3 and C4 were activated with a 25–75% distribution of the amount of current in the direction of the third segment, C2. This would provide a 15° resolution along the electrode and presumably improve accuracy in detecting electrode orientation.

4.5. Orientation Detection Accuracy and Number of Sensors

The accuracy of the electrode orientation detection depended on the number of MEG sensors and their local distribution on the sensor surface as shown in Figure 14a. For this purpose, the same sensor distribution as in Figure 11a was used. When the number of sensors on the sensor surface was uniformly reduced (uniform sensor distribution), 95 sensors were also sufficient to achieve the same detection result as with 102 sensors, but the detection error increased continuously thereafter when fewer than 95 sensors were considered. However, when the sensors were reduced unevenly depending on the distance of the sensor from the electrode (the sensor with the largest distance was reduced first), even approximately 80 sensors were sufficient to achieve the same detection result. Further reduction of the number of sensors by 50 sensors led to a slight decrease in accuracy. Accuracy decreased drastically with less than 30 sensors. Similar to electrode localization, this result indicates that a concentrated distribution of sensors near the electrode is preferable to a uniform distribution of sensors around the head.

4.6. Orientation Detection Accuracy and Measurement Time

The accuracy of the electrode orientation detection depended on the measurement duration and SNR (Figure 14b). Shortening the measurement duration from 180 s (SNR gain of 21.8 dB after 23,400 averages) to 77 s (SNR gain of 20 dB after 10,000 averages) resulted in no loss of detection accuracy. Reducing the measurement duration to approximately 30 s (SNR gain of 17.9 dB after 3900 averages) resulted in a degradation in the accuracy of only 1°. Further investigation revealed that a SNR of 20 dB (i.e., where the signal is two orders of magnitude larger than the noise) resulted in no loss of detection accuracy, while a SNR of 10 dB (i.e., where the signal is only one order of magnitude larger than the noise) resulted in an additional error of 2–3°.

4.7. Orientation Detection Accuracy and Sensor Orientation

The accuracy of electrode orientation detection depended on the orientation of the MEG sensors. The horizontal and symmetrical electrode configurations produced a mag-

netic field that mainly used a tangential field component at the sensor surface, marked as arrows in Figure 14d. However, each MEG sensor measured the normal field component, marked as arrows in Figure 14c, resulting in the measurement of an attenuated magnetic field, with the attenuation ranging from a factor of 3 (4.7 dB) to 62 (18 dB) depending on the angle between the sensor orientation and the direction of the magnetic field between approximately 80° and 110°, as shown in Figure 14e. On average, a SNR gain of approximately 8.1 dB was obtained, resulting in a dramatic reduction in measurement and an averaging time of less than 10 s.

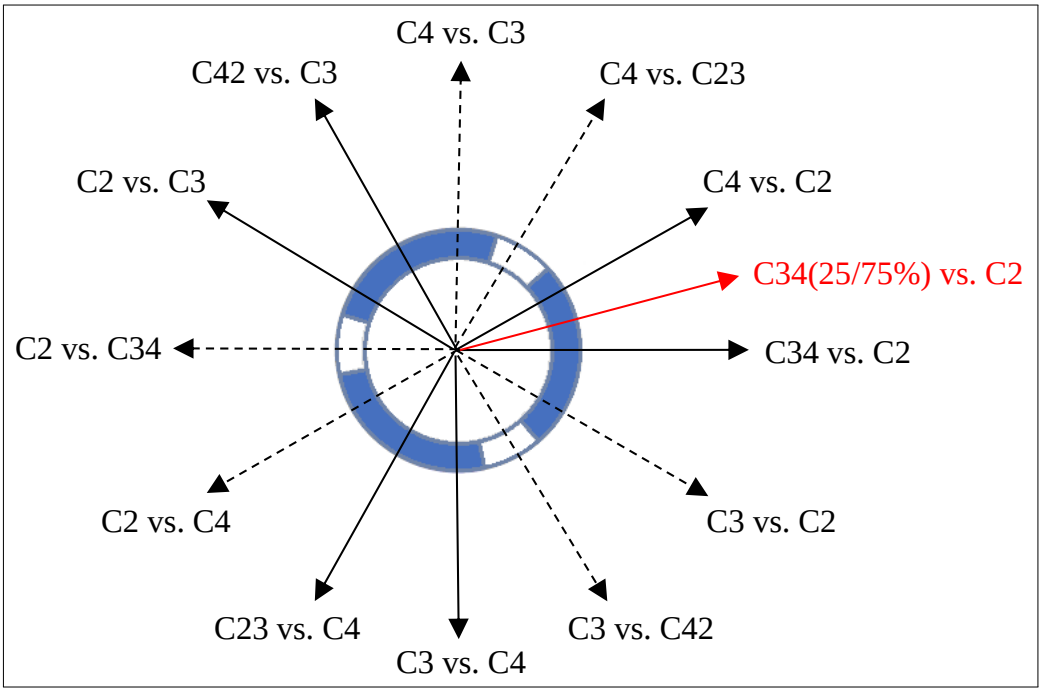

Figure 13. Bottom view of the electrode with arrows indicating the direction of current flow which is defined by the corresponding electrode configuration. Black solid arrows indicate the directions set by the electrode configurations investigated in this study. Dashed arrows indicate the direction of the currents by the corresponding change of anode and cathode contacts. The red arrow marks an example of a possible electrode configuration through MICC technology, which can be used to achieve finer resolution.

4.8. Orientation Detection Accuracy and Localization Error

The accuracy of the electrode orientation detection depended on the localization error of the electrode. We assumed that the electrode was in the correct position, so the maximum GoF value of 1 was shifted to the correct orientation position (i.e., 99°). The change in GoF value and accuracy in detecting electrode orientation as a function of electrode displacement in all three Cartesian directions, from −15 mm to 15 mm in 1 mm increments, are provided in Figure 14f,g. Both the GoF value and the inaccuracy in the electrode orientation detection depended on the direction in which the electrode had been moved. Moving the electrode 1 mm in any direction had no negative effect on the accuracy of the electrode orientation detection, but still resulted in a slight decrease in the GoF value. Moving the electrode in the *z*-direction had the least impact on accuracy (even a localization error of 2–3 mm did not result in inaccuracies). A localization error of 2–3 mm, as occurs in MEG measurements, resulted in a decrease in accuracy of 1–2° in electrode orientation detection.

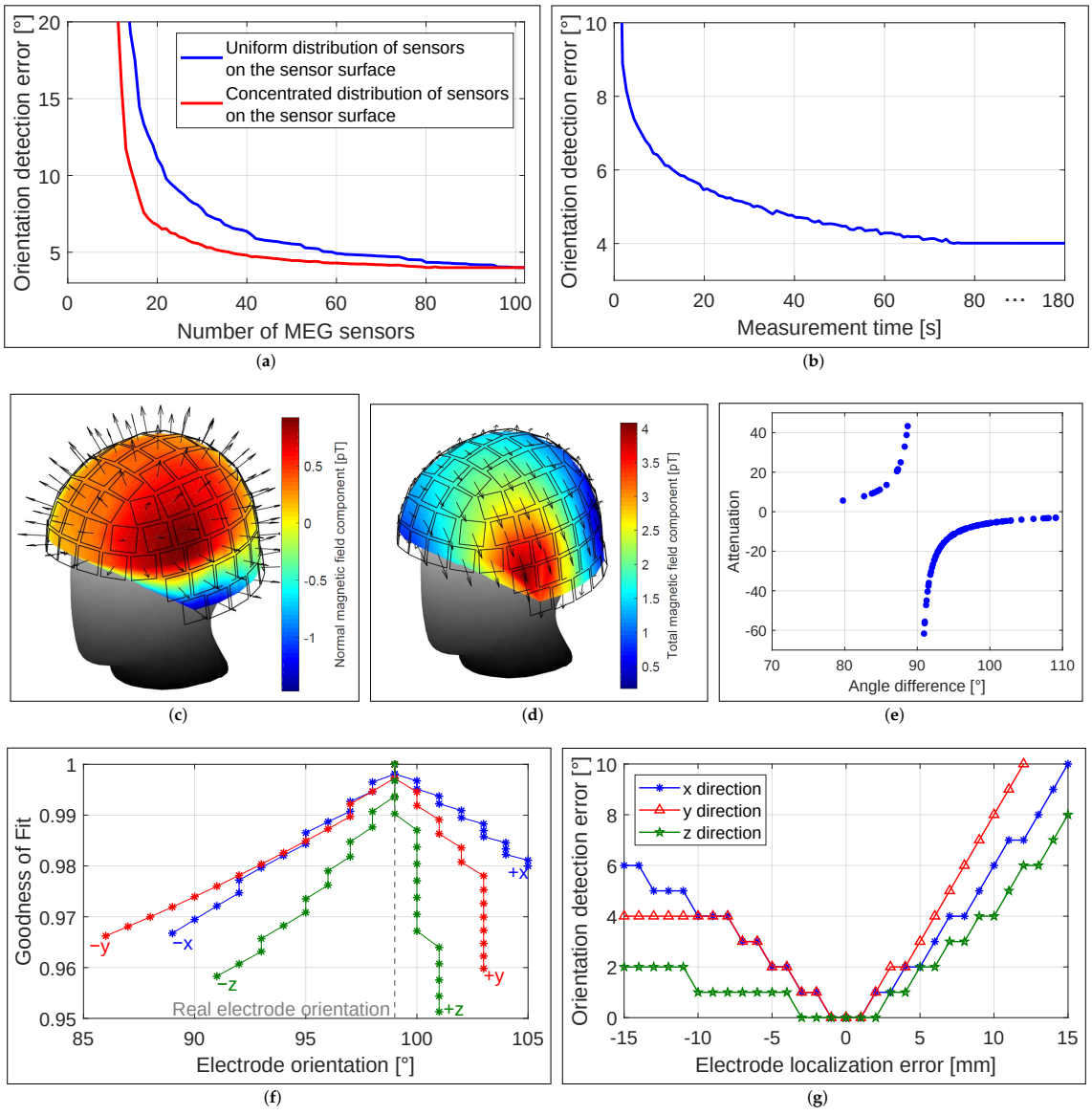

Figure 14. Orientation detection error as a function of (**a**) the number of MEG sensors and their distributions distributions and (**b**) the recording time of each measurement. (**c**) Measured magnetic field distribution with horizontal electrode configuration. Arrows indicate the orientations of the MEG sensors. (**d**) Expected magnetic field distribution for the magnitude of the magnetic field. Arrows indicate the direction of the magnetic field. (**e**) Attenuation of the measured magnetic fields due to the angle between the orientation of the MEG sensor and that of the magnetic field. (**f**) GoF value and (**g**) detection error as a function of electrode localization error.

5. Discussion

In this study, we presented a radiation-free method for determining the position and orientation of a directional DBS electrode using a series of short SQUID-MEG measurements with different predefined electrode configurations. The potential of MEG recordings for such an application has already been demonstrated in our previous work [20,22]. The aim

of this study was to develop a simple, realistic, and patient-friendly measurement method that can be used for clinical practice. The current step was necessary before measurements could be made with real DBS patients. A head–torso phantom with realistic dimensions was constructed to mimic a patient undergoing DBS therapy. The position and implantation angle of the electrode in the phantom were chosen to be as realistic as possible, and pre- and postoperative imaging were performed. Current state-of-the-art CT imaging techniques were applied to determine the position and rotational orientation of the electrode in the phantom, based on visual inspections of specific CT artifact patterns as the gold standard. These results were used to validate our MEG-based MaDoPO method. MEG measurements on the phantom were performed with different electrode configurations to find the sequence of measurements that achieves clinically reliable accuracy with the smallest amount of electrode contacts and the smallest possible number of recordings. Omnidirectional or directional configurations with clinically used stimulation parameters were applied for electrode localization and for electrode orientation detection, respectively.

The postoperative detection of electrode positions is essential for several aspects, such as to verify the implanted electrode position, to evaluate therapeutic and adverse effects of DBS, and to facilitate and guide stimulation programming [4]. Segmented contacts of a directional electrode may allow the stimulation field to be generated in a desired direction, so this technology also requires knowledge of the precise electrode orientation in the brain to fully realize its benefits. In addition, it is important to perform control localization and orientation detection when clinical doubts arise as to whether the stimulation is optimally adjusted for the patient, which requires CT imaging and/or fluoroscopy each time. The existing neuroimaging techniques have their own limitations and disadvantages, which were briefly discussed in the introduction. The major drawback is that all currently available techniques expose patients to ionizing radiation, and, in the case of orientation detection with X-ray or CT, none of the imaging techniques are currently able to resolve the 180° ambiguity in artifact symmetry without further measurements [16,32]. Therefore, possible imaging modalities such as EEG and MEG offer alternatives that eliminate these drawbacks, which are completely harmless and safe for the patient and do not involve an ambiguity problem. EEG has already been investigated for the feasibility of electrode localization, but insufficient accuracy for such problems has been reported [17].

In the method presented in this study, the magnetic field generated by the stimulation current is measured using MEG sensors and used to localize the electrode and detect its orientation. The accuracy in localization depended on the number of measurements with different non-directional electrode configurations. The DBS electrode in the phantom could be localized with an accuracy of approximately 2.25 mm, considering three specific measurements with bipolar non-directional configurations on each of the three levels of the electrode with a measurement duration of 50 s each. The accuracy could be improved to 2.02 mm when all six possible measurements with bipolar non-directional electrode configurations were considered. Three or six measurements per minute would result in a total pure measurement time of three to six minutes, i.e., a recording duration which can easily be tolerated by patients. The obtained inaccuracies can be attributed to the spatial resolution of the MEG system, since the sum of several inaccuracies in the preparation steps for the MEG measurements already caused a total error of 1.4 mm. This had the largest effect on the localization accuracy and indicated that the localization accuracy can be significantly improved if the spatial resolution of the MEG system is also improved. The accuracy in orientation detection depended on the number and combination of measurements with different directional electrode configurations. The orientation of the electrode was determined with an accuracy of 6° when three 77 s measurements were performed with the horizontal electrode configuration (i.e, where a segmented contact is activated against a neighboring segment). This error was reduced to 4° by using three additional measurements with the symmetrical electrode configuration (i.e., where two segmented contacts are activated against the third segment). Six measurements of one and a half minutes each would result in a pure measurement time of nine minutes in total, which would also be

tolerable for the patient. The combination of the horizontal and symmetrical electrode configurations produced the best results compared to the combination options with the diagonal electrode configuration (i.e., where the electrode tip is activated against a single segment at the next higher level). Investigations revealed that both types of configurations complemented each other in terms of the direction of current flow generated by stimulation in the phantom, so finer sampling by the IPG's MICC technology could further improve the accuracy in orientation detection. However, the accuracy was mainly limited by the spatial resolution of the MEG system, suggesting that a significant improvement in electrode orientation detection could be achieved if the measurement accuracy were improved.

Considering a postoperative localization accuracy of 2–3 mm and an orientation detection accuracy of 4–5°, according to our clinicians, these accuracies are acceptable for such DBS problems when gaining benefits of a radiation-free method. So, the presented method for detecting the position and orientation of a directional DBS electrode using magnetic field measurements continues to appear promising. Although the accuracies achieved in our study cannot compete with currently existing methods, the method we used is radiation-free and has the potential to be significantly improved with flexible head-casts for current SQUID-MEG devices [33] or with emerging MEG measurement systems, e.g., with OPM-MEG systems using optically pumped magnetometers (OPM) [23,24,34]. Recent technological developments have resulted in cap-shaped or on-scalp MEG sensor arrays that can move with the patients' head and adapt to the individual head shape. This could greatly improve the spatial resolution of the system (which limited our accuracy) by eliminating the need to estimate the position of the head or phantom in the MEG system using attached HPI coils. This method could become a breakthrough in solving such DBS problems if it achieves high detection precision, and it could be the postoperative modality of choice to enable the full potential of individualized programming of directional DBS systems. Another possible improvement of detection accuracy results from a higher resolution discretization of the localization area, which was set to 1 mm for computational time reasons. If the electrode is not directly on a defined grid point, the localization error is at least the distance between the nearest grid point and the location of the electrode. Increasing the resolution can increase the detection accuracy, but drastically increases the computational complexity. Further investigation in this study has shown that the cap-shaped MEG system must have the following characteristics: (1) suitable magnetic field sensors that have the sensitivity and bandwidth required for this application [21]; (2) at least 40 and 60 sensors with concentrated distribution of sensors near the electrode for electrode localization and electrode orientation detection, respectively; (3) alignment of the sensors to the expected direction of the magnetic field (tangential component), with the direction of the magnetic field rotated 90° between directional and non-directional stimulation; (4) a pure measurement duration for a single recording of 50 and 77 s for localization and orientation detection, respectively; and (5) a minimum of three measurements with non-directional electrode configuration and a minimum of six measurements with directional configuration to achieve decent accuracy, although additional measurements may be considered to improve accuracy.

The presented method has significant limitations. We are aware that our measurements were performed under ideal conditions, and that the obtained accuracies in electrode localization and electrode orientation detection may decrease in real patients. In further research, the presented method needs to prove its practicability and clinical applicability in real data from DBS patients. Such data will be more challenging, because, on the one hand, biological artifacts (heart, eyes, brain activity, and motion) interfere with the measurements and, on the other hand, the heterogeneous and anisotropic tissue properties of the brain reduce the accuracy of the required electromagnetic model. However, in contrast, we know that the artifact produced by DBS stimulation is much larger than other artifacts with a significant increase in DBS amplitudes by using on-scalp MEG due to the tangential sensor orientation and the smaller distance between the sensors and the electrode. Since the current only flows near the electrode due to the bipolar electrode configuration, accurate

modeling near the electrode and simplified modeling outside should also suffice. This needs to be clarified in future studies. Another disadvantage of this method is the time needed to localize the electrode and to detect the electrode's orientation. The time mainly depends on the duration of the simulation to generate modeled data (expected magnetic field values at the sensor surface) for the localization algorithm. The simulations in our case, where the electrode was moved in steps of 1 mm within a defined region (29 × 29 × 29 mm), took approximately two weeks of computation time, so a finer resolution of the model or a larger region would drastically increase the computation time and thus the time to determine electrode position and orientation. Therefore, this method cannot currently be used for real time applications, e.g., during surgery, but only post-operatively, where time is basically irrelevant.

6. Conclusions

In this study, we presented an improved, realistic, patient-friendly, and radiation-free method for the magnetic detection of the position and orientation (MaDoPO) of a directional DBS electrode using conventional MEG. For this purpose, the magnetic field around a head–torso phantom with an integrated DBS system was measured under different non-directional and directional electrode configurations. Three specific measurements with bipolar non-directional stimulation over each level of the electrode resulted in a localization accuracy of approximately 2 mm. Six specific measurements with bipolar directional stimulation around the electrode resulted in an orientation detection accuracy of 4°. If this can be confirmed in human applications, it would be more than sufficient for clinical use. However, the use of emerging cap-shaped or on-scalp MEG systems, in which the spatial resolution of the system is improved, would significantly increase the accuracy in detection.

Author Contributions: Conceptualization: M.Y. and G.D.; methodology: M.Y., M.H. and N.M.; software: M.Y., N.M. and L.M.J.-P.; validation: M.Y., N.M. and L.M.J.-P.; formal analysis: M.Y., G.D. and M.H.; investigation: M.Y.; resources: M.Y., M.H., A.-K.H. and A.S.; data curation: M.B. and A.S.; writing–original draft preparation: M.Y.; writing–review and editing: G.D., M.B., A.S., A.-K.H., M.H., L.M.J.-P. and N.M.; visualization: M.Y.; supervision: G.D. and M.H.; project administration: G.D., M.H., A.-K.H. and N.M.; funding acquisition: G.D. and M.H. All authors have read and agreed to the published version of the manuscript.

Funding: This work was supported by the German Research Foundation (Deutsche Forschungsgemeinschaft, DFG) through the project T1 of the Collaborative Research Centre CRC 1261 Magneto-electric Sensors: From Composite Materials to Biomagnetic Diagnostics.

Institutional Review Board Statement: Not applicable.

Informed Consent Statement: Not applicable.

Data Availability Statement: Not applicable.

Acknowledgments: The authors would like to thank Andrea Steuwe and Jörg Wittsack from the Institute of Diagnostic and Interventional Radiology for help with the CT scan in Düsseldorf.

Conflicts of Interest: The authors declare no conflict of interest.

References

1. Lozano, A.; Lipsman, N. Probing and Regulating Dysfunctional Circuits Using Deep Brain Stimulation. *Neuron* **2013**, *77*, 406–424. [CrossRef] [PubMed]
2. Vedam-Mai, V.; Deisseroth, K.; Giordano, J.; Lazaro-Munoz, G.; Chiong, W.; Suthana, N.; Langevin, J.P.; Gill, J.; Goodman, W.; Provenza, N.R.; et al. Proceedings of the Eighth Annual Deep Brain Stimulation Think Tank: Advances in Optogenetics, Ethical Issues Affecting DBS Research, Neuromodulatory Approaches for Depression, Adaptive Neurostimulation, and Emerging DBS Technologies. *Front. Hum. Neurosci.* **2021**, *15*, 169. [CrossRef]
3. Harmsen, I.E.; Elias, G.J.; Beyn, M.E.; Boutet, A.; Pancholi, A.; Germann, J.; Mansouri, A.; Lozano, C.S.; Lozano, A.M. Clinical trials for deep brain stimulation: Current state of affairs. *Brain Stimul.* **2020**, *13*, 378–385. [CrossRef] [PubMed]

4. Lange, F.; Steigerwald, F.; Malzacher, T.; Brandt, G.A.; Odorfer, T.M.; Roothans, J.; Reich, M.M.; Fricke, P.; Volkmann, J.; Matthies, C.; et al. Reduced Programming Time and Strong Symptom Control Even in Chronic Course through Imaging-Based DBS Programming. *Front. Neurol.* **2021**, *12*, 2072. [CrossRef]
5. Butson, C.R.; McIntyre, C.C. Current steering to control the volume of tissue activated during deep brain stimulation. *Brain Stimul.* **2008**, *1*, 7–15. [CrossRef]
6. Steigerwald, F.; Müller, L.; Johannes, S.; Matthies, C.; Volkmann, J. Directional deep brain stimulation of the subthalamic nucleus: A pilot study using a novel neurostimulation device. *Mov. Disord.* **2016**, *31*, 1240–1243. [CrossRef]
7. Pollo, C.; Kaelin-Lang, A.; Oertel, M.F.; Stieglitz, L.; Taub, E.; Fuhr, P.; Lozano, A.M.; Raabe, A.; Schüpbach, M. Directional deep brain stimulation: an intraoperative double-blind pilot study. *Brain* **2014**, *137*, 2015–2026. [CrossRef]
8. Schnitzler, A.; Mir, P.; Brodsky, M.; Verhagen, L.; Groppa, S.; Alvarez, R.; Evans, A.; Blazquez, M.; Nagel, S.; Pilitsis, J.; et al. Directional Deep Brain Stimulation for Parkinson's Disease: Results of an International Crossover Study With Randomized, Double-Blind Primary Endpoint. *Neuromodulation* **2021**. [CrossRef]
9. Engelhardt, J.; Guehl, D.; Damon-Perrière, N.; Branchard, O.; Burbaud, P.; Cuny, E. Localization of Deep Brain Stimulation Electrode by Image Registration Is Software Dependent: A Comparative Study between Four Widely Used Software Programs. *Stereotact. Funct. Neurosurg.* **2018**, *96*, 364–369. [CrossRef]
10. Ellenbogen, J.R.; Tuura, R.; Ashkan, K. Localisation of DBS Electrodes Post-Implantation, to CT or MRI? Which Is the Best Option? *Stereotact. Funct. Neurosurg.* **2018**, *96*, 347–348. [CrossRef]
11. Pinsker, M.; Herzog, J.; Falk, D.; Volkmann, J.; Deuschl, G.; Mehdorn, H.M. Accuracy and Distortion of Deep Brain Stimulation Electrodes on Postoperative MRI and CT. *Zentralblatt für Neurochirurgie* **2008**, *69*, 144–147. [CrossRef]
12. Reinacher, P.; Krüger, M.; Coenen, V.; Shah, M.; Roelz, R.; Jenkner, C.; Egger, K. Determining the Orientation of Directional Deep Brain Stimulation Electrodes Using 3D Rotational Fluoroscopy. *Am. J. Neuroradiol.* **2017**, *38*, 1111–1116. [CrossRef] [PubMed]
13. Hunsche, S.; Neudorfer, C.; Majdoub, F.E.; Maarouf, M.; Sauner, D. Determining the Rotational Orientation of Directional Deep Brain Stimulation Leads Employing Flat-Panel Computed Tomography. *Oper. Neurosurg.* **2018**, *16*, 465–470. [CrossRef]
14. Sitz, A.; Hoevels, M.; Hellerbach, A.; Gierich, A.; Luyken, K.; Dembek, T.A.; Klehr, M.; Wirths, J.; Visser-Vandewalle, V.; Treuer, H. Determining the orientation angle of directional leads for deep brain stimulation using computed tomography and digital X-ray imaging: A phantom study. *Med. Phys.* **2017**, *44*, 4463–4473. [CrossRef] [PubMed]
15. Dembek, T.A.; Hellerbach, A.; Jergas, H.; Eichner, M.; Wirths, J.; Dafsari, H.S.; Barbe, M.T.; Hunsche, S.; Visser-Vandewalle, V.; Treuer, H. DiODe v2: Unambiguous and Fully-Automated Detection of Directional DBS Lead Orientation. *Brain Sci.* **2021**, *11*, 1450. [CrossRef] [PubMed]
16. Kurtev-Rittstieg, R.; Achatz, S.; Nourinia, A.; Mittermeyer, S. Orientation of Directional Deep Brain Stimulation Leads on CT: Resolving the Ambiguity. *bioRxiv* **2020**. [CrossRef]
17. Iacono, M.I.; Atefi, S.R.; Mainardi, L.; Walker, H.C.; Angelone, L.M.; Bonmassar, G. A Study on the Feasibility of the Deep Brain Stimulation (DBS) Electrode Localization Based on Scalp Electric Potential Recordings. *Front. Physiol.* **2019**, *9*, 1788. [CrossRef]
18. Yalaz, M.; Teplyuk, A.; Muthuraman, M.; Deuschl, G.; Höft, M. The Magnetic Properties of Electrical Pulses Delivered by Deep Brain Stimulation Systems. *IEEE Trans. Instrum. Meas.* **2020**, *69*, 4303–4313. [CrossRef]
19. Yalaz, M.; Teplyuk, A.; Deuschl, G.; Höft, M. Dipole Fit Localization of the Deep Brain Stimulation Electrode Using 3D Magnetic Field Measurements. *IEEE Sens. J.* **2020**, *20*, 9550–9557. [CrossRef]
20. Yalaz, M.; Noor, M.S.; McIntyre, C.C.; Butz, M.; Schnitzler, A.; Deuschl, G.; Höft, M. DBS electrode localization and rotational orientation detection using SQUID-based magnetoencephalography. *J. Neural Eng.* **2021**, *18*, 026021. [CrossRef]
21. Yalaz, M.; Deuschl, G.; Butz, M.; Schnitzler, A.; Helmers, A.K.; Höft, M. Investigation of Magnetoelectric Sensor Requirements for Deep Brain Stimulation Electrode Localization and Rotational Orientation Detection. *Sensors* **2021**, *21*, 2527. [CrossRef]
22. Yalaz, M.; Deuschl, G.; Noor, M.S.; Butz, M.; Schnitzler, A.; Helmers, A.K.; Höft, M. Determining the rotational orientation of directional deep brain stimulation electrodes using magnetoencephalography. *J. Neural Eng.* **2021**, *18*, 056056. [CrossRef] [PubMed]
23. Boto, E.; Holmes, N.; Leggett, J.; Roberts, G.; Shah, V.; Meyer, S.; Muñoz, L.; Mullinger, K.; Tierney, T.; Bestmann, S.; et al. Moving magnetoencephalography towards real-world applications with a wearable system. *Nature* **2018**, *555*, 657–661. [CrossRef] [PubMed]
24. Hill, R.M.; Boto, E.; Rea, M.; Holmes, N.; Leggett, J.; Coles, L.A.; Papastavrou, M.; Everton, S.K.; Hunt, B.A.; Sims, D.; et al. Multi-channel whole-head OPM-MEG: Helmet design and a comparison with a conventional system. *NeuroImage* **2020**, *219*, 116995. [CrossRef] [PubMed]
25. Andersen, L.M.; Pfeiffer, C.; Ruffieux, S.; Riaz, B.; Winkler, D.; Schneiderman, J.F.; Lundqvist, D. On-scalp MEG SQUIDs are sensitive to early somatosensory activity unseen by conventional MEG. *NeuroImage* **2020**, *221*, 117157. [CrossRef]
26. Juárez-Paz, L.M. In silico Accuracy and Energy Efficiency of Two Steering Paradigms in Directional Deep Brain Stimulation. *Front. Neurol.* **2020**, *11*, 1360. [CrossRef]
27. Pasku, V.; De Angelis, A.; De Angelis, G.; Arumugam, D.D.; Dionigi, M.; Carbone, P.; Moschitta, A.; Ricketts, D.S. Magnetic Field-Based Positioning Systems. *IEEE Commun. Surv. Tutor.* **2017**, *19*, 2003–2017. [CrossRef]
28. Oostenveld, R.; Fries, P.; Maris, E.; Schoffelen, J.M. FieldTrip: Open Source Software for Advanced Analysis of MEG, EEG, and Invasive Electrophysiological Data. *Comput. Intell. Neurosci.* **2011**, *2011*, 156869. [CrossRef]

29. Horn, A.; Kühn, A.A. Lead-DBS: A toolbox for deep brain stimulation electrode localizations and visualizations. *NeuroImage* **2015**, *107*, 127–135. [CrossRef]
30. Horn, A.; Li, N.; Dembek, T.A.; Kappel, A.; Boulay, C.; Ewert, S.; Tietze, A.; Husch, A.; Perera, T.; Neumann, W.J.; et al. Lead-DBS v2: Towards a comprehensive pipeline for deep brain stimulation imaging. *NeuroImage* **2019**, *184*, 293–316. [CrossRef]
31. Mosher, J.C.; Lewis, P.S.; Leahy, R.M. Multiple dipole modeling and localization from spatio-temporal MEG data. *IEEE Trans. Biomed. Eng.* **1992**, *39*, 541–557. [CrossRef] [PubMed]
32. Hellerbach, A.; Dembek, T.A.; Hoevels, M.; Holz, J.A.; Gierich, A.; Luyken, K.; Barbe, M.T.; Wirths, J.; Visser-Vandewalle, V.; Treuer, H. DiODe: Directional Orientation Detection of Segmented Deep Brain Stimulation Leads: A Sequential Algorithm Based on CT Imaging. *Stereotact. Funct. Neurosurg.* **2018**, *96*, 335–341. [CrossRef] [PubMed]
33. Meyer, S.S.; Bonaiuto, J.; Lim, M.; Rossiter, H.; Waters, S.; Bradbury, D.; Bestmann, S.; Brookes, M.; Callaghan, M.F.; Weiskopf, N.; et al. Flexible head-casts for high spatial precision MEG. *J. Neurosci. Methods* **2017**, *276*, 38–45. [CrossRef] [PubMed]
34. Koshev, N.; Butorina, A.; Skidchenko, E.; Kuzmichev, A.; Ossadtchi, A.; Ostras, M.; Fedorov, M.; Vetoshko, P. Evolution of MEG: A first MEG-feasible fluxgate magnetometer. *Hum. Brain Mapp.* **2021**, *42*, 4844–4856. [CrossRef] [PubMed]

Key Findings and Scientific Implications

- The clinically applicable and radiation-free MaDoPO method of directional deep brain stimulation electrodes is based on a sequence of magnetic field measurements under various bipolar electrode configurations.
- At least three measurements with short recording time are required to minimize errors in determining the electrode position, and at least another three measurements are required to minimize the electrode orientation detection error.
- The electrode localization error can be minimized to an estimated 2.25 mm by considering three measurements with narrow bipolar omnidirectional electrode configurations at each of the three possible levels of the electrode.
- The electrode localization error can be minimized to approximately 2 mm if all six possible measurements with bipolar omnidirectional electrode configurations, consisting of three narrow bipolar and three wide bipolar stimulation modes, are considered.
- The electrode orientation detection error can be minimized to an estimated 6° by considering three measurements, each activating one of the three segmented contacts against an adjacent segment at the same level of the electrode.
- The electrode orientation detection error can be minimized to 4° if a total of six measurements are considered, three measurements each with activation of one of the three segmented contacts against an adjacent segment at the same level of the electrode, and another three measurements each with activation of two segmented contacts with the same current intensity against the third segment.
- The detection accuracy is limited mainly by the spatial resolution of the MEG system, which results from the inaccurate estimation of the measurement positions with respect to the head location.

Chapter 4

Conclusion

4.1 Summary

In this dissertation, a new approach for detecting the position and orientation of conventional and directional DBS electrodes was investigated with experiments on simplified and realistically shaped phantoms of the human head. The main objective was to develop a realistic and patient-friendly method to detect the position and rotational orientation of directional DBS electrodes that is based on measurements of the magnetic field induced by the stimulation. This was intended to provide an alternative approach that overcomes the drawbacks of existing neuroimaging-based methods and has the potential to be applied in clinical practice after clinically reliable and competitive accuracy has been achieved. The main advantage of the investigated method is the radiation-free approach, which does not expose the patient to any danger and, therefore, can be applied repeatedly to patients without concerns. By contrast, existing techniques involve radiation in the case of X-ray, CT, and fluoroscopy and risky magnetic field interactions with the DBS device in the case of MRI; therefore, they may not be used repeatedly without clinically important reasons. The MaDoPO method of segmented DBS electrodes was developed within the framework of this dissertation through a systematic workflow from several investigations and analyses; it is based on a series of short magnetic field measurements under various predefined electrode configurations. MaDoPO has emerged from a close collaboration with a number of research groups and industry. In addition to a strong internal collaboration within the Chair of Microwave Engineering at the Faculty of Engineering of Kiel University, clinically and medically relevant aspects were discussed with the Department of Neurosurgery and the Department of Neurology of Kiel University. The majority of the valuable magnetic field measurements were performed at the UKD. DBS modeling support from the group of Cameron McIntyre at Case Western Reserve University in Cleveland, Ohio (since July 2020 at Duke University), was indispensable, and extensive experience in this area was gained especially during a research stay with his group in Cleveland. The collaboration with Boston Scientific Corporation ensured that industry requirements were considered

and that the evaluation could be performed using state-of-the-art DBS systems and industrial routines. This dissertation contains a series of investigations that emerged from a systematic workflow and are described in more detail in the following.

Publication 1

First investigations were performed with a fluxgate magnetometer in the measurement-scanner system constructed in-house that is located inside the magnetically shielded chamber at the Faculty of Engineering of Kiel University. A simplified cylindrical head phantom with an integrated conventional four-contact electrode and a voltage-controlled neurostimulator was used, which allowed for adjustments only in the omnidirectional stimulation setting. The magnetic properties of electrical stimulation pulses delivered by the electrode were investigated in both monopolar and bipolar settings of the electrode configuration. The neurostimulator was programmed to high-stimulation parameters to take advantage of the use of a phantom to generate a larger magnetic field. The magnetic field induced by the monopolar and bipolar stimulation could be measured, with the monopolar mode producing a magnetic field approximately two orders of magnitude larger. Additionally, significant differences were found in the magnetic properties between both modes and especially in the topographical distribution of the magnetic field on the measurement sensor surface. The reason for this lies in the nature of the respective stimulation modes. Since the magnetic field generated at the sensor surface is a superposition of all field components generated by the stimulation current flowing in the entire system, the field generated only by the current in the phantom cannot be determined in the monopolar configuration because of the strong influence of the extension electrode wire. Moreover, the distribution of the magnetic field does not provide information about the height of the electrode in the phantom. For this reason, the monopolar stimulation mode cannot be used for electrode localization. In the bipolar electrode configuration, the magnetic field caused by the extension electrode wire is completely eliminated because the current flowing through the wire to the electrode flows back through the same wire in parallel and in close proximity, so that their magnetic contributions cancel each other out. Therefore, only the part of the current that flows between the pair of activated contacts contributes to the magnetic field at the sensor surface, resulting in a more concentrated spatial magnetic field distribution on the sensor surface. Accordingly, there is no alternative for using the bipolar configuration setting for electrode localization. In another study investigating the feasibility of electrode localization based on scalp electric potential recordings [Iac19], measurements were also performed under bipolar electrode configuration settings, which supported our findings. The behavior of the magnetic field generated by the bipolar stimulation mode can be described approximately by the model of an electric current dipole. The point-like dipole approximation, which can be thought of as an infinitely short length of current-carrying wire, is meaningful only when looking at the source from a compara-

ble large distance. This is the case in our application, because the distances between the measurement points and the electrode are much larger than the distance between activated contacts of the electrode. As a proof of concept, we have demonstrated that precise localization of the electrode is possible using magnetic field measurements with bipolar electrode configuration. For this purpose, the model of an electric current dipole was used to solve the forward problem. To solve the inverse problem, the dipole fitting approach was used, which searched for the model that had the best fit to the measured data. In this study, the measured data were obtained by transforming the measured signal into the frequency domain and considering the spectral amplitude only at the set stimulation frequency and ignoring the remainder of the signal. In this way, we aimed to demonstrate that a narrow-band magnetic field sensor can also be considered for electrode localization, such as the magnetoelectric sensor developed within the framework of the Collaborative Research Center 1261, which is sensitive to only a single stimulation frequency component. Although accurate localization of the electrode could be demonstrated with a single measurement, the approach of electrode localization needed to be validated in another study with more than one measurement.

Publication 2

The next study was conducted to demonstrate the feasibility of electrode localization using magnetic field measurements and to investigate the localization accuracy. Investigations were performed by magnetic field measurements on the same cylindrical head phantom inside the measurement system constructed in-house in the magnetically shielded chamber. In this study, the electrode was positioned in the phantom at five increasing depths, and the magnetic field distribution was measured around the phantom with a fluxgate magnetometer. Again, high-stimulation parameters were programmed on the neurostimulator to generate a larger magnetic field and to improve the signal-to-noise (SNR) of the measured data. To further improve the SNR, the measured signals were not transformed into the frequency domain as in the first study, but successive DBS pulse segments were averaged over the entire recording time. Instead of considering a single spectral component in the frequency domain and ignoring all other harmonic frequency components, the maximum value of the averaged time segment was taken, which included the entire bandwidth of the sensor and described the value with the highest SNR. Additionally, the modeling of the phantom for the forward problem was improved compared to the previous study. Although the electric current dipole model demonstrated a good approximation to describe the magnetic field of the bipolar electrode configuration, we found that the localization error increased with greater depth of the electrode in the phantom, indicating a slight inaccuracy of the underlying model. Therefore, the simplified model was replaced with a precise finite element electromagnetic model. By fitting the modeled data to the measured data, it was possible to localize the electrode with an average localization accu-

racy of less than 1 mm over all performed measurements for both near-surface and deep positions in the phantom. Although this work represented a promising step toward clinical application of the localization method in real DBS patients, this method first needed to be validated under clinically used stimulation parameters and using a newer generation of DBS systems, which was the focus of the next investigations.

Publication 3

For the next investigations, the DBS elements in the cylindrical head phantom used in the previous two studies were replaced by a state-of-the-art DBS system, in other words, a directional electrode and a current-controlled neurostimulator. The advantages of new-generation DBS systems have already been presented in the fundamentals of this dissertation. However, this resulted in the need to determine the orientation of the electrode in addition to the electrode position detection to fully exploit the technology of directional stimulation. The magnetic field generated at both very high and clinically applied stimulation settings of the neurostimulator could no longer be reliably measured with the fluxgate sensor in our measurement system constructed in-house. Therefore, we decided to move to a clinically available MEG system that is based on a significant number of highly sensitive SQUID sensors and is described as the current gold standard in the field of magnetic recordings. The next measurements were performed at the UKD using a 306-channel SQUID-based MEG system, which, due to the large number of simultaneously measuring sensors, allowed us to perform multiple measurements with various bipolar electrode configuration settings. For comparison, the previous two studies used only an omnidirectional bipolar electrode configuration with activation of a single pair of contacts. This was done because the use of a single sensor required moving the sensor to take samples at different locations, which was highly time-consuming and not practicable for a series of measurements. The purpose of this study was to investigate the accuracy in detecting the position and rotational orientation of a directional DBS electrode by using a state-of-the-art MEG system. Measurements with the bipolar omnidirectional stimulation mode — a conventional ring stimulation by activating all three segmented contacts at the same level of the electrode with the same amount of current against another level of the electrode — were used to determine the electrode position. The electrode could be localized with an average accuracy of approximately 3 mm, regardless of the location of the electrode in the phantom. To determine electrode orientation, measurements were made under the bipolar directional stimulation setting, in which the tip of the electrode was activated against one of the three segmented contacts at the next higher level of the electrode. The electrode orientation could be determined with an average accuracy of approximately 15°. These accuracies were achieved by considering each measurement separately for electrode localization and orientation detection. The accuracy can be improved significantly depending on the number of considered measurements, which differ

in the activation of contact pairs along the height of the electrode for omnidirectional electrode configurations and in the activation of contact pairs around the electrode for directional electrode configurations. Considering a sequence of three measurements with bipolar omnidirectional electrode configurations over each of the three electrode levels and using the a priori known physical distance between the electrode levels as a condition for localization, the error in electrode localization could be minimized to 2.2 mm. Considering a sequence of three measurements with bipolar directional electrode configurations, each with the electrode tip activated against one of the three segmented contacts at the next higher level of the electrode, and using the a priori known physical angle between the segments as a condition for electrode orientation detection, the error in orientation detection could be minimized to 11°. In this study, higher localization errors were obtained compared to previous results. The main reason for this was the limited spatial resolution of the MEG system due to the inaccurate estimation of the position of the sensor array with respect to the location of the phantom. However, this indicated that the accuracy could be improved significantly if the fixed helmet-shaped sensor array in the current generation of MEG devices was replaced with a flexible cap-shaped sensor array. Such novel sensing systems are currently the subject of intensive research [Hil20; Pra21; Kos21]. The utility of such systems would have the potential to overcome the limitations imposed by current MEG systems and to increase the accuracy of electrode localization and orientation detection. In this context, as part of another study, we investigated the minimum requirements for a magnetic field sensor that could be considered for use in such a novel system.

Publication 4

The conclusions of the previous study led to the next investigations, which addressed the minimum requirements that magnetic field sensors must meet to reliably measure the magnetic field generated by clinically used DBS settings, thereby allowing the sensor to be used for electrode localization and electrode orientation detection. The main focus was on the required minimum detection limit of the sensor, as the LOD is the most important sensor property, along with other properties such as sensitivity, dynamic range, spatial resolution, power consumption, cost, and robustness, to ensure the suitability of a sensor for this application. These sensors could find application in emerging cap-shaped sensor arrays that can be flexibly adapted to the individual head shape and can move with the patient's head. This could eliminate uncertainty about the position of the sensors relative to the head, thus providing the required spatial resolution. An LOD as high as that of a SQUID sensor is advantageous in all respects, but not absolutely necessary for our application. OPMs have been demonstrated to have sensitivity close to the gold standard of commercial SQUIDs, making them suitable for the development of cap-shaped OPM–MEGs. However, the bandwidth of these sensors is still too narrow for

use in DBS applications, since much higher frequencies are involved in DBS. Therefore, the development of a novel measurement system with suitable sensors for this application remains of great importance. The investigations were based on measurements performed with the MEG device at the UKD on the cylindrical head phantom with an integrated directional DBS system. The required minimum detection limit of a magnetic sensor depends mainly on the magnetic field to be detected and on the frequency bandwidth of the sensor. In our application, the magnetic field to be detected could be ensured by measurements under clinically used stimulation parameters and by considering a realistic distance between the electrode and the most distant sensor. This guaranteed that the magnetic field can be reliably detected at each measurement point around the patient's head and considering the patient-specific stimulation setting. Since DBS systems are based on stimulation with conventional square-wave pulses that include a stimulation pulse phase and a passive charge-balancing phase, the signal contains an infinite number of harmonics of the fundamental frequency. Therefore, the required detection limit had to be specified in the dependency of the bandwidth of the magnetic sensor. From the methodological perspective of electrode localization and orientation detection, it does not matter which bandwidth the sensor has and which frequency component of the stimulation signal is measured, as long as the sensor bandwidth includes at least one frequency component of the stimulation signal and the magnetic field can be reliably measured. However, the narrower the frequency bandwidth of a magnetic sensor, the higher the LOD requirement for the sensor, and the wider the bandwidth of a sensor, the lower the LOD requirement for the sensor. Investigations have indicated that an LOD of at least $0.04\,\mathrm{pT/Hz^{0.5}}$ is required for a sensor that is sensitive only to the stimulation frequency. The LOD requirement decreases by one order of magnitude to an estimated $0.4\,\mathrm{pT/Hz^{0.5}}$ for a sensor with a bandwidth of 1 kHz (between 0 and 1 kHz) and by approximately two orders of magnitude to $3\,\mathrm{pT/Hz^{0.5}}$ for a sensor with a bandwidth of 10 kHz (between 0 and 10 kHz). In comparison, the fluxgate sensor used in our first two studies had an LOD of $10\,\mathrm{pT/Hz^{0.5}}$ between 0 and 1 kHz and, thus, does not meet the minimum requirement for use in real applications. The SQUID sensors used in this work had an LOD of approximately $3\,\mathrm{fT/Hz^{0.5}}$ between the frequencies 0 and 1660 Hz specified by the MEG system and, thus, are ideally suited for DBS measurements even in clinical practice. The duration of the measurement was also considered to determine the minimum LOD, since periodic DBS waveforms can be used to average successive pulse segments to improve SNR and reduce LOD requirements for the sensor. For a one-minute averaging that can be easily tolerated by the patient, an LOD of approximately $3\,\mathrm{pT/Hz^{0.5}}$ is sufficient for a sensor that measures only at the fundamental frequency. An LOD of approximately $30\,\mathrm{pT/Hz^{0.5}}$ is sufficient for a sensor with 1 kHz bandwidth and approximately $250\,\mathrm{pT/Hz^{0.5}}$ for a sensor with 10 kHz bandwidth. Taking averaging into account, the fluxgate sensor now fulfills the condition for the minimum LOD requirement, which theoretically opens the possibility to perform real patient measurements with the in-house-constructed measurement system

inside the magnetically shielded chamber at the Faculty of Engineering of Kiel University. However, fine scanning of the magnetic field around the patient's head is required, which increases the measurement time by a factor of the number of measurement points. In particular, the large number of measurements with different electrode configurations required for electrode localization and orientation detection makes patient measurements practically infeasible.

Publication 5

The possibility of determining electrode orientation by magnetic field measurements has already been demonstrated in the third included publication of this dissertation, in which measurements were made using the following setting of directional stimulation: The tip of the electrode was activated against one of the three segments at the next higher level of the electrode. However, since there are multiple options for directional stimulation of segmented DBS electrodes, the goal of the next study was to investigate the effects of various directional electrode configurations on the accuracy of determining the rotational orientation of the electrode. Different settings of directional configuration could be ensured by the multiple independent current-controlled (MICC) technology of the used DBS system, which allowed for control of the current flow through each electrode contact individually. As in the previous two studies, the measurements for this study were performed with the MEG device at the UKD on the cylindrical head phantom with an integrated directional DBS system and with clinically relevant stimulation settings. The accuracy of electrode orientation detection was highly dependent on the type of directional electrode configuration, and three different configuration types were investigated. A sequence of three measurements, each with the activation of the electrode tip against one of the three segmented contacts at the next higher level of the electrode, minimized the error in electrode orientation detection to 13°. This value is similar to the value reported in the third included publication of this dissertation, in which measurements were performed under the same electrode configuration, demonstrating the reproducibility of the detection method. In a sequence of three measurements, each with the activation of one of the three segmented contacts against the corresponding segment at the next higher level of the electrode, an accuracy of 40° was observed. Due to the poor performance of this type of configuration, it can be claimed that it is not suitable for detecting electrode orientation. With a sequence of three measurements, each with the activation of one of the three segmented contacts against an adjacent segment at the same level of the electrode, the error could be minimized to 6°, which describes the most promising configuration type among the investigated cases. This can be justified by the fact that each individual configuration produces its own topographical pattern in the magnetic field distribution on the measurement surface, and the accuracy of electrode orientation detection depends on the change in this spatial distribution of the magnetic field when directional stimulation is

rotated around the electrode. In the latter configuration, the rotation of the stimulation had a significant effect on the magnetic field distribution, causing the magnetic field to differ between two rotations and, thus, facilitate the detection of the actual orientation of the electrode. However, the main restrictive factor was the limited spatial resolution of the MEG system, suggesting that the inaccuracy can be reduced further if a more precise measurement system with a higher spatial resolution is used.

Publication 6

Before the detection method can be finally tested on human subjects, a concluding study had to be conducted that would adhere as closely as possible to the human situation. This study was necessary for the development of a patient-friendly method for magnetic detection of the position and orientation of directional electrodes for application in clinical practice and before measurements can be performed with real DBS patients. A head-torso phantom with realistic dimensions was constructed to simulate a patient undergoing DBS therapy. First, preoperative imaging of the phantom was performed. The position and implantation angle of the electrode in the phantom were determined by our DBS neurosurgeons so that the final position of the electrode corresponded as realistically as possible to that of a real DBS patient. Then, postoperative imaging was performed. The imaging data were used to determine the position and orientation of the electrode using state-of-the-art neuroimaging techniques so that the corresponding results could be compared with those of our magnetic recordings. Measurements on the phantom were performed using the MEG device at the UKD under different omnidirectional and directional electrode configuration settings to identify the measurement sequence that achieved clinically reliable accuracy with the fewest number of electrode contacts and the smallest possible number of recordings. Precise finite element electromagnetic modeling of the realistic phantom and the fitting approach were used to determine the position and orientation of the electrode in the phantom. The developed clinically applicable and radiation-free MaDoPO method regarding directional DBS electrodes is based on a sequence of magnetic field measurements under various bipolar electrode configurations. The electrode in the phantom could be localized with an accuracy of approximately 2.25 mm, considering three measurements with narrow bipolar omnidirectional configurations on each of the three possible heights of the electrode. The error could be minimized to an estimated 2 mm when the remaining three possible measurements with wide bipolar omnidirectional electrode configurations were considered. According to our clinicians, six measurements with a measurement time of a few minutes each could be easily tolerated by patients. The orientation of the electrode was determined with an accuracy of 6° when three measurements were made, each with the activation of one of the three segmented contacts against an adjacent segment at the same level of the electrode. This value corresponds exactly to the value determined in the previous study

with measurements performed under the same electrode configuration setting. This again proves the reproducibility of our detection method. The error in electrode orientation detection could be minimized to 4° by performing three additional measurements under a similar directional electrode configuration, each with the activation of two of the three segmented contacts with the same current intensity against the third segment at the same level of the electrode. Six measurements with a measurement time of a few minutes each would also be easily tolerated by patients, according to our clinicians. As known from our previous studies, the inaccuracies in the detection of electrode position and orientation are due mainly to the limited spatial resolution of the MEG system. This suggested that the detection error can be further minimized if the spatial resolution of currently clinically applied MEG systems can be improved, for example, by the use of flexible head casts [Mey17] or the development of novel flexible cap-shaped measurement systems. Since the latter are currently under intense development, this study additionally investigated the conditions under which such a system could be used for this application. These included the following: the minimum number of sensors required for this application, how the sensors should be distributed on the measurement surface, in what direction the sensors should be oriented, and what the minimum measurement duration for each recording should be. The implementation of an improved measurement system that takes into account these answers would have the potential to further improve the observed detection accuracies and even to find application in the clinic after the applicability of this method is demonstrated in real DBS patients.

Concluding Words

In this dissertation, a simple, patient-friendly, radiation-free, and clinically applicable approach to determine the position and orientation of segmented DBS electrodes with magnetic field measurements was presented. In summary, six magnetic field measurements under omnidirectional electrode configuration settings and six measurements under directional configuration settings are required to minimize detection error. Considering the postoperative localization accuracy of 2–3 mm and the orientation detection accuracy of 4–5°, our clinicians believe that these accuracies are acceptable for such DBS problems in concert with the advantages gained by using a radiation-free method. Although the accuracies obtained in our study cannot really compete with currently existing methods, which have an accuracy of 1–2 mm for electrode localization and less than 2° for electrode orientation detection, the proposed method is only recognizably less accurate. Moreover, it is completely harmless to the patient and has the potential to be significantly improved by developing a suitable measurement system within the required specifications. Should even higher detection accuracy be achieved in clinical application, this method will undoubtedly represent a major advance in neurology and will be the postoperative modality

of choice to enable the full potential of individualized programming of directional DBS systems. Additionally, this method has the advantage of not introducing a 180° ambiguity problem into the solutions of electrode orientation detection, as is the case with most post-operative imaging techniques. Therefore, the presented method for detecting the position and orientation of a directional DBS electrode based on magnetic field measurements still seems to be quite promising for industry representatives and clinicians, although we are aware that the presented method has some limitations. First and foremost, it should be mentioned that the method was developed based on studies with phantoms and under ideal conditions, so the obtained detection accuracies actually represent the lower limit of achievable accuracies and will most likely increase in real-world applications. It should also be noted that the method localizes a single electrode in the patient's head based on the proposed magnetic field measurements, so the measurements must be repeated to determine the corresponding position of the second electrode implanted in the head. These and further limitations will be discussed in the next section with corresponding proposed solutions as an outlook to this dissertation.

4.2 Outlook

As the most useful next step, the developed method should first be tested and validated in a new study on real DBS patients. This will define clinically relevant aspects for further research. Additionally, further experiments should be performed on phantoms to investigate open aspects that were not considered in this dissertation. Furthermore, the developed approach for magnetic detection of the position and orientation of a DBS electrode should be extended with the modeling of the so-called volume of tissue activated (VTA) to ensure patient-specific DBS treatment.

4.2.1 Studies on Patients

The basis for the first patient measurements has already been established by this work. Significantly, the patient-friendly method proposed in the last included publication in this dissertation has helped to ensure that the approach can be used on real DBS patients. Therefore, the next reasonable step is to conduct a further study to validate the method in a small number of patients to evaluate the feasibility of electrode localization and electrode orientation detection using magnetic field measurements under real conditions and to investigate the limitations and restrictions of this methodology. The first measurements were already performed at the UKD with the SQUID-based MEG device on two Parkinsonian patients who underwent DBS surgery approximately one year before the measurements (Figure 4.1). Although the measurement data have not yet been analyzed in the context of this dissertation, first experiences with the handling of the patients for this application and the feasibility of performing a variety of measurements under dif-

(a) **(b)**

Figure 4.1: (a) Female and (b) male patient within the MEG scanner inside the magnetically shielded chamber at the University Hospital Düsseldorf.

ferent electrode configuration settings could be gained. Each patient's session lasted a total of three hours, including one hour for preparation of the patient in the waiting room of the MEG laboratory and two hours for the actual measurements in the magnetically shielded chamber, which, as expected, was tolerable for both the patient and the clinicians. Patient preparation consisted mainly of wiring the patient for the session and testing predefined electrode configuration settings for side effects in the patients. As suggested in the dissertation, 12 measurements were performed with each patient, six measurements with omnidirectional bipolar electrode configuration used for electrode localization and six measurements with directional configuration used for electrode orientation detection. Although the measurements were relatively short at 3 minutes, reprogramming the neurostimulator with the next configuration setting for the following measurement took most of the time. In addition to the data obtained with the 306-channel MEG, muscle activity in the right and left forearms was measured with electromyography-recording electrodes, cardiac activity with electrocardiography-recording electrodes, and vertical and horizon-

tal eye movements with electrooculography-recording electrodes. These additional data may help to develop potential artifact rejection methods to remove the influence of these artifact sources in the MEG signals, thus improving the SNR of the measured data and increasing localization accuracy. To filter out these artifacts, several methods have been proposed in the literature and can be used to suppress them: Hampel filter [All09], matched filter [Sun14], spectral signal space projection [Ram11], independent component analysis with mutual information [Abb16], and temporal signal space separation [Tau06].

Moreover, we found that the uncertainty regarding the position of the patient's head relative to the MEG sensors is approximately 0.5–1 mm higher than the value observed on phantoms. Furthermore, the movement of the patient's head in the MEG scanner cannot be excluded. Both sources of error have a nonlinear effect on the accuracy of forward modeling and, therefore, will most likely reduce localization accuracy. Although some progress has been made in minimizing errors, for example, by stabilizing the head during recording [Adj04; Mey17] or by compensating for movements during and after recording [Sto13; Lit14], implementation problems have persisted. Therefore, especially for electrode localization and electrode orientation detection, it is essential to develop a new flexible on-scalp measurement system. Recently, new sensor technologies with sensitivity sufficient for MEG have emerged [Pan11; Pfe19; Kos21; Pra21]. These new types of sensors do not require the same degree of thermal isolation as low-temperature SQUIDs and, therefore, can be placed almost directly on the scalp, significantly improving the spatial resolution [Bot18; Hil20].

The solutions for the forward and inverse problems must be adapted for real patient measurements. To solve the forward problem, the human head is modeled as a volume conductor whose accuracy depends on the head geometry and on the conductivity. Since the volume conductor model represents the conductivity distribution in the head, it requires an accurate conductivity for each head element. Segmenting the head into various tissues and using appropriate conductivity values for these tissues leads to more accurate localization results the closer the modeling is to reality [Bre12; Vor18]. If the inhomogeneity and anisotropy of tissue conductivity in the head is assigned inaccurately, it will have a significant impact on the source localization [Wol06; Gul10], so care must be taken to ensure accurate forward modeling. To solve the inverse problem, several source reconstruction algorithms can be used. Dipole models are widely used in both basic research and clinical practice. Although single-dipole reconstruction by dipole-fit approaches indicated sufficient performance in our application, beamformer methods should be taken into account as well, since they are also popular in basic MEG research and in clinical applications [Lit10; Moh10; Osw16; Jai20], and they might perform well in case of dipolar MEG topographies. Many variants of beamformers are implemented in various open-source toolboxes and commercial software for MEG analysis. Therefore, the performance of different localization algorithms, but primarily that of the beamformer algorithm, should be investigated using real patient data.

4.2.2 Experiments on Phantoms

The use of a phantom naturally opens up many areas of research that have not yet been considered or have only been partially considered in the context of this dissertation and cannot be directly investigated in patients. In the following, some aspects are addressed that can be used for further research.

- The studies within the framework of this dissertation were conducted with experiments on a simplified cylindrical head phantom and on a realistically shaped head-torso phantom. The phantoms were filled with saline solution to ensure electrical conductivity in the phantom and to have easy access to the electrodes within the phantom. Such single-layer phantoms have received the most attention but represent an extreme simplification of a real head. Therefore, far better phantoms are possible. More complex multilayer phantoms with a well-defined volume conduction configuration have been proposed, usually three layers representing the scalp, skull, and brain [Col12; Owd20]. The anisotropic conductivity structure (fiber track in white matter) can be modeled with tailored reed sticks inside a volume conductor [Hun20]. A variety of different materials have been investigated for the fabrication of such phantoms: gelatin, wax, agar, agarose, silicon, plastic clay, plastic molds, and saline solutions, with gelatin being by far the most commonly used to date [Owd20; Gui21; Owd21]. Such phantoms could be used to study the effects of DBS on the magnetic field at the measurement surface and to compare them with those obtained on simplified saline solution-filled phantoms. Investigators can learn whether magnetic fields can pass the head across different regions without any distortion, which is still considered to be a major advantage of MEG over EEG. Nevertheless, a stable and well-characterized setup for physical head phantom measurements can allow for more realistic analyses.

- The electrode localization and orientation detection method presented in this dissertation was developed based on investigations with directional DBS systems from Boston Scientific Corporation, Versice Cartesia™ directional lead with the Vercise™ PC or Versice Gevia™ neurostimulator. To broaden the scope of this proposed method, similar DBS systems from other DBS manufacturers that allow directional stimulation technology should be investigated as well. These include the directional electrode SenSight™ with the Percept™ PC neurostimulator from Medtronic plc or the St. Jude Medical Infinity™ DBS system from Abbott Laboratories. Additionally, an entirely new electrode design called Sapiens has been developed by Medtronic Eindhoven Design Center that consists of a total of 40 oval-shaped electrode contacts [Mar11; Van15]. These contacts are divided into ten rows of four contacts, and each row is rotated 45° from the adjacent row. The idea behind this development was that stimulation can be further shaped and radially directed by selecting various combinations of active contacts and splitting the current between them. This electrode design with multiple

small circular contacts was not successful due to uncertainties in the manufacturing process and the control of stimulation by the associated neurostimulator. However, this electrode would be promising for use in our application because it would allow for the setting of a variety of different electrode configurations.

- It has been mentioned several times in this thesis that OPMs have a high sensitivity, close to that of SQUID sensors, but that they cannot be used to measure the magnetic field induced by DBS due to the bandwidth of only 100 Hz. The DBS signal contains much higher frequency components (stimulation frequency and its harmonics). However, to take advantage of emerging OPM–MEG systems, the stimulation frequency could be decreased to below 100 Hz so that the signal becomes measurable for OPM sensors. The frequency could even be reduced significantly for the duration of the measurement so that the next couple of harmonics also become measurable, which would make the measured signal more robust against noise. This can be tested with experiments on phantoms. While it is well-known that relief of symptoms such as tremor, bradykinesia, and muscle rigidity is highly dependent on stimulation frequency and that high frequency stimulation above 100 Hz is required for efficacy, it has already been demonstrated that DBS with frequencies below 100 Hz may be a therapeutic option in selected cases of Parkinson's disease [Kar19; Vij21]. For example, stimulation at 20 Hz has already been indicated to have a positive effect on freezing of gait [Bai16], so OPM sensors could even measure the fourth harmonic DBS frequency in this case. Moreover, our clinicians believe that low-frequency stimulation for three-minute measurements should be tolerable for patients. Therefore, it is of significant interest to perform studies with OPM–MEG systems on real DBS patients, especially since the spatial resolution limitations of currently existing MEG systems are removed.

- It has been demonstrated that the accuracy of electrode localization depends on the number of measurements with an omnidirectional bipolar electrode configuration along the height of the electrode, and the accuracy of electrode orientation detection depends on the number of measurements with directional configuration around the electrode. Higher sampling along the longitudinal axis of the electrode and higher sampling of the electrode rotation could help to improve the localization and orientation detection accuracy, respectively. In the last included publication in this dissertation, the longitudinal axis of the electrode was sampled with five height points, and the distance between two points was 1 mm (see Figure 5a on page 8 of 26 in the last publication of this dissertation). With the MICC technology of current neurostimulators, finer scanning could be performed not only by activating two electrode levels against each other, as in the publication, but by activating three electrode levels, with two electrode levels activated with different current intensity against the third electrode level. It would be worth investigating whether a resolution along the electrode of less than 1 mm improves the accuracy of electrode localization. Similar considerations apply to

the detection of electrode orientation. The rotation of the electrode was sampled with six rotation points, and the distance between two points was 30° (see Figure 13 on page 20 of 26 in the last publication of the dissertation). With the MICC technology of current neurostimulators, finer scanning could be performed by activating two adjacent segments with different current intensity against the third segment at the same level of the electrode. An example was provided in the same figure. It could be investigated whether a resolution of less than 30° around the electrode improves the accuracy in detecting electrode orientation. Although a finer scan is associated with a longer series of measurements, it might be helpful to find a compromise between the number of measurements and clinically reliable accuracy.

- A major advantage of neuroimaging techniques for electrode localization and electrode orientation detection is that both electrodes are visible on the images, so that both can be localized and their orientation determined with a single scan. The method presented in this dissertation is designed to localize only a single electrode at a time. For practical application, this means that one electrode is turned off and measurements are made only to determine the position and orientation of the other corresponding electrode. Subsequently, the measurements must be repeated for the electrode that was switched off in the first pass. This leads to a significant increase in measurement time, considering that 12 measurements are required for the electrode in the phantom to minimize localization and orientation error, resulting in 24 measurements for two electrodes, thus doubling the measurement time. In the long term, the methodology should allow simultaneous localization and orientation detection of both implanted electrodes. The basis for this problem could be investigated by experiments on phantoms with two integrated electrodes.

- The standard pulse shape used in DBS today consists of a first, cathodic, activating pulse phase and a second, anodic, charge-balanced pulse phase. The second phase immediately follows the first phase but has a smaller amplitude and a longer duration. The ratio of the amplitudes of the pulse phases also determines the ratio of the widths of the pulse phases, which ensures the balancing of charges. However, recent work suggests that nonrectangular waveforms may have advantages over the conventional rectangular pulse [Fou10; Hof11; Gri15]. A number of charge-balanced biphasic waveforms have been tested with rectangular, exponential, triangular, Gaussian, and sinusoidal stimulation pulses, whereas the specific details of the optimal pulse and its direct applicability to specific clinical neurostimulation devices are less clear. Modifying the stimulation pulse could be of significant benefit to the application studied in this dissertation. Designing and matching the stimulation signal to the characteristic properties of the magnetic field sensor to be used would result in a reliable measurement of the entire signal. For example, the fluxgate magnetometer with a bandwidth of 1 kHz used in this work would measure not only 20% of the conventional rectangular

broadband DBS signal (stimulation frequency and its harmonics up to 1 kHz), but in the best case, all frequency components of the modified stimulation pulse if the pulse is bandlimited to 1 kHz. This would primarily have a positive effect on the SNR of the measured signal and on other aspects. Essentially, the requirements for the minimum detection limit of a magnetic sensor would decrease, allowing the development of a novel measurement system using alternative and currently irrelevant sensors.

- The modern Elekta Neuromag MEG device, as used at the UKD, contains 102 sensor triplets with one magnetometer and two planar gradiometers. Magnetometers measure the magnetic field component along the direction perpendicular to the surface of the sensor. The gradiometer is a more complex sensor that measures the spatial gradient rather than the magnitude of the field. While the availability of these two types of sensors at each site is attractive, it also leads to some controversy regarding the appropriate analysis pipeline. This is especially the case when it comes to source localization. One question frequently raised by researchers and reviewers concerns which data should be used for analysis: magnetometer only, gradiometer only, or magnetometer and gradiometer together. All three options have strong proponents and critics among experimenters and reviewers, and arguments such as "magnetometers can detect deeper sources," "gradiometers are less noisy," or "using only magnetometers (only gradiometers) means discarding two-thirds (one-third) of the data" are often heard [Moh12; Gar17]. The electrode localization and orientation detection method presented in this dissertation is based on magnetometer data and neglects gradiometer measurement data. The reason for this is mainly due to our experience with the analysis of magnetometer data and the fact that currently emerging measurement systems, such as OPM–MEG devices, are based mainly on magnetometer sensors. However, additional recorded gradiometer data may find application in analysis when the accuracy in determining electrode position and orientation is limited by lack of measurement data or low measurement resolution. Although electrode localization and orientation detection accuracy in MEG systems is limited primarily by the inaccurate estimation of phantom position in the MEG scanner, the performance of gradiometer data can still be tested and compared with that of magnetometer data.

- The sixth publication of this dissertation has already presented a possible solution for a novel measurement system to improve electrode localization and orientation detection accuracy, which could be developed specifically for this DBS application. The information sought included the following: the minimum number of sensors required, how the sensors should be distributed on the measurement surface, and in what direction the sensors should be oriented. To seek the answers, investigations were performed assuming that the spatial distribution and orientation of the sensors were the same as for fixed and helmet-shaped MEG systems. Thus, the proposed measurement system depended on the characteristics of the MEG system and represented a subset and the

maximum reduction of that system. An optimal solution to the questions regarding the optimal number of sensors and how must they be distributed on the measurement surface could not be found, and they should be investigated in a further study regardless of the characteristics of existing MEG systems. Furthermore, the question of how the sensors should be optimally oriented to detect both the position and the orientation of the electrode needs to be answered. Care must be taken to ensure that the direction of the magnetic field for bipolar omnidirectional stimulation (which is needed for electrode localization) is rotated 90° to the direction of the magnetic field for bipolar directional stimulation (which is needed for electrode orientation detection), since the current flows along the longitudinal axis of the electrode for omnidirectional stimulation and perpendicular to the longitudinal axis for directional stimulation. It can be investigated whether the measurement of a single magnetic field component is sufficient or whether a two- or even three-dimensional measurement of the magnetic field can be considered. Regarding the two measurement conditions investigated in this dissertation — the three-dimensional measurement of the magnetic field by means of rotation of the fluxgate sensor (in the first two publications) and the measurement of only the normal components of the magnetic field with SQUID sensors (in the remaining publications) — we could not identify any advantages for localizing the electrode. It is reported that for the localization of spatially concentrated sources, which is also true for the DBS electrode, both measurement conditions are sufficient, with the three-dimensional measurement being more suitable for the position determination of multiple and distributed sources [Iwa96; Kob01]. Nevertheless, a further investigation in this regard could be helpful to optimize the measurement system.

4.2.3 Individualized Deep Brain Stimulation

One of the challenges in both clinical application and DBS research is to make meaningful comparisons between the stimulation received by different patients, as the implanted DBS systems, electrode positions, and programming settings interact in complex ways that result in a unique stimulation profile for each patient. Since existing methods for quantifying the neuronal activation during DBS are limited, computational modeling is a useful tool for evaluating the stimulation effects on an individual patient basis [McI07; McI13]. The development of computational models has supported clinical studies to characterize DBS, investigate its underlying mechanisms, and identify strategies to optimize the effectiveness of DBS and reduce its side effects. Taking that into consideration, future perspectives of the application investigated within the framework of this dissertation should include the integration of an electrode localization and orientation detection method into an existing commercial or academic software to make use of its implemented functions of computational models. Figure 4.2 depicts a possible extension of the figure presented in the introduction of this dissertation by three additional steps. The use of

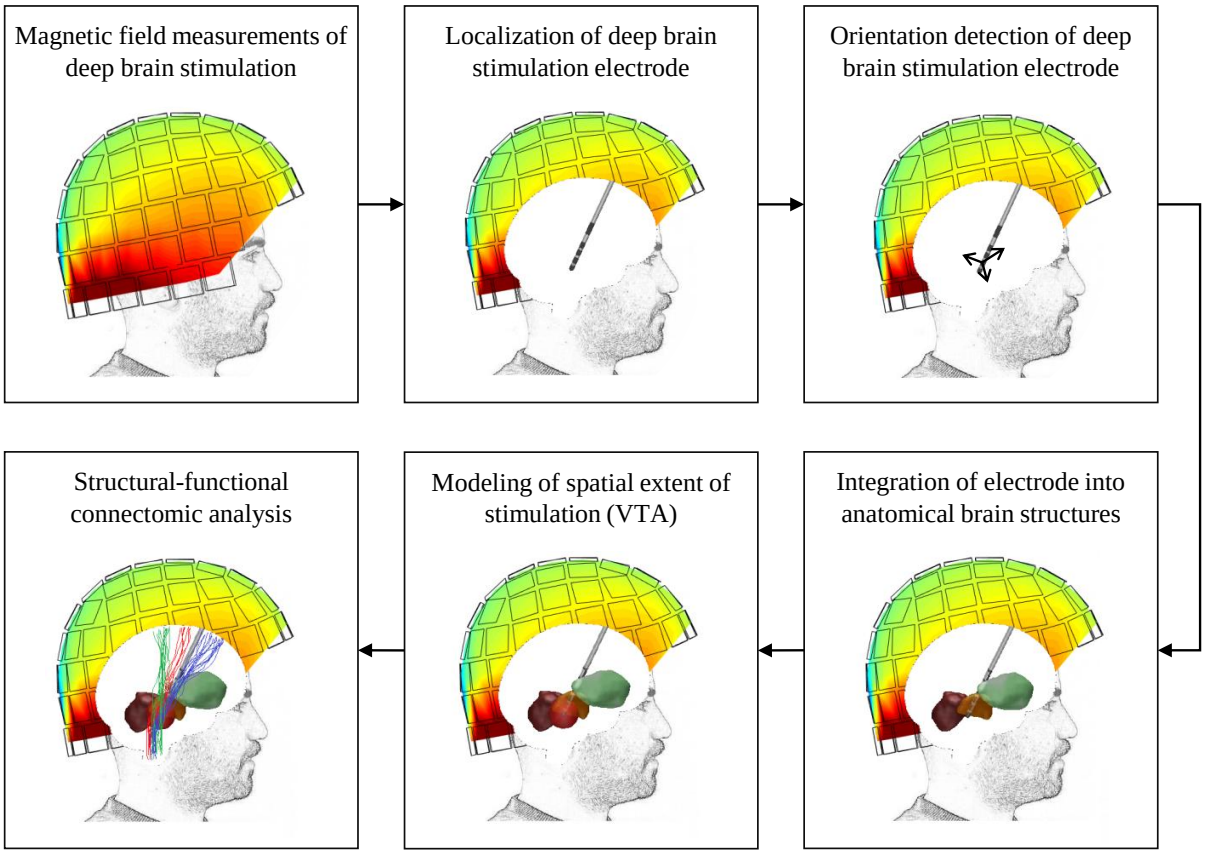

Figure 4.2: Method for patient-specific determination of stimulation parameters with the following steps: performing magnetic field measurements, determining the electrode position, detecting the rotational orientation of the electrode, integrating the detection results into the anatomical brain structures, modeling the spatial extent of stimulation or the volume of tissue activated (VTA), and analyzing the functional and structural connectivity between the VTA and other brain regions.

the academic and open-source toolbox Lead-DBS represents a promising opportunity to realize these steps. Lead-DBS was published in 2014 with the aim to reconstruct DBS electrodes in the anatomical brain structures by using pre- and postoperative neuroimaging data [Hor15]. This toolbox is continuously developed at various institutions and is currently the most established academic toolbox, with more than 7,000 downloads. In addition to the reconstruction of DBS electrodes in the human brain, it now offers a visualization of electrode localization results within the anatomical structures in 2D or 3D, to determine electrode orientation using postoperative CT, to calculate and visualize the so-called VTA based on the applied stimulation parameters, to estimate the connectivity from the VTA to other brain regions with diffusion tensor imaging and fiber tracking, and to perform structural-functional connectivity analysis [Odo11; Hor19]. The VTA is a computational model that has become widely accepted in both clinical and DBS research [McI04b; But07; But08]. It is a model that predicts the spatial extent of neural activation in response to external electrical stimulation via a DBS electrode. The gold

standard for VTA estimation is the coupling of finite element simulations of the electric field distribution with a model of multi-compartment axons that are arranged in a field around the electrode shaft [McI04c]. Axons that generate action potentials as a result of stimulation are considered active, and their spatial distribution defines the VTA. A significant amount of work has been done in this regard, and, over the years, more and more sophisticated models have been introduced [Cha10; Cha13; Ast15; Lau16; Hor17b; And18; Duf19; How19; Pet19b]. The downside of this approach is the high computational effort involved when considered in the context of possible clinical applications. Computing time, therefore, is an important issue for software tools in clinical practice. Studies were performed that attempted to identify activation thresholds for the electric field in relation to the simulated stimulation field that can be used to define the VTA without the need for computational axon models [Rat86]. Such a relationship between neural activation and the stimulation field strength is investigated by coupling finite element DBS models with novel axon models. The results indicated that the VTA can be estimated by a constant stimulation field threshold without the need to couple neuron models to finite element simulations [Kun08; Vas09; Mad12; Hor17b]. It has already been demonstrated that visualization of stimulation fields provides useful information for clinicians to achieve therapeutic improvement comparable to the traditional trial-and-error approach but with shorter and more efficient programming sessions [Pav20]. The ability to integrate the method of magnetic detection of electrode position and orientation developed within the framework of this dissertation into an existing and continuously developing software solution for modeling the VTA and analyzing the functional and structural effects of the VTA on other brain regions would provide clinicians with an alternative solution to minimize the complexity of stimulation programming and, therefore, to maximize patient-specific DBS treatment.

Bibliography

[Abb16] O. Abbasi, J. Hirschmann, G. Schmitz, A. Schnitzler, and M. Butz. "Rejecting deep brain stimulation artefacts from MEG data using ICA and mutual information". In: *Journal of Neuroscience Methods* 268 (2016), pp. 131–141. ISSN: 0165-0270. DOI: 10.1016/j.jneumeth.2016.04.010 (cit. on p. 152).

[Adj04] P. Adjamian, G. R. Barnes, A. Hillebrand, I. E. Holliday, K. D. Singh, P. L. Furlong, E. Harrington, C. W. Barclay, and P. J. G. Route. "Co-registration of magnetoencephalography with magnetic resonance imaging using bite-bar-based fiducials and surface-matching". In: *Clinical Neurophysiology* 115.3 (2004), pp. 691–698. ISSN: 1388-2457. DOI: 10.1016/j.clinph.2003.10.023 (cit. on p. 152).

[Agn13] F. Agnesi, M. D. Johnson, and J. L. Vitek. "Chapter 4 - Deep brain stimulation: how does it work?" In: *Brain Stimulation*. Vol. 116. Handbook of Clinical Neurology. Elsevier, 2013, pp. 39 –54. DOI: 10.1016/B978-0-444-53497-2.00004-8 (cit. on p. 8).

[All09] D. P. Allen. "A frequency domain Hampel filter for blind rejection of sinusoidal interference from electromyograms". In: *Journal of Neuroscience Methods* 177.2 (2009), pp. 303–310. ISSN: 0165-0270. DOI: 10.1016/j.jneumeth.2008.10.019 (cit. on p. 152).

[And18] D. N. Anderson, B. Osting, J. Vorwerk, A. D. Dorval, and C. R. Butson. "Optimized programming algorithm for cylindrical and directional deep brain stimulation electrodes". In: *Journal of Neural Engineering* 15.2 (Jan. 2018), p. 026005. DOI: 10.1088/1741-2552/aaa14b (cit. on pp. 2, 9, 159).

[Ast15] M. Astrøm, E. Diczfalusy, H. Martens, and K. Wårdell. "Relationship between Neural Activation and Electric Field Distribution during Deep Brain Stimulation". In: *IEEE Transactions on Biomedical Engineering* 62.2 (2015), pp. 664–672. DOI: 10.1109/TBME.2014.2363494 (cit. on p. 159).

[Bar15] I. Barnaure, P. Pollak, S. Momjian, J. Horvath, K. O. Lovblad, C. Boëx, J. Remuinan, P. Burkhard, and M. I. Vargas. "Evaluation of electrode position in deep brain stimulation by image fusion (MRI and CT)". In: *Neuroradiology*

57 (Sept. 2015), pp. 903–908. DOI: 10.1007/s00234-015-1547-z (cit. on p. 11).

[Bai16] J. F. Baizabal-Carvallo and M. Alonso-Juarez. "Low-frequency deep brain stimulation for movement disorders". In: *Parkinsonism & Related Disorders* 31 (2016), pp. 14–22. ISSN: 1353-8020. DOI: 10.1016/j.parkreldis.2016.07.018 (cit. on p. 154).

[Bre12] R. Brette and A. Destexhe. *Handbook of Neural Activity Measurement*. Cambridge University Press, 2012. DOI: 10.1017/CBO9780511979958 (cit. on p. 152).

[Ben87] A. L. Benabid, P. Pollak, A. Louveau, S. Henry, and J. de Rougemont. "Combined (Thalamotomy and Stimulation) Stereotactic Surgery of the VIM Thalamic Nucleus for Bilateral Parkinson Disease". In: *Applied Neurophysiology* 50 (1987), pp. 344–346. ISSN: 1011-6125. DOI: 10.1159/000100803 (cit. on p. 7).

[Bai97] S. Baillet and L. Garnero. "A Bayesian approach to introducing anatomo-functional priors in the EEG/MEG inverse problem". In: *IEEE Transactions on Biomedical Engineering* 44.5 (1997), pp. 374–385. DOI: 10.1109/10.568913 (cit. on p. 18).

[Ben00] A. Benazzouz and M. Hallett. "Mechanism of action of deep brain stimulation". In: *Neurology* 55.12 Suppl 6 (2000), S13–S16 (cit. on p. 8).

[But08] C. R. Butson and C. C. McIntyre. "Current steering to control the volume of tissue activated during deep brain stimulation". In: *Brain Stimulation* 1.1 (2008), pp. 7–15. ISSN: 1935-861X. DOI: 10.1016/j.brs.2007.08.004 (cit. on p. 158).

[Bai01] S. Baillet, J. C. Mosher, and R. M. Leahy. "Electromagnetic Brain Mapping". In: *IEEE Signal Processing Magazine* 18.6 (2001), pp. 14–30. DOI: 10.1109/79.962275 (cit. on pp. 17, 19).

[Bot18] E. Boto, N. Holmes, J. Leggett, G. Roberts, V. Shah, S. S. Meyer, L. D. Muñoz, K. J. Mullinger, T. M. Tierney, S. Bestmann, G. R. Barnes, R. Bowtell, and M. J. Brookes. "Moving magnetoencephalography towards real-world applications with a wearable system". In: *Nature* 555 (Mar. 2018), pp. 657–661. DOI: 10.1038/nature26147 (cit. on p. 152).

[Bou20] A. Boutet, C. T. Chow, K. Narang, G. J. B. Elias, C. Neudorfer, J. Germann, M. Ranjan, A. Loh, A. J. Martin, W. Kucharczyk, C. J. Steele, I. Hancu, A. R. Rezai, and A. M. Lozano. "Improving Safety of MRI in Patients with Deep Brain Stimulation Devices". In: *Radiology* 296.2 (2020), pp. 250–262. DOI: 10.1148/radiol.2020192291 (cit. on pp. 3, 11).

[Bro17] D. T. Brocker, B. D. Swan, R. Q. So, D. A. Turner, R. E. Gross, and W. M. Grill. "Optimized temporal pattern of brain stimulation designed by computational evolution". In: *Science Translational Medicine* 9.371 (2017), eaah3532. DOI: 10.1126/scitranslmed.aah3532 (cit. on p. 17).

[Bro20] E. C. Brown, D. L. Clark, N. D. D. Forkert, C. P. Molnar, Z. H. T. Kiss, and R. Ramasubbu. "Metabolic activity in subcallosal cingulate predicts response to deep brain stimulation for depression". In: *Neuropsychopharmacology* 45 (Sept. 2020), pp. 1681–1688. DOI: 10.1038/s41386-020-0745-5 (cit. on p. 8).

[Bur21] J. F. Burke, D. Tanzillo, P. A. Starr, D. A. Lim, and P. S. Larson. "CT and MRI Image Fusion Error: An Analysis of Co-Registration Error Using Commercially Available Deep Brain Stimulation Surgical Planning Software." In: *Stereotact Funct Neurosurg* 99.3 (June 2021), pp. 196–202. DOI: 10.1159/000511114 (cit. on pp. 3, 11).

[But07] C. R. Butson, S. E. Cooper, J. M. Henderson, and C. C. McIntyre. "Patient-specific analysis of the volume of tissue activated during deep brain stimulation". In: *NeuroImage* 34.2 (2007), pp. 661–670. ISSN: 1053-8119. DOI: 10.1016/j.neuroimage.2006.09.034 (cit. on p. 158).

[Cag19] H. Cagnan, T. Denison, C. C. McIntyre, and P. Brown. "Emerging technologies for improved deep brain stimulation". In: *Nature Biotechnology* 37 (Sept. 2019), pp. 1024–1033. DOI: 10.1038/s41587-019-0244-6 (cit. on p. 8).

[Cha10] A. Chaturvedi, C. R. Butson, S. F. Lempka, S. E. Cooper, and C. C. McIntyre. "Patient-specific models of deep brain stimulation: Influence of field model complexity on neural activation predictions". In: *Brain Stimulation* 3.2 (Apr. 2010), pp. 65–77. ISSN: 1935-861X. DOI: 10.1016/j.brs.2010.01.003 (cit. on p. 159).

[Che89] D. K. Cheng. *Field and Wave Electromagnetics*. Addison Wesley, 1989. ISBN: 9780201528206 (cit. on pp. 19, 20).

[Cha13] A. Chaturvedi, J. L. Lujan, and C. C. McIntyre. "Artificial neural network based characterization of the volume of tissue activated during deep brain stimulation". In: *Journal of Neural Engineering* 10.5 (Sept. 2013), p. 056023. DOI: 10.1088/1741-2560/10/5/056023 (cit. on p. 159).

[Coh68] D. Cohen. "Magnetoencephalography: Evidence of Magnetic Fields Produced by Alpha-Rhythm Currents". In: *Science* 161.3843 (1968), pp. 784–786. DOI: 10.1126/science.161.3843.784 (cit. on p. 16).

[Coh72] D. Cohen. "Magnetoencephalography: Detection of the Brain's Electrical Activity with a Superconducting Magnetometer". In: *Science* 175.4022 (1972), pp. 664–666. DOI: 10.1126/science.175.4022.664 (cit. on p. 16).

[Col12] T. J. Collier, D. B. Kynor, J. Bieszczad, W. E. Audette, E. J. Kobylarz, and S. G. Diamond. "Creation of a Human Head Phantom for Testing of Electroencephalography Equipment and Techniques". In: *IEEE Transactions on Biomedical Engineering* 59.9 (2012), pp. 2628–2634. DOI: 10.1109/TBME.2012.2207434 (cit. on p. 153).

[Cov07] K. S. Cover, J. P. A. Verbunt, J. C. de Munck, and B. W. van Dijk. "Fitting a single equivalent current dipole model to MEG data with exhaustive search optimization is a simple, practical and very robust method given the speed of modern computers". In: *International Congress Series* 1300 (2007). New Frontiers in Biomagnetism. Proceedings of the 15th International Conference on Biomagnetism, Vancouver, BC, Canada, August 21-25, 2006, pp. 121–124. DOI: 10.1016/j.ics.2007.01.026 (cit. on p. 17).

[Cro19] A. L. Crowell, P. Riva-Posse, P. E. Holtzheimer, S. J. Garlow, M. E. Kelley, R. E. Gross, L. Denison, S. Quinn, and H. S. Mayberg. "Long-Term Outcomes of Subcallosal Cingulate Deep Brain Stimulation for Treatment-Resistant Depression". In: *American Journal of Psychiatry* 176.11 (2019), pp. 949–956. DOI: 10.1176/appi.ajp.2019.18121427 (cit. on p. 8).

[DAl15] T. D'Albis, C. Haegelen, C. Essert, S. Fernandez-Vidal, F. Lalys, and P. Jannin. "PyDBS: an automated image processing workflow for deep brain stimulation surgery". In: *International Journal of Computer Assisted Radiology and Surgery* 10 (Feb. 2015), pp. 117–128. DOI: 10.1007/s11548-014-1007-y (cit. on p. 12).

[DiB04] B. Di Bartolo. *Classical Theory of Electromagnetism*. World Scientific Publishing Company Pte Limited, 2004. ISBN: 9789812382184. DOI: 10.1142/5150 (cit. on p. 19).

[Dem17] T. A. Dembek, P. Reker, V. Visser-Vandewalle, J. Wirths, H. Treuer, M. Klehr, J. Roediger, H. S. Dafsari, M. T. Barbe, and L. Timmermann. "Directional DBS increases side-effect thresholds—A prospective, double-blind trial". In: *Movement Disorders* 32.10 (2017), pp. 1380–1388. DOI: 10.1002/mds.27093 (cit. on pp. 10, 13).

[Dem19b] T. A. Dembek, M. Hoevels, A. Hellerbach, A. Horn, J. N. Petry-Schmelzer, J. Borggrefe, J. Wirths, H. S. Dafsari, M. T. Barbe, V. Visser-Vandewalle, and H. Treuer. "Directional DBS leads show large deviations from their intended implantation orientation". In: *Parkinsonism & Related Disorders* 67 (Oct. 2019), pp. 117–121. ISSN: 1353-8020. DOI: 10.1016/j.parkreldis.2019.08.017 (cit. on p. 15).

[Dem19a] T. A. Dembek, J. Roediger, A. Horn, P. Reker, C. Oehrn, H. S. Dafsari, N. Li, A. A. Kühn, G. R. Fink, V. Visser-Vandewalle, M. T. Barbe, and L. Timmermann. "Probabilistic sweet spots predict motor outcome for deep brain stimulation in Parkinson disease". In: *Annals of Neurology* 86.4 (2019), pp. 527–538. DOI: 10.1002/ana.25567 (cit. on p. 13).

[Dem21b] T. A. Dembek, A. L. Asendorf, J. Wirths, M. T. Barbe, V. Visser-Vandewalle, and H. Treuer. "Temporal Stability of Lead Orientation in Directional Deep Brain Stimulation". In: 99.2 (2021), pp. 167–170. DOI: 10.1159/000510883 (cit. on p. 15).

[Dem21a] T. A. Dembek, A. Hellerbach, H. Jergas, M. Eichner, J. Wirths, H. S. Dafsari, M. T. Barbe, S. Hunsche, V. Visser-Vandewalle, and H. Treuer. "DiODe v2: Unambiguous and Fully-Automated Detection of Directional DBS Lead Orientation". In: *Brain Sciences* 11.11 (2021). ISSN: 2076-3425. DOI: 10.3390/brainsci11111450 (cit. on p. 14).

[Den20] D. Denys, I. Graat, R. Mocking, P. de Koning, N. Vulink, M. Figee, P. Ooms, M. Mantione, P. van den Munckhof, and R. Schuurman. "Efficacy of Deep Brain Stimulation of the Ventral Anterior Limb of the Internal Capsule for Refractory Obsessive-Compulsive Disorder: A Clinical Cohort of 70 Patients". In: *American Journal of Psychiatry* 177.3 (2020), pp. 265–271. DOI: 10.1176/appi.ajp.2019.19060656 (cit. on p. 8).

[Deu11] G. Deuschl, J. Raethjen, H. Hellriegel, and R. Elble. "Treatment of patients with essential tremor". In: *The Lancet Neurology* 10.2 (2011), pp. 148–161. ISSN: 1474-4422. DOI: 10.1016/S1474-4422(10)70322-7 (cit. on pp. 1, 7).

[Van15] K. J. van Dijk, R. Verhagen, A. Chaturvedi, C. C. McIntyre, L. J. Bour, C. Heida, and P. H. Veltink. "A novel lead design enables selective deep brain stimulation of neural populations in the subthalamic region". In: *Journal of Neural Engineering* 12.4 (2015), p. 046003. DOI: 10.1088/1741-2560/12/4/046003 (cit. on p. 153).

[Duf19] G. Duffley, D. N. Anderson, J. Vorwerk, A. D. Dorval, and C. R. Butson. "Evaluation of methodologies for computing the deep brain stimulation volume of tissue activated". In: *Journal of Neural Engineering* 16.6 (2019), p. 066024. DOI: 10.1088/1741-2552/ab3c95 (cit. on p. 159).

[Egg21] K. Egger, A. Rau, H. Urbach, M. Reisert, and P. C. Reinacher. "3D X-ray based visualization of directional deep brain stimulation lead orientation". In: *Journal of Neuroradiology* (2021). ISSN: 0150-9861. DOI: 10.1016/j.neurad.2021.05.002 (cit. on pp. 3, 13).

[Erw00] B. Erwin, M. M. Jr, and K. K. Baker. “Mechanism of deep brain stimulation and future technical developments”. In: *Neurological Research* 22.3 (2000), pp. 259–66. DOI: 10.1080/01616412.2000.11740668 (cit. on p. 8).

[Eng18] J. Engelhardt, D. Guehl, N. Damon-Perrière, O. Branchard, P. Burbaud, and E. Cuny. “Localization of Deep Brain Stimulation Electrode by Image Registration Is Software Dependent: A Comparative Study between Four Widely Used Software Programs”. In: *Stereotact Funct Neurosurg* 96 (2018), pp. 364–369. DOI: 10.1159/000494982 (cit. on pp. 3, 11).

[Ewe18] S. Ewert, P. Plettig, N. Li, M. M. Chakravarty, D. L. Collins, T. M. Herrington, A. A. Kühn, and A. Horn. “Toward defining deep brain stimulation targets in MNI space: A subcortical atlas based on multimodal MRI, histology and structural connectivity”. In: *NeuroImage* 170 (Apr. 2018), pp. 271–282. ISSN: 1053-8119. DOI: 10.1016/j.neuroimage.2017.05.015 (cit. on p. 8).

[Fou10] T. J. Foutz and C. C. McIntyre. “Evaluation of novel stimulus waveforms for deep brain stimulation”. In: *Journal of Neural Engineering* 7.6 (2010), p. 066008. DOI: 10.1088/1741-2560/7/6/066008 (cit. on p. 155).

[Gar17] P. Garcés, D. López-Sanz, F. Maestú, and E. Pereda. “Choice of Magnetometers and Gradiometers after Signal Space Separation”. In: *Sensors* 17.12 (2017). ISSN: 1424-8220. DOI: 10.3390/s17122926 (cit. on p. 156).

[Gee16] R. Geevarghese, T. R. O’Gorman, D. E. Lumsden, M. Samuel, and K. Ashkan. “Registration Accuracy of CT/MRI Fusion for Localisation of Deep Brain Stimulation Electrode Position: An Imaging Study and Systematic Review”. In: *Stereotact Funct Neurosurg* 94.3 (Aug. 2016), pp. 159–163. DOI: 10.1159/000446609 (cit. on pp. 3, 11).

[Gra95] T. Grandke and J. Hesse. “Introduction”. In: *Sensors Set*. Ed. by W. Göpel, J. Hesse, and J. N. Zemel. Vol. 5. Weinheim, Deutschland: John Wiley & Sons, Ltd, 1995. Chap. 1, pp. 1–16. ISBN: 9783527619269 (cit. on p. 16).

[Gul10] D. Güllmar, J. Haueisen, and J. R. Reichenbach. “Influence of anisotropic electrical conductivity in white matter tissue on the EEG/MEG forward and inverse solution. A high-resolution whole head simulation study”. In: *NeuroImage* 51.1 (2010), pp. 145–163. ISSN: 1053-8119. DOI: 10.1016/j.neuroimage.2010.02.014 (cit. on p. 152).

[Goe19] L. Goetz, M. Bhattacharjee, M. U. Ferraye, V. Fraix, C. Maineri, D. Nosko, A. J. Fenoy, B. Piallat, N. Torres, A. Krainik, E. Seigneuret, O. David, M. Parent, A. Parent, P. Pollak, A. L. Benabid, B. Debu, and S. Chabardès. “Deep Brain Stimulation of the Pedunculopontine Nucleus Area in Parkinson Disease: MRI-Based Anatomoclinical Correlations and Optimal Target”. In:

Neurosurgery 84.2 (Feb. 2019), pp. 506–518. ISSN: 0148-396X. DOI: 10.1093/neuros/nyy151 (cit. on p. 8).

[Gor21] N. Göransson, J. D. Johansson, K. Wårdell, and P. Zsigmond. "Postoperative Lead Movement after Deep Brain Stimulation Surgery and the Change of Stimulation Volume". In: *Stereotact Funct Neurosurg* 99.3 (2021), pp. 221–229. DOI: 10.1159/000511406 (cit. on pp. 3, 12, 15).

[Gra17] S. L. Gratiy, G. Halnes, D. Denman, M. J. Hawrylycz, C. Koch, G. T. Einevoll, and C. A. Anastassiou. "From Maxwell's equations to the theory of current-source density analysis". In: *European Journal of Neuroscience* 45.8 (2017), pp. 1013–1023. DOI: 10.1111/ejn.13534 (cit. on pp. 19, 20).

[Gre08] R. Grech, T. Cassar, J. Muscat, K. P. Camilleri, S. G. Fabri, M. Zervakis, P. Xanthopoulos, V. Sakkalis, and B. Vanrumste. "Review on solving the inverse problem in EEG source analysis". In: *Journal of NeuroEngineering and Rehabilitation* 5 (2008). DOI: 10.1186/1743-0003-5-25 (cit. on p. 19).

[Gri15] W. M. Grill. "Chapter 7 - Model-based analysis and design of waveforms for efficient neural stimulation". In: *Computational Neurostimulation*. Vol. 222. Progress in Brain Research. Elsevier, 2015, pp. 147–162. DOI: 10.1016/bs.pbr.2015.07.031 (cit. on p. 155).

[Gri04] W. M. Grill, A. N. Snyder, and S. Miocinovic. "Deep brain stimulation creates an informational lesion of the stimulated nucleus". In: *NeuroReport* 15.7 (May 2004), pp. 1137–1140. DOI: 10.1097/00001756-200405190-00011 (cit. on p. 8).

[Gui21] K. Guido, C. Matos, J. Ramsey, and A. Kiourti. "Tissue-Emulating Phantoms for In Vitro Experimentation at Radio Frequencies: Exploring characteristics, fabrication, and testing methods". In: *IEEE Antennas and Propagation Magazine* 63.6 (Dec. 2021), pp. 29–39. DOI: 10.1109/MAP.2020.3003208 (cit. on p. 153).

[Gup11] A. A. Gupte, D. Shrivastava, M. A. Spaniol, and A. Abosch. "MRI-Related Heating near Deep Brain Stimulation Electrodes: More Data Are Needed". In: *Stereotact Funct Neurosurg* 89.3 (June 2011), pp. 131–140. DOI: 10.1159/000324906 (cit. on p. 11).

[Ham93] M. Hämäläinen, R. Hari, R. J. Ilmoniemi, J. Knuutila, and O. V. Lounasmaa. "Magnetoencephalography—theory, instrumentation, and applications to noninvasive studies of the working human brain". In: *Rev. Mod. Phys.* 65.2 (1993), pp. 413–497. DOI: 10.1103/RevModPhys.65.413 (cit. on pp. 17, 19).

[Hal07] H. Hallez, B. Vanrumste, R. Grech, J. Muscat, W. D. Clercq, A. Vergult, Y. D'Asseler, K. P. Camilleri, S. G. Fabri, S. V. Huffel, and I. Lemahieu. "Review on solving the forward problem in EEG source analysis". In: *Journal of NeuroEngineering and Rehabilitation* 4 (2007). DOI: 10.1186/1743-0003-4-46 (cit. on p. 19).

[Ham17] C. Hamani, G. Florence, H. Heinsen, B. R. Plantinga, Y. Temel, K. Uludag, E. Alho, M. J. Teixeira, E. Amaro, and E. T. Fonoff. "Subthalamic Nucleus Deep Brain Stimulation: Basic Concepts and Novel Perspectives". In: *eNeuro* 4.5 (Sept. 2017). DOI: 10.1523/ENEURO.0140-17.2017 (cit. on p. 8).

[Har19] C. J. Hartmann, S. Fliegen, S. J. Groiss, L. Wojtecki, and A. Schnitzler. "An update on best practice of deep brain stimulation in Parkinson's disease". In: *Therapeutic Advances in Neurological Disorders* 12 (Mar. 2019). DOI: 10.1177/1756286419838096 (cit. on p. 8).

[Has03] T. Hashimoto, C. M. Elder, M. S. Okun, S. K. Patrick, and J. L. Vitek. "Stimulation of the Subthalamic Nucleus Changes the Firing Pattern of Pallidal Neurons". In: *Journal of Neuroscience* 23.5 (Mar. 2003), pp. 1916–1923. DOI: 10.1523/JNEUROSCI.23-05-01916.2003 (cit. on p. 8).

[Hel18] A. Hellerbach, T. A. Dembek, M. Hoevels, J. A. Holz, A. Gierich, K. Luyken, M. T. Barbe, J. Wirths, V. Visser-Vandewalle, and H Treuer. "DiODe: Directional Orientation Detection of Segmented Deep Brain Stimulation Leads: A Sequential Algorithm Based on CT Imaging". In: *Stereotactic and Functional Neurosurgery* 96.5 (Dec. 2018), pp. 335–341. DOI: 10.1159/000494738 (cit. on pp. 3, 13–15).

[Hem09] S. Hemm, J. Coste, J. Gabrillargues, L. Ouchchane, L. Sarry, F. Caire, F. Vassal, C. Nuti, P. Derost, F. Durif, and J.-J. Lemaire. "Contact position analysis of deep brain stimulation electrodes on post-operative CT images". In: *Acta Neurochirurgica* 151 (July 2009), pp. 823–829. DOI: 10.1007/s00701-009-0393-3 (cit. on p. 12).

[Hen05] J. M. Henderson, J. Tkach, M. Phillips, K. Baker, F. G. Shellock, and A. R. Rezai. "Permanent Neurological Deficit Related to Magnetic Resonance Imaging in a Patient with Implanted Deep Brain Stimulation Electrodes for Parkinson's Disease: Case Report". In: *Neurosurgery* 57.5 (Nov. 2005), E1063. DOI: 10.1227/01.NEU.0000180810.16964.3E (cit. on p. 11).

[How19] B. Howell, K. Gunalan, and C. C. McIntyre. "A Driving-Force Predictor for Estimating Pathway Activation in Patient-Specific Models of Deep Brain Stimulation". In: *Neuromodulation: Technology at the Neural Interface* 22.4 (June 2019), pp. 403–415. DOI: 10.1111/ner.12929 (cit. on p. 159).

[Hil20] R. M. Hill, E. Boto, M. Rea, N. Holmes, J. Leggett, L. A. Coles, M. Papastavrou, S. K. Everton, B. A. Hunt, D. Sims, J. Osborne, V. Shah, R. Bowtell, and M. J. Brookes. "Multi-channel whole-head OPM-MEG: Helmet design and a comparison with a conventional system". In: *NeuroImage* 219 (Oct. 2020), p. 116995. ISSN: 1053-8119. DOI: 10.1016/j.neuroimage.2020.116995 (cit. on pp. 145, 152).

[Hor15] A. Horn and A. A. Kühn. "Lead-DBS: A toolbox for deep brain stimulation electrode localizations and visualizations". In: *NeuroImage* 107 (Feb. 2015), pp. 127–135. ISSN: 1053-8119. DOI: 10.1016/j.neuroimage.2014.12.002 (cit. on pp. 12, 158).

[Hun20] A. Hunold, R. Machts, and J. Haueisen. "Head phantoms for bioelectromagnetic applications: a material study". In: *BioMedical Engineering OnLine* 19 (Nov. 2020). DOI: 10.1186/s12938-020-00830-y (cit. on p. 153).

[Hof11] L. Hofmann, M. E. Ebert, P. A. Tass, and C. Hauptmann. "Modified pulse shapes for effective neural stimulation". In: *Frontiers in Neuroengineering* 4 (Sept. 2011). ISSN: 1662-6443. DOI: 10.3389/fneng.2011.00009 (cit. on p. 155).

[Hol18] J. A. H. Holslag, N. Neef, M. Beudel, G. Drost, D. L. M. Oterdoom, N. I. Kremer, T. van Laar, and J. M. C. van Dijk. "Deep Brain Stimulation for Essential Tremor: A Comparison of Targets". In: *World Neurosurgery* 110 (Feb. 2018), e580–e584. ISSN: 1878-8750. DOI: 10.1016/j.wneu.2017.11.064 (cit. on p. 8).

[Hor17a] A. Horn, W.-J. Neumann, K. Degen, G.-H. Schneider, and A. A. Kühn. "Toward an electrophysiological "sweet spot" for deep brain stimulation in the subthalamic nucleus". In: *Human Brain Mapping* 38.7 (Apr. 2017), pp. 3377–3390. DOI: 10.1002/hbm.23594 (cit. on p. 9).

[Hor17b] A. Horn, M. Reich, J. Vorwerk, N. Li, G. Wenzel, Q. Fang, T. Schmitz-Hübsch, R. Nickl, A. Kupsch, J. Volkmann, A. A. Kühn, and M. D. Fox. "Connectivity Predicts deep brain stimulation outcome in Parkinson disease". In: *Annals of Neurology* 82.1 (June 2017), pp. 67–78. DOI: 10.1002/ana.24974 (cit. on p. 159).

[Hor19] A. Horn, N. Li, T. A. Dembek, A. Kappel, C. Boulay, S. Ewert, A. Tietze, A. Husch, T. Perera, W.-J. Neumann, M. Reisert, H. Si, R. Oostenveld, C. Rorden, F.-C. Yeh, Q. Fang, T. M. Herrington, J. Vorwerk, and A. A. Kühn. "Lead-DBS v2: Towards a comprehensive pipeline for deep brain stimulation imaging". In: *NeuroImage* 184 (Jan. 2019), pp. 293–316. DOI: 10.1016/j.neuroimage.2018.08.068 (cit. on p. 158).

[Hun05] K. Hunka, O. Suchowersky, S. Wood, L. Derwent, and Z. H. T. Kiss. “Nursing Time to Program and Assess Deep Brain Stimulators in Movement Disorder Patients”. In: *Journal of Neuroscience Nursing* 37.4 (Aug. 2005), pp. 204–210. DOI: 10.1097/01376517-200508000-00006 (cit. on p. 9).

[Hun19] S. Hunsche, C. Neudorfer, F. E. Majdoub, M. Maarouf, and D. Sauner. “Determining the Rotational Orientation of Directional Deep Brain Stimulation Leads Employing Flat-Panel Computed Tomography”. In: *Operative Neurosurgery* 16.4 (Apr. 2019), pp. 465–470. DOI: 10.1093/ons/opy163 (cit. on pp. 3, 13).

[Hus18] A. Husch, M. V. Petersen, P. Gemmar, J. Goncalves, and F. Hertel. “PaCER - A fully automated method for electrode trajectory and contact reconstruction in deep brain stimulation”. In: *NeuroImage: Clinical* 17 (2018), pp. 80–89. ISSN: 2213-1582. DOI: 10.1016/j.nicl.2017.10.004 (cit. on p. 12).

[Hem10] S. Hemm and K. Wårdell. “Stereotactic implantation of deep brain stimulation electrodes: A review of technical systems, methods and emerging tools”. In: *Medical & Biological Engineering & Computing* 48 (July 2010), pp. 611–624. DOI: 10.1007/s11517-010-0633-y (cit. on p. 8).

[Iac19] M. I. Iacono, S. R. Atefi, L. Mainardi, H. C. Walker, L. M. Angelone, and G. Bonmassar. “A Study on the Feasibility of the Deep Brain Stimulation (DBS) Electrode Localization Based on Scalp Electric Potential Recordings”. In: *Frontiers in Physiology* 9 (Jan. 2019), p. 1788. ISSN: 1664-042X. DOI: 10.3389/fphys.2018.01788 (cit. on pp. 4, 13, 142).

[Iwa96] S. Iwaki and S. Ueno. “Comparison of the performance of distributed source estimation in the human brain using normal and vector magnetic field measurements”. In: *IEEE Transactions on Magnetics* 32.5 (Sept. 1996), pp. 5127–5129. DOI: 10.1109/20.539512 (cit. on p. 157).

[Jai20] A. Jaiswal, J. Nenonen, M. Stenroos, A. Gramfort, S. S. Dalal, B. U. Westner, V. Litvak, J. C. Mosher, J.-M. Schoffelen, C. Witton, R. Oostenveld, and L. Parkkonen. “Comparison of beamformer implementations for MEG source localization”. In: *NeuroImage* 216 (Aug. 2020), p. 116797. ISSN: 1053-8119. DOI: 10.1016/j.neuroimage.2020.116797 (cit. on p. 152).

[Jen09] A. L. Jensen and D. M. Durand. “High frequency stimulation can block axonal conduction”. In: *Experimental Neurology* 220.1 (Nov. 2009), pp. 57–70. DOI: 10.1016/j.expneurol.2009.07.023 (cit. on p. 8).

[Jun05] S. C. Jun, J. S. George, J. Paré-Blagoev, S. M. Plis, D. M. Ranken, D. M. Schmidt, and C. C. Wood. “Spatiotemporal Bayesian inference dipole analysis for MEG neuroimaging data”. In: *NeuroImage* 28.1 (Oct. 2005), pp. 84–98. DOI: 10.1016/j.neuroimage.2005.06.003 (cit. on p. 19).

[Kun08] A. M. Kuncel, S. E. Cooper, and W. M. Grill. "A method to estimate the spatial extent of activation in thalamic deep brain stimulation". In: *Clinical Neurophysiology* 119.9 (Sept. 2008), pp. 2148–2158. DOI: 10.1016/j.clinph.2008.02.025 (cit. on p. 159).

[Kun04] A. M. Kuncel and W. M. Grill. "Selection of stimulus parameters for deep brain stimulation". In: *Clinical Neurophysiology* 115.11 (Nov. 2004), pp. 2431–2441. DOI: 10.1016/j.clinph.2004.05.031 (cit. on p. 9).

[Kim10] Y. H. Kim, H. J. Kim, C. Kim, D. G. Kim, B. S. Jeon, and S. H. Paek. "Comparison of electrode location between immediate postoperative day and 6 months after bilateral subthalamic nucleus deep brain stimulation". In: *Acta Neurochirurgica* 152 (Dec. 2010), pp. 2037–2045. DOI: 10.1007/s00701-010-0771-x (cit. on pp. 12, 15).

[Kan20] A. L. Kandemir, V. Litvak, and E. Florin. "The comparative performance of DBS artefact rejection methods for MEG recordings". In: *NeuroImage* 219 (Oct. 2020), p. 117057. ISSN: 1053-8119. DOI: 10.1016/j.neuroimage.2020.117057 (cit. on p. 4).

[Koe19] T. Koeglsperger, C. Palleis, F. Hell, J. H. Mehrkens, and K. Bötzel. "Deep Brain Stimulation Programming for Movement Disorders: Current Concepts and Evidence-Based Strategies". In: *Frontiers in Neurology* 10 (May 2019), p. 410. ISSN: 1664-2295. DOI: 10.3389/fneur.2019.00410 (cit. on p. 13).

[Kar19] J. A. Karl, B. Ouyang, and L. V. Metman. "A Novel Dual-Frequency Deep Brain Stimulation Paradigm for Parkinson's Disease". In: *Neurology and Therapy* 8 (Dec. 2019), pp. 483–489. DOI: 10.1007/s40120-019-0140-5 (cit. on p. 154).

[Kos21] N. Koshev, A. Butorina, E. Skidchenko, A. Kuzmichev, A. Ossadtchi, M. Ostras, M. Fedorov, and P. Vetoshko. "Evolution of MEG: A first MEG-feasible fluxgate magnetometer". In: *Human Brain Mapping* 42.15 (2021), pp. 4844–4856. DOI: 10.1002/hbm.25582 (cit. on pp. 145, 152).

[Kur20] R. Kurtev-Rittstieg, S. Achatz, A. Nourinia, and S. Mittermeyer. "Orientation of Directional Deep Brain Stimulation Leads on CT: Resolving the Ambiguity". In: *bioRxiv* (2020). DOI: 10.1101/2020.09.16.298653 (cit. on p. 14).

[Kra19] P. Krack, J. Volkmann, G. Tinkhauser, and G. Deuschl. "Deep Brain Stimulation in Movement Disorders: From Experimental Surgery to Evidence-Based Therapy". In: *Movement Disorders* 34.12 (2019), pp. 1795–1810. DOI: 10.1002/mds.27860 (cit. on pp. 1, 7).

[Kra21] J. Kramme, T. A. Dembek, H. Treuer, H. S. Dafsari, M. T. Barbe, J. Wirths, and V. Visser-Vandewalle. "Potentials and Limitations of Directional Deep Brain Stimulation: A Simulation Approach". In: *Stereotactic and Functional Neurosurgery* 99.1 (Feb. 2021), pp. 65–74. DOI: 10.1159/000509781 (cit. on pp. 2, 13).

[Kob01] K. Kobayashi and Y. Uchikawa. "Estimation of multiple sources using spatio-temporal data on a three-dimensional measurement of MEG". In: *IEEE Transactions on Magnetics* 37.4 (July 2001), pp. 2915–2917. DOI: 10.1109/20.951346 (cit. on p. 157).

[Lan21] F. Lange, F. Steigerwald, D. Engel, T. Malzacher, T. Neun, P. Fricke, J. Volkmann, C. Matthies, and P. Capetian. "Longitudinal Assessment of Rotation Angles after Implantation of Directional Deep Brain Stimulation Leads". In: *Stereotactic and Functional Neurosurgery* 99.2 (2021), pp. 150–158. DOI: 10.1159/000511202 (cit. on p. 15).

[Lau16] P. M. Lauro, N. Vanegas-Arroyave, L. Huang, P. A. Taylor, K. A. Zaghloul, C. Lungu, Z. S. Saad, and S. G. Horovitz. "DBSproc: An open source process for DBS electrode localization and tractographic analysis". In: *Human Brain Mapping* 37.1 (Jan. 2016), pp. 422–433. DOI: 10.1002/hbm.23039 (cit. on pp. 12, 159).

[Lit14] G. Little, S. Boe, and T. Bardouille. "Head movement compensation in real-time magnetoencephalographic recordings". In: *MethodsX* 1 (2014), pp. 275–282. ISSN: 2215-0161. DOI: 10.1016/j.mex.2014.10.008 (cit. on p. 152).

[Lee10a] J.-Y. Lee, B. S. Jeon, S. H. Paek, Y. H. Lim, M.-R. Kim, and C. Kim. "Reprogramming guided by the fused images of MRI and CT in subthalamic nucleus stimulation in Parkinson disease". In: *Clinical Neurology and Neurosurgery* 112.1 (2010), pp. 47–53. ISSN: 0303-8467. DOI: 10.1016/j.clineuro.2009.10.008 (cit. on pp. 3, 11, 12).

[Lee10b] J. Y. Lee, J. W. Kim, J.-Y. Lee, Y. H. Lim, C. Kim, D. G. Kim, B. S. Jeon, and S. H. Paek. "Is MRI a reliable tool to locate the electrode after deep brain stimulation surgery? Comparison study of CT and MRI for the localization of electrodes after DBS". In: *Acta Neurochirurgica* 152 (Dec. 2010), pp. 2029–2036. DOI: 10.1007/s00701-010-0779-2 (cit. on p. 11).

[Lee19] D. J. Lee, C. S. Lozano, R. F. Dallapiazza, and A. M. Lozano. "Current and future directions of deep brain stimulation for neurological and psychiatric disorders". In: *Journal of neurosurgery* 131.2 (Aug. 2019), pp. 333–342. DOI: 10.3171/2019.4.JNS181761 (cit. on p. 8).

[Lei19] F. Leimbach, J. Gratwicke, T. Foltynie, P. Limousin, L. Zrinzo, and M. Jahanshahi. “The effects of deep brain stimulation of the pedunculopontine nucleus on cognition in Parkinson’s disease and Progressive Supranuclear Palsy”. In: *Clinical Parkinsonism & Related Disorders* 1 (2019), pp. 48–51. ISSN: 2590-1125. DOI: 10.1016/j.prdoa.2019.08.001 (cit. on p. 8).

[Lit10] V. Litvak, A. Eusebio, A. Jha, R. Oostenveld, G. R. Barnes, W. D. Penny, L. Zrinzo, M. I. Hariz, P. Limousin, K. J. Friston, and P. Brown. “Optimized beamforming for simultaneous MEG and intracranial local field potential recordings in deep brain stimulation patients”. In: *NeuroImage* 50.4 (May 2010), pp. 1578–1588. DOI: 10.1016/j.neuroimage.2009.12.115 (cit. on p. 152).

[Loz19] A. M. Lozano, N. Lipsman, H. Bergman, P. Brown, S. Chabardes, J. W. Chang, K. Matthews, C. C. McIntyre, T. E. Schlaepfer, M. Schulder, Y. Temel, J. Volkmann, and J. Krauss. “Deep brain stimulation: current challenges and future directions”. In: *Nature Reviews Neurology* 15 (Jan. 2019), pp. 148–160. DOI: 10.1038/s41582-018-0128-2 (cit. on pp. 7, 8).

[Mar11] H. C. F. Martens, E. Toader, M. M. J. Decré, D. J. Anderson, R. Vetter, D. R. Kipke, K. B. Baker, M. D. Johnson, and J. L. Vitek. “Spatial steering of deep brain stimulation volumes using a novel lead design”. In: *Clinical Neurophysiology* 122.3 (Mar. 2011), pp. 558–566. ISSN: 1388-2457. DOI: 10.1016/j.clinph.2010.07.026 (cit. on p. 153).

[Van21] P. van den Munckhof, M. Bot, and P. R. Schuurman. “Targeting of the Subthalamic Nucleus in Patients with Parkinson’s Disease Undergoing Deep Brain Stimulation Surgery”. In: *Neurology and Therapy* 10 (2021), pp. 61–73. DOI: 10.1007/s40120-021-00233-8 (cit. on p. 11).

[Mad12] B. Mädler and V. A. Coenen. “Explaining Clinical Effects of Deep Brain Stimulation through Simplified Target-Specific Modeling of the Volume of Activated Tissue”. In: *American Journal of Neuroradiology* 33.6 (2012), pp. 1072–1080. ISSN: 0195-6108. DOI: 10.3174/ajnr.A2906 (cit. on p. 159).

[McI04c] C. C. McIntyre, W. M. Grill, D. L. Sherman, and N. V. Thakor. “Cellular Effects of Deep Brain Stimulation: Model-Based Analysis of Activation and Inhibition”. In: *Journal of Neurophysiology* 91.4 (Apr. 2004), pp. 1457–1469. DOI: 10.1152/jn.00989.2003 (cit. on p. 159).

[McI04b] C. C. McIntyre, S. Mori, D. L. Sherman, N. V. Thakor, and J. L. Vitek. “Electric field and stimulating influence generated by deep brain stimulation of the subthalamic nucleus”. In: *Clinical Neurophysiology* 115.3 (Mar. 2004), pp. 589–595. DOI: 10.1016/j.clinph.2003.10.033 (cit. on p. 158).

[McI04a] C. C. McIntyre, M. Savasta, L. Kerkerian-Le Goff, and J. L. Vitek. "Uncovering the mechanism(s) of action of deep brain stimulation: activation, inhibition, or both". In: *Clinical Neurophysiology* 115.6 (June 2004). DOI: 10.1016/j.clinph.2003.12.024 (cit. on p. 8).

[Mey17] S. S. Meyer, J. Bonaiuto, M. Lim, H. Rossiter, S. Waters, D. Bradbury, S. Bestmann, M. Brookes, M. F. Callaghan, N. Weiskopf, and G. R. Barnes. "Flexible head-casts for high spatial precision MEG". In: *Journal of Neuroscience Methods* 276 (2017), pp. 38–45. ISSN: 0165-0270. DOI: 10.1016/j.jneumeth.2016.11.009 (cit. on pp. 149, 152).

[McI13] C. C. McIntyre and T. J. Foutz. "Chapter 5 - Computational modeling of deep brain stimulation". In: *Brain Stimulation*. Ed. by A. M. Lozano and M. Hallett. Vol. 116. Handbook of Clinical Neurology. Elsevier, 2013, pp. 55–61. DOI: 10.1016/B978-0-444-53497-2.00005-X (cit. on p. 157).

[Mos92] J. C. Mosher, P. S. Lewis, and R. M. Leahy. "Multiple dipole modeling and localization from spatio-temporal MEG data". In: *IEEE Transactions on Biomedical Engineering* 39.6 (1992), pp. 541–557. DOI: 10.1109/10.141192 (cit. on pp. 19, 23).

[Mos99] J. C. Mosher, R. M. Leahy, and P. S. Lewis. "EEG and MEG: forward solutions for inverse methods". In: *IEEE Transactions on Biomedical Engineering* 46.3 (1999), pp. 245–259. DOI: 10.1109/10.748978 (cit. on p. 18).

[McI07] C. C. McIntyre, S. Miocinovic, and C. R. Butson. "Computational analysis of deep brain stimulation". In: *Expert Review of Medical Devices* 4.5 (2007), pp. 615–622. DOI: 10.1586/17434440.4.5.615 (cit. on p. 157).

[Moh10] H. R. Mohseni, M. L. Kringelbach, P. P. Smith, A. L. Green, C. E. Parsons, K. S. Young, J.-S. Brittain, J. A. Hyam, P. M. Schweder, J. F. Stein, and T. Z. Aziz. "Application of a null-beamformer to source localisation in MEG data of deep brain stimulation". In: *2010 Annual International Conference of the IEEE Engineering in Medicine and Biology*. 2010, pp. 4120–4123. DOI: 10.1109/IEMBS.2010.5627325 (cit. on p. 152).

[Moh12] H. R. Mohseni, M. W. Woolrich, M. L. Kringelbach, H. Luckhoo, P. P. Smith, and T. Z. Aziz. "Fusion of Magnetometer and Gradiometer Sensors of MEG in the Presence of Multiplicative Error". In: *IEEE Transactions on Biomedical Engineering* 59.7 (2012), pp. 1951–1961. DOI: 10.1109/TBME.2012.2195001 (cit. on p. 156).

[Mor02] E. Moro, R. J. A. Esselink, J. Xie, M. Hommel, A. L. Benabid, and P. Pollak. "The impact on Parkinson's disease of electrical parameter settings in STN stimulation". In: *Neurology* 59.5 (2002), pp. 706–713. ISSN: 0028-3878. DOI: 10.1212/WNL.59.5.706 (cit. on p. 17).

[Mor11] A. Moran, E. Stein, H. Tischler, K. Belelovsky, and I. Bar-Gad. "Dynamic Stereotypic Responses of Basal Ganglia Neurons to Subthalamic Nucleus High-Frequency Stimulation in the Parkinsonian Primate". In: *Frontiers in Systems Neuroscience* 5 (2011). ISSN: 1662-5137. DOI: 10.3389/fnsys.2011.00021 (cit. on p. 8).

[Mor17] T. Morishita, J. D. Hilliard, M. S. Okun, D. Neal, K. A. Nestor, D. Peace, A. A. Hozouri, M. R. Davidson, F. J. Bova, J. M. Sporrer, G. Oyama, and K. D. Foote. "Postoperative lead migration in deep brain stimulation surgery: Incidence, risk factors, and clinical impact". In: *PLOS ONE* 12.9 (2017), pp. 1–22. DOI: 10.1371/journal.pone.0183711 (cit. on pp. 3, 12, 15).

[Van10] P. van den Munckhof, M. F. Contarino, L. J. Bour, J. D. Speelman, R. M. A. de Bie, and P. R. Schuurman. "Postoperative Curving and Upward Displacement of Deep Brain Stimulation Electrodes Caused by Brain Shift". In: *Neurosurgery* 67.1 (July 2010), pp. 49–54. ISSN: 0148-396X. DOI: 10.1227/01.NEU.0000370597.44524.6D (cit. on p. 12).

[Nam15] A. Nambu and S. Chiken. "Mechanism of DBS: Inhibition, Excitation, or Disruption?" In: *Deep Brain Stimulation for Neurological Disorders: Theoretical Background and Clinical Application*. Springer International Publishing, Aug. 2015, pp. 13–20. ISBN: 978-3-319-08476-3. DOI: 10.1007/978-3-319-08476-3_2 (cit. on p. 8).

[Neu17] W.-J. Neumann, A. Horn, S. Ewert, J. Huebl, C. Brücke, C. Slentz, G.-H. Schneider, and A. A. Kühn. "A localized pallidal physiomarker in cervical dystonia". In: *Annals of Neurology* 82.6 (Dec. 2017), pp. 912–924. DOI: 10.1002/ana.25095 (cit. on p. 9).

[Ngu19] T. A. K. Nguyen, M. Djilas, A. Nowacki, A. Mercanzini, M. Schüpbach, P. Renaud, and C. Pollo. "Analysis of patient-specific stimulation with segmented leads in the subthalamic nucleus". In: *PLOS ONE* 14.6 (June 2019), pp. 1–15. DOI: 10.1371/journal.pone.0217985 (cit. on p. 13).

[Nie20] J. Niederer, R. Patriat, O. Rosenberg, T. Palnitkar, D. Darrow, M. C. Park, L. Schrock, L. E. Eberly, and N. Harel. "Factors Influencing Electrode Position and Bending of the Proximal Lead in Deep Brain Stimulation for Movement Disorders". In: *Stereotactic and Functional Neurosurgery* 98.5 (2020), pp. 300–312. DOI: 10.1159/000507029 (cit. on p. 12).

[Now06] H. Nowak. "Biomagnetic Instrumentation". In: *Magnetism in Medicine*. John Wiley & Sons, Ltd, Oct. 2006. Chap. 2.2, pp. 101–163. ISBN: 9783527610174. DOI: 10.1002/9783527610174.ch2b (cit. on p. 16).

[Ond05] W. G. Ondo and H. Bronte-Stewart. “The North American Survey of Placement and Adjustment Strategies for Deep Brain Stimulation”. In: *Stereotactic and Functional Neurosurgery* 83.5 (Dec. 2005), pp. 142–147. DOI: 10.1159/000088654 (cit. on p. 9).

[Owd20] A. Y. Owda and A. J. Casson. “Electrical properties, accuracy, and multi-day performance of gelatine phantoms for electrophysiology”. In: *bioRxiv* (2020). DOI: 10.1101/2020.05.30.125070 (cit. on p. 153).

[Owd21] A. Y. Owda and A. J. Casson. “Investigating Gelatine Based Head Phantoms for Electroencephalography Compared to Electrical and Ex Vivo Porcine Skin Models”. In: *IEEE Access* 9 (2021), pp. 96722–96738. DOI: 10.1109/ACCESS.2021.3095220 (cit. on p. 153).

[Gor09] R. L. O’Gorman, J. M. Jarosz, M. Samuel, C. Clough, R. P. Selway, and K. Ashkan. “CT/MR Image Fusion in the Postoperative Assessment of Electrodes Implanted for Deep Brain Stimulation”. In: *Stereotactic and Functional Neurosurgery* 87.4 (Aug. 2009), pp. 205–210. DOI: 10.1159/000225973 (cit. on p. 11).

[Osw16] A. Oswal, A. Jha, S. Neal, A. Reid, D. Bradbury, P. Aston, P. Limousin, T. Foltynie, L. Zrinzo, P. Brown, and V. Litvak. “Analysis of simultaneous MEG and intracranial LFP recordings during Deep Brain Stimulation: a protocol and experimental validation”. In: *Journal of Neuroscience Methods* 261 (Mar. 2016), pp. 29–46. ISSN: 0165-0270. DOI: 10.1016/j.jneumeth.2015.11.029 (cit. on p. 152).

[Odo11] L. J. O’Donnell and C.-F. Westin. “An Introduction to Diffusion Tensor Image Analysis”. In: *Neurosurgery Clinics of North America* 22.2 (Apr. 2011), pp. 185–196. DOI: 10.1016/j.nec.2010.12.004 (cit. on p. 158).

[Pae11] S. H. Paek, H. J. Kim, J. Y. Yoon, J. H. Heo, C. Kim, M. R. Kim, Y. H. Lim, K. R. Kim, J. W. Kim, J. H. Han, D. G. Kim, and B. S. Jeon. “Fusion Image–Based Programming After Subthalamic Nucleus Deep Brain Stimulation”. In: *World Neurosurgery* 75.3 (2011), pp. 517–524. ISSN: 1878-8750. DOI: 10.1016/j.wneu.2010.12.003 (cit. on pp. 3, 11).

[Pav20] N. Pavese, Y. F. Tai, N. Yousif, D. Nandi, and P. G. Bain. “Traditional Trial and Error versus Neuroanatomic 3-Dimensional Image Software-Assisted Deep Brain Stimulation Programming in Patients with Parkinson Disease”. In: *World Neurosurgery* 134 (2020), e98–e102. ISSN: 1878-8750. DOI: 10.1016/j.wneu.2019.09.106 (cit. on p. 159).

[Pet19b] M. V. Petersen, J. Mlakar, S. N. Haber, M. Parent, Y. Smith, P. L. Strick, M. A. Griswold, and C. C. McIntyre. "Holographic Reconstruction of Axonal Pathways in the Human Brain". In: *Neuron* 104.6 (2019), pp. 1056–1064. ISSN: 0896-6273. DOI: 10.1016/j.neuron.2019.09.030 (cit. on p. 159).

[Pfe19] C. Pfeiffer, S. Ruffieux, L. Jönsson, M. L. Chukharkin, A. Kalaboukhov, M. Xie, D. Winkler, and J. F. Schneiderman. "A 7-channel high-Tc SQUID-based on-scalp MEG system". In: *bioRxiv* (2019). DOI: 10.1101/534107 (cit. on p. 152).

[Plo67] R. Plonsey and D. B. Heppner. "Considerations of quasi-stationarity in electrophysiological systems". In: *Bulletin of Mathematical Biophysics* 29 (Dec. 1967), pp. 657–664. DOI: 10.1007/BF02476917 (cit. on p. 20).

[Pic16] M. Picillo, A. M. Lozano, N. Kou, R. P. Munhoz, and A. Fasano. "Programming Deep Brain Stimulation for Parkinson's Disease: The Toronto Western Hospital Algorithms". In: *Brain Stimulation* 9.3 (May 2016), pp. 425–437. DOI: 10.1016/j.brs.2016.02.004 (cit. on p. 2).

[Pan11] M. Pannetier-Lecoeur, L. Parkkonen, N. Sergeeva-Chollet, H. Polovy, C. Fermon, and C. Fowley. "Magnetocardiography with sensors based on giant magnetoresistance". In: *Applied Physics Letters* 98.15 (2011), p. 153705. DOI: 10.1063/1.3575591 (cit. on p. 152).

[Pra21] E. J. Pratt, M. Ledbetter, R. Jiménez-Martínez, B. Shapiro, A. Solon, G. Z. Iwata, S. Garber, J. Gormley, D. Decker, D. Delgadillo, A. T. Dellis, J. Phillips, G. Sundar, J. Leung, J. Coyne, M. McKinley, G. Lopez, S. Homan, L. Marsh, M. Zhang, V. Maurice, B. Siepser, T. Giovannoli, B. Leverett, G. Lerner, S. Seidman, V. DeLuna, K. Wright-Freeman, J. Kates-Harbeck, T. Lasser, H. Mohseni, T. Sharp, A. Zorzos, A. H. Lara, A. Kouhzadi, A. Ojeda, P. Chopra, Z. Bednarke, M. Henninger, and J. K. Alford. "Kernel Flux: a whole-head 432-magnetometer optically-pumped magnetoencephalography (OP-MEG) system for brain activity imaging during natural human experiences". In: *Optical and Quantum Sensing and Precision Metrology*. Vol. 11700. SPIE, 2021, pp. 162–179. DOI: 10.1117/12.2581794 (cit. on pp. 145, 152).

[Pet19a] J. N. Petry-Schmelzer, M. Krause, T. A. Dembek, A. Horn, J. Evans, K. Ashkan, A. Rizos, M. Silverdale, W. Schumacher, C. Sack, P. A. Loehrer, G. R. Fink, E. T. Fonoff, P. Martinez-Martin, A. Antonini, M. T. Barbe, V. Visser-Vandewalle, K. Ray-Chaudhuri, L. Timmermann, H. S. Dafsari, EUROPAR, and the IPMDS Non-Motor PD Study Group. "Non-motor outcomes depend on location of neurostimulation in Parkinson's disease". In: *Brain* 142.11 (Nov. 2019), pp. 3592–3604. ISSN: 0006-8950. DOI: 10.1093/brain/awz285 (cit. on p. 13).

[Pet20] J. N. Petry-Schmelzer, T. A. Dembek, J. K. Steffen, H. Jergas, H. S. Dafsari, G. R. Fink, V. Visser-Vandewalle, and M. T. Barbe. "Selecting the Most Effective DBS Contact in Essential Tremor Patients Based on Individual Tractography". In: *Brain Sciences* 10.12 (2020). ISSN: 2076-3425. DOI: 10.3390/brainsci10121015 (cit. on p. 13).

[Pyc18] L. Pycroft, J. Stein, and T. Aziz. "Deep brain stimulation: An overview of history, methods, and future developments". In: *Brain and Neuroscience Advances* 2.12 (2018). DOI: 10.1177/2398212818816017 (cit. on p. 8).

[Ram11] R. R. Ramírez, B. H. Kopell, C. R. Butson, B. C. Hiner, and S. Baillet. "Spectral signal space projection algorithm for frequency domain MEG and EEG denoising, whitening, and source imaging". In: *NeuroImage* 56.1 (2011), pp. 78–92. ISSN: 1053-8119. DOI: 10.1016/j.neuroimage.2011.02.002 (cit. on p. 152).

[Rat86] F. Rattay. "Analysis of Models for External Stimulation of Axons". In: *IEEE Transactions on Biomedical Engineering* BME-33.10 (1986), pp. 974–977. DOI: 10.1109/TBME.1986.325670 (cit. on p. 159).

[Rau21] A. Rau, H. Urbach, V. A. Coenen, K. Egger, and P. C. Reinacher. "Deep brain stimulation electrodes may rotate after implantation—an animal study". In: *Neurosurgical Review* 44 (Aug. 2021), pp. 2349–2353. DOI: 10.1007/s10143-020-01429-6 (cit. on p. 15).

[Reb18] P. Rebelo, A. L. Green, T. Z. Aziz, A. Kent, D. Schafer, L. Venkatesan, and B. Cheeran. "Thalamic Directional Deep Brain Stimulation for tremor: Spend less, get more". In: *Brain Stimulation* 11.3 (2018), pp. 600–606. ISSN: 1935-861X. DOI: 10.1016/j.brs.2017.12.015 (cit. on pp. 10, 13).

[Rei17] P. C. Reinacher, M. T. Krüger, V. A. Coenen, M. Shah, R. Roelz, C. Jenkner, and K. Egger. "Determining the Orientation of Directional Deep Brain Stimulation Electrodes Using 3D Rotational Fluoroscopy". In: *American Journal of Neuroradiology* 38.6 (2017), pp. 1111–1116. ISSN: 0195-6108. DOI: 10.3174/ajnr.A5153 (cit. on pp. 3, 13, 15).

[Rez04] A. R. Rezai, M. Phillips, K. B. Baker, A. D. Sharan, J. Nyenhuis, J. Tkach, J. Henderson, and F. G. Shellock. "Neurostimulation System Used for Deep Brain Stimulation (DBS): MR Safety Issues and Implications of Failing to Follow Safety Recommendations". In: *Investigative Radiology* 39.5 (May 2004), pp. 300–303. DOI: 10.1097/01.rli.0000124940.02340.ab (cit. on p. 11).

[Rez05] A. R. Rezai, K. B. Baker, J. A. Tkach, M. Phillips, G. Hrdlicka, A. D. Sharan, J. Nyenhuis, P. Ruggieri, F. G. Shellock, and J. Henderson. "Is Magnetic Resonance Imaging Safe for Patients with Neurostimulation Systems Used for

Deep Brain Stimulation?" In: *Neurosurgery* 57.5 (Nov. 2005), pp. 1056–1062. DOI: 10.1227/01.NEU.0000186935.87971.2a (cit. on p. 11).

[Ros14] R. Rosenbaum, A. Zimnik, F. Zheng, R. S. Turner, C. Alzheimer, B. Doiron, and J. E. Rubin. "Axonal and synaptic failure suppress the transfer of firing rate oscillations, synchrony and information during high frequency deep brain stimulation". In: *Neurobiology of Disease* 62 (Feb. 2014), pp. 86–99. DOI: 10.1016/j.nbd.2013.09.006 (cit. on p. 8).

[Ros69] P. Rosenfalck. "Intra- and extracellular potential fields of active nerve and muscle fibres. A physico-mathematical analysis of different models". In: *Acta Physiologica Scandinavica Supplementum* 321 (1969), pp. 1–168. ISSN: 0302-2994 (cit. on p. 20).

[Sal16] C. Saleh, G. Dooms, C. Berthold, and F. Hertel. "Post-operative imaging in deep brain stimulation: A controversial issue". In: *The Neuroradiology Journal* 29.4 (Aug. 2016), pp. 244–249. DOI: 10.1177/1971400916639960 (cit. on p. 11).

[Sar87] J. Sarvas. "Basic mathematical and electromagnetic concepts of the biomagnetic inverse problem." In: *Physics in Medicine and Biology* 32.1 (1987), pp. 11–22. DOI: 10.1088/0031-9155/32/1/004 (cit. on p. 22).

[Sch09] T. Schönecker, A. Kupsch, A. A. Kühn, G.-H. Schneider, and K.-T. Hoffmann. "Automated Optimization of Subcortical Cerebral MR Imaging-Atlas Coregistration for Improved Postoperative Electrode Localization in Deep Brain Stimulation". In: *American Journal of Neuroradiology* 30.10 (Nov. 2009), pp. 1914–1921. DOI: 10.3174/ajnr.A1741 (cit. on p. 11).

[Shi07] M. Shin, J.-P. Lefaucheur, M. F. Penholate, P. Brugières, J.-M. Gurruchaga, and J.-P. Nguyen. "Subthalamic nucleus stimulation in Parkinson's disease: Postoperative CT–MRI fusion images confirm accuracy of electrode placement using intraoperative multi-unit recording". In: *Neurophysiologie Clinique/Clinical Neurophysiology* 37.6 (2007), pp. 457–466. ISSN: 0987-7053. DOI: 10.1016/j.neucli.2007.09.005 (cit. on p. 11).

[Shi10] M. Shin, M. F. Penholate, J.-P. Lefaucheur, J.-M. Gurruchaga, P. Brugieres, and J.-P. Nguyen. "Assessing Accuracy of the Magnetic Resonance Imaging-Computed Tomography Fusion Images to Evaluate the Electrode Positions in Subthalamic Nucleus After Deep-Brain Stimulation". In: *Neurosurgery* 66.6 (June 2010), pp. 1193–1202. ISSN: 0148-396X. DOI: 10.1227/01.NEU.0000369190.46510.42 (cit. on p. 11).

[Sit17] A. Sitz, M. Hoevels, A. Hellerbach, A. Gierich, K. Luyken, T. A. Dembek, M. Klehr, J. Wirths, V. Visser-Vandewalle, and H. Treuer. "Determining the orientation angle of directional leads for deep brain stimulation using computed tomography and digital x-ray imaging: A phantom study". In: *Medical Physics* 44.9 (June 2017), pp. 4463–4473. DOI: 10.1002/mp.12424 (cit. on pp. 3, 13).

[Ste19] F. Steigerwald, C. Matthies, and J. Volkmann. "Directional Deep Brain Stimulation". In: *Neurotherapeutics* 16 (Jan. 2019). DOI: 10.1007/s13311-018-0667-7 (cit. on pp. 2, 9, 10).

[Sha14] R. R. Shamir, A. Noecker, and C. C. McIntyre. "Deep Brain Stimulation". In: *Frontiers for Young Minds* 2.12 (Apr. 2014). DOI: 10.3389/frym.2014.00012 (cit. on p. 2).

[Spi03] J. Spiegel, G. Fuss, M. Backens, W. Reith, T. Magnus, G. Becker, J.-R. Moringlane, and U. Dillmann. "Transient dystonia following magnetic resonance imaging in a patient with deep brain stimulation electrodes for the treatment of Parkinson disease - Case report". In: *Journal of Neurosurgery* 99.4 (2003), pp. 772–774. DOI: 10.3171/jns.2003.99.4.0772 (cit. on p. 11).

[DaS15] N. M. da Silva, V. E. Rozanski, and J. P. Silva Cunha. "A 3D multimodal approach to precisely locate DBS electrodes in the basal ganglia brain region". In: *2015 7th International IEEE/EMBS Conference on Neural Engineering (NER)*. 2015, pp. 292–295. DOI: 10.1109/NER.2015.7146617 (cit. on p. 12).

[Ste07] A. Stefani, A. M. Lozano, A. Peppe, P. Stanzione, S. Galati, D. Tropepi, M. Pierantozzi, L. Brusa, E. Scarnati, and P. Mazzone. "Bilateral deep brain stimulation of the pedunculopontine and subthalamic nuclei in severe Parkinson's disease". In: *Brain* 130.6 (June 2007), pp. 1596–1607. ISSN: 0006-8950. DOI: 10.1093/brain/awl346 (cit. on p. 17).

[Ste16] F. Steigerwald, L. Müller, S. Johannes, C. Matthies, and J. Volkmann. "Directional deep brain stimulation of the subthalamic nucleus: A pilot study using a novel neurostimulation device". In: *Movement Disorders* 31.8 (2016), pp. 1240–1243. DOI: 10.1002/mds.26669 (cit. on pp. 10, 13).

[Sto13] A. Stolk, A. Todorovic, J.-M. Schoffelen, and R. Oostenveld. "Online and offline tools for head movement compensation in MEG". In: *NeuroImage* 68 (2013), pp. 39–48. ISSN: 1053-8119. DOI: 10.1016/j.neuroimage.2012.11.047 (cit. on p. 152).

[Sun14] Y. Sun, F. Farzan, L. Garcia Dominguez, M. S. Barr, P. Giacobbe, A. M. Lozano, W. Wong, and Z. J. Daskalakis. "A novel method for removal of deep brain stimulation artifact from electroencephalography". In: *Journal of*

Neuroscience Methods 237 (2014), pp. 33–40. ISSN: 0165-0270. DOI: 10.1016/j.jneumeth.2014.09.002 (cit. on p. 152).

[Sch86] M. Scherg and D. Von Cramon. "Evoked dipole source potentials of the human auditory cortex". In: *Electroencephalography and Clinical Neurophysiology/Evoked Potentials Section* 65.5 (1986), pp. 344–360. DOI: 10.1016/0168-5597(86)90014-6 (cit. on p. 19).

[Tha11] N. B. Thani, A. Bala, G. B. Swann, and C. R. P. Lind. "Accuracy of Postoperative Computed Tomography and Magnetic Resonance Image Fusion for Assessing Deep Brain Stimulation Electrodes". In: *Neurosurgery* 69.1 (July 2011), pp. 207–214. ISSN: 0148-396X. DOI: 10.1227/NEU.0b013e318218c7ae (cit. on p. 11).

[Tau06] S. Taulu and J. Simola. "Spatiotemporal signal space separation method for rejecting nearby interference in MEG measurements". In: *Physics in Medicine and Biology* 51.7 (2006), pp. 1759–1768. DOI: 10.1088/0031-9155/51/7/008 (cit. on p. 152).

[Tum11] S. Tumanski. *Handbook of Magnetic Measurements*. CRC Press, 2011. DOI: 10.1201/b10979 (cit. on p. 16).

[Vas09] X. Vasques, L. Cif, O. Hess, S. Gavarini, G. Mennessier, and P. Coubes. "Stereotactic model of the electrical distribution within the internal globus pallidus during deep brain stimulation". In: *Journal of Computational Neuroscience* 26 (June 2009). DOI: 10.1007/s10827-008-0101-y (cit. on p. 159).

[Vij21] N. Vijiaratnam, C. Girges, T. Wirth, T. Grover, F. Preda, E. Tripoliti, J. Foley, E. Scelzo, A. Macerollo, H. Akram, J. Hyam, L. Zrinzo, P. Limousin, and T. Foltynie. "Long-term success of low-frequency subthalamic nucleus stimulation for Parkinson's disease depends on tremor severity and symptom duration". In: *Brain Communications* 3.3 (July 2021). ISSN: 2632-1297. DOI: 10.1093/braincomms/fcab165 (cit. on p. 154).

[Ved21] V. Vedam-Mai, K. Deisseroth, J. Giordano, G. Lazaro-Munoz, W. Chiong, N. Suthana, J.-P. Langevin, J. Gill, W. Goodman, N. R. Provenza, C. H. Halpern, R. S. Shivacharan, T. N. Cunningham, S. A. Sheth, N. Pouratian, K. W. Scangos, H. S. Mayberg, A. Horn, K. A. Johnson, C. R. Butson, R. Gilron, C. de Hemptinne, R. Wilt, M. Yaroshinsky, S. Little, P. Starr, G. Worrell, P. Shirvalkar, E. Chang, J. Volkmann, M. Muthuraman, S. Groppa, A. Kühn, L. Li, M. Johnson, K. J. Otto, R. Raike, S. Goetz, C. Wu, P. Silburn, B. Cheeran, Y. J. Pathak, M. Malekmohammadi, A. Gunduz, J. K. Wong, S. Cernera, W. Hu, A. Wagle Shukla, A. Ramirez-Zamora, W. Deeb, A. Patterson, K. D. Foote, and M. S. Okun. "Proceedings of the Eighth Annual Deep Brain Stimulation Think Tank: Advances in Optogenetics, Ethical Issues Af-

fecting DBS Research, Neuromodulatory Approaches for Depression, Adaptive Neurostimulation, and Emerging DBS Technologies". In: *Frontiers in Human Neuroscience* 15 (2021). ISSN: 1662-5161. DOI: 10.3389/fnhum.2021.644593 (cit. on pp. 1, 7).

[Vor18] J. Vorwerk, R. Oostenveld, M. C. Piastra, L. Magyari, and C. H. Wolters. "The FieldTrip-SimBio pipeline for EEG forward solutions". In: *BioMedical Engineering OnLine* 17 (Mar. 2018). DOI: 10.1186/s12938-018-0463-y (cit. on p. 152).

[Whi03] K. Whittingstall, G. Stroink, L. Gates, J. F. Connolly, and A. Finley. "Effects of dipole position, orientation and noise on the accuracy of EEG source localization". In: *BioMedical Engineering OnLine* 2 (2003). DOI: 10.1186/1475-925X-2-14 (cit. on p. 18).

[Wid19] A. S. Widge, S. Zorowitz, I. Basu, A. C. Paulk, S. S. Cash, E. N. Eskandar, T. Deckersbach, E. K. Miller, and D. D. Dougherty. "Deep brain stimulation of the internal capsule enhances human cognitive control and prefrontal cortex function". In: *Nature Communications* 10 (Apr. 2019). DOI: 10.1038/s41467-019-09557-4 (cit. on p. 8).

[Wol06] C. H. Wolters, A. Anwander, X. Tricoche, D. Weinstein, M. A. Koch, and R. S. MacLeod. "Influence of tissue conductivity anisotropy on EEG/MEG field and return current computation in a realistic head model: A simulation and visualization study using high-resolution finite element modeling". In: *NeuroImage* 30.3 (2006), pp. 813–826. ISSN: 1053-8119. DOI: 10.1016/j.neuroimage.2005.10.014 (cit. on p. 152).

[Xia17] J. Xia, P. He, X. Cai, D. Zhang, and N. Xie. "Magnetic resonance and computed tomography image fusion technology in patients with Parkinson's disease after deep brain stimulation". In: *Journal of the Neurological Sciences* 381 (2017), pp. 250–255. ISSN: 0022-510X. DOI: 10.1016/j.jns.2017.08.3267 (cit. on pp. 3, 11).

[Yam00] T. Yamazaki, K. Kamijo, A. Kenmochi, S Fukuzumi, T. Kiyuna, Y. Takaki, and Y. Kuroiwa. "Multiple Equivalent Current Dipole Source Localization of Visual Event-Related Potentials During Oddball Paradigm With Motor Response". In: *Brain Topography* 12 (2000), pp. 159–175. DOI: 10.1023/A:1023467806268 (cit. on p. 19).

[Zar20] M. Z. Zarzycki and I. Domitrz. "Stimulation-induced side effects after deep brain stimulation – a systematic review". In: *Acta Neuropsychiatrica* 32.2 (2020), 57–64. DOI: 10.1017/neu.2019.35 (cit. on p. 2).

[Zha13] J. Zhang, T. Raij, M. Hämäläinen, and D. Yao. "MEG Source Localization Using Invariance of Noise Space". In: *PLOS ONE* 8.3 (2013), e58408. DOI: 10.1371/journal.pone.0058408 (cit. on p. 19).

[Zri11] L. Zrinzo, F. Yoshida, M. I. Hariz, J. Thornton, T. Foltynie, T. A. Yousry, and P. Limousin. "Clinical Safety of Brain Magnetic Resonance Imaging with Implanted Deep Brain Stimulation Hardware: Large Case Series and Review of the Literature". In: *World Neurosurgery* 76.1 (2011), pp. 164–172. ISSN: 1878-8750. DOI: 10.1016/j.wneu.2011.02.029 (cit. on p. 11).

[Zim70] J. E. Zimmerman, P. Thiene, and J. T. Harding. "Design and Operation of Stable rf-Biased Superconducting Point-Contact Quantum Devices, and a Note on the Properties of Perfectly Clean Metal Contacts". In: *Journal of Applied Physics* 41.4 (1970), pp. 1572–1580. DOI: 10.1063/1.1659074 (cit. on p. 16).